

HIGHLIGHTS IN CARDIOVASCULAR IMAGING: 2021

EDITED BY: Christos Bourantas, Karthik H. Chandrasekharan,
Djawid Hashemi and Sebastian Kelle
PUBLISHED IN: Frontiers in Cardiovascular Medicine



frontiers

Frontiers eBook Copyright Statement

The copyright in the text of individual articles in this eBook is the property of their respective authors or their respective institutions or funders. The copyright in graphics and images within each article may be subject to copyright of other parties. In both cases this is subject to a license granted to Frontiers.

The compilation of articles constituting this eBook is the property of Frontiers.

Each article within this eBook, and the eBook itself, are published under the most recent version of the Creative Commons CC-BY licence.

The version current at the date of publication of this eBook is CC-BY 4.0. If the CC-BY licence is updated, the licence granted by Frontiers is automatically updated to the new version.

When exercising any right under the CC-BY licence, Frontiers must be attributed as the original publisher of the article or eBook, as applicable.

Authors have the responsibility of ensuring that any graphics or other materials which are the property of others may be included in the CC-BY licence, but this should be checked before relying on the CC-BY licence to reproduce those materials. Any copyright notices relating to those materials must be complied with.

Copyright and source acknowledgement notices may not be removed and must be displayed in any copy, derivative work or partial copy which includes the elements in question.

All copyright, and all rights therein, are protected by national and international copyright laws. The above represents a summary only. For further information please read Frontiers' Conditions for Website Use and Copyright Statement, and the applicable CC-BY licence.

ISSN 1664-8714

ISBN 978-2-88976-487-7

DOI 10.3389/978-2-88976-487-7

About Frontiers

Frontiers is more than just an open-access publisher of scholarly articles: it is a pioneering approach to the world of academia, radically improving the way scholarly research is managed. The grand vision of Frontiers is a world where all people have an equal opportunity to seek, share and generate knowledge. Frontiers provides immediate and permanent online open access to all its publications, but this alone is not enough to realize our grand goals.

Frontiers Journal Series

The Frontiers Journal Series is a multi-tier and interdisciplinary set of open-access, online journals, promising a paradigm shift from the current review, selection and dissemination processes in academic publishing. All Frontiers journals are driven by researchers for researchers; therefore, they constitute a service to the scholarly community. At the same time, the Frontiers Journal Series operates on a revolutionary invention, the tiered publishing system, initially addressing specific communities of scholars, and gradually climbing up to broader public understanding, thus serving the interests of the lay society, too.

Dedication to Quality

Each Frontiers article is a landmark of the highest quality, thanks to genuinely collaborative interactions between authors and review editors, who include some of the world's best academicians. Research must be certified by peers before entering a stream of knowledge that may eventually reach the public - and shape society; therefore, Frontiers only applies the most rigorous and unbiased reviews.

Frontiers revolutionizes research publishing by freely delivering the most outstanding research, evaluated with no bias from both the academic and social point of view. By applying the most advanced information technologies, Frontiers is catapulting scholarly publishing into a new generation.

What are Frontiers Research Topics?

Frontiers Research Topics are very popular trademarks of the Frontiers Journals Series: they are collections of at least ten articles, all centered on a particular subject. With their unique mix of varied contributions from Original Research to Review Articles, Frontiers Research Topics unify the most influential researchers, the latest key findings and historical advances in a hot research area! Find out more on how to host your own Frontiers Research Topic or contribute to one as an author by contacting the Frontiers Editorial Office: frontiersin.org/about/contact

HIGHLIGHTS IN CARDIOVASCULAR IMAGING: 2021

Topic Editors:

Christos Bourantas, University College London, United Kingdom

Karthik H. Chandrasekharan, Barts Heart Centre, United Kingdom

Djawid Hashemi, Charité Universitätsmedizin Berlin, Germany

Sebastian Kelle, Deutsches Herzzentrum Berlin, Germany

Citation: Bourantas, C., Chandrasekharan, K. H., Hashemi, D., Kelle, S., eds. (2022). Highlights in Cardiovascular Imaging: 2021. Lausanne: Frontiers Media SA.
doi: 10.3389/978-2-88976-487-7

Table of Contents

- 05 Editorial: Highlights in Cardiovascular Imaging: 2021**
Djawid Hashemi, Sebastian Kelle, Christos V. Bourantas and Karthik H. Chandrasekharan
- 09 Cinematic Rendering in Mixed-Reality Holograms: A New 3D Preoperative Planning Tool in Pediatric Heart Surgery**
Pia Gehrsitz, Oliver Rompel, Martin Schöber, Robert Cesnjevar, Ariawan Purbojo, Michael Uder, Sven Dittrich and Muhannad Alkassar
- 21 Extraction of Coronary Atherosclerotic Plaques From Computed Tomography Imaging: A Review of Recent Methods**
Haipeng Liu, Aleksandra Wingert, Jian'an Wang, Jucheng Zhang, Xinhong Wang, Jianzhong Sun, Fei Chen, Syed Ghufraan Khalid, Jun Jiang and Dingchang Zheng
- 43 Partitioning the Right Ventricle Into 15 Segments and Decomposing Its Motion Using 3D Echocardiography-Based Models: The Updated ReVISION Method**
Márton Tokodi, Levente Staub, Ádám Budai, Bálint Károly Lakatos, Máté Csákvári, Ferenc Imre Suhai, Liliána Szabó, Alexandra Fábán, Hajnalka Vágó, Zoltán Tösér, Béla Merkely and Attila Kovács
- 61 Micro-CT-Based Quantification of Extracted Thrombus Burden Characteristics and Association With Angiographic Outcomes in Patients With ST-Elevation Myocardial Infarction: The QUEST-STEMI Study**
Efstratios Karagiannidis, Andreas S Papazoglou, Georgios Sofidis, Evangelia Chatzinikolaou, Kleoniki Keklikoglou, Eleftherios Panteris, Anastasios Kartas, Nikolaos Stalikas, Thomas Zegkos, Fotios Girtovitis, Dimitrios V. Moysidis, Leandros Stefanopoulos, Kleanthis Koupidis, Stavros Hadjimiltiades, George Giannakoulas, Christos Arvanitidis, James S. Michaelson, Haralambos Karvounis and Georgios Sianos
- 72 Rational and Design of the SIMULATOR Study: A Multicentre Randomized Study to Assess the Impact of SIMulation-bAseD Training on Transoesophageal echocardiOgraphy leaRning for Cardiology Residents**
Théo Pezel, Anne Bernard, Yoan Lavie Badie, Julien Dreyfus, Etienne Audureau, Yohann Bohbot, Damien Fard, Arnaud Hubert, Lee S. Nguyen, Cécile Monteil, Loïc Bière, Florent Le Ven, Marjorie Canu, Sophie Ribeyrolles, Baptiste Mion, Basile Mouhat, Baptiste Bazire, Charles Fauvel, Julien Ternacle, Jennifer Cautela, Théo Cambet, Thierry Le Tourneau, Erwan Donal, Stéphane Lafitte, Nicolas Mansencal and Augustin Coisne
- 80 Etiology-Discriminative Multimodal Imaging of Left Ventricular Hypertrophy and Synchrotron-Based Assessment of Microstructural Tissue Remodeling**
Filip Loncaric, Patricia Garcia-Canadilla, Ana Garcia-Alvarez, Laura Sanchis, Susana Prat, Adelina Doltra, Eduard Quintana, Daniel Pereda, Hector Dejea, Anne Bonnin, Marta Sitges and Bart Bijmens

- 93** *Age- and Sex-Specific Changes in CMR Feature Tracking-Based Right Atrial and Ventricular Functional Parameters in Healthy Asians*
Shuang Leng, Jiajun Guo, Ru-San Tan, Ping Chai, Lynette Teo, Marielle V. Fortier, Chao Gong, Xiaodan Zhao, Ching Ching Ong, John C. Allen, Wen Ruan, Angela S. Koh, Teng Hong Tan, James W. Yip, Ju Le Tan, Yucheng Chen and Liang Zhong
- 106** *Left Ventricular Remodeling and Myocardial Work: Results From the Population-Based STAAB Cohort Study*
Floran Sahiti, Caroline Morbach, Vladimir Cejka, Judith Albert, Felizitas A. Eichner, Götz Gelbrich, Peter U. Heuschmann and Stefan Störk on behalf of the STAAB Consortium
- 118** *The Predictive Value of Right Ventricular Longitudinal Strain in Pulmonary Hypertension, Heart Failure, and Valvular Diseases*
Marijana Tadic, Nicoleta Nita, Leonhard Schneider, Johannes Kersten, Dominik Buckert, Birgid Gonska, Dominik Scharnbeck, Christine Reichart, Evgeny Belyavskiy, Cesare Cuspidi and Wolfgang Rottbauer
- 129** *Automated Quality-Controlled Cardiovascular Magnetic Resonance Pericardial Fat Quantification Using a Convolutional Neural Network in the UK Biobank*
Andrew Bard, Zahra Raisi-Estabragh, Maddalena Ardissino, Aaron Mark Lee, Francesca Pugliese, Damini Dey, Sandip Sarkar, Patricia B. Munroe, Stefan Neubauer, Nicholas C. Harvey and Steffen E. Petersen



Editorial: Highlights in Cardiovascular Imaging: 2021

Djawid Hashemi^{1,2,3*}, Sebastian Kelle^{1,2,3}, Christos V. Bourantas^{4,5,6} and Karthik H. Chandrasekharan⁴

¹ Department of Internal Medicine and Cardiology, German Heart Center Berlin, Berlin, Germany, ² Department of Internal Medicine and Cardiology, Charité – Universitätsmedizin Berlin, Corporate Member of Freie Universität Berlin and Humboldt Universität zu Berlin, Berlin, Germany, ³ Deutsches Zentrum Für Herz-Kreislaufforschung (German Centre for Cardiovascular Research), Berlin, Germany, ⁴ Department of Cardiology, Barts Heart Centre, Barts Health National Health Service (NHS) Trust, London, United Kingdom, ⁵ Centre for Cardiovascular Medicine and Devices, William Harvey Research Institute, Queen Mary University London, London, United Kingdom, ⁶ Institute of Cardiovascular Sciences, University College London, London, United Kingdom

Keywords: cardiovascular, artificial intelligence (AI), imaging, atherosclerosis, heart failure

Editorial on the Research Topic

Highlights in Cardiovascular Imaging: 2021

INTRODUCTION

This Research Topic presents the highlights in Cardiovascular Imaging and includes a range of studies and reviews across multiple imaging modalities and subspecialties, that describe recent advances in established modalities, including echocardiography, cardiac computed tomography (CT), and cardiac magnetic resonance imaging (CMR). It also presents novel applications of micro-CT and X-ray phase-contrast imaging, as well as innovative techniques e.g., 3D holograms, and discusses the use of artificial intelligence (AI) in cardiovascular imaging. We selected the studies from the most read and downloaded articles in 2021 in this journal. The selection of articles by the authors aimed to highlight novel techniques and applications across the broad range of cardiovascular imaging.

ARTIFICIAL INTELLIGENCE

Artificial intelligence (AI) algorithms have revolutionized image analysis and improved the predictive value of imaging parameters as shown by Bard et al. as well as Kameshina et al.

Bard et al. successfully compared an AI approach to both segment and quantify pericardial adipose tissue (PAT) by CMR in a dataset from the UK Biobank. The results were compared to the gold standard of PAT quantification by cardiac CT. This study showed that the CMR-derived PAT volumes were comparable to the PAT estimated by CT and that PAT volume was associated with the presence of diabetes independently from other clinical characteristics.

In the study of Kameshima et al. machine learning (ML) methods were used to phenotype heart failure (HF) patients with diastolic dysfunction. These patients from a Japanese HF registry were grouped using two approaches: the first relied on a ML based approach and the second on the grading system recommended by the echocardiographic guidelines for assessing diastolic

OPEN ACCESS

Edited and reviewed by:

Ali Yilmaz,
University Hospital Münster, Germany

*Correspondence:

Djawid Hashemi
djawid.hashemi@charite.de

Specialty section:

This article was submitted to
Cardiovascular Imaging,
a section of the journal
Frontiers in Cardiovascular Medicine

Received: 02 May 2022

Accepted: 20 May 2022

Published: 08 June 2022

Citation:

Hashemi D, Kelle S, Bourantas CV
and Chandrasekharan KH (2022)
Editorial: Highlights in Cardiovascular
Imaging: 2021.
Front. Cardiovasc. Med. 9:934668.
doi: 10.3389/fcvm.2022.934668

dysfunction. The ML approach showed to be superior to the echocardiography guideline categories in predicting HF hospitalization in these patients highlighting its value for more accurate risk stratification.

CORONARY IMAGING STUDIES

Novel micro-CT technology was used by Karagiannidis et al. to visualize and analyse extracted thrombus material in 113 patients undergoing primary percutaneous coronary intervention (PCI) for ST-elevation myocardial infarction (STEMI) in a single center. Micro-CT provided non-destructive visualization of aspirated thrombus, allowing reproducible quantification of thrombus volume, surface, and density. The authors found that patients with high angiographic thrombus burden and higher residual thrombus had larger thrombus aspirated; more importantly they showed that, higher thrombus volume and surface area were associated with adverse angiographic outcomes (distal embolization and no-reflow phenomenon).

This analysis highlighted the value of micro-CT in assessing the extracted thrombus burden and its clinical implications. This is especially significant as a meta-analysis of 3 randomized trials demonstrated that there is no prognostic benefit of the routine use of thrombus aspiration in patients with STEMI but in patients with high thrombus burden thrombus aspiration can be beneficial as it is associated with a reduction in cardiovascular mortality and all cause mortality, at the expense of an increased risk of stroke or TIA at 30 days (1).

The review of Liu et al. summarized the methods introduced for coronary plaque segmentation in cardiac CT. Thirty one approaches were presented and categorized into either 2D or 3D plaque extraction methods, with each relevant study within each category subsequently characterized with respect to data quality, methodological innovation and performance.

This detailed review not only highlighted recent advances in CT image but also underscored the need for further research in the field. There is apparently an unmet need to validate the developed methods in large databases and improve plaque extraction accuracy using advanced methods that will allow not only fast and accurate quantification of the atheroma burden but also assessment of plaque vulnerability.

MYOCARDIAL IMAGING STUDIES

Reference ranges are key elements for diagnosis of cardiovascular disease, risk stratification and treatment planning and can be assessed by the distribution of the relevant variable or its predictive value. The study of Leng et al. examined 360 healthy subjects from West China prospectively, and included patients aged 21–79 years with no known cardiovascular disease or uncontrolled cardiovascular risk factors. CMR was used to measure right heart function parameters, including tricuspid annular dynamics as well as longitudinal strain

values of the right ventricle and the right atrium. This data allowed for the first time the definition of established age and sex specific reference ranges for tricuspid annular dynamics derived by CMR in healthy individuals which are expected to allow more accurate evaluation of right ventricular function.

Zhao et al. compared LV geometry by three-dimensional (3D) echocardiography and CMR. The authors analyzed 70 subjects (18 patients, 52 healthy volunteers) who had both an 3D-echocardiography and CMR, within 1 h. The authors found there was a systematic bias between the volumes assessed by 3D-echocardiography and those by CMR. They concluded that the systematic signal dropout and the differences in appearances of trabeculae have led to discrepancies in the delineation of LV geometry at anterior and lateral regions resulting in an underestimation of the LV volumes by echocardiography.

Myocarditis

Suspected acute myocarditis is a leading indication for CMR. State-of-the-art diagnostic criteria for myocarditis are based on the consensus Lake Louise Criteria (LLC) published in 2018 which are an update of the LLC presented in 2009 (2, 3). Li et al. prospectively assessed in 73 patients with a clinically suspected myocarditis which CMR parameters from the 2009 and 2018 LLC can diagnose myocarditis most accurately at a 3.0 Tesla scanner. The gold standard in that study was the presence of inflammation on endomyocardial biopsy (EMB). T1 and T2 mapping techniques showed the highest positive predictive value and were superior compared to the LLC 2018 and LLC 2009 criteria: the area under the curve for T1 mapping + T2 mapping was 0.95 while it was 0.91 for LLC 2018 alone, 0.76 for LLC 2009.

Right Ventricular Function

Meng et al., examined the value of right ventricular 3D speckle-tracking strain and ejection fraction in predicting heart failure (HF) related hospitalizations or death in patients with HF with preserved ejection fraction (HFpEF). During a median of 17 months 48% of the included patients ($n = 93$) reached the primary endpoint; in that study impaired 3D-speckle-tracking echocardiography values showed to be strongly associated with the occurrence of the primary endpoint of the study suggesting that these variables may be a useful tool for risk stratification in this population.

Furthermore, Tadic et al. noted that right ventricular LS is not routinely assessed, and summarized the existing methodologies for evaluating right ventricular longitudinal strain (LS) using transthoracic echocardiography and presented the evidence supporting its prognostic value in patients with pulmonary hypertension, heart failure and valvular heart disease. For example, a meta-analysis of 1,169 patients with pulmonary hypertension found that those with an RV free-wall strain $> -22\%$ had a significantly higher risk of all-cause mortality. The authors suggest that routine measurement of right ventricular LS may therefore aid risk stratification, with patients possibly being reclassified into higher risk groups when it is taken into account.

With the growing evidence supporting the value of assessing RV function, the ReVISION method was described in 2017

(4). This uses 3D echocardiography (3DE) to quantify the relative contribution of longitudinal, radial, and anteroposterior shortening in the global RV ejection fraction. Tokodi et al. have recently provided details of the updated ReVISION method and algorithm, particularly for volumetric partitioning of the RV cavity and calculation of longitudinal, circumferential, and area strains using 3DE datasets, and also compared the reproducibility of RV function obtained from 3DE and CMR. This method can be used to further evaluate RV function in different disease states, providing further valuable information when compared with routine echocardiographic evaluation.

Left Ventricular Hypertrophy

A pilot study of 3 patients undertaken by Loncaric et al. provided novel insight into visualizing myocardial remodeling in left ventricular hypertrophy (LVH). Synchrotron radiation-based X-ray phase-contrast imaging (X-PCI) is a research methodology that enables direct measurement of myocardial structure based on changes in X-ray intensity and phase, and enables visualization of individual myocytes and analysis of cardiac microstructure. The authors used 3D X-PCI on myocardial tissue samples obtained during surgical myectomy for three patients with obstructive LVH to assess myocyte organization, 3D connective tissue distribution, and vasculature and compared these findings with the non-invasive cardiac imaging findings (transthoracic echocardiography and CMRI) performed prior to myectomy. The authors found that the myocyte and connective tissue microstructural organization was different in different myocardial pathologies. This is a small pilot study which highlights the potential utility of 3D X-PCI and is expected to provide the substrate for the conduction of larger scale studies that will provide compelling evidence which will justify its routine use in clinical setting (e.g. more compact synchrotrons), with the aim of establishing the etiology of LVH when non-invasive imaging is non-diagnostic.

RISK PREDICTION AND OPTIMAL TREATMENT PLANNING

Rank et al. examined the long term implications of aortic valve replacement on reverse ventricular remodeling. The authors analyzed CMR data acquired 1, 5, and 10 years after aortic valve replacement (AVR) for both aortic stenosis (AS) and aortic regurgitation (AR). The authors found that patients with AR had more long term alteration of myocardial function compared with patients with AS, for example patients with AR had no improvement in myocardial longitudinal strain following AVR, whereas patients with AS show an improvement 1 year after AVR and this remains constant after. The authors conclude that CMR is a useful tool to monitor patients with aortic valve disease, helping to plan AVR at an appropriate stage prior to irreversible structural heart damage.

Moreover, Sahiti et al. use myocardial work analysis derived from echocardiographic and blood pressure measurements, to show that increased LV volume and mass reduce global

work efficiency as the cardiac cycle demands more energy. They also found altered myocardial work patterns in hypertensive patients even with normal LV volume and mass. These findings indicate that increased wasted energy combined with LV hypertrophy might be an early sign of hypertensive heart disease; however, further longitudinal studies and more compelling evidence are required to prove this hypothesis.

Gehrsitz et al. described how preoperative planning in pediatric patients with congenital heart disease can be optimized by using cinematic rendering to create three-dimensional (3D) images from two-dimensional (2D) CT or CMR. These 3D images were shown to the surgeon preoperatively on a 2D screen, as a hologram with special glasses (HoloLens®) and as a 3D print. This value of this information was assessed using questionnaires. It was shown that the combination of an extremely photo-realistic presentation via cinematic rendering and the spatial presentation in 3D space via mixed-reality technology enabled detailed assessment of the anatomy and pathology prior to the surgery which was helpful for treatment planning.

The implications of COVID-19 infection on cardiovascular pathology is of great interest. Li et al. demonstrated that routine non-contrast chest CT imaging in patients with COVID-19, performed to evaluate lung disease, also provided useful prognostic implications and prediction of cardiovascular complications. In that study 241 consecutive hospitalized patients with confirmed COVID-19 were enrolled; three cardiac measurements were taken on CT imaging: left atrial diameter (LAD), left ventricular (LV) length and the cardiothoracic ratio (CTR). The authors found that a combination of LAD+LV (cutoff of 11.8 cm) and the CTR (cutoff of 0.8) was a predictor of major adverse cardiovascular events with a sensitivity of 82.6% and specificity of 80.2%.

Tanacli et al. evaluated the value of endomyocardial biopsies (EMB) in COVID-19 compared to CMR to assess myocardial injury. They included 32 patients with persistent symptoms after COVID-19, 22 patients with acute myocarditis not related to COVID-19 and 16 healthy volunteers. These subjects had a baseline CMR as well as a follow-up scan; 10 of the post-COVID-19 and 15 of the non-COVID-19 patients had an EMB. All COVID-19 patients showed impaired myocardial deformation as well as altered functional and anatomical characteristics (e.g., RV mass and T1 times), nevertheless the LLC criteria for myocarditis were only fulfilled in 9% of patients. In these patients traces of previous myocardial inflammation were identifiable without evidence of ongoing inflammation in EMB.

CONCLUSION

These papers were the most frequently downloaded and distinguishing manuscripts of 2021. It is clear from the breadth of research and data presented in this topic, that cardiovascular imaging research is a fast moving field, with advances that

have potential clinical applications across a wide range of cardiac pathologies, contributing in improved diagnosis, risk stratification and better treatment planning.

AUTHOR CONTRIBUTIONS

DH and KC drafted and revised the manuscript. SK and CB initiated the manuscript and guided with editorial comments

after review. All authors contributed to the article and approved the submitted version.

FUNDING

DH received a CMR specific research grant from the German Centre for Cardiovascular Research (DZHK, Grant Number: 81X3100214).

REFERENCES

1. Jolly SS, James S, Džavík V, Cairns JA, Mahmoud KD, Zijlstra F, et al. Thrombus aspiration in ST-segment-elevation myocardial infarction: an individual patient meta-analysis: thrombectomy trialists collaboration. *Circulation*. (2017) 135:143–52. doi: 10.1161/CIRCULATIONAHA.116.025371
2. Ferreira VM, Schulz-Menger J, Holmvang G, Kramer CM, Carbone I, Sechtem U, et al. Cardiovascular magnetic resonance in nonischemic myocardial inflammation: expert recommendations. *J Am Coll Cardiol*. (2018) 72:3158–76. doi: 10.1016/j.jacc.2018.09.072
3. Friedrich MG, Sechtem U, Schulz-Menger J, Holmvang G, Alakija P, Cooper LT, et al. Cardiovascular magnetic resonance in myocarditis: a JACC white paper. *J Am Coll Cardiol*. (2009) 53:1475–87. doi: 10.1016/j.jacc.2009.02.007
4. Lakatos B, Tosér Z, Tokodi M, Doronina A, Kosztin A, Muraru D, et al. Quantification of the relative contribution of the different right ventricular wall motion components to right ventricular ejection fraction: the ReVISION method. *Cardiovasc Ultrasound*. (2017) 15:8. doi: 10.1186/s12947-017-0100-0

Conflict of Interest: The authors declare that the research was conducted in the absence of any commercial or financial relationships that could be construed as a potential conflict of interest.

Publisher's Note: All claims expressed in this article are solely those of the authors and do not necessarily represent those of their affiliated organizations, or those of the publisher, the editors and the reviewers. Any product that may be evaluated in this article, or claim that may be made by its manufacturer, is not guaranteed or endorsed by the publisher.

Copyright © 2022 Hashemi, Kelle, Bourantas and Chandrasekharan. This is an open-access article distributed under the terms of the Creative Commons Attribution License (CC BY). The use, distribution or reproduction in other forums is permitted, provided the original author(s) and the copyright owner(s) are credited and that the original publication in this journal is cited, in accordance with accepted academic practice. No use, distribution or reproduction is permitted which does not comply with these terms.



Cinematic Rendering in Mixed-Reality Holograms: A New 3D Preoperative Planning Tool in Pediatric Heart Surgery

Pia Gehrsitz¹, Oliver Rompel², Martin Schöber¹, Robert Cesnjevar³, Ariawan Purbojo³, Michael Uder², Sven Dittrich¹ and Muhannad Alkassar^{1*}

¹ Department of Pediatric Cardiology, University Hospital Erlangen, Friedrich-Alexander University Erlangen-Nürnberg (FAU), Erlangen, Germany, ² Institute of Radiology, University Hospital Erlangen, Friedrich-Alexander University Erlangen-Nürnberg (FAU), Erlangen, Germany, ³ Department of Pediatric Cardiac Surgery, University Hospital Erlangen, Friedrich-Alexander University Erlangen-Nürnberg (FAU), Erlangen, Germany

OPEN ACCESS

Edited by:

Sebastian Kelle,
Deutsches Herzzentrum
Berlin, Germany

Reviewed by:

Dirk Loßnitzer,
Universität Mannheim, Germany
Radu Tanacii,
German Heart Center
Berlin, Germany

*Correspondence:

Muhannad Alkassar
muhannad.alkassar@uk-erlangen.de

Specialty section:

This article was submitted to
Cardiovascular Imaging,
a section of the journal
Frontiers in Cardiovascular Medicine

Received: 25 November 2020

Accepted: 13 January 2021

Published: 09 February 2021

Citation:

Gehrsitz P, Rompel O, Schöber M, Cesnjevar R, Purbojo A, Uder M, Dittrich S and Alkassar M (2021) Cinematic Rendering in Mixed-Reality Holograms: A New 3D Preoperative Planning Tool in Pediatric Heart Surgery. *Front. Cardiovasc. Med.* 8:633611. doi: 10.3389/fcvm.2021.633611

Cinematic rendering (CR) is based on a new algorithm that creates a photo-realistic three-dimensional (3D) picture from cross-sectional images. Previous studies have shown its positive impact on preoperative planning. To date, CR presentation has only been possible on 2D screens which limited natural 3D perception. To depict CR-hearts spatially, we used mixed-reality technology and mapped corresponding hearts as holograms in 3D space. Our aim was to assess the benefits of CR-holograms in the preoperative planning of cardiac surgery. Including 3D prints allowed a direct comparison of two spatially resolved display methods. Twenty-six patients were recruited between February and September 2019. CT or MRI was used to visualize the patient's heart preoperatively. The surgeon was shown the anatomy in cross-sections on a 2D screen, followed by spatial representations as a 3D print and as a high-resolution hologram. The holographic representation was carried out using mixed-reality glasses (HoloLens®). To create the 3D prints, corresponding structures were segmented to create STL files which were printed out of resin. In 22 questions, divided in 5 categories (3D-imaging effect, representation of pathology, structure resolution, cost/benefit ratio, influence on surgery), the surgeons compared each spatial representation with the 2D method, using a five-level Likert scale. The surgical preparation time was assessed by comparing retrospectively matched patient pairs, using a paired *t*-test. CR-holograms surpassed 2D-monitor imaging in all categories. CR-holograms were superior to 3D prints in all categories (mean Likert scale 4.4 ± 1.0 vs. 3.7 ± 1.3 , $P < 0.05$). Compared to 3D prints it especially improved the depth perception (4.7 ± 0.7 vs. 3.7 ± 1.2) and the representation of the pathology (4.4 ± 0.9 vs. 3.6 ± 1.2). 3D imaging reduced the intraoperative preparation time ($n = 24$, 59 ± 23 min vs. 73 ± 43 min, $P < 0.05$). In conclusion, the combination of an extremely photo-realistic presentation via cinematic rendering and the spatial presentation in 3D space via mixed-reality technology allows a previously unattained level of comprehension of anatomy and pathology in preoperative planning.

Keywords: mixed-reality, cinematic rendering, 3D printing, preoperative planning, pediatric heart surgery, congenital heart disease

INTRODUCTION

Due to the complex and highly individual anatomy of patients with congenital heart disease (CHD), it is essential to have precise preoperative planning and good morphologic imaging for surgical success. Currently, three-dimensional (3D) imaging offers the most realistic representation of cardiac structures, and has therefore gained importance in recent years (1–5).

3D images are generated from two-dimensional (2D) cross-sectional images produced using computed tomography (CT) and magnetic resonance imaging (MRI). There are two methods for generating 3D images from 2D datasets: (1) creating 3D segmentation by manually selecting interesting structures, and (2) calculating a 3D image automatically, based on rendering algorithms. Siemens Healthineers has developed a new volume rendering technique called cinematic rendering (CR). CR generates a more photo-realistic 3D depiction than previously used rendering algorithms, by imitating natural light interactions (3, 6). Multiple previous studies have confirmed that CR provides a more photo-realistic view and improvements in shape and depth perception compared with cross-sectional imaging or volume rendering (7–10).

Until recently, 3D-rendered images can be presented only on a 2D screen. Currently, it is possible to present these 3D images in 3D space with either physical or virtual 3D imaging. Physical 3D imaging is generated by producing a 3D-printed model from a manually-generated 3D image. Virtual 3D imaging is generated by creating a hologram by using mixed-reality technology. The latest development is an application that integrates CR and mixed-reality techniques for use with the HoloLens® (Microsoft, Redmond, USA) (11). The current gold standard for spatial imaging in preoperative planning is 3D printing. However, it has mostly been described in case reports and systematic reviews of its advantages are still rare. Furthermore, a significant benefit compared to 2D imaging regarding the overall surgery time could not be shown yet for 3D printing. Therefore, we compared both 3D imaging methods additional to the standard preoperative imaging on 2D screen.

The aim of this study was to determine the benefits of spatial representation of CR-reconstructed heart structures in the preoperative planning of pediatric heart surgery. By including 3D prints, a direct comparison of two spatially resolving display methods was possible.

MATERIALS AND METHODS

This prospective study was performed in accordance with the Guidelines for Good Clinical Practice. All CT and MRI datasets were accessed with permission through informed consent from both parents; in no case were the images taken exclusively for this study.

The patients were recruited between February and September 2019. All patients who underwent cross-sectional imaging in preparation for surgery were included in the study. The decision to perform cross-sectional imaging was based on comprehensive echocardiography performed previously. Because high-quality cross-sectional images from MRI and CT are equally suitable

for 3D imaging (2–4, 6, 7, 12–15), cross-sectional images were recorded using MRI or CT depending on the clinical question. If morphology was the only question, CT was used. If there were additional functional questions, MRI was carried out.

Data Acquisition

The CT scans were performed during the post venous phase, after injecting contrast medium peripheral. The images were acquired in 0.6 mm slices, using either a second-generation 128-slice dual-source CT scanner (SOMATOM Definition Flash; Siemens Healthcare GmbH, Erlangen, Germany) or a third-generation 192-slice dual-source CT scanner (SOMATOM Definition Force; Siemens Healthcare, Erlangen, Germany). Modern low-dose (0.2–0.5 mSv) protocols were used. The MRI datasets were collected in diastolic heart phase, in a whole-heart sequence, in 0.8 mm slices, with a 1.5-Tesla MRI-scanner (MAGNETOM Aera; Siemens Healthcare GmbH, Erlangen, Germany).

Spatial View

To set up the spatial representation, datasets were exported from the advanced visualization imaging software, *syngo.via* (Version VB30A; Siemens Healthcare GmbH, Erlangen, Germany), and saved in the standard “Digital Imaging and Communications in Medicine” (DICOM)-format.

DICOM-data were used to visualize the heart directly in the cinematically rendered view with the newly developed prototype mixed-reality *syngo.via* application “Cinematic Reality.” The new *syngo.via* application generated a cinematically rendered hologram (CR-hologram), which could be viewed with the HoloLens®. The hologram was projected in a firmly fixed position in the room, so the observer could walk around the heart and examine it from every side. **Figure 1** shows a surgeon looking at a CR-hologram through the HoloLens®.

To create a realistic 3D-printed model from cross-sectional images, various pre-processing steps were necessary. First, DICOM-data were exported into the open-source software, 3D Slicer (Version 4.11; <http://www.slicer.org>). In this software, the image was segmented based on an adjustable threshold chosen so that only the voxels of interest were marked. The marking depended on the master volume intensity range of the individual voxels. In addition to the whole heart, neighboring vessels were marked that were relevant to later surgery.

The created model was saved in standard tessellation language (STL) file format, which was compatible with the 3D printer. Next, the model was produced by 3D printer (Form 2, Formlabs, Sommerville, USA) out of resin at a resolution of 0.1 mm layers using standardized printing plans. As a post-processing step, important structures such as coronary arteries were marked in different colors to facilitate orientation. An overview of the main steps for generating a 3D-printed model in comparison to a CR-hologram is given in **Figure 2**. The imaging processing time for each technique was recorded.

Study Design

First, the patient’s cross-sectional images were presented on a 2D screen, which was previously the common technique for presenting preoperative imaging material. The CR-hologram,



FIGURE 1 | Surgeon looking at a CR-hologram of a patient's heart with dextro-transposition of the great arteries using HoloLens®. The figure illustrates an image for which the view of the surgeon through the HoloLens® was combined with a photo in which he is working with the HoloLens®.

and subsequently the 3D-printed model, were then presented to the surgeon in an upright position. To provide a comparison of the newly introduced spatial 3D-imaging techniques and the representation on the 2D screen, the surgeons were asked to complete a questionnaire for each spatial 3D-imaging technique. The two 3D techniques were also directly compared with each other.

Questionnaire

In total, the questionnaire comprised 22 items, each rated on a 5-point Likert scale. The five response options ranged from “clearly superior” (5 points) to “clearly inferior” (1 point). The questionnaire items were structured in five subgroups to provide a better overview: 3D-imaging effect, representation of the pathology, anatomical structure resolution, cost/benefit ratio, and influence on the surgery (Table 2). The reliability of the different items of each dimension was checked using Cronbach's alpha.

Analysis of Surgical Preparation Time

In order to investigate the influence of preoperative spatial representation on the surgical procedure, we compared intraoperative preparation times. Intraoperative preparation

time was defined as the time from the initial cut until the first vessel was clamped. The intraoperative preparation times for study participants were compared with intraoperative preparation times for patients with matching characteristics for whom preoperative imaging in 3D space was not used. The patients were matched for age, weight, operative procedure, previous operations, and the general state of health preoperatively (Table 1). As intraoperative preparation time was analyzed, only patients who underwent the same surgical procedures with the same complexity were matched. Additionally, the intraoperative preparation times of the matched patient pairs were analyzed after being divided into groups in which the “facilitation of preparation” was, respectively, rated of excellent benefit (5 points on the Likert scale) or not (≤ 4 points). A Wilcoxon test was performed to compare the two groups because the *F*-test showed no equality of variance for the “advantageous” group.

Statistical Evaluation

Statistical analyses were performed using IBM SPSS statistics (Version 21; IBM, Armonk, USA). Results of the questionnaires were expressed as mean values with standard deviation

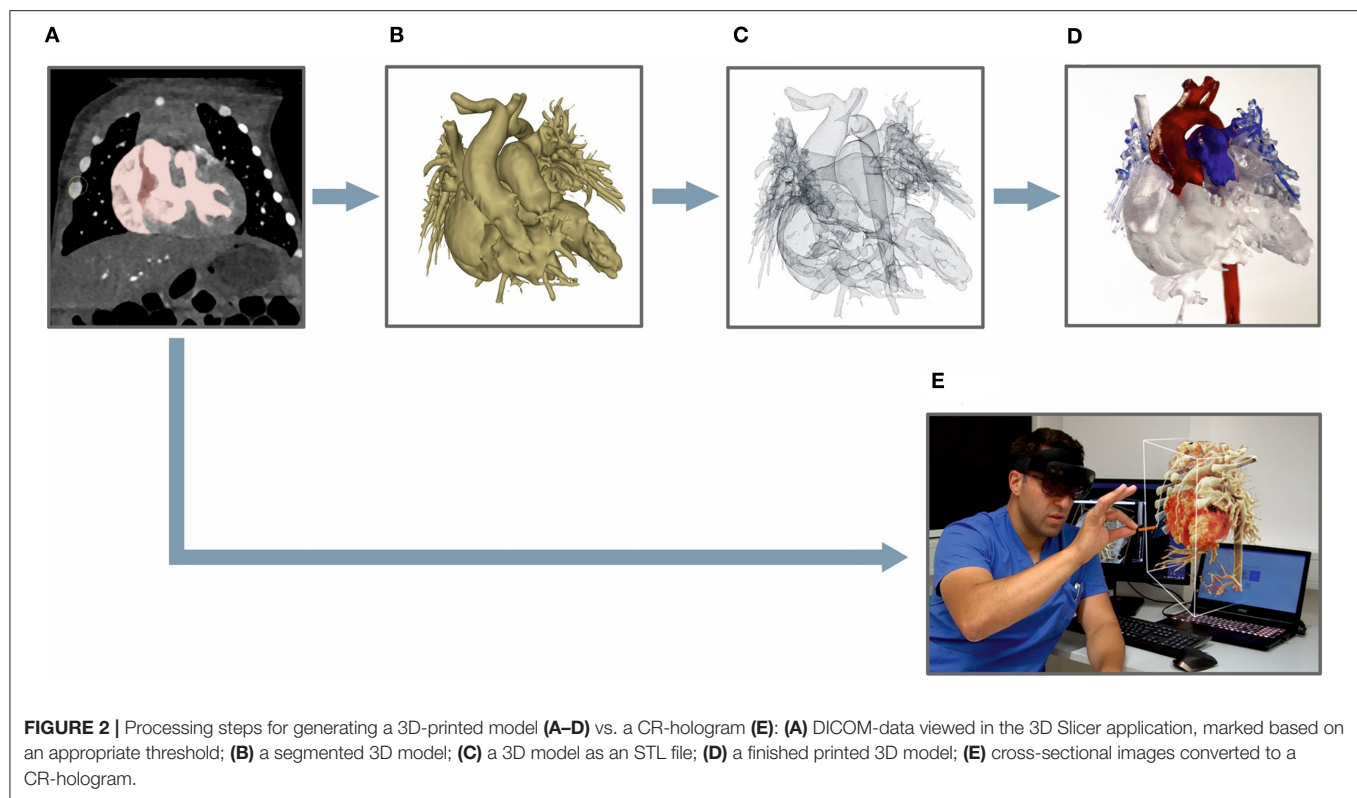


TABLE 1A | Demographic information about the analyzed patient population.

Patient characteristics		Cases	Matched controls
Number		$n = 26$	$n = 24$
Gender	Male	61.5%	58.3%
	Female	38.5%	41.7%
Age (years)		2.0 ± 3.9	2.0 ± 4.7
Weight (kg)		10.5 ± 12.9	10.7 ± 15
Heart lung machine	Yes	92.3%	95.8%
	No	7.7%	4.2%
Access	Median sternotomy	84.6%	87.5%
	Posterolateral	15.4%	12.5%
Previous operations	Yes	34.6%	29.2%
	No	65.4%	70.8%

(SD). Each questionnaire item was analyzed separately and summarized in the five subgroups.

A paired *t*-test was performed to compare the questionnaire results (Likert scale data) of CR-holograms with those of 3D-printed models. As Jeffrey and Norman have shown, parametric tests are superior to non-parametric tests when analyzing Likert scale data (16, 17). To compare the intraoperative preparation times between the patients and matched controls a paired *t*-test was used. The statistical significance level was defined as $P < 0.05$ for all analyses.

The contrast-to-noise ratio (CNR) and signal-to-noise ratio (SNR) were determined independently for CT and MRI via regions of interest (ROIs) using the software *syngo.via*. The SNR was calculated by dividing the mean signal intensity of the aorta in cross-section ($ROI = 1.2 \pm 0.1 \text{ mm}^2$) by the SD of the extra thoracic background noise ($ROI = 2.2 \pm 0.1 \text{ cm}^2$) measured from the air surrounding the patient. For the CNR the mean signal intensity of the left ventricular muscle ($ROI = 1.2 \pm 0.1 \text{ mm}^2$) was subtracted from the mean signal intensity of the aorta and afterwards divided by the SD of the background noise.

RESULTS

We recruited 26 patients with an average age of 2.0 ± 3.9 years. Of the surgeries, 77% concerned mainly outer cardiovascular structures (e.g., great vessels) and 23% inner cardiovascular structures (e.g., valves). Twenty-four patients underwent CT as preoperative imaging modality and 2 patients MRI. CT and MRI datasets were of comparable quality (CNR: MRI: 16.4 ± 1.4 , CT: 13.7 ± 6.4 ; SNR: MRI: 19.8 ± 2.1 , CT: 20.28 ± 8.5). Cross-sectional images for all 26 patients were of high quality without artifacts and could be used successfully for both rendering and 3D printing. Further demographic information about the patients and the conducted surgeries is shown in **Table 1**. The cross-sectional imaging was taken on average 13 days before the surgery took place. The patients' images were of comparable quality; in particular, no difference between the cases and the matched

TABLE 1B | Demographic information about the analyzed patient population.

Case	Imaging	Cases			Matched controls		
		Main diagnosis and kind of operation	Age (years)	Weight (kg)	Main diagnosis and kind of operation	Age (years)	Weight (kg)
1	CT	Single ventricle (1)	<1	3.3	Single ventricle (1)	<1	2.7
2	CT	Pulmonary atresia + VSD ^a (1)	<1	8.0	Pulmonary atresia + VSD (1)	2	12.0
3	CT	CoA ^b (2)	<1	3.1	CoA (2)	<1	4.7
4	CT	Ductus arteriosus aneurysm (3)*	<1	3.4	Ductus arteriosus aneurysm (3)	<1	5.6
5	CT	Single ventricle (4)	<1	3.5	Single ventricle (4)	<1	3.5
6	CT	Pulmonary atresia + VSD (1)	4	18.4	Pulmonary atresia + VSD (1)	2	14.7
7	CT	Single ventricle (1)	<1	3.0	ToF ^c (1)	<1	3.0
8	CT	Truncus arteriosus (1)	<1	3.8	Truncus arteriosus (1)	<1	3.1
9	CT	Single ventricle (5)	<1	7.7	Single ventricle (5)	<1	6.4
10	CT	d-TGA ^d (6)*	<1	3.5	d-TGA (6)	<1	3.3
11	CT	AVSD ^e (7)*	2	11.0	AVSD (7)	1	8.3
12	CT	Aortopulmonary window (7)*	<1	4.1	Aortopulmonary window (7)	<1	3.4
13	MRI	Pulmonary valve disease (8)*	13	52.0	Pulmonary valve disease (8)	14	48.0
14	CT	Tracheomalacia (9)	2	7.7	Tracheomalacia (9)	<1	7.0
15	CT	CoA (2)*	<1	4.6	CoA (2)	<1	3.7
16	CT	ToF (7)*	<1	6.8	AVSD (7)	<1	7.0
17	CT	CoA (2)*	3	15.0	CoA (2)	5	20.0
18	MRI	Hypoplasia of the aortic root (8)	13	50.0	Aortic valve disease (8)	19	65.0
19	CT	ALCAPA ^f (10)*	<1	5.2	ALCAPA (10)	<1	3.7
20	CT	Single ventricle (11)	<1	6.9	Hypoplasia of the aorta (11)	<1	4.5
21	CT	Single ventricle (12)	5	13.5	Single ventricle (12)	5	15.0
22	CT	Tracheomalacia (13)	<1	5.8	–	–	–
23	CT	cc-TGA ^d + multiple comorbidities (14)	10	22.6	–	–	–
24	CT	Single ventricle (4)	<1	2.8	Single ventricle (4)	<1	3.5
25	CT	ToF (1)	<1	4.3	Pulmonary atresia + VSD (1)	<1	6.2
26	CT	d-TGA (6)	<1	4.2	d-TGA (6)	<1	3.0

^aVentricular septal defect; ^bCoarctation of the aorta; ^cTetralogy of Fallot; ^ddextro/congenital corrected-transposition of the great arteries; ^eAtrioventricular septal defect; ^fAnomalous left coronary artery from the pulmonary artery.

In brackets: kind of operation: (1) Shunt between right ventricle and pulmonary artery; (2) end-to-end anastomosis; (3) aneurysm resection; (4) aortopulmonary shunt; (5) upper cavopulmonary connection; (6) atrial switch; (7) closure with bovine pericardial patch; (8) valve replacement; (9) trachea reconstruction; (10) coronary artery transfer; (11) aortic arch reconstruction; (12) DORV-correction; (13) aortopexy; (14) VSD closure.

*Patients rated with no benefit of holographic presentation for the surgeon's preparation.

control patients could be identified (CNR: cases: 14.0 ± 6.4 , control: 14.5 ± 7.8 ; SNR: cases: 20.3 ± 8.5 , control: 21.9 ± 12.3).

The average time required to create a CR-hologram was 9.0 ± 2.1 min. The generation of a 3D-printed model required an average of 141.8 ± 27.7 min for the pre-processing steps, 240–1,185 min for the printing process (depending on size and complexity), and an average of 38.2 ± 10.0 min for the post-processing steps.

The HoloLens® Surpassed 2D Imaging in All Subgroups

The items of the questionnaire were divided into five subgroups. The group affiliation was tested using Cronbach's alpha, which showed good inter-item correlation without unnecessary redundancy for all subgroups: 3D-imaging effect (CR-holograms:

0.72; 3D print: 0.81), representation of the pathology (CR-holograms: 0.87; 3D print: 0.88), anatomical structure resolution (CR-holograms: 0.81; 3D print: 0.80), cost/benefit ratio (CR-holograms: 0.70; 3D print: 0.73), influence on surgery (CR-holograms: 0.88; 3D print: 0.88) (18).

The analysis of the questionnaire results showed benefits for CR-holograms compared with 2D imaging in all five subgroups (Table 2). Further examination of the single items showed no benefit only for two items: assessment of intracardial structures (3.3 ± 1.1) and the coronaries (3.4 ± 1.4).

Neighboring Structures and Holographic Visibility Are Essential for the Superiority of the HoloLens®

We investigated potential differences between different patient cohorts. The Likert scale values of all patients in chronological

TABLE 2 | Evaluation of CR-holograms and 3D-printed models divided in subgroups.

Items	CR-holograms vs. 2D imaging	3D printing vs. 2D imaging	P-value [#]
	mean (SD)	mean (SD)	
3D-imaging effect	4.4 (0.8)	3.4 (1.1)*	0.000[§]
Comparison with CR on 2D screen	4.1 (1.3)	2.7 (1.5)*	0.000 [§]
Sufficient visualization options	4.5 (1.0)	3.7 (1.4)	0.001 [§]
Sufficient quality	4.4 (1.1)	3.5 (1.4)	0.000 [§]
Improved depth perception	4.7 (0.7)	3.7 (1.2)	0.000 [§]
Representation of the pathology	4.4 (0.9)	3.6 (1.2)	0.001[§]
All necessary areas presented	4.3 (1.1)	3.5 (1.4)	0.001 [§]
Important details not hidden	3.9 (1.5)	3.2 (1.6)*	0.010 [‡]
Improved comprehensibility	4.6 (0.9)	3.9 (1.3)	0.008 [§]
Adequate pathology assessment	4.7 (0.7)	4.0 (1.2)	0.003 [§]
Anatomical structure resolution	4.3 (0.5)	3.8 (0.7)	0.000[§]
Confluence of vessels	4.8 (0.5)	4.4 (0.9)	0.022 [‡]
Out-flowing vessels	4.7 (0.6)	4.2 (1.0)	0.005 [§]
Aortic arch	4.9 (0.3)	4.9 (0.3)	1.000 [‡]
Coronaries	3.4 (1.4)*	2.5 (1.3)*	0.003 [§]
Pulmonary veins	4.7 (0.5)	4.1 (1.2)	0.023 [‡]
Atrial appendages	4.8 (0.4)	4.4 (0.7)	0.010 [‡]
Structures of the inner heart	3.3 (1.1)*	3.0 (1.3)*	0.397 [‡]
Neighboring structures	4.3 (1.0)	3.1 (1.4)*	0.000 [§]
Cost/benefit ratio	4.5 (0.7)	4.0 (0.9)	0.012[‡]
Appropriate expenditure of time	4.5 (1.0)	3.9 (1.1)	0.03 [‡]
Educational potential	4.7 (0.6)	4.5 (0.8)	0.056 [‡]
Adequate costs and benefits	4.2 (1.1)	3.7 (1.3)	0.020 [‡]
Influence on the surgery	4.4 (0.8)	3.8 (1.0)	0.004[§]
Concordant intraoperative view	4.7 (0.7)	4.1 (1.0)	0.006 [§]
Facilitation of preparation	4.5 (0.8)	3.9 (1.0)	0.003 [§]
Positive impact on surgery time	4.2 (1.0)	3.5 (1.2)	0.016 [‡]

[#]paired t-test for analysis, [‡]No significant difference, [‡] $p < 0.05$, [§] $p < 0.01$. *presentation on 2D screen superior to presentation in 3D space. The bold values correspond to the five subgroups that were evaluated. The corresponding items from which a subgroup was composed are listed below the respective bold subgroup.

order are shown in **Figure 3**. There was no indication of a chronological dependency of the ratings. In 3 of 26 patients, no benefit for the average values could be identified in comparison with 2D imaging (patients 11, 12, and 13). On closer examination it became apparent that these patients underwent a repair of inner cardiovascular structures that cannot be adequately presented via CR-holograms. Additionally, for these cases the usefulness of the hologram for the preparation received no excellent ratings (3.6 ± 0.5). To assess whether these two aspects (neighboring structures and holographic visibility) influenced the overall evaluation, the patients were evaluated after separation into groups that, respectively, did and did not benefit from the representation of the pathology. There was only a benefit for the representation of intracardial pathologies when additional vascular surgery aspects were present. In **Figure 4A**, only patients with an excellent rating of the usefulness for preparation were included (*Likert scale* =

5, $n = 17$). No disadvantage in the overall rating was seen, even if the main pathology could not be presented holographically. For patients for whom the preparation was rated worse, a significant deterioration of the ratings in all subgroups could be shown (**Figure 4B**, $n = 9$). A particularly poor evaluation could be shown for patients in whom, additionally, the holographic presentation of the pathology was not possible.

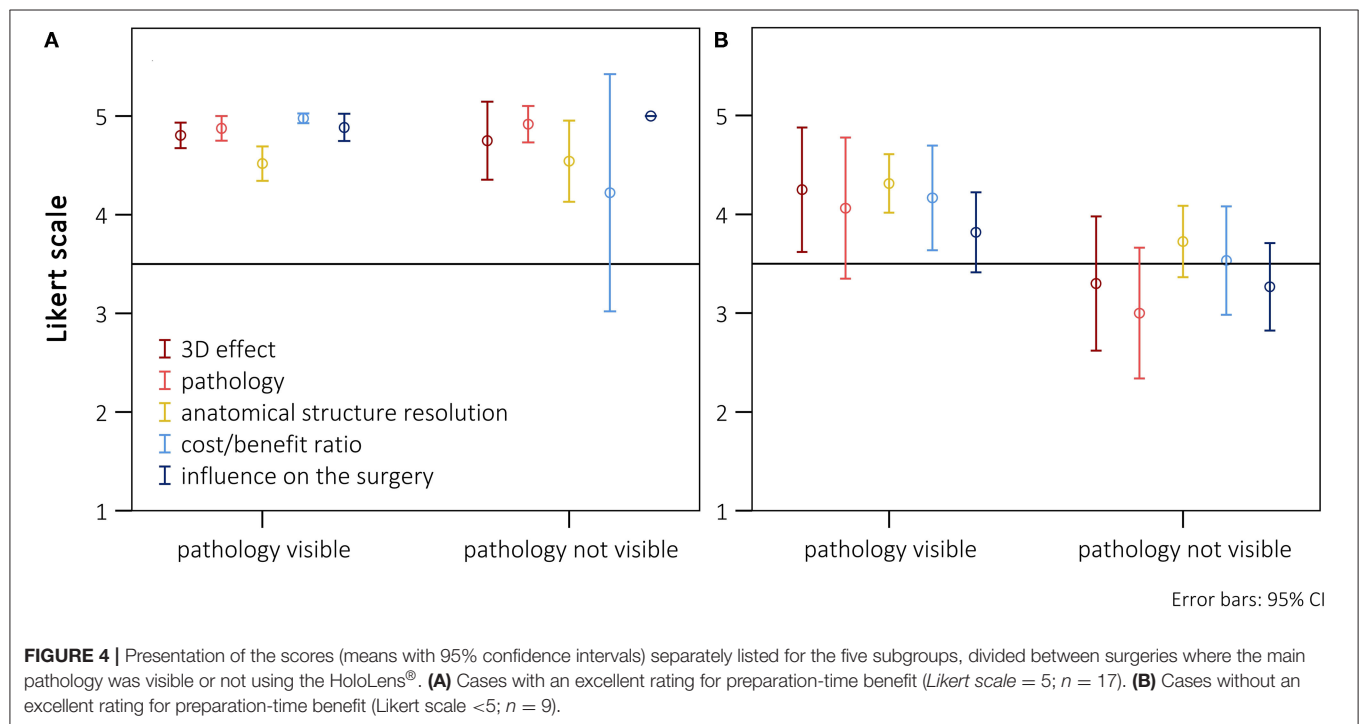
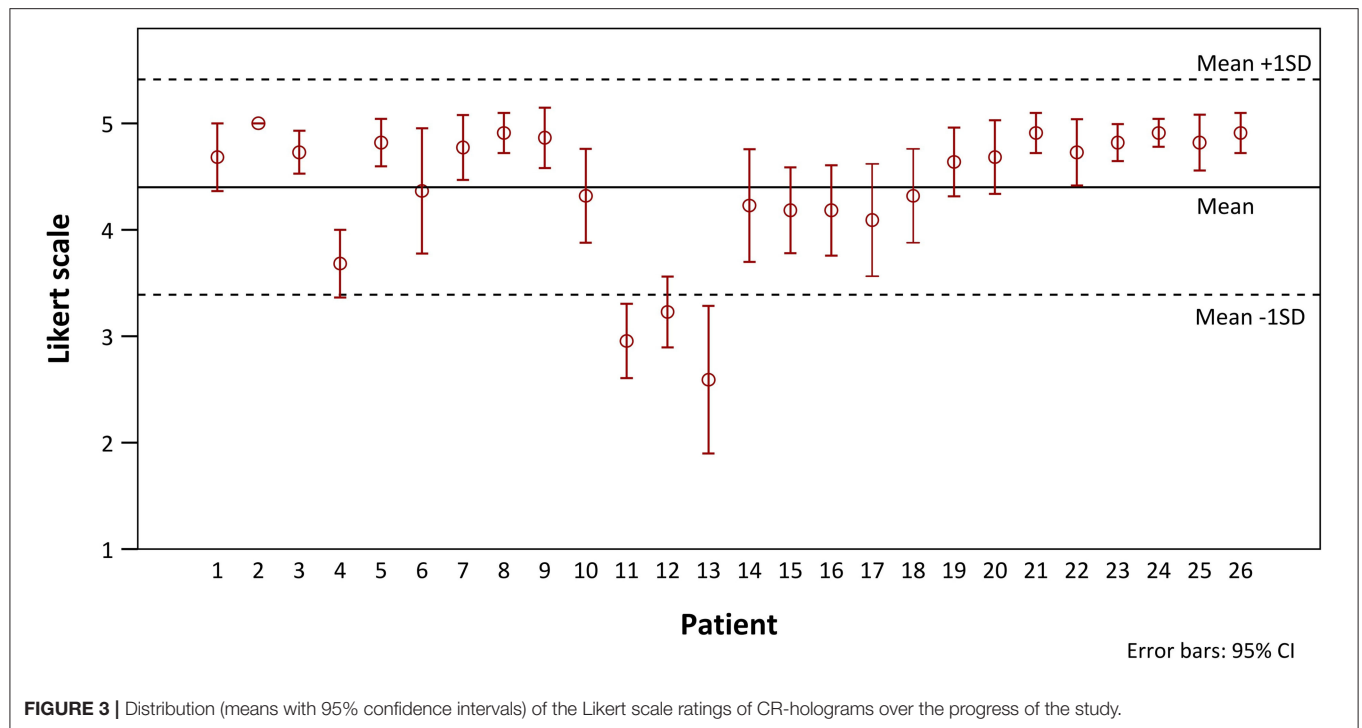
Superiority of the HoloLens® Over Previously Used 3D-Imaging Techniques

The CR-holograms were rated significantly higher than the 3D-printed models in all categories (**Table 2**). Nevertheless, clear differences in the ratings of the individual subgroups could be identified. Concerning cost/benefit ratio, only a small benefit could be shown for the holographic presentation compared to 3D-printed models (CR-holograms: 4.5 ± 0.7 ; 3D print: 4.0 ± 0.9 ; $P < 0.05$), while no significant difference between the 3D-imaging methods was observed for use in education. The surgeons rated the time expenditure for 3D printing only a bit higher. In the overall evaluation of the anatomical structure resolution, CR-holograms showed significantly better results (CR-holograms: 4.3 ± 0.5 ; 3D print: 3.8 ± 0.7 ; $P < 0.05$). Nevertheless, both evaluated 3D-imaging methods showed no benefit compared with 2D imaging regarding the representation of the coronaries as well as the intracardial structures. However, CR-holograms were rated significantly higher than 3D-printed models for the representation of the coronaries. Concerning the remaining anatomical structures, only a small significant difference could be observed between the two spatial representation methods, especially considering large vessel structures. While the benefit of CR-holograms in representing the pathology was clearly higher compared with 2D imaging, for 3D printing the benefit was only marginal (CR-holograms: 4.4 ± 0.9 ; 3D print: 3.6 ± 1.2 ; $P < 0.05$). In the assessment of the 3D-imaging effect, the HoloLens® was clearly superior to 3D printing (CR-holograms: 4.4 ± 0.8 ; 3D print: 3.4 ± 1.1 ; $P < 0.05$).

Significant Shortening of the Intraoperative Preparation Time

We evaluated the measurable influence of spatial 3D methods in preoperative planning on the course of surgery by analyzing the intraoperative preparation times. Two cases could not be included, because no suitable case could be found for comparison, due to the complexity of the respective surgery. In five cases, the main diagnosis of cases and matched controls differed, but the operative procedure and other conditions were the same in these patients.

The mean intraoperative preparation time was 58.5 ± 22.6 min ($n = 24$, minimum: 23 min, maximum: 104 min), when spatial 3D models were used for preoperative planning. In contrast, the preoperative planning for the relevant control group was carried out completely on a 2D monitor, and no representation in 3D space was used. The control intraoperative preparation time was 72.8 ± 43.1 min ($n = 24$, minimum: 24 min, maximum: 186 min). The intraoperative preparation times of



the patients who received preoperative planning based on 3D-printed models and CR-holograms were significantly lower compared with the control group ($P < 0.05$). To examine whether this significant shortening corresponded with the surgeon's assessment, we performed an additional analysis. The matched patient pairs were separated in two groups according to the

surgeon's estimate (benefit/no benefit). The preparation time was then compared between the patients and controls in these smaller groups. As illustrated in **Figure 5**, this conformity was good. In the 15 patients rated "advantageous" by the surgeon, the preparation time for the study patients was just significant shorter than the measured preparation time for the controls. In the nine

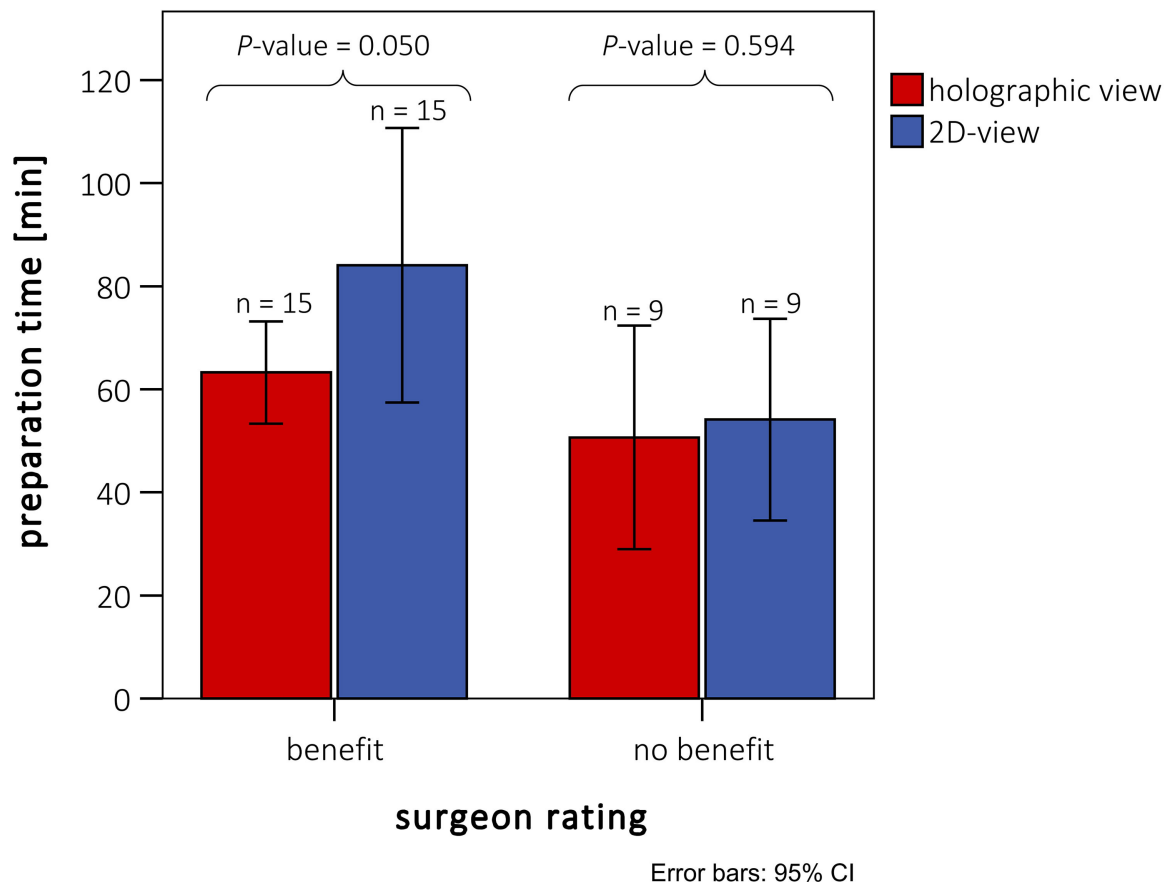


FIGURE 5 | Intraoperative preparation times of patients with preoperative holographic representation (red) and matched patient pairs (blue) without spatial representation. Ratings are divided between cases rated with and without benefit for preparation by the surgeons. Patients rated with “no benefit” did not differ from the rest either in diagnosis or in kind of surgery (see also **Table 1B**).

patients rated “non-advantageous” by the surgeon, there was no significant benefit measured for the preparation time.

DISCUSSION

Recent developments made the use of CR in 3D space possible for the first time. This study is the first to compare CR-holograms with previously used imaging techniques in which the images were projected onto a 2D screen (CT or MRI). Precise morphological imaging is essential for surgical success, especially in complex cases.

A direct comparison of CR-holograms to 2D imaging and 3D printing quickly reveals the superiority of the photo-realistic 3D holographic representation (**Figure 6**). The holographic representation by the HoloLens® surpassed the standard representation on a 2D screen in all five analyzed parameters (**Table 2**). Furthermore, the assessment of an already established method of 3D imaging, 3D printing, was used as a spatial comparison method (2, 12–15, 19–21). The questions used to create the questionnaire were carefully selected. The absence of unnecessary redundancy and good inter-item correlation in the

subgroups were confirmed using Cronbach’s alpha, validating the selection criteria. MRI was performed in two cases because additional functional parameters were needed. The quality of these images did not differ from that of CT. Furthermore, the possibility that discrepancies in the results arose from differences between the cases and the controls in the quality of the underlying images could be rejected.

CR-Holograms as the Most Realistic Representation Method

In fields like engineering or design review, the fundamental advantage of 3D imaging in 3D space is already proven. Spatial 3D representation has been established for many years in those areas of expertise. It has already been shown that the spatial 3D presentation improves shape and depth perception, reduces mental workload, and makes it possible to complete tasks faster and with higher quality results (22, 23). In accordance with these observations, our results showed the advantage of using spatial 3D imaging as, the most significant improvement in preoperative planning by enhancing depth perception and the representation of the pathology (**Table 2**). These aspects were rated better for

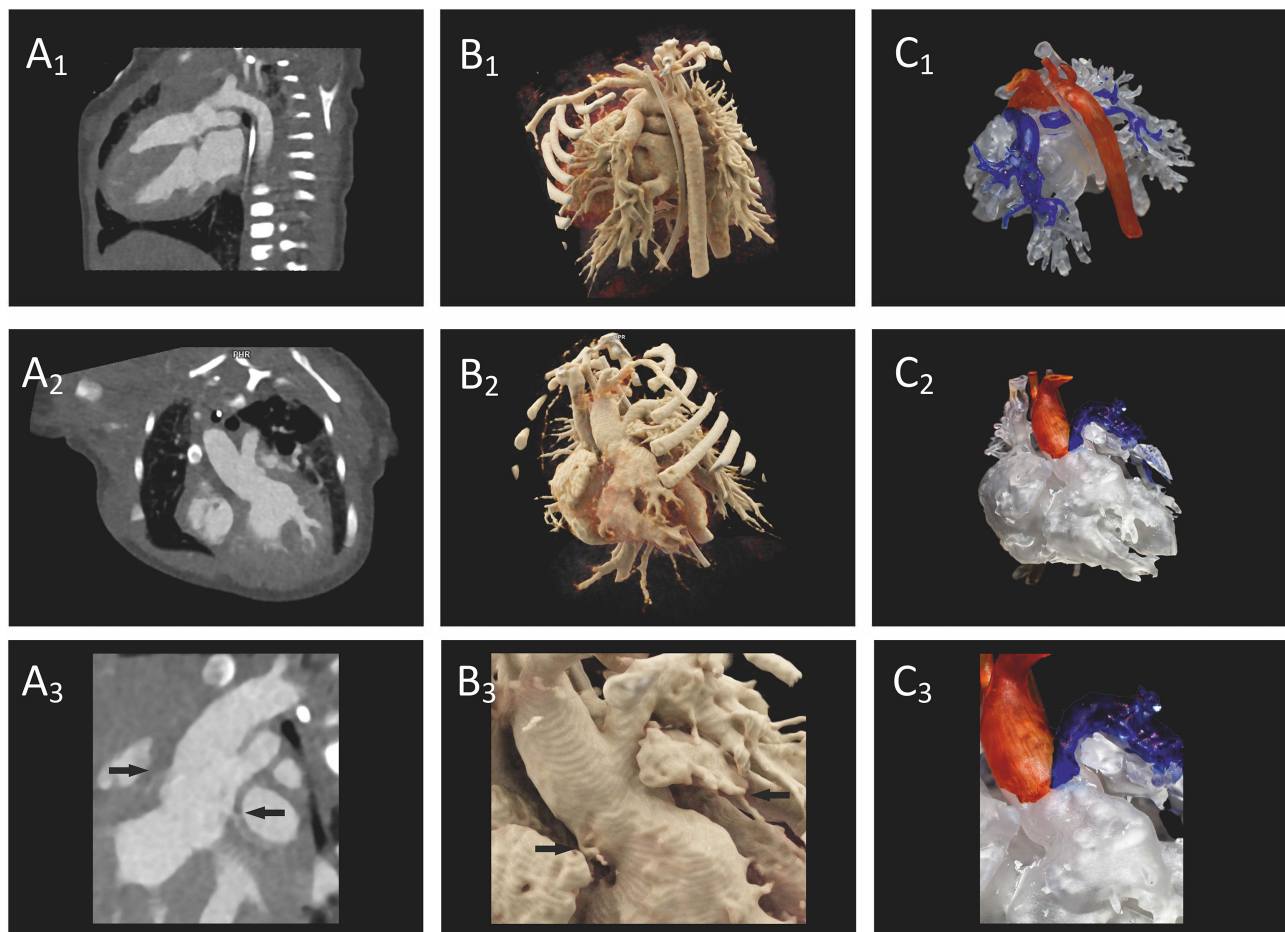


FIGURE 6 | Preoperative imaging of a patient's heart with truncus arteriosus communis from two different perspectives. **(A1–A3)** A direct comparison of CT on a 2D screen (2D imaging), **(B1–B3)** cinematically rendered hologram, and **(C1–C3)** 3D printing. In **(A3)**, the coronaries (arrows) show only a weak contrast, but the 3D view can be demonstrated as a cinematically rendered hologram **(B3)**. A reconstruction of the coronary structure for 3D printing was not possible in this case **(C3)**.

CR-holograms than for 3D-printed models, even though the 3D prints correspond in dimensions and anatomical presentation exactly to the patient's heart and have a haptic advantage. The main difference between the 3D print and a real heart is the representation of surface features like color, texture, and lighting characteristics. The absence of these realistic features makes additional mental transformational work necessary since an intuitive recognition intraoperatively is not possible. In contrast, CR makes it possible to create a 3D image which strongly corresponds to the familiar intraoperative tissue texture. This is achieved by using an algorithm that takes the interaction between light photons and human tissue into account (3, 6–10). This could already prove to be a significant advantage, especially in shape and depth perception, over previously used rendering algorithms (e.g., volume rendering) when presented on 2D screen (7–10). However, our results showed that CR on a 2D screen improved the 3D perception so that it could show results even equal to those obtained using 3D printing (Table 2). This explains the consistently excellent review of the 3D perception of the holographic representation of CR-images. The combination of

the realistic spatial 3D view with an extremely realistic rendering algorithm clearly improved depth perception and provided a better delineation of complex anatomical structures.

It is known that repeatedly visually presented objects can be processed much faster than unknown structures (24). The exact preoperative visualization of the operative field allows the surgeon to plan the operation's steps directly. Therefore, the aim of preoperative imaging is to provide the surgeon a virtual operative field in advance that is as close to reality as possible. Our study showed that the intraoperative findings corresponded to the preoperative images significantly better when the latter were presented as CR-holograms than when visualized on a 2D screen or by 3D printing (Table 2). We assume that this is the reason for the facilitated visual comprehension of the pathology.

The only barriers to easier comprehension of pathologies using CR-holograms were structures which were either not imaged in the primary dataset or could not be presented holographically (intracardial structures). The lack of information in the primary data set is most evident in the representation of the coronary arteries. The representation is dependent on

the perfusion and the phase in which the single shot was taken. Since the images were not taken especially to display the coronary arteries, contrast was lacking in some patients and this limited the coronary arteries' visibility. Nevertheless, CR-holograms exhibited an advantage over 3D printing in cases with limited coronary representation in raw 2D images. In these cases, 3D printing is inferior to 2D representation, because a weak coronary contrast makes 3D reconstruction impossible. On the other hand, CR-holograms enable weakened coronary visibility, which allows equivalent visibility of coronaries as in 2D images (**Figure 6**). Apart from this, it is currently not possible to view intracardial structures using the HoloLens®. However, even in cases in which intracardial pathology is the main diagnosis, surgical preparation could be facilitated by the presentation of outer cardiovascular and neighboring structures.

Comparing the distribution of all ratings for the individual patients, in three cases the holographic presentation provided no benefit for preoperative planning compared with imaging on a 2D screen (**Figure 3**). In these cases, the rating of the facilitation of the preparation seemed to be most important for the overall evaluation. If this advantage was missing, the total benefit was clearly reduced (**Figure 4**). If there was no benefit for the representation of the pathology (e.g., intracardial) and the preparation (e.g., very superficial pathology), the holographic representation was overall inferior to the representation on a 2D screen.

Considering the responses of the surgeons to the patients in chronological order, no chronological dependency could be identified (**Figure 3**). The partly observed fluctuations in the graphics can be explained by patient-dependent weaknesses of the holographic representation. This rules out the possibility that the benefit of the method was seriously influenced by its first-time use as a new preoperative planning tool or by a habituation effect.

CR-Holograms Led in Cost/Benefit Analysis

Looking at the costs and benefits of the evaluated methods, two different aspects must be considered: the cost (e.g., time expenditure)/benefit (e.g., reduction surgery time) balance for the surgeon in preoperative usage and the cost/benefit balance from a financial perspective of synthesizing the different types of 3D representations.

For the surgeon, CR-holograms as well as 3D-printed models provided a clear benefit in comparison with monitor-imaging (**Table 2**). The time required for both 3D imaging modalities was rated better than the time needed for 2D imaging, whereas CR-holograms were superior to 3D printing. The actual planning time was not measured due to the retrospective study design, but the surgeons' assessments revealed a clear cost-benefit advantage when 3D spatial representation was used for preoperative planning. Regarding their educational potential, both 3D-imaging methods were rated better than imaging on a 2D screen and thus equally useful. This finding was consistent with results from previous studies regarding the valuable educational potential of 3D printing (13, 14, 25, 26).

Nevertheless, the holographic representation was superior, considering the time expense. In the preparation process the cost/benefit of 3D printing is clearly inferior to CR-holograms. While the acquisition costs are similar for the 3D printer and the HoloLens®, the processing costs are much higher for 3D printing. Each print adds personnel and material costs. Furthermore, the intraoperative preparation time for a 3D print is much longer, which is why short-term production—for example, from an emergency CT for subsequent surgery—is not possible. In contrast, a CR-hologram can be prepared in little time.

CR-Holograms Shorten the Intraoperative Preparation Time

To assess whether the subjectively identified benefit influenced the clinical outcome, we performed an objective evaluation of the spatial 3D-presentation methods by comparing the intraoperative preparation times between retrospectively matched pairs of patients. We found that the group that received preoperative planning based on 3D-printed models and CR-holograms showed significant reductions in the average intraoperative preparation time compared with the control group (cases: 58.5 ± 22.6 min vs. matched controls: 72.8 ± 43 min). Both spatial imaging techniques thus proved to be superior to standard imaging on 2D screen. We analyzed the intraoperative preparation time because our 3D-imaging methods are especially suitable for the representation of outer cardiovascular structures. Furthermore, as illustrated in **Figure 4**, the usefulness of the preoperative representation in reducing the intraoperative preparation time was decisive for the total benefit. We assumed that the 3D tissue imaging allows faster recognition of the outer structures, which makes a more precise and rapid preparation of the operative field possible. An assessment of the overall operative time would be influenced by a wide range of additional parameters, making the comparison much more difficult.

In nine patients the 3D imaging provided, according to the surgeon's opinion, no benefit to preparation time, independent of the reason for surgery. When examining the intraoperative preparation times of these patients, we identified no benefit relative to the matched patients ($P = 0.59$). Therefore, the subjective assessment by the surgeons corresponded to our objective findings regarding the preparation time. On the other hand, a significant reduction in the intraoperative preparation time could be measured in the "as advantageous" rated patients ($P = 0.05$). Though only a small patient cohort was analyzed, a clear difference was identified with slight significance. A few studies have suggested that using spatial 3D imaging preoperatively can improve surgical outcomes and reduce operative times in patients with CHD (15, 21, 27). However, a systematically measured significant shortening of the operative time has not before been determined. This is probably due to the fact that the overall operative time or the aortic cross-clamp time were analyzed, and no test of correlation with the surgeon's assessment was performed. For the first time, a significant positive influence of 3D spatial imaging in preoperative planning on the operative time in patients with CHD could be proven.

Shortening of the overall operative time has already been shown to greatly influence postoperative outcome in cardiovascular surgery (28, 29). Nevertheless, the intraoperative preparation time is only one factor; many other factors, such as cross-clamp time and preoperative complications play an important role influencing overall operation time and outcome. To demonstrate this correlation, a prospective study with larger patient cohorts (e.g., multicenter study) is needed. This has the potential to improve the total outcome (e.g., by reducing postoperative complications and improving long-term survival). Since CR-holograms surpassed 3D printing in all analyzed subgroups, we assume that the benefit can be attributed mainly to the CR-holograms. It can therefore be concluded that detailed preoperative planning has a significant influence on the operation procedure, depending on the realism of the representation.

Limitations

Due to the study design, the surgeon assessed the imaging material of the patient more intensively. A bias regarding the reduction of the intraoperative preparation time through this cannot be excluded. Additionally, the surgeon could not be blinded to the used imaging technique. Furthermore, since the patient pairs were matched retrospectively, it could not be granted that both patients were respectively treated by the same surgeon. A small patient cohort was used for analyses. The intraoperative benefit identified here was significant but should be validated in a larger study.

Summary

In conclusion, this study demonstrated that spatial imaging provides a clear benefit in preoperative planning of pediatric heart surgery compared with the previously used representation on a 2D screen. The combination of an extremely photo-realistic surface representation by cinematic rendering and the presentation of the cardiovascular structures in 3D space improves the 3D perception enormously. This provides a better subjective assessment as well as a measurable shortening of the intraoperative preparation time. The cinematically rendered holographic presentation using mixed-reality glasses surpassed the previously used spatial 3D presentation method (3D printing) in all analyzed aspects. Therefore, it is reasonable to assume that the future of preoperative imaging lies in 3D-spatial representations, and particularly in CR-holograms.

REFERENCES

1. Brun H, Bugge RA, Suther LK, Birkeland S, Kumar R, Pelanis E, et al. Mixed reality holograms for heart surgery planning: first user experience in congenital heart disease. *Eur Heart J Cardiovasc Imaging*. (2018) 20:883–8. doi: 10.1093/ehjci/jej184
2. Sun Z, Lau I, Wong YH, Yeong CH. Personalized three-dimensional printed models in congenital heart disease. *J Clin Med*. (2019) 8:522. doi: 10.3390/jcm8040522
3. Comaniciu D, Engel K, Georgescu B, Mansi T. Shaping the future through innovations: from medical imaging to precision medicine. *Med Image Anal*. (2016) 33:19–26. doi: 10.1016/j.media.2016.06.016

Prospects

There are clear limits to the representation of intracardial and intravascular structures since the current version of the HoloLens® only allows viewing of the outer surface without interactive cutting through the patient's heart. In the next version of the HoloLens®, an interactive cutting through the hologram will be possible. A further potential expansion of the presentation of CR-holograms would be a multi-user system that would enable joint discussion in 3D space. Furthermore, the visualization of hemodynamic information will likely be possible in future versions. The presentation of functional examinations (e.g., heart beating, 4D phase contrast, 4D speckle tracking) in 3D space is conceivable and would facilitate locating anatomical structures.

DATA AVAILABILITY STATEMENT

The raw data supporting the conclusions of this article will be made available by the authors, without undue reservation.

ETHICS STATEMENT

Written informed consent was obtained from the individual(s) for the publication of any potentially identifiable images or data included in this article.

AUTHOR CONTRIBUTIONS

PG, RC, SD, and MA contributed to conception and design of the study. PG organized the database and performed together with MA the statistical analysis. PG, MA, RC, and AP were involved in the implementation of the study. SD and MA were responsible for the supervision of the study. PG and MA wrote the first draft of the manuscript. MS and SD reviewed and edited all sections of the manuscript. MU and OR provided cross-sectional imaging resources for the study. All authors read and approved the submitted manuscript version.

ACKNOWLEDGMENTS

The present work was performed in fulfillment of the requirements for obtaining the degree Dr. med.

4. Goo HW, Park SJ, Yoo SJ. Advanced medical use of three-dimensional imaging in congenital heart disease: augmented reality, mixed reality, virtual reality, and three-dimensional printing. *Korean J Radiol*. (2020) 21:133–45. doi: 10.3348/kjr.2019.0625
5. Sørensen TS, Beerbaum P, Mosegaard J, Greil GF. Developing and evaluating virtual cardiotomy for preoperative planning in congenital heart disease. *Stud Health Technol Inform*. (2009) 142:340–5. doi: 10.3233/978-1-58603-964-6-340
6. Fellner FA. Introducing cinematic rendering: a novel technique for post-processing medical imaging data. *JBISE*. (2016) 9:170–5. doi: 10.4236/jbise.2016.93013
7. Dappa E, Higashigaito K, Fornaro J, Leschka S, Wildermuth S, Alkadhi H. Cinematic rendering—an alternative to volume rendering for 3D

- computed tomography imaging. *Insights Imaging*. (2016) 7:849–56. doi: 10.1007/s13244-016-0518-1
8. Röschl F, Purbojo A, Rüffer A, Cesnjevar R, Dittrich S, Glöckler M. Initial experience with cinematic rendering for the visualization of extracardiac anatomy in complex congenital heart defects. *Interact Cardiovasc Thorac Surg*. (2019) 28:916–21. doi: 10.1093/icvts/ivy348
 9. Ebert LC, Schweitzer W, Gascho D, Ruder TD, Flach PM, Thali MJ, et al. Forensic 3D visualization of CT data using cinematic volume rendering: a preliminary study. *AJR Am J Roentgenol*. (2017) 208:233–40. doi: 10.2214/AJR.16.16499
 10. Elshafei M, Binder J, Baecker J, Brunner M, Uder M, Weber GF, et al. Comparison of cinematic rendering and computed tomography for speed and comprehension of surgical anatomy. *JAMA Surg*. (2019) 154:738–44. doi: 10.1001/jamasurg.2019.1168
 11. Tepper OM, Rudy HL, Lefkowitz A, Weimer KA, Marks SM, Stern CS, et al. Mixed reality with HoloLens: where virtual reality meets augmented reality in the operating room. *Plast Reconstr Surg*. (2017) 140:1066–70. doi: 10.1097/PRS.0000000000003802
 12. Batteux C, Haidar MA, Bonnet D. 3D-Printed models for surgical planning in complex congenital heart diseases: a systematic review. *Front Pediatr*. (2019) 7:23. doi: 10.3389/fped.2019.00023
 13. Valverde I, Gomez-Ciriza G, Hussain T, Suarez-Mejias C, Velasco-Forte MN, Byrne N, et al. Three-dimensional printed models for surgical planning of complex congenital heart defects: an international multicentre study. *Eur J Cardiothorac Surg*. (2017) 52:1139–48. doi: 10.1093/ejcts/ezx208
 14. Lau I, Sun Z. Three-dimensional printing in congenital heart disease: a systematic review. *J Med Radiat Sci*. (2018) 65:226–36. doi: 10.1002/jmrs.268
 15. Bateman MG, Durfee WK, Iles TL, Martin CM, Liao K, Erdman AG, et al. Cardiac patient-specific three-dimensional models as surgical planning tools. *Surgery*. (2019) 167:259–63. doi: 10.1016/j.surg.2018.11.022
 16. Norman G. Likert scales, levels of measurement and the “laws” of statistics. *Adv Health Sci Educ Theory Pract*. (2010) 15:625–32. doi: 10.1007/s10459-010-9222-y
 17. Rasmussen JL. Analysis of Likert-scale data: a reinterpretation of gregoire and driver. *Psychol Bull*. (1989) 105:167–70.
 18. Streiner DL. Starting at the beginning: an introduction to coefficient alpha and internal consistency. *J Pers Assess*. (2003) 80:99–103. doi: 10.1207/S15327752JPA8001_18
 19. Lau IW, Liu D, Xu L, Fan Z, Sun Z. Clinical value of patient-specific three-dimensional printing of congenital heart disease: quantitative and qualitative assessments. *PLoS ONE*. (2018) 13:e0194333. doi: 10.1371/journal.pone.0194333
 20. Xu J-J, Luo Y-J, Wang J-H, Xu W-Z, Shi Z, Fu J-Z, et al. Patient-specific three-dimensional printed heart models benefit preoperative planning for complex congenital heart disease. *World J Pediatr*. (2019) 15:246–54. doi: 10.1007/s12519-019-00228-4
 21. Zhao L, Zhou S, Fan T, Li B, Liang W, Dong H. Three-dimensional printing enhances preparation for repair of double outlet right ventricular surgery. *J Card Surg*. (2018) 33:24–7. doi: 10.1111/jocs.13523
 22. Wang X, Dunston PS. User perspectives on mixed reality tabletop visualization for face-to-face collaborative design review. *Autom Constr*. (2008) 17:399–412. doi: 10.1016/j.autcon.2007.07.002
 23. Gabriel B Dadi, Paul M Goodrum, Timothy RB Taylor, William F Maloney. Effectiveness of communication of spatial engineering information through 3D CAD and 3D printed models. *Vis Eng*. (2014) 2:9. doi: 10.1186/s40327-014-0009-8
 24. Grill-Spector K, Henson R, Martin A. Repetition and the brain: neural models of stimulus-specific effects. *Trends Cogn Sci*. (2006) 10:14–23. doi: 10.1016/j.tics.2005.11.006
 25. Su W, Xiao Y, He S, Huang P, Deng X. Three-dimensional printing models in congenital heart disease education for medical students: a controlled comparative study. *BMC Med Educ*. (2018) 18:178. doi: 10.1186/s12909-018-1293-0
 26. White SC, Sedler J, Jones TW, Seckeler M. Utility of three-dimensional models in resident education on simple and complex intracardiac congenital heart defects. *Congenit Heart Dis*. (2018) 13:1045–9. doi: 10.1111/chd.12673
 27. Smith ML, McGuinness J, O'Reilly MK, Nolke L, Murray JG, Jones JF. The role of 3D printing in preoperative planning for heart transplantation in complex congenital heart disease. *Ir J Med Sci*. (2017) 186:753–6. doi: 10.1007/s11845-017-1564-5
 28. Santarpino G, Pfeiffer S, Concistré G, Grossmann I, Hinzmann M, Fischlein T. The Perceval S aortic valve has the potential of shortening surgical time: does it also result in improved outcome? *Ann Thorac Surg*. (2013) 96:77–81; discussion 81–2. doi: 10.1016/j.athoracsur.2013.03.083
 29. Jiang W-L, Hu X-P, Hu Z-P, Tang Z, Wu H-B, Chen L-H, et al. Morbidity and mortality of nosocomial infection after cardiovascular surgery: a report of 1606 cases. *Curr Med Sci*. (2018) 38:329–35. doi: 10.1007/s11596-018-1883-4

Conflict of Interest: The authors declare that the research was conducted in the absence of any commercial or financial relationships that could be construed as a potential conflict of interest.

Copyright © 2021 Gehrsitz, Rempel, Schöber, Cesnjevar, Purbojo, Uder, Dittrich and Alkassar. This is an open-access article distributed under the terms of the Creative Commons Attribution License (CC BY). The use, distribution or reproduction in other forums is permitted, provided the original author(s) and the copyright owner(s) are credited and that the original publication in this journal is cited, in accordance with accepted academic practice. No use, distribution or reproduction is permitted which does not comply with these terms.



Extraction of Coronary Atherosclerotic Plaques From Computed Tomography Imaging: A Review of Recent Methods

Haipeng Liu^{1,2†}, Aleksandra Wingert^{2†}, Jian'an Wang³, Jucheng Zhang⁴, Xinhong Wang⁵, Jianzhong Sun⁵, Fei Chen⁶, Syed Ghufuran Khalid¹, Jun Jiang^{3*} and Dingchang Zheng^{1*}

¹ Research Centre for Intelligent Healthcare, Coventry University, Coventry, United Kingdom, ² Faculty of Health, Education, Medicine, and Social Care, Anglia Ruskin University, Chelmsford, United Kingdom, ³ Department of Cardiology, School of Medicine, The Second Affiliated Hospital, Zhejiang University, Hangzhou, China, ⁴ Department of Clinical Engineering, School of Medicine, The Second Affiliated Hospital, Zhejiang University, Hangzhou, China, ⁵ Department of Radiology, School of Medicine, The Second Affiliated Hospital, Zhejiang University, Hangzhou, China, ⁶ Department of Electrical and Electronic Engineering, Southern University of Science and Technology, Shenzhen, China

OPEN ACCESS

Edited by:

Christos Bourantas,
Barts Health NHS Trust,
United Kingdom

Reviewed by:

Filippo Cademartiri,
IRCCS SDN, Italy
Anantharaman Ramasamy,
Barts Health NHS Trust,
United Kingdom

*Correspondence:

Jun Jiang
jiang-jun@zju.edu.cn
Dingchang Zheng
dingchang.zheng@coventry.ac.uk

[†]These authors share first authorship

*ORCID:

Haipeng Liu
orcid.org/0000-0002-4212-2503

Specialty section:

This article was submitted to
Cardiovascular Imaging,
a section of the journal
Frontiers in Cardiovascular Medicine

Received: 21 August 2020

Accepted: 18 January 2021

Published: 10 February 2021

Citation:

Liu H, Wingert A, Wang J, Zhang J,
Wang X, Sun J, Chen F, Khalid SG,
Jiang J and Zheng D (2021) Extraction
of Coronary Atherosclerotic Plaques
From Computed Tomography
Imaging: A Review of Recent
Methods.
Front. Cardiovasc. Med. 8:597568.
doi: 10.3389/fcvm.2021.597568

Background: Atherosclerotic plaques are the major cause of coronary artery disease (CAD). Currently, computed tomography (CT) is the most commonly applied imaging technique in the diagnosis of CAD. However, the accurate extraction of coronary plaque geometry from CT images is still challenging.

Summary of Review: In this review, we focused on the methods in recent studies on the CT-based coronary plaque extraction. According to the dimension of plaque extraction method, the studies were categorized into two-dimensional (2D) and three-dimensional (3D) ones. In each category, the studies were analyzed in terms of data, methods, and evaluation. We summarized the merits and limitations of current methods, as well as the future directions for efficient and accurate extraction of coronary plaques using CT imaging.

Conclusion: The methodological innovations are important for more accurate CT-based assessment of coronary plaques in clinical applications. The large-scale studies, de-blooming algorithms, more standardized datasets, and more detailed classification of non-calcified plaques could improve the accuracy of coronary plaque extraction from CT images. More multidimensional geometric parameters can be derived from the 3D geometry of coronary plaques. Additionally, machine learning and automatic 3D reconstruction could improve the efficiency of coronary plaque extraction in future studies.

Keywords: coronary artery disease, atherosclerosis, plaque morphology, cardiac computed tomography, three-dimensional reconstruction

INTRODUCTION

With the increasing incidence, coronary artery disease (CAD) is the most common type of heart disease and the leading cause of death globally (1). The stenosis of coronary arteries incurred by the growth of atherosclerotic plaques is the major cause of CAD and related cardiac events such as acute myocardial infarctions (MI) (2). Therefore, the accurate evaluation of atherosclerotic plaques in coronary arteries is important for the diagnosis and treatment of CAD.

In the diagnosis of CAD, computerized tomography (CT) imaging is the most commonly used imaging technique. Cardiac or cardiovascular CT (CCT), also named as coronary computed tomography angiography (CCTA, sometimes short as coronary CTA), or CT coronary angiography (CTCA), has a high spatial resolution to reflect the anatomic severity and morphology of coronary plaques. The anatomic severity of coronary plaques estimated by CT imaging was in accordance with the results derived from intravascular ultrasound (IVUS) imaging (3). CT imaging has a higher resolution than the cardiac magnetic resonance imaging (MRI) (4). Compared with MRI and IVUS, CT is low-cost, non-invasive, and available on patients with implants (5). Furthermore, CT imaging could reflect the morphology of plaques by differentiating various compositions. Non-calcified, partially calcified, and calcified plaques could be differentiated based on their x-ray attenuation values (in Hounsfield units, or HU) which reflect the brightness of certain areas in CT images (6).

Since the early 2000s, the development of multi-slice CT (MSCT) technology, which refers to a special CT system equipped with a multiple-row (4, 8, 16, and 64) detector array that can collect a high volume of patient data in each gantry rotation, provides the possibility of reconstructing the three-dimensional (3D) geometry of atherosclerotic plaques in coronary arteries (7, 8). Especially, the 64-detector CT scanners showed better accuracy than the 4- or 8-detector ones in the diagnosis of significant coronary arterial stenosis (diameter stenosis >50%) (9). Based on the analysis of coronary CT images, the diameter stenosis and calcification volume have been widely used in the CAD-related clinical applications (10). In the meantime, the automatic 3D reconstruction and quantification of the non-calcified component was also achievable (11). The standardized, quantitative analysis of coronary CTA datasets was reproducible for the measurement of plaque geometrical and compositional parameters (e.g., plaque length, percentage area stenosis, and percentage of atheroma volume) in different geometric dimensions with high intra-observer and inter-observer agreement (12). Based on the comparison with histological images, the MSCT images have been applied in the analysis of coronary plaque morphology (13). Since the late 2000s, the 3D geometry of coronary plaque reconstructed from MSCT images has been widely applied in the computational simulation of plaque stress (14), wall shear stress (15), and the accumulation of low-density lipoprotein (16). The accurate extraction and reconstruction of coronary plaques from CT images plays a key role in improving the quality of diagnosis and treatment of CAD, as well as the pathophysiological studies of coronary arteries.

Currently, the majority of the studies on the extraction of coronary plaques from CT images are based on the difference in attenuation values, which is not sufficient for the accurate evaluation of coronary plaques. For calcified plaques, the blooming artifact could cause the overestimation of plaque areas, especially in the cases with significant calcification (17). For non-calcified plaque, it is difficult to differentiate between fibrotic and lipid plaques. Another challenge is the demarcation between the non-calcified or mixed plaques, the outer vessel border consisting

of the tunica adventitia, and the surrounding tissues, which are similar in intensity (18). To achieve the accurate evaluation of coronary plaques using CT images, technical innovations are needed to overcome these challenges.

Recently, some novel methods and algorithms have been proposed to improve the accuracy of coronary plaque extraction from CT images. In this review, the novel methods and algorithms are categorized, analyzed, compared, and summarized to disclose the future directions toward more accurate CT-based evaluation of coronary plaques.

METHODS

The keywords for the literature search are “coronary artery” or “coronary” combined with “atherosclerotic plaque” or “plaque,” and “CT” or “computerized tomography”. Publications written in English from 2015 to June 2019 were searched on PubMed, Web of Science Core Collection, IEEE Xplore Digital Library, and <https://scholar.google.com>.

Over 50 papers have been found. Based on the titles, keywords, and abstracts, more than 20 papers were excluded which did not propose methodological or technological innovation of coronary plaque extraction. Finally, 31 papers were selected for the review including 27 journal articles and 4 conference papers.

The selected publications were categorized according to the dimension of the plaque extraction method. In the two-dimensional (2D) methods, the coronary arteries and plaques are directly segmented and extracted from the 2D images. In the 3D methods, the 3D structures of coronary arteries and plaques are reconstructed from the 2D images. At present, the clinical diagnosis and research of CAD are based on the CTCA images derived from the MSCT scan. The MSCT scan provides a solid basis for 3D CTCA analysis. Whereas, the original CT images derived from MSCT scans are still the transverse 2D images. The 3D CTCA images and the 2D CTCA images on coronal and sagittal cross-sections are obtained through reconstruction. As the original data, 2D CTCA images are essentially more accurate than other reconstructed images. Therefore, the 2D CTCA images are still widely used in some recent studies (19). The reconstructed 2D images, including the coronal, sagittal, and curved planar reformation images, also play an important role in clinical diagnosis (20). Additionally, the current diagnostic standards and guidelines are based on the geometric parameters (especially the diameter stenosis) derived from 2D images of coronary arteries (21). Therefore, the 2D methods are included and analyzed in this review while the 3D methods will be increasingly important in future studies.

Some studies included 3D reconstruction and volumetric measurement. However, in these studies, the 3D reconstruction was automatically performed by software without any technical details disclosed (22), and the aim was the comparison or validation of 2D image processing algorithms (23–27), without methodological innovation in 3D volumetric analysis (17). Therefore, they were categorized as 2D methods. Some studies used the automatic 3D reconstruction of coronary plaques, but

volumetric measurement is a major objective (28–32), or the 2D images were extracted from 3D CTA images (33), therefore, they were classified as 3D studies.

In the following sections, 2D methods and 3D methods will be separately analyzed and summarized in three aspects: data, method, and evaluation. Regarding the data, we listed the details of data source (*in vivo*, *in vitro*, *ex vivo*, or phantom), inclusion criteria on arterial segment and plaques, numbers of human subjects and arterial segments. Regarding the method, we analyzed the classification of plaques (calcified and non-calcified; calcified, lipid and fibrotic; etc.), attenuation values of different plaques, methods of plaque extraction and reconstruction, as well as the technical innovations. Regarding the evaluation, we analyzed the geometric parameters in different dimensions, the intra- and inter-observer repeatability of the results, and the reference for the evaluation of accuracy (IVUS, histopathologic examination, etc.).

RESULTS

2D Methods of Coronary Plaque Extraction From CT Images

Classification of Data

We found 13 studies on 2D plaque extraction, including 12 original studies and a review paper (34). The majority (10 out of 12) of original studies used *in vivo* data which were collected non-invasively (17, 22–27, 35–37). Three studies used phantoms for data collection, in which 2 studies used phantom data in parallel with *in vivo* data (17, 37) while one used exclusively the phantom data (38). One study used *ex vivo* data (39).

In terms of the medical imaging techniques, *in vivo* data are the imaging data collected from living and functional organisms. *In vivo* imaging data are patient-specific. *In vivo* CT imaging data could be derived before and after the clinical treatment as the baseline and the follow-up observations to evaluate the severity of the CAD and the efficiency of treatment. Therefore, *in vivo* data play a key role in the diagnosis and treatment of CAD. However, CT scans are mainly performed on patients with CAD. *In vivo* data of healthy individuals are relatively rare.

CT imaging data could be collected from phantoms. A major benefit of phantoms is their controllable geometry. By presetting the geometric parameters (diameters, length, severity of stenosis, etc.) of plaque phantoms, and comparing with the geometry reconstructed from CT imaging, the accuracy of plaque extraction algorithms could be quantitatively evaluated. In a recent study, the accuracy of a vendor-specific model-based iterative reconstruction algorithm was evaluated on phantoms for both calcified and non-calcified plaques (37). A straight acrylic tube (length: 50 mm, diameter: 3 mm) was used as the model of coronary artery. Polystyrene, mono cast nylon, and acrylonitrile butadiene styrene copolymer were mixed to simulate soft, intermediate, and calcified plaques, with stenotic attenuation value of 40, 80, and 150 HU. Two stenotic degrees of 50% and 75% were used to evaluate the accuracy of plaque extraction in different plaques.

Using different plaque components, different anatomic structures, and different sizes, phantoms can be used in the comprehensive evaluation of plaque extraction methods. To optimize the CTCA protocol for more accurate extraction of plaques and coronary arteries, as well as early detection of the vulnerable plaques (non-obstructive atherosclerotic plaques with a thin fibrous cap covering fatty debris, leading to thrombus formation and embolization when ruptured), Kashani et al. used a phantom which contained 7 channels with different diameters between 3 and 5 mm. The channels were filled with different materials to simulate cholesterol and adipose tissues of the plaques, and surrounding myocardial tissues (38). The authors suggested that CTCA imaging of lipid-rich plaques can be optimized through using intermediate x-ray tube currents of 300 and 400 mA and the adjustment of the x-ray tube potential. To investigate the accuracy of iodine quantification with dual-energy CT imaging of coronary arteries, Pelgrim et al. developed an anthropomorphic phantom including artificial lungs, spine, body fat, and a cavity at the position of the heart. The cavity was filled with a holder carrying five separate tubes to simulate coronary arteries. Different patient sizes were simulated using extension rings with densities comparable to fat (40).

Another benefit of using phantoms is the avoidance of complex operation and clinical risks of *in vivo* imaging on human subjects or animals. To fully validate the results derived from phantoms, and investigate their clinical applications, two studies included both phantoms and *in vivo* data (17, 37). The first study focused on the calcified plaques with $\geq 50\%$ and $\geq 70\%$ luminal stenosis on CT images, and simulated them in phantoms to evaluate if the de-blooming algorithm would derive more accurate plaque extraction (17). The second study included both calcified and non-calcified plaques with 50% and 75% stenosis in a coronary vessel model whose length and radius were 50.0 and 3.0 mm, respectively (37).

Nevertheless, the use of phantoms also has some limitations. Firstly, phantoms have highly simplified geometry which could not present the patient-specific anatomy. It is commonly observed that the anatomy of human coronary arteries is highly diverse among the population. Secondly, it is difficult to use phantoms to simulate the mixed plaques consisting of lipid and fibrotic components with speckled calcifications (diameter < 2 mm), which are widely observed especially in the early phase of calcification (41).

One study used *ex vivo* imaging data which were derived from three *ex vivo* human hearts during post-mortem. Both CCTA and IVUS imaging were performed. Coronary computed tomography angiography and IVUS images of arterial cross-sections in 1-mm increments were co-registered. To evaluate the accuracy of the proposed algorithm of plaque reconstruction, the plaque areas reconstructed from CCTA images were compared with the plaque areas in the corresponding IVUS images (39). The *ex vivo* imaging data could be desirable than *in vivo* data in some aspects. Firstly, imaging is much easier to perform on *ex vivo* specimen than on *in vivo* organ. Additionally, the *ex vivo* data are free from the motion artifact which is inevitable in *in-vivo* data. Therefore, *ex vivo* data could be used for quantitative evaluation of plaque reconstruction from patient-specific CT images. However, *ex*

vivo imaging data were rare, therefore difficult to be used in large-scales studies.

Inclusion Criteria on Arterial Segments and Plaques

We included different types of articles covering scientific, engineering, and clinical studies. Normal subjects and CAD patients were recruited in different studies in which the inclusion (or exclusion) criteria of human subject are highly diverse. Therefore, we focused on the inclusion (or exclusion) criteria of arterial segments and plaques.

For arterial segments, due to the limited accuracy of CT imaging in small branches, some studies included only the arterial segments with a radius larger than 1.5 mm (22, 34). The inclusion of only the proximal 40 mm of each coronary artery and the exclusion of left main coronary lesions were also used as criteria (39). In three phantom studies, the first one used the inner diameter between 3.5 and 4.5 mm (17). The second one used the length of 50.0 mm and a diameter of 3.0 mm for lumen (37). The third one included lumen diameter between 3 and 5 mm, wall thickness between 1.5 and 3.5 mm, with 10 mm as the segment length (38).

The severity of luminal stenosis, defined as the ratio between lumen diameters in stenotic and normal segments, was widely used as the inclusion criterion of plaques, especially non-calcified plaques. In the studies on 2D plaque extraction, the severity of luminal stenosis varies between 25% and 75% (37). In clinical diagnosis, luminal stenosis larger than 50% is widely used as the criterion of significant stenosis (22, 35–37).

Numbers of Human Subjects and Arterial Segments

Most of the studies on 2D plaque extraction included <100 human subjects. However, multiple arterial segments can be extracted from the imaging data of one subject. Therefore, in some studies, there are more arterial segments than human subjects. As mentioned, the only study using *ex vivo* data included three *ex vivo* human hearts (39). The following paragraphs are focused on the studies using *in vivo* data.

There were 2 pilot studies, which included <10 human subjects (27, 37). In the first study, 12 arterial segments were extracted from the imaging data of 10 human participants (37). In the second study, to investigate the automatic extraction of both calcified and non-calcified plaques, three male patients with acute myocardial infarct were included. For each subject, three CCTA scans were performed with different imaging parameters. In each scan, 17 coronary segments were extracted following the coronary arterial model proposed by the American Heart Association (AHA) (27).

Two studies included 10–50 human subjects. The first one included 31 human participants as well as 2 phantoms, from which 375 coronary arterial segments and 77 calcified plaques were extracted (17). This study was focused on the reduction of blooming artifact in extracting calcified plaques; therefore, patients with non-calcified plaques were excluded. Another study included 43 subjects to investigate the derivation of coronary calcium scoring (CCS) from low-radiation-dose (24). The analysis was based on individuals; therefore, the number of arterial segments was not provided.

Six studies included more than 50 (range: 53–99) subjects. Rossi et al. extracted 144 stenosed segments of coronary arteries from 99 patients to investigate if CTCA could be used in screening the functionally significant coronary lesions (35). To investigate the semi-automatic coronary plaque quantification, Øvrehus et al. collected the CTA data of 50 patients in which 627 arterial segments were confirmed as evaluable (diameter > 1.5 mm, without motion artifact) by observers. Luminal stenosis of > 70% and 50–70% was found in 1 and 4 patients, respectively. Non-calcified and mixed plaques were found in 17 and 55 arterial segments (22). Li et al. proposed a new algorithm to improve the accuracy of reconstructing non-calcified plaques (36). Seventy-seven non-calcified plaques were extracted from 66 patients. The analysis was plaque-based therefore the number of arterial segments was not disclosed (36). Similarly, two studies investigated the reconstruction of calcified plaques based on Agatston coronary artery calcium scoring (CAC) scoring, with CT data collected from 63 (23) to 60 (25) subjects, respectively, without mentioning the number of arterial segments. Another study investigated plaque compositions divided by five ranges of HU values. Totally 160 plaques were extracted from 53 patients, without mentioning the number of arterial segments (26).

In addition, there is a clinical literature review which includes over 6,000 cases (34). This large and diverse population was used to cover a wide range of vulnerable and non-vulnerable plaques, which differ in severity and composition.

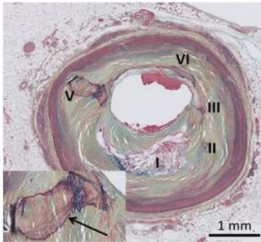
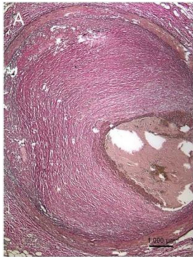
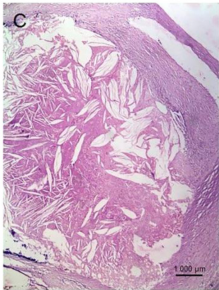
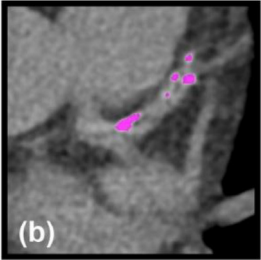
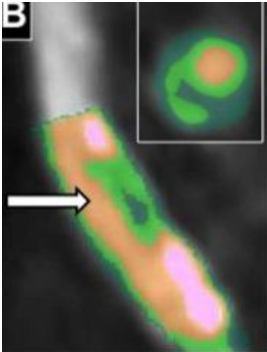
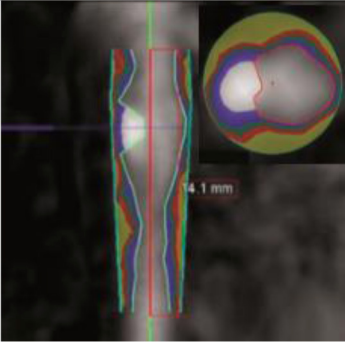

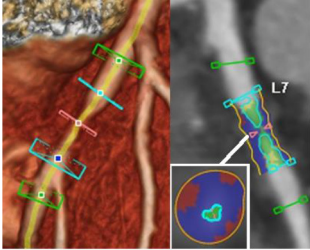

Considering the individual differences in the geometry of coronary arteries and plaques, recruiting large numbers of subjects could provide enough data for reliable statistical analysis. However, some of the presented studies have a small number of participants as they are pilot studies or phantom-based validation of algorithms. The extraction of multiple arterial segments from one subject is an important method to enlarge the sample size of arteries.

Classification of Coronary Plaques

The development of atherosclerosis starts from the filtration of low-density lipoprotein through the endothelium, which forms the fatty streaks in the arterial wall. The consequent inflammatory response involves macrophages, T-cells, and complex biochemical mechanisms, forming lipid-rich atherosclerotic plaques which finally become calcified and fibrous. According to the criteria proposed by AHA, the development of atherosclerotic plaques in coronary arteries consists of eight major stages: 1. Isolated macrophage foam cells; 2. Multiple foam cell layers formed; 3. Isolated extracellular lipid pools added; 4. Confluent extracellular lipid core formed; 5. Fibromuscular tissue layers produced; 6. Surface defect, hematoma, and thrombosis; 7. Calcification predominates; and 8. Fibrous tissue changes predominate (42).

Based on the AHA criteria, in grating-based phase-contrast computed-tomography (gb-PCCT) imaging of coronary arteries, four types of plaques could be differentiated: 1. Plaque with lipid or necrotic core surrounded by fibrous tissue with possible calcification; 2. Complex plaque with possible surface defect, hemorrhage or thrombus; 3. Calcified plaque; and 4. Fibrotic plaque without lipid core and with possible small

TABLE 1 | Graphical representation of described examples of calcified and non-calcified plaques.

Methodology	Calcified plaques	Non-calcified plaques	
		Fibrotic	Lipid
Histological sample			
	I: late fibro-atheroma (LFA) lesion (necrotic core covered by a fibrous cap). II-V: consolidated former lesions [fibrotic calcified plaque (FCP)]. Adapted from Lindeman et al. (44) © 2018 by the authors. CC BY 4.0.	Fibrous plaque, which is fibrocellular and also rich in proteoglycans (Elastic van Gieson, 100) Adapted from Vaideeswar et al. (45) © 2019 by the authors. CC BY 4.0.	Fatty plaque, comprising a large lipid-rich core separated from the lumen by a thin fibrous cap. The lipid material may in the form of collections of foamy macrophages and/or extra-cellular lipid material (HE, 100). Adapted from Vaideeswar et al. (45) © 2019 by the authors. CC BY 4.0.
2D plaque reconstruction			
	Calcification marked with purple mask. Adapted from Messerli et al. (25) © 2016 with permission from The Association of University Radiologists.	The necrotic core (35.3%, dark green) surrounded by fibrous plaque (51.5%, light green). Lumen and calcification (13.2%) are marked orange and pink, respectively. Inset shows cross-sectional images at arrows. Adapted from Obaid et al. (46) © 2017 by the authors. CC BY 4.0.	A lipid plaque: yellow <51 HU, red 51–100 HU, green 101–150 HU, blue 151–350 HU, white >350 HU. Adapted from Chen et al. (26) © 2016 with permission from The Foundation Acta Radiologica.
3D plaque reconstruction			

(Continued)

TABLE 1 | Continued

Methodology	Calcified plaques	Non-calcified plaques	
		Fibrotic	Lipid
	Lumen and calcified plaque reconstructed by semi-automatic and manual methods. Adapted from Kigka et al. (47) © 2017 with permission from Elsevier Ltd.	The semi-automatic analysis of a fibrotic plaque in LAD: lipid (red), fibrous (blue) and calcified (yellow) components. Adapted from Cui et al. (48) © 2017 by the authors. CC BY 4.0.	Semi-automatic segmentation of coronary vessel: calcified (yellow), lipid (green) and fibrotic (blue). The cross-section shows a lipid plaque. Adapted from Infante et al. (49) © 2019 by the authors. CC BY 4.0.

TABLE 2 | Methods of coronary plaque classification.

		Plaque classification	
	Calcified and non-calcified	Calcified, mixed, and non-calcified	Lipid-rich, fibrous, and calcified
2D reconstruction	Calcified and non-calcified plaques (22, 27, 35, 39). Calcified and non-calcified plaques, as well as high-risk plaques. The main CTCA features related to high-risk plaques are: (1) positive remodeling, PR [remodeling index (RI) ≥ 1.1]; (2) low-attenuation plaque, LAP (<30 HU); (3) napkin-ring sign, NRS (description below); and (4) spotty calcifications, SCs (<3 mm) (34).		Different plaque combinations (soft, intermediate, and calcified), different stenosis (50% and 75%), different lumen densities (low and high lumen), positive remodeling and spotty calcium (37). Non-calcified plaques, including fibrous and lipid-rich ones, components segmented using different thresholds: <51, 51–100, 101–150, 151–350, and >350 HU intervals (26).
3D reconstruction	Calcified and non-calcified plaques (32, 47, 51, 52).	Calcified plaque, non-calcified plaque, and mixed plaque, i.e., a plaque containing calcified and non-calcified components (53). Mixed (51%), non-calcified (31%), and calcified (18%) plaques (54). 729 non-calcified plaques, 511 calcified plaques, and 546 mixed plaques (33). The plaque area was stratified into <60 HU (lipid-rich plaque) and >180 HU (calcified plaque) parts (29). Soft lipid-rich plaques, mixed plaques, calcified plaques (55).	Lipid, fibrous, and calcified components as < 60 HU, 60–200 HU, and > 200 HU (31). Lipid-rich, fibrotic, and calcified plaques (28). Non-calcified plaque, low-density non-calcified plaque, and calcified plaque (56). Low-density non-calcified plaques (different thresholds of attenuation values used) and calcified plaques (30).

calcification (43). In the histological analysis, the calcified (44), fibrotic (or fibrous), and lipid (or lipid-rich) plaques (45) can be easily differentiated by the image features (**Table 1**). In general CT imaging, atherosclerotic plaques in coronary arteries can be classified into three categories: calcified, non-calcified, and partially calcified (or mixed) (50). Based on the advanced analysis of CT images, the non-calcified plaques could be further classified as lipid and fibrotic plaques (46), as illustrated in **Table 1**, which has been applied in 2D plaque extraction (26). Different classification methods of coronary plaques have been summarized in **Table 2**. Considering the difference between studies in the resolution of CT imaging, the accurate separation between lipid-rich and fibrotic plaques remains challenging (50). In clinical CT imaging, calcified and fibrotic plaques are frequently observed in fully developed stenoses since they reflect the late stages in the progression of atherosclerosis. Whereas, lipid-rich plaques are less commonly

observed since they mainly represent the initial stage of atherosclerosis, when the plaque could not cause severe stenosis and hemodynamic effects.

In the 13 studies on 2D plaque extraction, 4 studies included only calcified plaques (17, 23–25). Two studies were mainly focused on non-calcified coronary plaques (36, 38). Seven papers included both calcified and non-calcified coronary plaques, which gives us an overview of the progression of atherosclerosis in CAD patients (22, 26, 27, 34, 35, 37, 39).

Attenuation Values of Different Plaques

The attenuation value of calcification is much higher than that of the surrounding tissues. Therefore, the differentiation of calcified and non-calcified plaques on CT images could be achieved by setting thresholds of attenuation (24). The threshold for calcified plaques varies in different studies (see **Table 3**). An earlier study in 2011 used the ranges of 30–70 HU for non-calcified plaques

TABLE 3 | Comparison of attenuation values used in selected studies.

Study	Year	Dimension of reconstruction	Attenuation values (in HU units)	
			Calcified plaques	Non-calcified plaques
Li et al. (36)	2019	2	N/A	<60 for low-attenuation plaques <200 for high-attenuation rim with an inner hypo-attenuation area (<130)
Li et al. (17)	2018	2	1097–2910	N/A
Funama et al. (37)	2017	2	150	40 for soft plaques 80 for intermediate plaques
Braber et al. (24)	2016	2	>130 for Agatston Scores >351 and >600 for plaque reclassification	N/A
Messerli et al. (25)	2016	2	>130	N/A
Rodriguez-Granillo et al. (34)	2016	2	>130	<30 for low-attenuation plaques
Matsumoto et al. (30)	2019	3	>500	<150 for non-calcified plaques <30 and <45 for lipid-rich plaques
Kigka et al. (47)	2018	3	>400	<50
Wang et al. (31)	2017	3	>200	<60 for lipid plaques 60–200 for fibrotic plaques
You et al. (28)	2016	3	≥130	0–49 for lipid plaques 50–129 for fibrotic plaques
Puchner et al. (29)	2015	3	>180	<60

and >70 HU for calcified plaques (57). Another study in 2014 used the ranges of –10–69, 70–129, and >400 HU to differentiate lipid, fibrotic, and calcified plaques (58).

Attenuation scale has been used to differentiate non-calcified coronary plaques (59). However, the differentiation of non-calcified plaques is difficult due to the limited contrast between the fibrotic and lipid tissues in attenuation value (Table 3). Additionally, the attenuation values of a non-calcified plaque and its neighboring tissues are not significantly different around the boundary. Therefore, it is difficult to develop the fully automatic methods to reconstruct the non-calcified plaques and differentiate the components of non-calcified plaques.

For calcified plaques, Agatston CAC scoring is widely used as an estimation of the total amount of calcium for the prediction of adverse cardiovascular events in people with CAD. It is calculated using high calcium area slice of the CT image, multiplied by the maximal attenuation of the calcification in individual case (60). The attenuation value qualitatively reflects the different types (calcified and non-calcified) of plaques whereas the Agatston score quantitatively represents the calcification in coronary arteries.

Methods of Plaque Extraction and Reconstruction

The methods of 2D plaque extraction can be categorized as semi-automatic and automatic. During extraction, manual interaction is indispensable in semi-automatic methods but is infrequent in automatic methods. The manual interactions include: setting the boundaries of areas for analysis such as the start and end points of arterial segments and plaques, adjusting the automatic segmentation and extraction results to revise the geometric errors, and using the manual extraction results to train or validate new algorithms. Other manual interactions include

setting parameters in image processing and selecting CT images for analysis. The details are listed in Table 4.

Messerli et al. proposed a semi-automatic method to evaluate CAC on software (syngo.via CT CaScoring, Siemens Healthcare) (25). Firstly, coronary lesions with attenuation >130 HU were automatically color-coded. Then the calcified coronary structures were manually selected. Finally, the software automatically calculated the Agatston score, CAC volume (mm³), and CAC mass (mg/cm³). Similarly, Szilveszter et al. (23) used software to identify the coronary artery plaques with area ≥1 mm² and density >130 HU. Coronary plaques were selected manually to enable the semi-automatic software to calculate CAC scores.

The manual segmentation by tracing the proximal and distal plaque boundaries (26), and the visual examination and manual adjustment (24) were common in semi-automatic methods. Øvrehus et al. used manual interactions in imaging reconstruction and plaque segmentation (22). In multiplanar reformats of CTA images, a circular region of interest was placed in the aorta to define the “normal reference bloodpool.” The proximal and distal boundaries of each lesion were identified and marked by the reader. The software then automatically tracked the centerline of the coronary artery and quantitatively analyzed the plaques. Rossi et al. proposed a semi-automatic method to compare the visual and quantitative evaluations of plaques in CTCA images, in which various manual interactions were involved (35). Firstly, the CTCA data sets were evaluated visually, and the coronary lesion was graded as non-obstructive (<50% lumen narrowing), moderate (50% ≤ lumen narrowing <70%), and severe (≥70% lumen narrowing). Afterwards, the proximal and distal endpoints of coronary vessels with lumen diameter reduction ≥30% were manually marked. The lumen and vessel borders were generated automatically and

TABLE 4 | Manual manipulations in automatic and semi-automatic methods of plaque extraction.

Study			With manual manipulation				Others
			Set the boundary of analysis	Adjust the result when needed	Generate results to train the algorithm	Generate results to validate the algorithm	
2D reconstruction	Semi-automatic	Messerli et al. (25)	✓				
		Rossi et al. (35)	✓	✓		✓	
		Precht et al. (27)	✓	✓			
		Øvrehus et al. (22)	✓				
	Automatic	Szilveszter et al. (23)	✓				Window level and width of image reconstruction were adjusted for optimal visualization at the discretion of the observer.
		Chen et al. (26)	✓				
		Braber et al. (24)		✓			
		Li et al. (17)				✓	
		Li et al. (36)				✓	
		Funama et al. (37) (not explicitly pointed out as automatic)				✓	
		Kashani et al. (38) (not explicitly pointed out as automatic)	✓				
		Puchner et al. (39) (comparison between automatic and semi-automatic algorithms)		✓			
3D reconstruction	Semi-automatic	Kigka et al. (47)				✓	
		Matsumoto et al. (30)	✓			✓(extract IVUS images)	
	Automatic	Sakellarios et al. (52)			✓		Co-registration of IVUS and CTA images
		Gaur et al. (56)	✓				
		Puchner et al. (29)		✓			
		Wang et al. (31)		✓			
		You et al. (28)		✓			
		Sun et al. (61)		✓			
		Athanasίου et al. (62)			✓	✓	
		Wei et al. (63)	✓		✓	✓	
		Jawaid et al. (64)				✓	
		Ghanem et al. (55)				✓	
		Károlyi et al. (32)	✓				
		Zhao et al. (33)	✓			✓	
		Zreik et al. (53)			✓	✓	Using Rotterdam Coronary Artery Evaluation Dataset
		Kang et al. (51)			✓	✓	
		Park et al. (54) (comparison between automatic and semi-automatic algorithms)		✓		✓	

adjusted by an experienced observer. The quantitative analysis of plaques was automatically completed by software. Precht et al. adopted similar semi-automatic method to estimate plaque volume in low-dose CCTA (27). The centerlines of the coronary arteries were automatically extracted and manually corrected when needed. The extracted arteries were manually partitioned according to the AHA 17-segment model. For each artery, the contours of lumen and outer vessel wall were automatically detected and manually fine-tuned by two independent observers with more than 7 years of experience. The manual fine-tuning of the automatic contour detection only showed a 0–7.3% deviation which did not significantly influence the final results. Puchner et al.'s compared the automatic and semi-automatic methods in generating vessel wall boundaries (39). The boundaries of vessel wall (inner, outer, or both) were manually corrected.

The manual segmentation results play an important role in the validation of automatic algorithms. Li et al. developed an automatic algorithm for CT image processing (36). For validation, two experienced radiologists independently identified plaque characteristics on the images reconstructed with different algorithms. Similarly, Funama et al. used the consensus of two CT image reviewers in plaque evaluation to compare different image processing algorithms (37). The reconstructed CT images were manually classified into four levels of quality, in vessel and plaque areas, respectively. Li et al. proposed an automatic de-blooming algorithm (17). Coronary computed tomography angiography images of phantoms were manually selected by the operator to find the images at the optimal cardiac phase with the least motion artifact. For *in vivo* CCTA images, an experienced reader independently reviewed all data sets, noted coronary calcification, and measured the volume of calcified plaques, coronary diameter stenosis (%), as well as the coronary area stenosis (%) on software as the reference for validation. Kashani et al. optimized the parameters of CCTA by comparing the quality of images derived by different parameter values (38). The contrast-to-noise ratio (CNR) was measured manually by prescribing a 0.018–0.021 cm² region of interest in the center of the plaque and pericoronary fat in 8 different locations.

For 2D plaque extraction, there are more semi-automatic methods than automatic methods. Automatic methods are efficient and convenient for the large-scale extraction of coronary arteries and plaques from the CT images. However, the plaque size is often over- or underestimated when using automatic software. Hence, the manual interactions including editing and analysis are useful to improve the accuracy of 2D plaque extraction (22).

Technical Innovations

Filtered back projection (FBP) is a traditional type of algorithm that can indicate an attenuation value to each pixel (65) on CTA images. Filtered back projection reconstruction assumes that each pixel accurately indicates the attenuation. In 2D coronary plaque reconstruction, FBP is widely used to derive the reference values for the validation of new algorithms. Iterative reconstruction (IR) algorithms have the potential to improve the quality of CT image by reducing image noises and blooming artifacts when compared with FBP. IR algorithms are the majority

of new algorithms in 2D coronary plaque reconstruction. In the following paragraphs, the algorithmic innovations will be summarized in terms of the improvement of accuracy in extracting different types of plaques.

Calcified Plaques

Calcified plaques are easy to extract from CT images due to their high attenuation values. Nevertheless, the brightness of a calcified plaque could affect its neighboring pixels by increasing their attenuation values. Consequently, the overestimation of the calcification size is common. Li et al. developed a de-blooming algorithm and applied it on CCTA images of 31 patients (17). They found that the de-blooming algorithm reduced the calcification volume and the stenosis in diameter by $48.1 \pm 10.3\%$ $52.4 \pm 24.2\%$, respectively. However, the details of this algorithm were not disclosed (17).

Szilveszter et al. investigated the impact of iterative model reconstruction (IMR) on coronary artery calcium quantification as compared with the standard FBP and hybrid iterative reconstruction (HIR) algorithms (23). CT images of 63 individuals were reconstructed with FBP, HIR, and IMR. HIR and IMR resulted in lower CAC scores as compared with FBP (both $p < 0.001$). There was no difference between HIR and IMR ($p = 0.855$). The authors concluded that the utilization of IMR for CAC scoring can reduce the measured calcium quantity (23).

Braber et al. investigated the quantification of calcification in low-dose CCTA images using IR (24). Coronary artery calcium was quantified with Agatston scores on the CCS images using a semi-automatic software package (HeartBeat-CS; Philips Healthcare, Best, the Netherlands). For Agatston scoring, CAC was defined as regions with ≥ 130 HU within coronary arteries. All regions with density higher than 130 HU were automatically indicated by the software package. Calcification volumes were derived with a semi-automatic software package (QAngio CT v2; Medis Medical Imaging Systems, Leiden, the Netherlands) (24).

However, it was also suggested that IR could underestimate the calcification. Messerli et al. evaluated the influence of advanced modeled iterative reconstruction (ADMIRE) on the coronary artery calcium (CAC) scores, with FBP algorithm as the reference (25). CT images of 60 patients were reconstructed with FBP and ADMIRE at incremental strength levels of 1, 2, 3, 4, and 5, resulting in a total of 6 datasets. In four patients with low calcium burden, the use of ADMIRE 2 or higher resulted in the disappearance of calcium that was detectable using FBP. The authors concluded that ADMIRE causes a substantial reduction of the CAC scores measured by cardiac CT, which leads to an underestimation of cardiovascular risk scores in some patients (25).

Non-calcified Plaques

As to non-calcified plaques, the contrast in grayscale values between plaques, arterial walls, and surrounding tissues is low in CT images. The attenuation values or CAC/Agatston scales could not reflect the exact geometry of non-calcified plaques. To accurately separate the non-calcified plaques from the surrounding tissues, the morphological properties of non-calcified plaques need to be considered. Therefore, new

algorithms based on IR (23) have been proposed to improve the quality of CT image in order to find the morphological and geometrical properties of the boundary between non-calcified plaques and surrounding tissues (17).

Li et al. assessed the effects of IMR algorithm on image quality in demonstrating the characteristics of high-risk non-calcified plaques in coronary arteries, in comparison with the HIR algorithm (36). The 256-slice CT images were derived from 66 patients with 77 non-calcified plaques. Paired CT image sets were reconstructed by HIR and IMR, respectively, on which plaque characteristics were compared. The signal-to-noise ratio (SNR) and CNR of the images, as well as the CNR between the plaque and adjacent adipose tissue, were also compared between the two reformatted methods. The napkin-ring sign appeared in 40 and 19 plaques reconstructed with IMR and HIR, respectively, which are significantly different ($p < 0.001$). Compared with HIR, IMR derived lower image noise (10 ± 2 HU vs. 12 ± 2 HU; $p < 0.01$), higher SNR and CNR, and especially higher CNR between plaques and surrounding adipose tissues ($p < 0.01$). The authors concluded that IMR can significantly improve image quality compared with HIR for the demonstration of atherosclerotic plaques in coronary arteries (36).

Furthermore, Chen et al. applied IR algorithm in the assessment of plaque vulnerability (26). They compared coronary plaque volume and low attenuation (lipid-rich) component derived by IR and FBP, respectively, from CTA images of 53 patients. Coronary plaques were identified by a board-certified radiologist (14 years of experience in cardiac CT). Then post-processing was performed by a research assistant trained in plaque volumetric analysis. The analysis was done in multiplanar reformat (MPR) using a semi-automated software (Aquarius iNtuition 4.4.6, TeraRecon Inc., Foster City, CA, USA). Proximal and distal plaque boundaries were traced manually. Total plaque volume was then obtained automatically. Plaque composition was assessed using attenuation (HU) intervals. It was found that IR significantly decreased the noise and increased SNR and CNR compared with FBP. Plaque characterization was performed in 41 patients for a total of 125 plaques. Regarding the total plaque volume and the low attenuation plaque component, there was no statistically significant difference between all IR levels and FBP. The authors concluded that no significant impact on plaque vulnerability assessment should be expected when using IR vs. FBP for plaque reconstruction from CTA images (26).

Different Plaques

Puchner et al. applied IR algorithm in semi-automated extraction of different plaques (fibrous, fatty, or fibrofatty, and the presence of calcification) (39). Coronary computed tomography angiography and IVUS images of seven coronary arteries were acquired *ex vivo*. Images of 173 cross-sections of coronary arteries were coregistered between CCTA and IVUS in 1-mm increments. Coronary computed tomography angiography images were reconstructed using FBP with adaptive statistical (ASIR), and model-based (MBIR) iterative reconstruction algorithms. Fully automated (without manual corrections) and semi-automated (allowing manual corrections of vessel wall boundaries) plaque burden assessments were performed for each reconstruction

algorithm. Agreement between CCTA results and IVUS was evaluated with Pearson correlation. It was found that manual correction of the semi-automated assessments improved plaque burden correlation with the IVUS assessment independently of reconstruction algorithm ($p < 0.0001$). Furthermore, MBIR was superior to FBP and ASIR in semi-automated and fully automated plaque extraction (all $p < 0.001$). It was concluded that MBIR with semi-automated assessment could improve the accuracy of plaque burden assessment in CCTA images (39).

Overall Plaque Burden

Precht et al. compared ASIR and MBIR reconstruction algorithms on quantitative measurements of plaque volumes and intensities in coronary arteries (27). Dose-reduced CCTA were derived from 3 patients and reconstructed with 30% ASIR (CTDIvol at 6.7 mGy), 60% ASIR (CTDIvol 4.3 mGy) and MBIR (CTDIvol at 1.9 mGy). Quantitative coronary plaque analysis was performed. Centerlines of the coronary arteries were automatically extracted and manually corrected. The extracted vessels were manually partitioned according to the AHA 17-segment model. The contours of lumen and outer vessel wall were automatically detected and manually fine-tuned. The plaque burden was calculated as the ratio between total plaque volume and total vessel volume. It was found that plaque volume and plaque burden show a decreasing tendency from ASIR to MBIR. The lumen and vessel volume decrease slightly from 30% ASIR to 60% ASIR. The intensities did not change overall between the ASIR and MBIR reconstructions for either lumen or plaque (27).

Funama et al. investigated the effect of contrast enhancement on the stabilities of plaque attenuation, using FBP and IR algorithms in imaging reconstruction (37). 320-detector volume scanning was performed on phantoms of vessel tubes with stenosis and a tube without stenosis using three types of plaque attenuation values. CTA images were reconstructed with FBP and two types of IR [AIDR3D and FIRST (forward-projected model-based iterative reconstruction solution)], with stenotic attenuation value of ~40, 80, and 150 HU, respectively. In each case, the tubing of the coronary vessel was filled with diluted contrast material and distilled water to reach the target lumen attenuation values of ~350, 450, and 0 HU, respectively. It was found that at 50% stenosis, the plaque attenuation value with contrast enhancement increased for FBP and AIDR3D, and the difference in the plaque attenuation value with and without contrast enhancement was 15–44 HU for FBP and 10–31 HU for AIDR3D. However, the plaque attenuation value for FIRST had a smaller variation and the difference with and without contrast enhancement was –12–8 HU. The validation study was performed on CT images of 10 patients where FIRST derived the highest CNR in vessels and plaques. The authors concluded that the FIRST method improves the visualization of coronary plaques in coronary CT angiography (37).

Geometric Parameters in Measurement

In 2D reconstruction, some geometric parameters could be directly measured from the 2D images, including cross-sectional area, lesion length, minimal area diameter, and mean vessel size

for the affected blood vessels (39). These parameters reflect the size of plaques and affected arterial segments.

The extent of coronary plaque could also be quantitatively evaluated by plaque burden, which is defined as the percentage of plaque in cross-section area: $PB = (ACN - ACS) / ACS$, where PB denotes plaque burden while ACN and ACS denote the cross-section areas in normal and stenotic arterial segments, respectively (39, 66).

Intra- and Inter-Observer Repeatability

Intra-observer and inter-observer repeatability reflect the consistency between repeated measurements performed by one observer and different observers, respectively. The expertise in coronary CT imaging and diagnosis can improve the intra- and inter-observer repeatability (67). Acquiring expertise in CTA interpretation may take more than a year. It has been reported that, for coronary CT imaging, the intra- and inter-observer repeatability on plaque volume estimation depends on the size of plaque (68). Furthermore, the repeatability results indicated that the percentage of plaque composition is more reliable than plaque volume (69). Therefore, the estimation of intra- and inter-observer repeatability is important to validate the reliability of plaque extraction methods.

In the 13 studies on 2D plaque extraction, the intra-observer repeatability was evaluated in five studies (22–24, 26, 38). Inter-observer repeatability was evaluated in 7 studies, (17, 22, 23, 26, 27, 36, 37). Six studies reported that the measurements were repeated by at least one expert with more than 5 years of experience (17, 26, 27, 36, 37). Comparatively, the experience of expert was between 1 and 5 years in other two studies (22, 23).

Reference of Accuracy

To evaluate the accuracy of plaque extraction algorithms, the reconstructed coronary plaques from 2D CT images were often compared with the results derived from invasive coronary angiography (ICA) (35), IVUS (39), or pre-defined geometric parameters in phantoms (38). Compared with CT imaging, the ICA and IVUS are more accurate in reflecting the geometric details of lumen, therefore have been widely used as the reference in related studies (70, 71).

3D Methods of Coronary Plaque Extraction From CT Images

Classification of Data

We found 17 papers focused on the 3D methods of coronary plaques extraction and reconstruction, including 16 original studies (28–33, 47, 51–56, 61, 62, 64), and a review paper (72). The same method was adopted in Athanasiou et al. (73) and Sakellarios et al. (52). The imaging data used in 3D plaque extraction include phantom, *ex vivo*, *in vitro*, and *in vivo* data.

A study used 17 plaque phantoms in three different types of attenuation, to investigate the reliability of low radiation dose CT imaging in representing the 3D geometry of plaques. By using phantoms, the accuracy of plaque extraction could be quantitatively evaluated in volume (31).

In 3D plaque extraction, *ex vivo* imaging data enable the researchers to perform accurate 3D geometric measurements

(29). The results of plaque extraction could be compared with the histopathological measurement as the ground truth (29). Nevertheless, the lumen of an *ex vivo* artery is hollow whereas the lumen of the corresponding *in vivo* artery is filled with blood which has cyclic changes in pressure, velocity, and wall shear stress. Consequently, considering the effects of cyclic fluctuations of blood flow on the deformation and mechanical properties of arterial walls, the geometry of *ex vivo* arteries could be different from *in vivo* ones, which is a major limitation of *ex vivo* data (74).

In vitro data, here defined as the imaging data derived from patient-specific models of coronary arteries, could provide patient-specific geometry parameters of plaques and affected arteries. Compared with *in vivo* and *ex vivo* data, *in vitro* data could accurately reflect the geometry of arteries without motion artifact. Sun et al. used *in vitro* data of calcified plaques with different severities from three subjects to investigate the effect of slice thickness and beam energy on the accuracy of synchrotron radiation CT imaging. The *in vitro* arterial models were generated from the original high-resolution CCTA images using 3D printing technique. The plaques reconstructed from the synchrotron radiation CT images of the *in vitro* models were compared with those reconstructed from the origin CCTA images (61). Using *in vitro* data, the accuracy of plaque extraction could be quantitatively evaluated in anatomical details of patient-specific geometry. However, the high-resolution images for *in vitro* model reconstruction, the materials and devices for 3D printing, as well as the multiple imaging operations for comparison, limited the further application of *in vitro* data in clinical diagnosis.

In vivo data were used in the majority (14 out of 17) of the original studies on 3D plaque extraction (28, 30, 32, 33, 47, 51–56, 62, 64) and was mentioned in the review paper [(63) in (72)]. With 3D reconstruction, the diversity in the geometry and composition of plaques could be fully disclosed and represented not only on cross-sections but also in the longitudinal direction along the vessel, as well as in volume. Therefore, *in vivo* data play a key role in investigating the 3D geometry and composition of coronary plaques.

Inclusion Criteria on Arterial Segments and Plaques

The inclusion criteria in 3D plaque extraction studies are more diverse compared with 2D studies. In 3D reconstruction, the geometric details in different dimensions and the combination with plaque composition generated more detailed inclusion criteria for arterial segments and plaques compared with 2D reconstruction.

For arterial segments, the diameter (28) [as summarized in (72)] and length of segment (56, 64) were widely used as in 2D reconstruction studies. In a study on the prediction of all-cause mortality in CAD patients based on CCTA images (55), 16 arterial segments were extracted and 3D reconstructed according to a 16-segment model of coronary arterial tree (75). In another study, to investigate the difference between proximal and distal segments of the main coronary arteries [anterior descending artery (LAD), left circumflex artery (LCX), right

TABLE 5 | Characters of data in the studies of 3D coronary plaque analysis.

Study	Year	Type of data	Number of subjects	Number of stenosis or sections	Standards of inclusion or exclusion of artery segment (length of diameter)
Gaur et al. (56)	2016	<i>in vivo</i>	254	484 vessels	Coronary segments ≥ 2 mm with plaque were analyzed. Spotty calcification was visually identified as calcifications comprising $<90^\circ$ of the vessel circumference and <3 mm in length
Jawaid et al. (64)	2018	<i>in-vivo</i>	8	13 non-calcified segments	Maximum arterial segment length of 6 mm used for segmentation
Sakellarios et al. (52) Athanasίου et al. (73)	2016	<i>in-vivo</i>	20	20	N/A
You et al. (28)	2016	<i>in-vivo</i>	87	N/A	diameter >2.0 mm
Ghanem et al. (55)	2019	<i>in-vivo</i>	41	122 plaques	16 arterial segments in each case, according to a modified coronary arterial tree model (75).
Wei et al. (63) as summarized in the review by Jawaid et al. (72)	2018	<i>in-vivo</i>	83	120 soft plaques	Radius <3 mm to ensure that whole arterial cross-section is covered since 2.5 mm is the maximum radius of coronary arteries
Athanasίου et al. (62)	2016	<i>in-vivo</i>	10	8 calcified plaques deposits	N/A
Park et al. (54)	2015	<i>in-vivo</i>	142	150 coronary artery segments	11 segments excluded due to the insufficient IVUS or CT image quality (seven segments) caused by severe calcification or motion artifacts
Kigka et al. (47)	2018	<i>in-vivo</i>	12	12 arteries	N/A
Károlyi et al. (32)	2017	<i>in-vivo</i>	52	468 segments, with 41 calcified or partially calcified plaques identified	proximal and distal coronary segments, with middle coronary segments and side branches excluded
Zhao et al. (33)	2019	<i>in-vivo</i>	48	1,786 cross-sections: 729 non-calcified plaques, 511 calcified plaques, and 546 mixed plaques	N/A
Matsumoto et al. (30)	2019	<i>in-vivo</i>	77	118 plaques without extensive calcifications	4 plaques excluded due to extensive echo attenuation on IVUS
Wang et al. (31)	2018	<i>In-vitro</i>	N/A	17	N/A
Puchner et al. (29)	2015	<i>ex-vivo</i>	3	26 and 67 cross-sections of lipid-core and calcified plaques	Lipid-core plaque was included and defined as any fibroatheroma with a lipid core $>60^\circ$ in circumferential extent, with a core width of $>200 \mu\text{m}$ and a cap thickness of $<450 \mu\text{m}$
Sun et al. (61)	2018	<i>In-vitro</i>	3	3	N/A
Kang et al. (51)	2015	<i>In-vivo</i>	42	252 segments of 126 arteries in total, 45 lesions with stenosis $\geq 25\%$	N/A
Zreik et al. (53)	2019	<i>In-vivo</i>	163	1,259 segments of 534 arteries, 37 non-calcified, 161 mixed and 317 calcified plaques	N/A

coronary artery (RCA)], the middle segments and side branches were excluded (32). In some studies, arterial segments especially distal branches were excluded due to low quality of images (30, 54).

Regarding the coronary plaques, the severity of included stenoses ranged from 25% to more than 90% (47, 51). More detailed inclusion criteria have been proposed based on the analysis of plaque geometry in different dimensions. Gaur et al. investigated the difference between calcified and non-calcified plaques in FFR, where the criterion of spotty calcification was defined as visually identified calcifications comprising $<90^\circ$ of the vessel circumference and <3 mm in length (56). Similarly, in another study which investigated the accuracy of 3D reconstruction of lipid-core plaques, a lipid-core plaque was defined as any

fibroatheroma with a lipid core $>60^\circ$ in circumferential extent, with a core width of $>200 \mu\text{m}$ and a cap thickness of $<450 \mu\text{m}$ (29).

Numbers of Human Subjects and Arterial Segments

The number of human subjects covers a wide range (3–254) in different studies on 3D reconstruction of coronary plaques. Firstly, only three human subjects were included in the two pilot studies using exclusively *ex vivo* and *in vitro* data (29, 61). In contrast, the studies using *in vivo* data included at least 8 human subjects (Table 5). Secondly, regarding the studies using *in vivo* data, those included <30 human subjects were focused on algorithmic development with limited validation (52, 64) or initial validation (47, 62, 73). In contrast, the studies including more than 80 subjects were aimed for the full validation of

existing algorithm (63), the pathological indication of results (28), and clinical applications (54, 56).

In many large-scale studies, the inclusion (or exclusion) criteria and information of subjects are provided in details. To investigate the effects of plaque properties (severity, volume, length, etc.) on the occurrence of myocardial ischemia, a clinical study included 484 coronary arteries extracted from 254 participants. The plaques were categorized according to their severity: 0, 1–29, 30–50, 51–70, 71–90, 91–99, or 100% (56). For machine learning algorithms, it is significant to generate a large-scale dataset for training and validation. Kang et al. investigated the differentiation between obstructive and non-obstructive plaques using machine learning, where CTA data were collected from 42 patients in which 45 stenotic coronary lesions with $\geq 25\%$ luminal stenosis were extracted from 21 patients (51). Zreik et al. used deep learning to classify coronary plaques (no plaque, non-calcified, mixed, and calcified), where CCTA data of 98 and 65 patients were used for the training and validation of algorithm, respectively. In total, 1,259 arterial segments were extracted from 534 arteries (53). In large-scale studies, the diversity and individual difference in plaque geometry could be comprehensively investigated. However, the data collection for large-scale studies could be time-consuming and expensive.

In the studies on 3D plaque extraction, similar as in 2D studies, the numbers of arterial segments and plaques are generally more than the number of subjects. In some studies, the analysis of plaques is based on the cross-sections, where the number of cross-sections is much higher than that of subjects (29, 32, 33). In a recent study, 1,786 cross-sections were extracted from a CTA dataset of 48 patients to generate enough data for the 10-fold cross-validation of the proposed algorithm (33). The extraction of cross-sections could enlarge the dataset for analysis. Nevertheless, only 2D geometry is represented on cross-sections. Plaque-based analysis is needed to comprehensively evaluate the accuracy of 3D plaque extraction.

Classification of Coronary Plaques

The 3D structure of calcified, fibrotic (48), and lipid (49) plaques could be reconstructed from CT images. There are 2 studies which exclusively included non-calcified plaques (64, 72). Two studies were focused on the manual extraction of calcified plaques (61, 62). In these studies, the calcified or non-calcified plaques were not further classified. In the majority of studies on 3D plaque extraction (13 out of 17), both calcified and non-calcified coronary plaques were included (28–33, 47, 51–56). In these studies, we observed diverse standards in the classification of non-calcified plaques, as shown in **Table 2**. The plaques could be classified according to the main component as soft lipid-rich plaques, mixed plaques, and calcified plaques (55), or non-calcified plaques, low-density non-calcified plaques, and calcified plaques (56). The volume of extracted component heavily depends on the threshold of attenuation value applied in the study (30).

Attenuation Values of Different Plaques

As shown in **Table 3**, in 3D plaque extraction, 130 HU was used as the lower threshold of calcified plaques (28) similar as in 2D studies, while higher attenuation values such as 400 HU (47) and 500 HU (30) were also observed. For non-calcified plaques, the 3D reconstruction studies provided more details on the separation between lipid-rich and fibrous plaques. Matsumoto et al. used different thresholds attenuation (30 and 45 HU) to extract low-density non-calcified plaques (30), and concluded that the upper threshold of 45 HU improved the accuracy of lipid-rich plaque assessment from CTA.

Methods of Plaque Extraction and Reconstruction

As in 2D studies, the studies on 3D coronary plaque extraction could be classified as automatic and semi-automatic ones. Manual interactions are common in semi-automatic methods. Additionally, in 3D coronary plaque extraction, there is manual co-registration of IVUS and CTA images (30, 62) which has been applied in detecting vulnerable plaques (76). The details are listed in **Table 4**.

The boundaries of interested areas can be manually set for 3D analysis. For example, in Gaur et al.'s study, plaque components were quantified within the manually designated area using adaptive algorithms (56).

Manual adjustment of the segmentation and extraction results is common in 3D semi-automatic plaque extraction (29). In Puchner et al.'s study, the vessel wall boundaries obtained by the automated software were reviewed and manually adjusted by an experienced (>5 years of experience in the field of cardiovascular imaging) cardiovascular radiologist. Similarly, in Wang et al.'s study (31), the software automatically traced the plaque boundaries and determined the luminal area, then manual adjustment of the vessel center line and boundaries was performed. In You et al.'s study (28), the plaques were automatically color-coded and manually adjusted. The volume of each plaque component was then automatically measured. In Sun et al.'s study (61), manual editing and image filtering were applied to remove the unwanted structures and smooth the surface of coronary artery lumen.

Manual segmentation results have been widely used in training and validating 3D plaque extraction algorithms. In Sakellarios et al.'s study (52), the initial parameters of their classification mode were set by the median value of the attenuation value of the artery. Manual Expectation-Maximization algorithm based adaption was applied in order to best fit the model to artery's attenuation histogram. In Kigka et al.'s study (47), the result derived by the proposed algorithm was compared with the expert's manual annotation of artery and calcified plaques.

In some studies, multiple manual interactions were used in the semi-automatic 3D reconstruction of coronary plaques. In Wei et al.'s study, after the manual segmentation of arteries, the locations of plaques were manually marked for the training and validation of the algorithm (63). In Athanasiou et al.'s study, the CT and IVUS images were manually co-registered, with the results of manual plaque extraction as the reference for algorithm training (62). In Matsumoto et al.'s study (30), the vessel (external

elastic membrane) and lumen contours on IVUS images were manually delineated every 1 mm to calculate plaque volume. Plaque co-registration between CTA and IVUS was performed manually by another investigator, who was not involved in the processing of CTA images. The proximal and distal reference limits of the plaque were matched to IVUS using anatomical landmarks, such as the distance from the aorto-coronary ostium, target lesions, side branches, or calcifications.

In automatic 3D plaque extraction, manual segmentation of the region of interest and marking of the proximal and distal endpoints of plaques (32, 33) have been applied, while the manual segmentation results for algorithm training and validation are more commonly observed (33, 51, 53, 55, 64). Especially, the Rotterdam database provided experts' manual annotations of plaques as the ground truth. The motive behind using Rotterdam data is the availability of the manual ground truth in terms of expert annotations i.e., segment-wise status (normal/abnormal) and the precise position of non-calcified plaque for the abnormal coronary segments. Therefore, it provides a reliable source of reference data for the development of new plaque extraction algorithms (33, 64).

Manual extraction is important for automatic methods based on machine learning. In Zreik et al.'s study (53), plaque type and anatomical significance of the stenosis were manually annotated by an expert using custom-built software following the guidelines of the Society of Cardiovascular Computed Tomography (SCCT) for reporting CAD. Kang et al. used the consensus of three experts' visual assessment as the reference datasets for the 10-fold cross-validation of a structured learning technique to detect all coronary arterial lesions with stenosis $\geq 25\%$ (51).

Park et al. developed an automatic 3D plaque quantification algorithm and compared the results derived by automatic and semi-automatic methods (54). The results of the automatic algorithm were also compared with the IVUS results for validation. In the semi-automatic method, the boundaries of inner lumen and outer vessel wall were manually edited when needed. Both experts and non-experts participated in the manual segmentation of plaques. While both expert and non-expert groups used automatic centerline extraction, the experts edited the inner lumen and the outer vessel wall contours manually, whereas, the non-expert readers used the longitudinal contours for manual manipulation with minimal cross-sectional editing. Lastly, the analysis was performed on the same segments using the fully automatic contour detection algorithm without manual editing. The automatic and semi-automatic methods derived comparable results in plaque quantification analysis.

Technical Innovations

For data processing and analysis, most of the 3D reconstruction used specific algorithms whose names are disclosed while 2 studies used the algorithms embedded in the software (28, 54).

Park et al. used QAngio CT Research Edition (v2.02; Medis medical imaging systems bv, Leiden, The Netherlands) for the semi-automatic and automatic quantitative CT analysis (54). The 3D reconstruction started with an automatic centerline extraction. Based on these centerlines, straightened multiplanar

reformatted (MPR) volumes were reconstructed for the segmentation and quantification. Longitudinal inner lumen and outer vessel wall contours were detected by an automatic algorithm and were segmented automatically in the transversal images. The extracted geometry was then reviewed by experts, and manually edited if necessary (54).

You et al. combined different novel algorithms embedded in software in 3D plaque reconstruction (28). The 15-segment coronary arterial model proposed by AHA was adopted to select the arteries with diameter >2.0 mm for further analysis, with blurred segments excluded. Maximum intensity projection, volume rendering, multiplanar reformation, and curved multiplanar reformation results were routinely constructed using the algorithms embedded on a commercial workstation (EBW, Philips Medical Systems). If an abnormal segment was identified, that coronary artery was evaluated on an Aquarius workstation (TeraRecon, San Mateo, CA) where non-calcified plaques were divided into lipid-rich (0–49 HU) and fibrous (50–129 HU) plaques. The lesions on the baseline and follow-up images were matched using adjacent anatomical landmarks. The CAC Agatston calcium scores were calculated using semi-automated software (EBW; Philips Medical Systems, Best, The Netherlands), which identified the areas of at least 0.5 mm^2 and a density ≥ 130 HU on CT images as calcification (28). The authors concluded that the application of different embedded algorithms could get the analysis results in a relatively short period for clinical use.

FBP is the current standard CT image reconstruction technique (30), therefore, it is widely used as the reference for the validation of 3D (29, 32) and 2D (39) plaque reconstruction algorithms. Nevertheless, FBP is sensitive to the large variations in attenuation value between pixels caused by noises, with the quality of reconstructed plaques affected (77).

Compared with FBP, IR algorithms are more robust in the existence of noises. Hybrid IR could reduce the noise or artifacts in CT images (32) and improve the quality of low-dose chest CT images compared with FBP (77). Especially, Model-Based IR (MBIR) uses optic parameters of the CT scanner to improve the imaging quality, and has been applied in the reconstruction of medical images in low radiation dose (31, 78). As in 2D studies, the IR algorithms consist the majority of new algorithms in 3D reconstruction of coronary plaques.

Takahashi et al. compared ASIR, MBIR, and FBP algorithms in extracting calcified and non-calcified plaques from the CCTA images of 352 patients (29). They found that image noise, Agatston score, and calcium volume decreased significantly with ASIR compared to FBP (each $p < 0.001$) (79). MBIR had higher accuracy in detecting lipid-core plaques on CCTA images compared with FBP and ASIR ($p = 0.01$, in 173 cases).

In Károlyi et al.'s study (32), compared with FBP and HIR, IMR derived the highest CNR ($p < 0.01$), and the lowest overall plaque volumes as well as calcified (>130 HU) volumes ($p < 0.05$ for all). For non-calcified plaques, compared with FBP and HIR, IMR derived lower high-attenuation non-calcified volumes (90–129 HU) ($p < 0.05$ for both), but similar intermediate- (30–89 HU) and low-attenuation (<30 HU) non-calcified volumes ($p > 0.05$ for all).

Different 3D reconstruction algorithms could lead to different hemodynamic parameter estimations. The computational fluid dynamics (CFD) simulation on 3D-reconstructed coronary artery models showed that the FFR values derived from the 3D coronary artery models reconstructed by FBP and iterative reconstruction in image space (IRIS) are different but linearly related [$r = 0.74, 0.76$, and 0.70 in left main coronary artery (LMCA), LAD, and RCA] (80).

In 3D plaque extraction, some automatic methods have been proposed based on machine learning or deep learning algorithms including convolutional neural network (CNN), Support Vector Machine (SVM), and Gaussian Mixture Model (GMM).

CNN is the commonest architecture in cardiovascular image analysis (81). Zreik et al. investigated the automatic detection and classification of plaques using a multi-task recurrent convolutional neural network (RCNN) (53). Centerlines of the coronary arteries were extracted from CCTA images of 163 patients to reconstruct MPR images. The type (no plaque, non-calcified, mixed, calcified) and anatomical significance (no stenosis, non-significant, i.e., $<50\%$ luminal narrowing, and significant, i.e., $\geq 50\%$ luminal narrowing) of plaques in the coronary arteries were manually annotated in the MPR images as the reference. To perform an automatic analysis, a multi-task RCNN was applied on the MPR images of coronary arteries using cubes of $25 \times 25 \times 25$ voxels. The network was trained and tested using the CCTA images of 98 and 65 patients, respectively. In detecting the plaque type and anatomic significance, the method achieved the accuracy of 0.77 and 0.80, respectively. Authors concluded that CNN algorithm could be applied in the automatic detection and classification of coronary artery plaques, which could benefit the automated triage of CAD patients (53).

SVMs are supervised machine learning techniques. An SVM achieves the classification by constructing a multidimensional hyperplane that optimally discriminates between two classes, by maximizing the margin between two data clusters. Support Vector Machine has been widely used in the reconstruction of different organs from CT images (82). Zhao et al. proposed an automatic multi-class coronary atherosclerosis plaque detection and classification framework based on SVM. Firstly, the transverse cross-sections were retrieved along centerlines in CCTA images, with the region of interest extracted by coarse segmentation. Secondly, a random radius symmetry (RRS) feature vector was extracted, which incorporated multiple descriptions into a random strategy and greatly augmented the training data. Finally, the RRS feature vector was fed into the multi-class coronary plaque classifier. The proposed SVM-based algorithm outperformed intensity feature vector and the random forest classifier on the Rotterdam Coronary Datasets which includes 729 non-calcified plaques, 511 calcified plaques, and 546 mixed plaques (average precision: 92.6%) (33).

Kang et al. developed a robust automated algorithm of plaque detection based on SVM (51). All coronary arterial lesions with stenosis $\geq 25\%$ were detected by a structured learning technique. The plaque detection algorithm consists of two stages: (1) two independent base decisions indicating the existence of lesions in each arterial segment based on SVM and formula-based analytic

method and (2) the final decision made by combining the base decisions. The SVM algorithm extracted the geometric and shape features from small volume patches of arterial lesions. On 42 CTA patient datasets where 21 datasets had 45 lesions with stenosis $\geq 25\%$, the proposed method achieved high sensitivity (93%), specificity (95%), and accuracy (94%), with consensus reading of lesions with stenosis $\geq 25\%$ by three expert readers as the reference. Authors concluded that their SVM-based algorithm was promising for automated detection of obstructive and non-obstructive lesions from CTA images (51).

A GMM is a probabilistic model based on a Gaussian distribution for expressing the presence of sub-populations/sub-classes within an overall population/class without requiring the identification of the sub-class of interest (observational data). The GMM specifies the features of the clusters which indicate different tissues, and estimates which features are likely to differ between clusters (83).

Sakellarios et al. proposed a 3D reconstruction method based on the Radial Intensity Projection (RIP) (52). At each equally distant (2 mm) point on the centerline, a radial image was produced perpendicular to the centerline using the B-spline derivatives extracted at the specific point. The centerline was modified using an iterative radial image correction to avoid surface intersections in highly curved segments. Lumen, calcified plaque, and non-calcified plaque were modeled as a 3-component GMM. The initial parameters were set by the median value of the HU intensity of the artery. Manual or automated Expectation-Maximization algorithm based adaption was applied in order to best fit the model to artery's HU histogram. Using the GMM model, each pixel was classified to one of the five classes: (i) inner wall, (ii) outer wall, (iii) calcified plaque, (iv) non-calcified plaque, and (v) background, based on the class/component with the maximum posterior probability. The algorithms were integrated into a tool for semi-automatic extraction of coronary and carotid arteries (52). Similarly, in Athanasiou et al.'s work, the Perpendicular Radial Image (RPI) was generated along the centerline for the detection of lumen wall and potential plaque lesion borders (62). Based on the attenuation values, the PRI image was classified into lumen, non-calcified plaque, calcified plaque, and background pixels using a 4-component GMM. The parameters of the GMM were fitted to each CT dataset, based on a set of regions (from each dataset) manually annotated by an expert to lumen, non-calcified plaque, calcified plaque, and background.

Jawaid et al. proposed a hybrid energy model to extract the coronary artery tree. A tubular model and an elliptical model were used to present the geometry of arterial segment and cross-sections, respectively. The boundary of stenosed segment was reconstructed from adjacent normal segments. The reconstructed non-calcified plaques were compared with the manually extracted lumen deformations. This automated plaque segmentation method achieved the accuracy equivalent to human experts, but a bulk of data is needed for adequate training of the CNN (64).

The level-set model could simplify the numerical computations of curves and surfaces in the 3D reconstruction of plaques. Kigka et al. developed a semi-automated method using

level sets to extract calcified and non-calcified plaques as well as arterial walls (47). The results were in accordance with the manual annotation by experts and the results reconstructed from IVUS images.

Motion artifacts could cause the deformation of the reconstructed 3D arterial geometry. To eliminate the artifact-defective segmentation, Ghanem et al. proposed a robust framework for the 3D reconstruction of coronary arteries. Firstly, the initial contour of lumen inner wall was derived using Hessian analysis and region growing. Secondly, the initial contour of arterial outer wall was derived using mathematical morphology. Finally, the lumen and vessel wall were segmented using level sets. Based on the extracted geometry, the 3D meshes of lumen and vessel wall were generated using marching cube methods. Curved multi-planar reformation was used to modify the geometry (55).

Geometric Parameters in Measurement

As summarized in Table 6, the 1D and 2D geometric parameters used in 2D plaque extraction could also be measured in 3D plaque extraction. The severity of stenosis and plaque burden could therefore be calculated as in 2D reconstruction. The severity of stenosis could be estimated by the ratio of lumen diameters at the stenotic center (Ds) and normal segment (Dn): severity = $1 - D_s/D_n$. This parameter reflects the thickening of arterial wall due to the accumulation of adipose tissue, and is directly related to the decrease in myocardial blood flow (53). Kang et al. proposed a new parameter to evaluate the shape of an arterial cross-section from its area and perimeter: *circularity* = $4\pi \cdot \text{area}/\text{perimeter}^2$ (51). Additionally, the maximal lumen area stenosis percentage was also used to estimate the severity of stenosis (54). For the lipid-rich non-calcified plaques, the percentage of the lipid core on the arterial cross-sections and cap thickness (μm) were measured (29) to evaluate the extent of lipid core development.

Besides aforementioned 1D and 2D parameters, some 3D geometric parameters could be measured in 3D plaque extraction, including the volume of plaque and different components, the length of arterial segment centerline, surface area, and the angle between the vector of centerline and plaque surface (62). Figure 1 illustrates the geometric parameters commonly used in 3D plaque extraction.

Intra- and Inter-Observer Repeatability

In the 16 original studies on 3D plaque extraction, 4 included the intra-observer repeatability (32, 33, 54, 55), and 8 included the inter-observer repeatability (28, 30, 32, 51, 53–56).

The repeated measurements were performed by experts including experienced radiologists or technicians (32). Most of these studies included 2 experts on coronary imaging. Exceptionally, a study included three expert readers of CT images to make a consensus reading as the reference which was compared with the reading made by a blinded reader (51). It was suggested that intra- and inter-observer repeatability is important for algorithm validation and has been widely used in recent studies on 3D plaque extraction (72).

Reference of Accuracy

As in 2D studies, IVUS and ICA were used as the reference for the evaluation of 3D plaque extraction methods (39, 64). In addition, different types of scans such as MTCT or biplane X-ray angiography have also been used as the reference of accuracy (47). One study reported using 3D remodeling, which is a relatively new method for the coronary plaque assessment (64).

DISCUSSION

Summary: Merits and Limitations of Current Methods

In this review, we focus on the summarization of the merits and limitations of recent studies in three aspects (data, method, and evaluation), not the detailed analysis of algorithmic innovations. The methods and algorithms in these studies are highly diverse with different theoretical bases. Therefore, we introduced some innovations in these methods and algorithms but did not list the details.

Data

In both 2D and 3D studies, *in vivo* data were commonly used. *In vivo* data reflect the patient-specific anatomical structures, therefore are indispensable for the full validation of plaque extraction algorithms. However, for *in vivo* data, motion artifacts caused by cardiac movements could affect the quality of CT images. In comparison, motion artifacts are excluded from *ex vivo* data. Therefore, *ex vivo* data could be used to evaluate the accuracy of algorithms in reflecting anatomic details. Regarding *in vitro* and phantom data, geometric parameters could be directly measured on the models; therefore the accuracy of plaque extraction algorithms could be evaluated quantitatively. For phantom data, geometric parameters such as the radius of arterial segment, the thickness of plaque, as well as the material components, are all adjustable for the evaluation in different levels. Additionally, biomechanical or hemodynamic experiments could be performed on the *in vitro* models and phantoms to evaluate the plaque extraction algorithms in different pathophysiological conditions.

Most of the reviewed studies used 1–2 types of data. More types of data can be included for the comprehensive evaluation of new algorithms in geometrical details. The majority of studies included <100 human subjects. Considering the individual difference in the anatomy of coronary arteries, multi-center large-scale studies are necessary to validate the proposed algorithms for clinical applications.

2D and 3D Algorithms

The majority of 2D reconstruction methods are based on FBP and IR. The machine learning algorithms are widely used in the 3D reconstruction of coronary plaques (33, 51–53, 62).

IR algorithms could reduce noises and radiation dose in CT scanning, and improve the quality of CT images of obese patients, coronary atherosclerotic plaques, coronary stents, and myocardial perfusion (84). Therefore, IR algorithms have been widely embedded in the software. Despite the benefits in dose reduction, it is still unclear exactly which kV and mAs for a

TABLE 6 | Geometric parameters in CT-based coronary plaque evaluation.

Study	Geometric parameters	
	2D	3D
Gaur et al. (56)	Numbers of obstructive lesions (stenosis > 50%), plaque length (mm).	Volume of non-calcified plaques; low-density non-calcified plaques, calcified plaques, and all plaques (mm ³), aggregate plaque volume (%).
Jawaid et al. (64)	Arterial wall thickness, lumen area.	N/A
Sakellarios et al. (52)	Artery outer border, area of plaques on cross-sections.	Centreline, volume.
You et al. (28)	N/A	Volume of calcified, fibrous and lipid-rich plaques (mm ³)
Ghanem et al. (55)	Vessel wall thickness (mm), plaque length (mm), luminal stenosis (%).	Volume of calcified, mixed, and soft lipid-rich plaques (mm ³)
Wei et al. (63), as summarized in the review by Jawaid et al. (72)	N/A Stenosis volume in %	Centreline and length of vessels
Athanasiou et al. (62)	N/A	Volume (mm ³), surface area (mm ²), maximum length (mm), and inner angle (degree) of plaques. Overlapping volume between different objects (lumen, wall and plaque).
Park et al. (54)	Minimal lumen area (mm ²), maximal lumen diameter stenosis percentage (%), maximal lumen area stenosis percentage (%), mean plaque burden (%).	Volume of lumen, vessel, and plaques (mm ³)
Kigka et al. (47)	Degree of stenosis (%). Minimal lumen diameter (mm). Minimal lumen area (mm ²). Plaque burden (%).	N/A
Károlyi et al. (32)	Lesion length (mm)	Plaque volume (mm ³), lumen volume (mm ³), vessel volume (mm ³).
Zhao et al. (33)	Estimated radius of plaque area segmented from cross-section (mm).	N/A
Puchner et al. (29)	Area of calcified and lipid-core plaques on cross-sections (mm ²), circumference, width, and cap thickness of lipid core (μm), plaque burden (%)	N/A
Wang et al. (31)	Lumen area (mm ²)	volume of plaque components (mL) and their relative values (%)
Matsumoto et al. (30)	Plaque thickness (mm), plaque area (mm ²) on cross-section, Plaque burden (%).	Plaque composition volume (mm ³) and the ratio in total plaque volume
Sun et al. (61)	Degree of lumen stenosis (%).	N/A
Kang et al. (51)	Degree of lumen stenosis (%). Circularity of cross-section.	Location of stenosis (mm) from ostium.
Zreik et al. (53)	Degree of lumen stenosis (%).	N/A

given body habitus is optimal with each IR algorithm (85). Furthermore, IR could influence many factors that are important for the clinical risk stratification of CAD, including coronary calcification, plaque burden and composition, as well as stenosis severity (85). There is a lack of comprehensive evaluation of different IR algorithms regarding diagnostic accuracy and patient management. In most of the studies included in this review, the results of IR algorithms were compared with the results of standard FBP method only (see sections Technical Innovations). Additionally, there is a lack of quantitative evaluation of IR algorithms based on *ex vivo* or phantom data.

Tsompou et al. compared the 3D reconstruction methods based on different cardiovascular images (86). It was found that, with de-blooming algorithms, the geometric parameters (normal and stenosed lumen diameters, severity and length of plaque) and wall shear stress calculated from the 3D models reconstructed from CCTA images were not significantly different from the results derived from quantitative coronary analysis and IVUS (86). Therefore, the accurate estimation of 3D plaque geometry could be achieved by using CT images. However, the

majority of 3D plaque reconstruction algorithms are based on attenuation value or diameter estimation (Table 3). There is a lack of investigation on the 3D geometric characteristics of coronary plaques.

Machine learning has been widely used in the analysis of cardiac images and signals and has been proven to be effective in predicting heart failure and other clinical events (87). Especially, fully automated machine learning algorithms may facilitate the processing of large-scale image datasets. For clinical application, images from picture archiving and communication systems can be segmented out and fed into other machine learning layers in order to establish a diagnostic and a prognostic course (87). For example, the risk of plaque rupture is associated with stress concentration, which depends on the mechanical properties and the geometry of the reconstructed plaques (88). Thus, machine learning could assist the clinical professionals to estimate the vulnerability of the atheroma plaque (88). In comparison, traditional 3D finite element analysis of plaque rupture requires huge computational resources, therefore is not suitable for clinical use. The machine learning methods

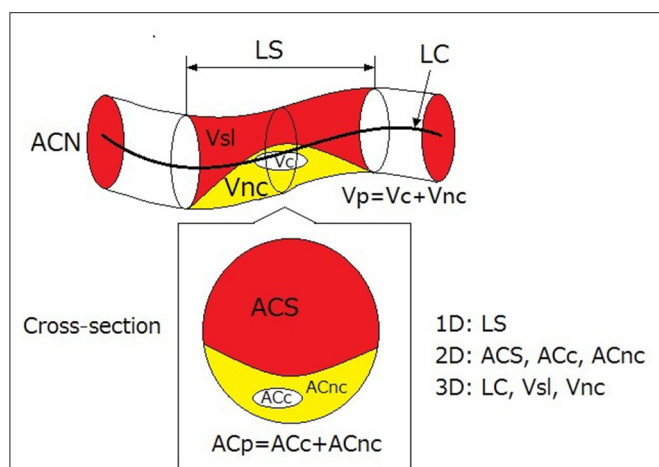


FIGURE 1 | 1D, 2D, and 3D geometric parameters used in 3D plaque reconstruction. LS, length of stenosis; LC, length of centreline of arterial segment; Vsl, volume of lumen in stenosed segment; Vnc, volume of non-calcified components; Vc, volume of calcification; Vp, volume of plaque; ACN, area of lumen cross-section in normal segment; ACS, area of lumen cross-section in stenosed segment; ACc, cross-section area of calcification; ACnc, cross-section area of non-calcified (lipid or fibrotic) components; ACp, cross-section area of plaque. The red, yellow, and white areas illustrate the stenosed lumen, the non-calcified components, and the calcification.

have been applied in the classification of plaque type (33, 53) and anatomic significance (51, 53, 64), whereas, there is a lack of clinical validation and application. Additionally, machine learning can be used in the estimation of hemodynamic parameters of coronary arteries such as FFR from CTA images (89). The application of machine learning in the CT-based coronary plaque assessment deserves further investigation under multidisciplinary collaboration.

Automatic Algorithms and Manual Interactions

As shown in **Table 4**, setting the boundaries and adjusting the results are the commonest manual interactions in semi-automatic plaque extraction methods (72). However, manual adjustment is time-consuming and dependent on operator skills (24). There is a high need to develop automated methods that can achieve the reliable extraction of coronary plaques.

Advanced algorithms based on AI (machine learning, deep learning, etc.) provide an important approach toward the automation of coronary plaque extraction. For example, Wolterink et al. have successfully developed an automatic method to identify the calcified voxels using paired convolutional neural networks (90). Furthermore, based on the big data and new technologies such as radiomics, more information could be extracted in parallel with the reconstruction of plaque geometry, achieving the preliminary diagnosis and automatic screening of CAD patients based on clinico-radiological information (91).

In both semi-automatic and automatic methods of plaque extraction, the manual extraction results have been widely used for training and validating the algorithms. In 2013, Kirisli et al. compared 11 automatic and semi-automatic algorithms of coronary plaque extraction on a dataset of 48 symptomatic CAD patients (92). The authors quantitatively evaluated the

accuracy of these algorithms. They concluded that current stenosis detection/quantification algorithms are not sufficiently reliable to be used stand-alone in clinical practice, but that some could be used for triage or as a second-reader. They also suggested that automatic lumen segmentation could achieve the precision comparable to experts' manual segmentation. Thus, the manual extraction results with high accuracy still play a key role in algorithm evaluation. The standardized datasets such as Rotterdam dataset (33, 64) provided an appropriate choice. Nevertheless, due to the limitations in data sharing, very few datasets are currently available.

IVUS images have high resolution, which makes them adequate for clinical diagnosis and algorithm validation. Additionally, to improve the accuracy of plaque extraction, IVUS images could be used as a virtual reality tool to explore and understand the outer and inner structure of coronary arteries (76). Compared with manually extracted results, IVUS images could serve as a more reliable reference for the validation of plaque extraction algorithms. However, the validation requires the co-registration of CT and IVUS images, which is still often performed manually.

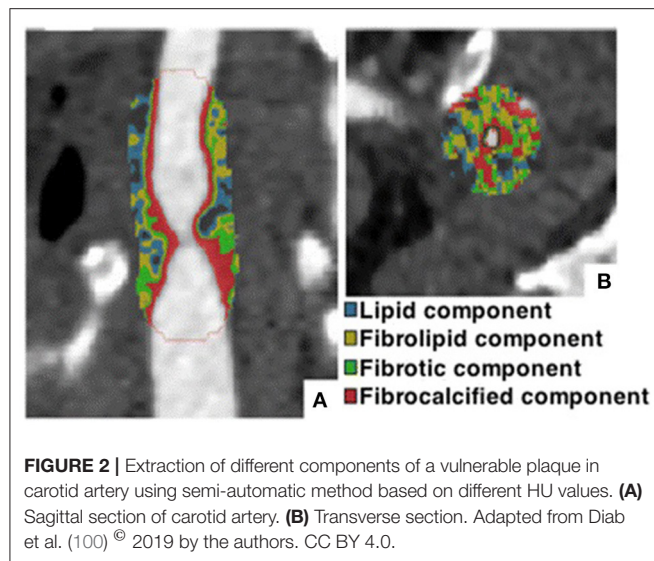
Geometric Parameters

The geometry of coronary arteries and plaques could influence the development of atherosclerosis and the occurrence of cardiovascular events (93). In the majority of 2D studies, the geometric parameters are measured from the cross-sections or other 2D images. In 3D studies, 1D, 2D, and 3D parameters are all included. It has been proven that the geometric parameters (cross-section area, area severity, etc.) of coronary plaques are reproducible with high intra- and inter-observer agreement (94). The severity of plaques has been estimated by the ratios in diameter (53) and area (39, 66). Some secondary parameters could be derived from the 3D geometry of coronary plaques. For example, radius gradient of the plaque, which reflects longitudinal lesion asymmetry, has been proven to be associated with the location of plaque rupture and consequent clinical events (95). The curvature and tortuosity of coronary arteries might be related to the development of atherosclerosis and plaque size (96, 97). These secondary parameters and their clinical indication need further investigation.

Extraction and Classification of Different Plaques

As to the extraction of calcified plaques, de-blooming algorithms (17, 86) have been proposed and proven to be effective in reducing blooming artifacts (86). However, it was found that the calcium density, which is directly related with blooming artifacts, has little effect on the accuracy of CTA (98). Therefore, other details such as the dose, individual difference, and the de-blooming of co-existing plaques and stents (99), need further investigation to improve the accuracy and reliability of calcified plaque extraction.

For non-calcified plaques, we observed different classification standards (**Table 2**) and attenuation thresholds (**Table 3**). The most detailed classification included lipid-rich, fibrous, and calcified plaques. In a parallel study on plaque extraction in carotid arteries on CTA images, the components of non-calcified



plaques have been classified as lipid, fibrofatty, fibrotic, and fibro-calcified (100) (**Figure 2**). In another study, carotid plaques are classified as intimal lipid accumulation, lipid-rich necrotic cores, calcification, fibrosis, and calcification (101). Lipid-rich necrotic core is a major characteristic of high-risk vulnerable plaques, which is an important reference for clinical diagnosis and intervention. It has been known that lipid-rich lesions can be separated from more fibrous ones on CT images, which could be used to estimate the risk of plaque rupture (102). In 2013, Obaid et al. evaluated the accuracy of a 3D plaque extraction method in estimating different components of coronary plaques on CT images (103). The accuracies of CT and VH-IVUS were comparable in detecting calcified plaque (83 vs. 92%), necrotic core (80 vs. 65%), and fibroatheroma (80 vs. 79%), with *ex vivo* histology as the reference. A plaque containing large amounts of lipid may be classified by VH-IVUS as fibro-fatty tissue but have low attenuation, and be classified as the necrotic core on

CT images. Accurate and quantitative estimation of different components of non-calcified plaques on CT images is still challenging due to the limited temporal, spatial, and contrast resolutions of current scanners (102).

Future Directions

In future studies, the application of machine learning and automatic methods (extraction of the centerline of coronary arteries, segmentation, quantification of calcification and other components, etc.) could improve the efficiency of coronary plaque extraction from CT images. More geometric parameters could be derived from the 3D geometry of extracted plaques. The accuracy of plaque extraction could be improved in the following aspects: the inclusion of more data types, the comprehensive evaluation of IR algorithms on *ex vivo* and *in vitro* data, the multi-center large-scale studies, more standardized datasets, the investigation on the geometric properties of coronary plaques, further investigation and standardization of de-blooming algorithms, and more detailed classification of non-calcified plaques.

AUTHOR CONTRIBUTIONS

HL proposed the structure of the review. AW searched for the literature. HL and AW analyzed the literature and drafted the manuscript. DZ supervised the project that led to production of the results. All contributed to the discussion and revision of the manuscript and concur with the current submitted version.

FUNDING

This study was supported by the Newton Funds Industry Academia Partnership Programme (Grant No. IAPP1R2\100204), the Zhejiang Provincial Department of Science and Technology (Grant No. 2020C03016), the High-level University Fund of Southern University of Science of Technology (Grant No. G02236002), and the National Key Research and Development Program of China (Grant No. 2018YFE0198400).

REFERENCES

- Benjamin EJ, Virani SS, Callaway CW, Chamberlain AM, Chang AR, Cheng S, et al. Heart disease and stroke statistics-2018 update: a report from the American Heart Association. *Circulation*. (2018). 137:e67–492. doi: 10.1161/CIR.0000000000000558
- Govindaraju K, Badruddin IA, Viswanathan GN, Ramesh SV, Badarudin A. Evaluation of functional severity of coronary artery disease and fluid dynamics' influence on hemodynamic parameters: a review. *Physica Medica*. (2013) 29:225–32. doi: 10.1016/j.ejmp.2012.03.008
- Lee S-E, Villines TC, Chang H-J. Should CT replace IVUS for evaluation of CAD in large-scale clinical trials: effects of medical therapy on atherosclerotic plaque. *J Cardiovasc Comput Tomogr*. (2019) 13:248–53. doi: 10.1016/j.jcct.2019.06.017
- Dweck MR, Puntmann VO, Vesey AT, Fayad ZA, Nagel E. MR imaging of coronary arteries and plaques. *JACC Cardiovasc Imaging*. (2016) 9:306–16. doi: 10.1016/j.jcmg.2015.12.003
- Wang Y, Osborne MT, Tung B, Li M, Li Y. Imaging cardiovascular calcification. *J Am Heart Assoc*. (2018) 7:e008564. doi: 10.1161/JAHA.118.008564
- Daghem M, Bing R, Fayad ZA, Dweck MR. Noninvasive imaging to assess atherosclerotic plaque composition and disease activity: coronary and carotid applications. *JACC Cardiovasc Imaging*. (2019). 13:1055–68. doi: 10.1016/j.jcmg.2019.03.033
- Becker CR, Ohnesorge BM, Schoepf UJ, Reiser MF. Current development of cardiac imaging with multidetector-row CT. *Eur J Radiol*. (2000) 36:97–103. doi: 10.1016/S0720-048X(00)00272-2
- Vogl TJ, Abolmaali ND, Diebold T, Engelmann K, Ay M, Dogan S, et al. Techniques for the detection of coronary atherosclerosis: multi-detector row CT coronary angiography. *Radiology*. (2002) 223:212–20. doi: 10.1148/radiol.2231010515
- Vanhoenacker PK, Heijnenbroek-Kal MH, Van Heste R, Decramer I, Van Hoe LR, Wijns W, et al. Diagnostic performance of multidetector CT angiography for assessment of coronary artery disease: meta-analysis. *Radiology*. (2007) 244:419–28. doi: 10.1148/radiol.2442061218

10. Budoff Matthew J, Achenbach S, Blumenthal Roger S, Carr JJ, Goldin Jonathan G, Greenland P, et al. Assessment of coronary artery disease by cardiac computed tomography. *Circulation*. (2006) 114:1761–91. doi: 10.1161/CIRCULATIONAHA.106.178458
11. Dey D, Cheng VY, Slomka PJ, Nakazato R, Ramesh A, Gurudevan S, et al. Automated 3-dimensional quantification of noncalcified and calcified coronary plaque from coronary CT angiography. *J Cardiovasc Comput Tomogr*. (2009) 3:372–82. doi: 10.1016/j.jcct.2009.09.004
12. Rinehart S, Vazquez G, Qian Z, Murrieta L, Christian K, Voros S. Quantitative measurements of coronary arterial stenosis, plaque geometry, and composition are highly reproducible with a standardized coronary arterial computed tomographic approach in high-quality CT datasets. *J Cardiovasc Comput Tomogr*. (2011) 5:35–43. doi: 10.1016/j.jcct.2010.09.006
13. Springer I, Dewey M. Comparison of multislice computed tomography with intravascular ultrasound for detection and characterization of coronary artery plaques: a systematic review. *Eur J Radiol*. (2009) 71:275–82. doi: 10.1016/j.ejrad.2008.04.035
14. Holzapfel GA, Mulvihill JJ, Cunnane EM, Walsh MT. Computational approaches for analyzing the mechanics of atherosclerotic plaques: a review. *J Biomech*. (2014) 47:859–69. doi: 10.1016/j.jbiomech.2014.01.011
15. Zhang J-M, Zhong L, Su B, Wan M, Yap JS, Tham JPL, et al. Perspective on CFD studies of coronary artery disease lesions and hemodynamics: a review. *Int J Numerical Methods Biomed Eng*. (2014) 30:659–80. doi: 10.1002/cnm.2625
16. Olgac U, Poulikakos D, Saur SC, Alkadhi H, Kurtcuoglu V. Patient-specific three-dimensional simulation of LDL accumulation in a human left coronary artery in its healthy and atherosclerotic states. *Am J Physiol Heart Circ Physiol*. (2009) 296:H1969–82. doi: 10.1152/ajpheart.01182.2008
17. Li P, Xu L, Yang L, Wang R, Hsieh J, Sun Z, et al. Blooming artifact reduction in coronary artery calcification by a new de-blooming algorithm: initial study. *Sci Rep*. (2018) 8:6945. doi: 10.1038/s41598-018-25352-5
18. Liu J, Jin C, Feng J, Du Y, Lu J, Zhou J, editors. *A Vessel-Focused 3D Convolutional Network for Automatic Segmentation and Classification of Coronary Artery Plaques in Cardiac CTA. Statistical Atlases and Computational Models of the Heart Atrial Segmentation and LV Quantification Challenges 2019*. (2019). Cham: Springer International Publishing.
19. Henein MY, Vancheri S, Bajraktari G, Vancheri F. Coronary atherosclerosis imaging. *Diagnostics*. (2020) 10:65. doi: 10.3390/diagnostics10020065
20. Li Y, Yu M, Dai X, Lu Z, Shen C, Wang Y, et al. Detection of hemodynamically significant coronary stenosis: CT myocardial perfusion versus machine learning CT fractional flow reserve. *Radiology*. (2019) 293:305–14. doi: 10.1148/radiol.2019190098
21. Moss AJ, Williams MC, Newby DE, Nicol ED. The updated NICE guidelines: cardiac CT as the first-line test for coronary artery disease. *Curr Cardiovasc Imaging Rep*. (2017) 10:15. doi: 10.1007/s12410-017-9412-6
22. Øvrehus KA, Schuhbaeck A, Marwan M, Achenbach S, Nørgaard BL, Bøtker HE, et al. Reproducibility of semi-automatic coronary plaque quantification in coronary CT angiography with sub-mSv radiation dose. *J Cardiovasc Comput Tomogr*. (2016) 10:114–20. doi: 10.1016/j.jcct.2015.11.003
23. Szilveszter B, Elzomor H, Károlyi M, Kolossváry M, Raaijmakers R, Benke K, et al. The effect of iterative model reconstruction on coronary artery calcium quantification. *Int J Cardiovasc Imaging*. (2016) 32:153–60. doi: 10.1007/s10554-015-0740-9
24. Braber TL, Willemink MJ, Bohté EH, Mosterd A, Leiner T, Velthuis BK. Assessment of coronary artery calcium on low-dose coronary computed tomography angiography with iterative reconstruction. *J Comput Assist Tomogr*. (2016) 40:266–71. doi: 10.1097/RCT.0000000000000347
25. Messerli M, Rengier F, Desbiolles L, Ehl NF, Bauer RW, Leschka S, et al. Impact of advanced modeled iterative reconstruction on coronary artery calcium quantification. *Acad Radiol*. (2016) 23:1506–12. doi: 10.1016/j.acra.2016.08.008
26. Chen Z, Boldeanu I, Nepveu S, Durand M, Chin AS, Kauffmann C, et al. *In vivo* coronary artery plaque assessment with computed tomography angiography: is there an impact of iterative reconstruction on plaque volume and attenuation metrics? *Acta Radiologica*. (2016) 58:660–9. doi: 10.1177/0284185116664229
27. Precht H, Kitslaar PH, Broersen A, Gerke O, Dijkstra J, Thygesen J, et al. First experiences with model based iterative reconstructions influence on quantitative plaque volume and intensity measurements in coronary computed tomography angiography. *Radiography*. (2017) 23:77–9. doi: 10.1016/j.radi.2016.08.003
28. You S, Sun JS, Park SY, Baek Y, Kang DK. Relationship between indexed epicardial fat volume and coronary plaque volume assessed by cardiac multidetector CT. *Medicine*. (2016) 95:e4164. doi: 10.1097/MD.00000000000004164
29. Puchner SB, Ferencik M, Maurovich-Horvat P, Nakano M, Otsuka F, Kauczor H-U, et al. Iterative image reconstruction algorithms in coronary CT angiography improve the detection of lipid-core plaque—a comparison with histology. *Eur Radiol*. (2015) 25:15–23. doi: 10.1007/s00330-014-3404-6
30. Matsumoto H, Watanabe S, Kyo E, Tsuji T, Ando Y, Otaki Y, et al. Standardized volumetric plaque quantification and characterization from coronary CT angiography: a head-to-head comparison with invasive intravascular ultrasound. *Eur Radiol*. (2019) 29:6129–39. doi: 10.1007/s00330-019-06219-3
31. Wang C, Liao Y, Chen H, Zhen X, Li J, Xu Y, et al. Influence of tube potential on quantitative coronary plaque analyses by low radiation dose computed tomography: a phantom study. *Int J Cardiovasc Imaging*. (2018) 34:1315–22. doi: 10.1007/s10554-018-1344-y
32. Károlyi M, Szilveszter B, Kolossváry M, Takx RAP, Celeng C, Bartykowszki A, et al. Iterative model reconstruction reduces calcified plaque volume in coronary CT angiography. *Eur J Radiol*. (2017) 87:83–9. doi: 10.1016/j.ejrad.2016.12.012
33. Zhao F, Wu B, Chen F, Cao X, Yi H, Hou Y, et al. An automatic multi-class coronary atherosclerosis plaque detection and classification framework. *Med Biol Eng Comput*. 2019;57(1):245–57. doi: 10.1007/s11517-018-1880-6
34. Rodriguez-Granillo GA, Carrascosa P, Bruining N, Waksman R, Garcia-Garcia HM. Defining the non-vulnerable and vulnerable patients with computed tomography coronary angiography: evaluation of atherosclerotic plaque burden and composition. *Eur Heart J Cardiovasc Imaging*. (2016) 17:481–91. doi: 10.1093/ehjci/jew012
35. Rossi A, Papadopoulou S-L, Pugliese F, Russo B, Dharampall AS, Dedic A, et al. Quantitative computed tomographic coronary angiography. *Circ Cardiovasc Imaging*. (2014) 7:43–51. doi: 10.1161/CIRCIMAGING.112.000277
36. Li T, Tang T, Yang L, Zhang X, Li X, Luo C. Coronary CT angiography with knowledge-based iterative model reconstruction for assessing coronary arteries and non-calcified predominant plaques. *Korean J Radiol*. (2019) 20:729–38. doi: 10.3348/kjr.2018.0435
37. Funama Y, Utsunomiya D, Hirata K, Taguchi K, Nakaura T, Oda S, et al. Improved estimation of coronary plaque and luminal attenuation using a vendor-specific model-based iterative reconstruction algorithm in contrast-enhanced CT coronary angiography. *Acad Radiol*. (2017) 24:1070–8. doi: 10.1016/j.acra.2017.02.006
38. Kashani H, Wright G, Ursani A, Liu G, Hashemi M, Paul NS. Optimization of computed tomography coronary angiography for improved plaque detection. *J Comput Assist Tomogr*. (2018) 42:240–7. doi: 10.1097/RCT.0000000000000663
39. Puchner SB, Ferencik M, Maehara A, Stolzmann P, Ma S, Do S, et al. Iterative image reconstruction improves the accuracy of automated plaque burden assessment in coronary CT angiography: a comparison with intravascular ultrasound. *Am J Roentgenol*. (2017) 208:777–84. doi: 10.2214/AJR.16.17187
40. Pelgrim GJ, van Hamersvelt RW, Willemink MJ, Schmidt BT, Flohr T, Schilham A, et al. Accuracy of iodine quantification using dual energy CT in latest generation dual source and dual layer CT. *Eur Radiol*. (2017) 27:3904–12. doi: 10.1007/s00330-017-4752-9
41. Otsuka F, Sakakura K, Yahagi K, Joner M, Virmani R. Has our understanding of calcification in human coronary atherosclerosis progressed? *Arterioscler Thromb Vasc Biol*. (2014) 34:724–36. doi: 10.1161/ATVBAHA.113.302642
42. Stary HC. Natural history and histological classification of atherosclerotic lesions. *Arterioscler Thromb Vasc Biol*. (2000) 20:1177–8. doi: 10.1161/01.ATV.20.5.1177
43. Hetterich H, Webber N, Willner M, Herzen J, Birnbacher L, Hipp A, et al. AHA classification of coronary and carotid atherosclerotic plaques

- by grating-based phase-contrast computed tomography. *Eur Radiol.* (2016) 26:3223–33. doi: 10.1007/s00330-015-4143-z
44. Lindeman JH, Hulsbos L, van den Bogaert AJ, Geerts M, van Gool AJ, Hamming JF, et al. Qualitative evaluation of coronary atherosclerosis in a large cohort of young and middle-aged Dutch tissue donors implies that coronary thrombo-embolic manifestations are stochastic. *PLoS ONE.* (2018) 13:e0207943. doi: 10.1371/journal.pone.0207943
 45. Vaideeswar P, Tyagi S, Singaravel S. Pathology of atherosclerotic coronary artery disease in the young Indian population. *Forensic Sci Res.* (2019) 4:241–6. doi: 10.1080/20961790.2019.1592315
 46. Obaid DR, Calvert PA, Brown A, Gopalan D, West NEJ, Rudd JHF, et al. Coronary CT angiography features of ruptured and high-risk atherosclerotic plaques: correlation with intra-vascular ultrasound. *J Cardiovasc Comput Tomogr.* (2017) 11:455–61. doi: 10.1016/j.jcct.2017.09.001
 47. Kigka VI, Rigas G, Sakellarios A, Siogkas P, Andrikos IO, Exarchos TP, et al. 3D reconstruction of coronary arteries and atherosclerotic plaques based on computed tomography angiography images. *Biomed Signal Process Control.* (2018) 40:286–94. doi: 10.1016/j.bspc.2017.09.009
 48. Cui Y, Zeng W, Yu J, Lu J, Hu Y, Diao N, et al. Quantification of left coronary bifurcation angles and plaques by coronary computed tomography angiography for prediction of significant coronary stenosis: a preliminary study with dual-source CT. *PLoS ONE.* (2017) 12:e0174352. doi: 10.1371/journal.pone.0174352
 49. Infante T, Forte E, Schiano C, Punzo B, Cademartiri F, Cavaliere C, et al. Evidence of association of circulating epigenetic-sensitive biomarkers with suspected coronary heart disease evaluated by Cardiac Computed Tomography. *PLoS ONE.* (2019) 14:e0210909. doi: 10.1371/journal.pone.0210909
 50. Kolossváry M, Szilveszter B, Merkely B, Maurovich-Horvat P. Plaque imaging with CT—a comprehensive review on coronary CT angiography based risk assessment. *Cardiovas Diagn Ther.* (2017) 7:489–506. doi: 10.21037/cdt.2016.11.06
 51. Kang D, Dey D, Slomka P, Arsanjani R, Nakazato R, Ko H, et al. Structured learning algorithm for detection of nonobstructive and obstructive coronary plaque lesions from computed tomography angiography. *J Med Imaging.* (2015) 2:014003. doi: 10.1117/1.JMI.2.1.014003
 52. Sakellarios AI, Rigas G, Exarchos TP, Fotiadis DI, editors. A methodology and a software tool for 3D reconstruction of coronary and carotid arteries and atherosclerotic plaques. *2016 IEEE International Conference on Imaging Systems and Techniques (IST) 2016 4-6 Oct.* Chania (2016). doi: 10.1109/IST.2016.7738284
 53. Zreik M, Hamersvelt RWV, Wolterink JM, Leiner T, Viergever MA, Išgum I. A recurrent CNN for automatic detection and classification of coronary artery plaque and stenosis in coronary CT angiography. *IEEE Trans Med Imaging.* (2019) 38:1588–98. doi: 10.1109/TMI.2018.2883807
 54. Park H-B, Lee BK, Shin S, Heo R, Arsanjani R, Kitslaar PH, et al. Clinical feasibility of 3D automated coronary atherosclerotic plaque quantification algorithm on coronary computed tomography angiography: comparison with intravascular ultrasound. *Eur Radiol.* (2015) 25:3073–83. doi: 10.1007/s00330-015-3698-z
 55. Ghanem AM, Hamimi AH, Matta JR, Carass A, Elgarf RM, Gharib AM, et al. Automatic coronary wall and atherosclerotic plaque segmentation from 3D coronary CT angiography. *Sci Rep.* (2019) 9:47. doi: 10.1038/s41598-018-37168-4
 56. Gaur S, Øvrehus KA, Dey D, Leipsic J, Botker HE, Jensen JM, et al. Coronary plaque quantification and fractional flow reserve by coronary computed tomography angiography identify ischaemia-causing lesions. *Eur Heart J.* (2016) 37:1220–7. doi: 10.1093/eurheartj/ehv690
 57. Maffei E, Nieman K, Martini C, Catalano O, Seitun S, Arcadi T, et al. Classification of noncalcified coronary atherosclerotic plaque components on CT coronary angiography: impact of vascular attenuation and density thresholds. *La radiologia medica.* (2012) 117:230–41. doi: 10.1007/s11547-011-0744-z
 58. Takx RAP, Willemink MJ, Nathoe HM, Schilham AMR, Budde RPJ, de Jong PA, et al. The effect of iterative reconstruction on quantitative computed tomography assessment of coronary plaque composition. *Int J Cardiovas Imaging.* (2014) 30:155–63. doi: 10.1007/s10554-013-0293-8
 59. Szilveszter B, Celeng C, Maurovich-Horvat P. Plaque assessment by coronary CT. *Int J Cardiovas Imaging.* (2016) 32:161–72. doi: 10.1007/s10554-015-0741-8
 60. Blaha MJ, Budoff MJ, Tota-Maharaj R, Dardari ZA, Wong ND, Kronmal RA, et al. Improving the CAC score by addition of regional measures of calcium distribution: multi-ethnic study of atherosclerosis. *JACC Cardiovas Imaging.* (2016) 9:1407–16. doi: 10.1016/j.jcmg.2016.03.001
 61. Sun Z, Ng CKC, Squelch A. Synchrotron radiation computed tomography assessment of calcified plaques and coronary stenosis with different slice thicknesses and beam energies on 3D printed coronary models. *Quant Imaging Med Surg.* (2018) 9:6–22. doi: 10.21037/qims.2018.09.11
 62. Athanasiou LS, Rigas GA, Sakellarios AI, Exarchos TP, Siogkas PK, Michalis LK, et al. editors. Three-dimensional reconstruction of coronary arteries and plaque morphology using CT angiography—comparison and registration using IVUS. *2015 37th Annual International Conference of the IEEE Engineering in Medicine and Biology Society (EMBC); 2015 25-29 Aug.* Milan (2015). doi: 10.1109/EMBC.2015.7319671
 63. Wei J, Zhou C, Chan H-P, Chughtai A, Agarwal P, Kuriakose J, et al. Computerized detection of noncalcified plaques in coronary CT angiography: evaluation of topological soft gradient prescreening method and luminal analysis. *Med Phys.* (2014) 41:081901. doi: 10.1118/1.4885958
 64. Jawaid MM, Narejo S, Pirzada N, Baloch J, Reyes-Aldasoro CC, Slabaugh GG. Automated quantification of non-calcified coronary plaques in cardiac CT angiographic imagery. *Int J Adv Comput Sci Appl.* (2018) 9:216–22. doi: 10.14569/IJACSA.2018.090731
 65. Renker M, John W, Nance J, Schoepf UJ, O'Brien TX, Zwerner PL, Meyer M, et al. Evaluation of heavily calcified vessels with coronary CT angiography: comparison of iterative and filtered back projection image reconstruction. *Radiology.* (2011) 260:390–9. doi: 10.1148/radiol.11103574
 66. Stolzmann P, Schlett CL, Maurovich-Horvat P, Maehara A, Ma S, Scheffl H, et al. Variability and accuracy of coronary CT angiography including use of iterative reconstruction algorithms for plaque burden assessment as compared with intravascular ultrasound—an *ex vivo* study. *Eur Radiol.* (2012) 22:2067–75. doi: 10.1007/s00330-012-2464-8
 67. Shukla DR, McLaughlin RJ, Lee J, Cofield RH, Sperling JW, Sánchez-Sotelo J. Intraobserver and interobserver reliability of the modified Walch classification using radiographs and computed tomography. *J Shoulder Elbow Surg.* (2019) 28:625–30. doi: 10.1016/j.jse.2018.09.021
 68. Hoffmann H, Frieler K, Hamm B, Dewey M. Intra- and interobserver variability in detection and assessment of calcified and noncalcified coronary artery plaques using 64-slice computed tomography. *Int J Cardiovas Imaging.* (2008) 24:735–42. doi: 10.1007/s10554-008-9299-z
 69. Cheng VY, Nakazato R, Dey D, Gurudevan S, Tabak J, Budoff MJ, et al. Reproducibility of coronary artery plaque volume and composition quantification by 64-detector row coronary computed tomographic angiography: an intraobserver, interobserver, and interscan variability study. *J Cardiovasc Comput Tomogr.* (2009) 3:312–20. doi: 10.1016/j.jcct.2009.07.001
 70. Doh J-H, Koo B-K, Nam C-W, Kim J-H, Min JK, Nakazato R, et al. Diagnostic value of coronary CT angiography in comparison with invasive coronary angiography and intravascular ultrasound in patients with intermediate coronary artery stenosis: results from the prospective multicentre FIGURE-OUT (Functional Imaging criteria for Guiding REview of invasive coronary angiOgraphy, intravascular Ultrasound, and coronary computed Tomographic angiography) study. *Eur Heart J Cardiovas Imaging.* (2014) 15:870–7. doi: 10.1093/ehjci/jeu009
 71. Nakazato R, Shalev A, Doh J-H, Koo B-K, Dey D, Berman DS, et al. Quantification and characterisation of coronary artery plaque volume and adverse plaque features by coronary computed tomographic angiography: a direct comparison to intravascular ultrasound. *Eur Radiol.* (2013) 23:2109–17. doi: 10.1007/s00330-013-2822-1
 72. Jawaid MM, Narejo S, Qureshi IA, Pirzada N. A review of the state-of-the-art methods for plaque detection in cardiac CT angiography. *Int J Comput Theory Eng.* (2018) 10:84–92. doi: 10.7763/IJCTE.2018.V10.1204
 73. Athanasiou L, Rigas G, Sakellarios AI, Exarchos TP, Siogkas PK, Bourantas CV, et al. Three-dimensional reconstruction of coronary arteries and plaque morphology using CT angiography—comparison and registration

- with IVUS. *BMC Med Imaging*. (2016) 16:9. doi: 10.1186/s12880-016-0111-6
74. Fok P-W. Multi-layer mechanical model of glagov remodeling in coronary arteries: differences between *in-vivo* and *ex-vivo* measurements. *PLoS ONE*. (2016) 11:e0159304-e. doi: 10.1371/journal.pone.0159304
 75. Min JK, Shaw LJ, Devereux RB, Okin PM, Weinsaft JW, Russo DJ, et al. Prognostic value of multidetector coronary computed tomographic angiography for prediction of all-cause mortality. *J Am Coll Cardiol*. (2007) 50:1161–70. doi: 10.1016/j.jacc.2007.03.067
 76. Kutty SB, Rahmat RWOK, Kassim S, Madzin H, Hamdan H, editors. A review of 3D reconstruction of coronary arteries based on the co-registration of IVUS and coronary angiogram. *International Conference on Computer Assisted System in Health; 2014 19-21 Dec*. Kuala Lumpur (2014). doi: 10.1109/CASH.2014.21
 77. Kim C, Lee KY, Shin C, Kang E-Y, Oh Y-W, Ha M, et al. Comparison of filtered back projection, hybrid iterative reconstruction, model-based iterative reconstruction, and virtual monoenergetic reconstruction images at both low- and standard-dose settings in measurement of emphysema volume and airway wall thickness: a CT phantom study. *Korean J Radiol*. (2018) 19:809–17. doi: 10.3348/kjr.2018.19.4.809
 78. Smith EA, Dillman JR, Goodsitt MM, Christodoulou EG, Keshavarzi N, Strouse PJ. Model-based iterative reconstruction: effect on patient radiation dose and image quality in pediatric body CT. *Radiology*. (2013) 270:526–34. doi: 10.1148/radiol.13130362
 79. Takahashi M, Kimura F, Umezawa T, Watanabe Y, Ogawa H. Comparison of adaptive statistical iterative and filtered back projection reconstruction techniques in quantifying coronary calcium. *J Cardiovasc Comput Tomogr*. (2016) 10:61–8. doi: 10.1016/j.jcct.2015.07.012
 80. Mastrodicasa D, Albrecht MH, Schoepf UJ, Varga-Szemes A, Jacobs BE, Gassenmaier S, et al. Artificial intelligence machine learning-based coronary CT fractional flow reserve (CT-FFRML): impact of iterative and filtered back projection reconstruction techniques. *J Cardiovasc Comput Tomogr*. (2019) 13:331–5. doi: 10.1016/j.jcct.2018.10.026
 81. Litjens G, Ciompi F, Wolterink JM, de Vos BD, Leiner T, Teuwen J, et al. State-of-the-art deep learning in cardiovascular image analysis. *JACC Cardiovasc Imaging*. (2019) 12:1549–65. doi: 10.1016/j.jcmg.2019.06.009
 82. Wang Z-L, Zhou Z-G, Chen Y, Li X-T, Sun Y-S. Support vector machines model of computed tomography for assessing lymph node metastasis in esophageal cancer with neoadjuvant chemotherapy. *J Comp Assist Tomogr*. (2017) 41:455–60. doi: 10.1097/RCT.0000000000000555
 83. Moraru L, Moldovanu S, Dimitrievici LT, Dey N, Ashour AS, Shi F, et al. Gaussian mixture model for texture characterization with application to brain DTI images. *J Adv Res*. (2019) 16:15–23. doi: 10.1016/j.jare.2019.01.001
 84. Halliburton SS, Tanabe Y, Partovi S, Rajiah P. The role of advanced reconstruction algorithms in cardiac CT. *Cardiovasc Diagn Ther*. (2017) 7:527–38. doi: 10.21037/cdt.2017.08.12
 85. Tayal U, King L, Schofield R, Castellano I, Stirrup J, Pontana F, et al. Image reconstruction in cardiovascular CT: Part 2 – Iterative reconstruction; potential and pitfalls. *J Cardiovasc Comput Tomogr*. (2019) 13:3–10. doi: 10.1016/j.jcct.2019.04.009
 86. Tsompou PI, Sakellarios AI, Siogkas PK, Andrikos IO, Kigka VI, Lemos PA, et al. editors. Comparison of 3D reconstruction methods based on different cardiovascular imaging: a study of multimodality reconstruction method. *2018 40th Annual International Conference of the IEEE Engineering in Medicine and Biology Society (EMBC); 2018 18-21 July* (2018).
 87. Al'Aref SJ, Anchouche K, Singh G, Slomka PJ, Kolli KK, Kumar A, et al. Clinical applications of machine learning in cardiovascular disease and its relevance to cardiac imaging. *Eur Heart J*. (2018) 40:1975–86. doi: 10.1093/eurheartj/ehy404
 88. Cilla M, Martinez J, Pena E, Martínez MÁ. Machine learning techniques as a helpful tool toward determination of plaque vulnerability. *IEEE Trans Biomed Eng*. (2012) 59:1155–61. doi: 10.1109/TBME.2012.2185495
 89. Coenen A, Kim Y-H, Kruk M, Tesche C, De Geer J, Kurata A, et al. Diagnostic accuracy of a machine-learning approach to coronary computed tomographic angiography-based fractional flow reserve. *Circ Cardiovasc Imaging*. (2018) 11:e007217. doi: 10.1161/CIRCIMAGING.117.007217
 90. Wolterink JM, Leiner T, de Vos BD, van Hamersvelt RW, Viergever MA, Išgum I. Automatic coronary artery calcium scoring in cardiac CT angiography using paired convolutional neural networks. *Med Image Anal*. (2016) 34:123–36. doi: 10.1016/j.media.2016.04.004
 91. Kolossváry M, De Cecco CN, Feuchtner G, Maurovich-Horvat P. Advanced atherosclerosis imaging by CT: radiomics, machine learning and deep learning. *J Cardiovasc Comput Tomogr*. (2019) 13:274–80. doi: 10.1016/j.jcct.2019.04.007
 92. Kirişli HA, Schaap M, Metz CT, Dharampal AS, Meijboom WB, Papadopoulou SL, et al. Standardized evaluation framework for evaluating coronary artery stenosis detection, stenosis quantification and lumen segmentation algorithms in computed tomography angiography. *Med Image Anal*. (2013) 17:859–76. doi: 10.1016/j.media.2013.05.007
 93. Ferencik M. About the twists and turns: relationship of coronary artery geometry and atherosclerosis. *J Cardiovasc Comput Tomogr*. (2018) 12:261–2. doi: 10.1016/j.jcct.2018.04.004
 94. Papadopoulou S-L, Garcia-Garcia HM, Rossi A, Girasis C, Dharampal AS, Kitslaar PH, et al. Reproducibility of computed tomography angiography data analysis using semiautomated plaque quantification software: implications for the design of longitudinal studies. *Int J Cardiovasc Imaging*. (2013) 29:1095–104. doi: 10.1007/s10554-012-0167-5
 95. Lee JM, Choi G, Hwang D, Park J, Kim HJ, Doh J-H, et al. Impact of longitudinal lesion geometry on location of plaque rupture and clinical presentations. *JACC Cardiovasc Imaging*. (2017) 10:677–88. doi: 10.1016/j.jcmg.2016.04.012
 96. van Zandwijk JK, Tuncay V, Vliegenthart R, Pelgrim GJ, Slump CH, Oudkerk M, et al. Assessment of dynamic change of coronary artery geometry and its relationship to coronary artery disease, based on coronary CT angiography. *J Digit Imaging*. (2019) 33:480–9. doi: 10.1007/s10278-019-00300-5
 97. Bulant CA, Blanco PJ, Clausse A, Assunção AN, Lima TP, Ávila LFR, et al. Association between three-dimensional vessel geometry and the presence of atherosclerotic plaques in the left anterior descending coronary artery of high-risk patients. *Biomed Signal Process Control*. (2017) 31:569–75. doi: 10.1016/j.bspc.2016.09.023
 98. Kruk M, Noll D, Achenbach S, Mintz GS, Pregowski J, Kaczmarska E, et al. Impact of coronary artery calcium characteristics on accuracy of CT angiography. *JACC Cardiovasc Imaging*. (2014) 7:49–58. doi: 10.1016/j.jcmg.2013.07.013
 99. Pesenti-Rossi D, Allouch P, Gibault-Genty G, Baron N, Augusto S, Convers-Domart R, et al. Évaluation des stents coronaires en scanner cardiaque: revue de la littérature. *Annales de Cardiologie et d'Angéiologie*. (2015) 64:362–7. doi: 10.1016/j.ancard.2015.09.041
 100. Diab HMM, Rasmussen LM, Duvnjak S, Diederichsen A, Jensen PS, Lindholt JS. Computed tomography scan based prediction of the vulnerable carotid plaque. *BMC Med Imaging*. (2017) 17:61. doi: 10.1186/s12880-017-0233-5
 101. Sheahan M, Ma X, Paik D, Obuchowski NA, St. Pierre S, Newman WP, et al. Atherosclerotic plaque tissue: noninvasive quantitative assessment of characteristics with software-aided measurements from conventional CT angiography. *Radiology*. (2017) 286:622–31. doi: 10.1148/radiol.2017170127
 102. Saremi F, Achenbach S. Coronary plaque characterization using CT. *Am J Roentgenol*. (2015) 204:W249–60. doi: 10.2214/AJR.14.13760
 103. Obaid Daniel R, Calvert Patrick A, Gopalan D, Parker Richard A, Hoole Stephen P, West Nick EJ, et al. Atherosclerotic plaque composition and classification identified by coronary computed tomography. *Circ Cardiovasc Imaging*. (2013) 6:655–64. doi: 10.1161/CIRCIMAGING.112.000250

Conflict of Interest: The authors declare that the research was conducted in the absence of any commercial or financial relationships that could be construed as a potential conflict of interest.

Copyright © 2021 Liu, Wingert, Wang, Zhang, Wang, Sun, Chen, Khalid, Jiang and Zheng. This is an open-access article distributed under the terms of the Creative Commons Attribution License (CC BY). The use, distribution or reproduction in other forums is permitted, provided the original author(s) and the copyright owner(s) are credited and that the original publication in this journal is cited, in accordance with accepted academic practice. No use, distribution or reproduction is permitted which does not comply with these terms.



Partitioning the Right Ventricle Into 15 Segments and Decomposing Its Motion Using 3D Echocardiography-Based Models: The Updated ReVISION Method

Márton Tokodi^{1*}, Levente Staub², Ádám Budai³, Bálint Károly Lakatos¹, Máté Csákvári², Ferenc Imre Suhai¹, Liliána Szabó¹, Alexandra Fábián¹, Hajnalka Vágó¹, Zoltán Tőssér², Béla Merkely¹ and Attila Kovács^{1*}

OPEN ACCESS

Edited by:

Sebastian Kelle,
Deutsches Herzzentrum
Berlin, Germany

Reviewed by:

Cezary Szmigielski,
Medical University of Warsaw, Poland
Radu Tanacii,
German Heart Center Berlin, Germany
Charlotte Manisty,
University College London,
United Kingdom

*Correspondence:

Márton Tokodi
tokmarton@gmail.com
Attila Kovács
attila.kovacs@
med.semmelweis-univ.hu

Specialty section:

This article was submitted to
Cardiovascular Imaging,
a section of the journal
Frontiers in Cardiovascular Medicine

Received: 27 October 2020

Accepted: 08 January 2021

Published: 04 March 2021

Citation:

Tokodi M, Staub L, Budai Á,
Lakatos BK, Csákvári M, Suhai FI,
Szabó L, Fábián A, Vágó H, Tőssér Z,
Merkely B and Kovács A (2021)
Partitioning the Right Ventricle Into 15
Segments and Decomposing Its
Motion Using 3D
Echocardiography-Based Models:
The Updated ReVISION Method.
Front. Cardiovasc. Med. 8:622118.
doi: 10.3389/fcvm.2021.622118

¹ Heart and Vascular Center, Semmelweis University, Budapest, Hungary, ² Argus Cognitive, Inc., Lebanon, NH, United States, ³ Department of Automation and Applied Informatics, Budapest University of Technology and Economics, Budapest, Hungary

Three main mechanisms contribute to global right ventricular (RV) function: longitudinal shortening, radial displacement of the RV free wall (bellows effect), and anteroposterior shortening (as a consequence of left ventricular contraction). Since the importance of these mechanisms may vary in different cardiac conditions, a technology being able to assess their relative influence on the global RV pump function could help to clarify the pathophysiology and the mechanical adaptation of the chamber. Previously, we have introduced our 3D echocardiography (3DE)-based solution—the Right Ventricular Separate wall motion quantification (ReVISION) method—for the quantification of the relative contribution of the three aforementioned mechanisms to global RV ejection fraction (EF). Since then, our approach has been applied in several clinical scenarios, and its strengths have been demonstrated in the in-depth characterization of RV mechanical pattern and the prognostication of patients even in the face of maintained RV EF. Recently, various new features have been implemented in our software solution to enable the convenient, standardized, and more comprehensive analysis of RV function. Accordingly, in our current technical paper, we aim to provide a detailed description of the latest version of the ReVISION method with special regards to the volumetric partitioning of the RV and the calculation of longitudinal, circumferential, and area strains using 3DE datasets. We also report the results of the comparison between 3DE- and cardiac magnetic resonance imaging-derived RV parameters, where we found a robust agreement in our advanced 3D metrics between the two modalities. In conclusion, the ReVISION method may provide novel insights into global and also segmental RV function by defining parameters that are potentially more sensitive and predictive compared to conventional echocardiographic measurements in the context of different cardiac diseases.

Keywords: 3D echocardiography, right ventricle, right ventricular function, right ventricular mechanics, decomposed wall motion

INTRODUCTION

For many years, emphasis in clinical cardiology was placed on left ventricular (LV) performance, overshadowing the study of the right ventricle (RV). However, RV function has been recently proven to be an important prognostic factor in heart failure with reduced or preserved ejection fraction (EF) and pulmonary hypertension (1–4). Moreover, the precise assessment of RV function has emerged as a cornerstone of patient management in specific subgroups, such as in patients with mechanical circulatory support devices or grown-up congenital heart disease (5–7). Therefore, the detailed evaluation of RV function to detect even subtle but prognostic changes and to support clinical decision-making represents a compelling demand.

Mechanistically, the RV shows a distinctive contractile pattern with three main mechanisms: (i) shortening along the longitudinal axis with the traction of the tricuspid annulus toward the apex; (ii) inward (radial) movement of the RV free wall (often referred to as the “bellows effect”); and (iii) bulging of the interventricular septum into the RV during the LV contraction and stretching of the free wall over the septum (causing shortening along the anteroposterior direction) (3, 8). Since the importance of these mechanisms may vary in different cardiac conditions, a technology being able to assess their relative influence on the global RV pump function could help to clarify the pathophysiology and the mechanical adaptation of the RV (3).

For this purpose, we developed the Right Ventricular Separate wall motion quantification (ReVISION) method a few years ago, which is a 3D echocardiography (3DE)-based solution for the quantification of the relative contribution of longitudinal, radial, and anteroposterior shortening to global RV EF (9). Since then, our technology has been applied in several clinical scenarios (10–12), and the strengths of the ReVISION method have been demonstrated in the in-depth characterization of RV mechanical pattern and the prognostication of patients even in the face of maintained RV EF (13). The ReVISION method and the associated online platform (demo version available at <https://www.revisionmethod.com>) are improved continuously, and recently, various new features, such as the assessment of longitudinal, circumferential, and area strains have been implemented to enable the convenient, standardized, and more comprehensive analysis of RV function using 3DE datasets.

In addition to the parameters of global ventricular function and geometry, segmental metrics bear clinically relevant information. Concerning the LV, standardized segmentation is widely performed in different cardiovascular imaging modalities mainly to correlate regional dysfunction with coronary perfusion territories (14) or to appreciate and quantify distinct patterns in LV myocardial function, which could be a characteristic of certain pathological processes (15). The same applies to the RV, as pulmonary hypertension or arrhythmogenic cardiomyopathy are just two clinical examples among several others, where established regional dysfunction exists (1, 16, 17). Nevertheless, only a few options are available for the comprehensive and quantitative assessment of the regional RV function due to its complex 3D shape and mechanics. Therefore, we designed

and implemented a volumetric segmentation (i.e., partitioning) algorithm in our current software solution.

In this technical paper, we aimed to provide a detailed description of the updated ReVISION analysis pipeline with special regards to the volumetric partitioning of the RV cavity and the calculation of longitudinal, circumferential, and area strains using 3DE datasets. We also sought to compare our echocardiography-based findings concerning the relative contribution of the three aforementioned motion components with those obtained by cardiac magnetic resonance imaging (CMRI)-based 3D reconstruction.

MATERIALS AND METHODS

The ReVISION Analysis Pipeline

The updated ReVISION analysis pipeline comprises four consecutive steps: (i) image acquisition and 3D RV model reconstruction, (ii) adjusting orientation, (iii) volumetric segmentation, and (iv) calculation of global and segmental metrics, including the quantification of the relative contribution of longitudinal, radial, and anteroposterior motion components (Figure 1). Our software solution was implemented as a user-friendly and convenient online platform (<https://www.revisionmethod.com>), where the user can upload and analyze the reconstructed 3D models of the RV. The analytical components were written in C++, relying on the Eigen linear algebra library (version 3.3.7). The rest of the software stack uses the Play Framework (Scala, version 2.8.2) in the backend and Typescript (version 3.9.5) in the frontend.

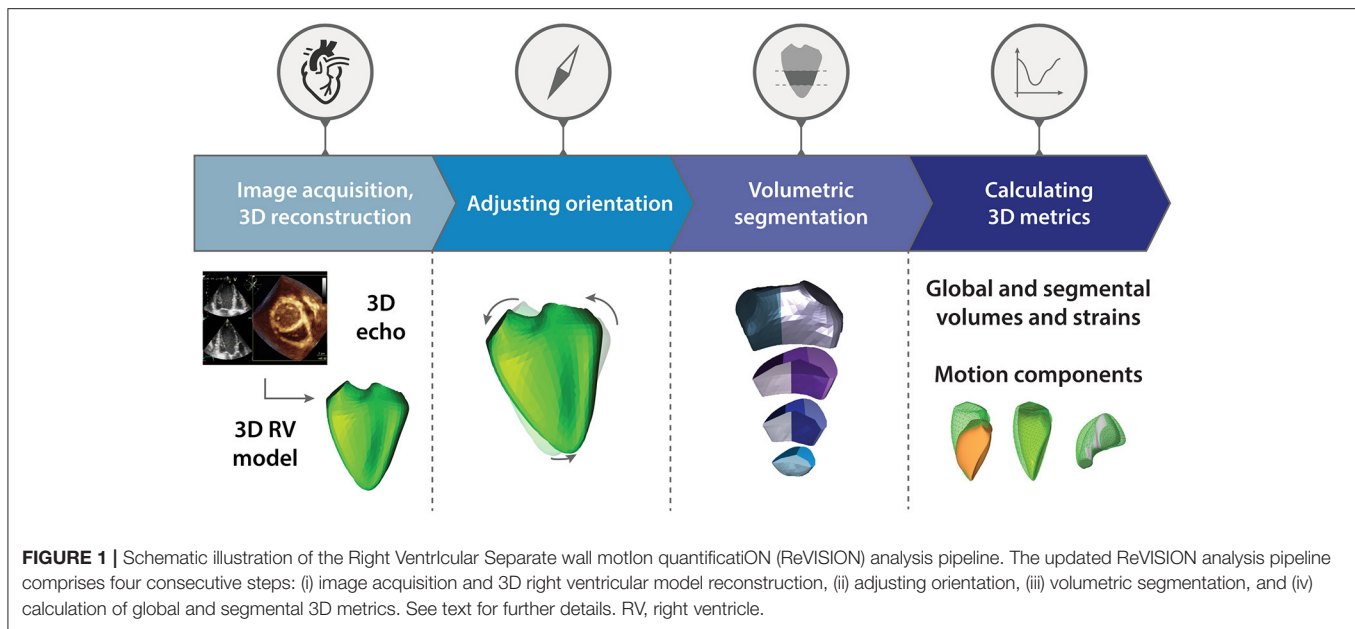
Image Acquisition and 3D RV Model Reconstruction

3DE datasets can be acquired with 3D capable commercially available cardiac ultrasound systems. Then, these datasets are required to be processed using a dedicated software solution (4D RV-Function 2, TomTec Imaging, Unterschleissheim, Germany) to generate 3D models of the RV suitable for the ReVISION analysis. Following the image acquisition and 3D model reconstruction process, a series of UCD files and a header file can be exported for each subject from the dedicated software. Each UCD file contains a 3D polygon mesh representing a time instant (a frame) in the cardiac cycle. Each vertex in a mesh corresponds to a specific anatomical position, and this correspondence is consistent across time instants and patients. These files serve as the input for the next steps of the analysis.

Adjusting Orientation

The exported files contain a series of m_1, \dots, m_n meshes where $m_i = \{(x_1^i, y_1^i, z_1^i), \dots, (x_k^i, y_k^i, z_k^i)\}$ denotes a set of 3D coordinates. A local coordinate system is defined for the end-diastolic mesh of each mesh series, where the basis vectors correspond to the longitudinal, radial, and anteroposterior directions (Figure 2). We denote these basis vectors as $B_l, B_r, B_a \in R^3$, respectively, and we use them to transform each mesh (m_i) of the given mesh series into $\hat{m}_i = \{B^{-1}v_k | v_k \in m_i\}$ where $B = [B_l, B_r, B_a]$.

To define B , the following multistep analysis is performed. First, the points of the septum-free wall boundary ($P =$



$\{p_1, p_2, \dots, p_m\}$ are selected automatically from predefined groups of vertices so that they have a maximal local mean curvature. Then, a plane is fitted to the selected points using orthogonal distance regression (18), and B_r is defined as the normal vector of this plane. B_l should point from the apex (v_a – the vertex corresponding to the apex) toward the midpoint of the most basal vertex of the anterior and the most basal vertex of the posterior septum-free wall boundary ($v_e = \frac{p_1 + p_m}{2}$, where p_1 is the most basal vertex of the anterior and p_m is the most basal vertex of the posterior septum-free wall boundary). These two points are projected to the plane defined by B_r and denoted as \hat{e} and \hat{a} , respectively. Then, the longitudinal basis vector is defined as $B_l = \frac{\hat{e} - \hat{a}}{\|\hat{e} - \hat{a}\|}$. Finally, we define the anteroposterior basis vector as $B_a = B_r \times B_l$. As the result of the orientation adjustment, the longitudinal direction will correspond to the vertical axis, and the radial and anteroposterior directions will be parallel to the horizontal plane.

Volumetric Segmentation

Volumetric segmentation is performed on the end-diastolic mesh of each series to obtain 15 RV segments (Figure 3). First, the fraction of the mesh containing the inflow and outflow segments is separated by a horizontal slicing plane positioned at a predefined height along the longitudinal (i.e., vertical) axis (d_1 – a vector defining the height of the slicing plane along the vertical axis). Then, the remainder of the mesh is trisected by two other horizontal planes at equidistant heights. The following parametric equation represents each horizontal slicing plane:

$$a^T n_i + d_i = 0$$

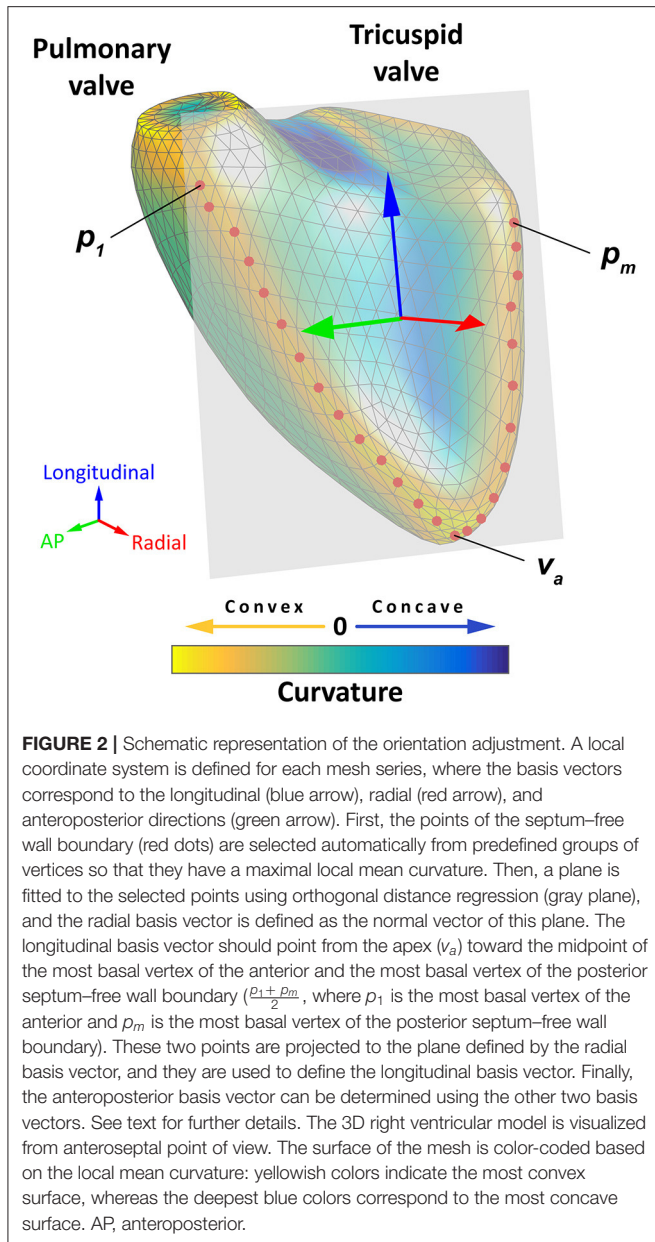
where the $n_1 = n_2 = n_3$ normal vectors of the slicing planes are vertical, and d_3 and d_2 are placed at equidistant heights between

d_1 and the most apical point of the RV (i.e., the vertex with the minimal y-coordinate).

Next, the horizontal slices are divided further. The inflow segment is separated from the outflow segment by a vertical slicing plane along the midpoint of the central vertices of the tricuspid and pulmonary annuli. Using vertically aligned standard planes, the septal and free wall portions of the horizontal slices are divided into further segments. The vertical slicing planes split the slices into three free wall and two septal segments on the basal and mid-levels and into two free wall and one apical segments on the apical level aiming for equal volume distribution among the segments within the given slice. After the parcellation is completed, the newly generated (non-closed) sides of the segments are covered by smooth biharmonic surfaces. As the segmentation is performed on the end-diastolic mesh, the positions of the newly generated vertices are interpolated in all other frames using their barycentric coordinates.

Calculation of Global and Segmental Metrics and Quantifying the Relative Contribution of Longitudinal, Radial, and Anteroposterior Motion Components

To calculate global longitudinal strain (GLS), 45 longitudinally oriented contours (i.e., longitudes) are generated by connecting the apex (v_a) and the predefined vertices of the RV base ($E = \{v_e^{(k)}\}_{k=1}^n$) through specific vertices of the middle section of the RV ($C = \{v_c^{(k)}\}_{k=1}^n$) with geodesic lines. This method ensures that the longitudes are distributed evenly on the surface of the mesh. The length of the j^{th} longitude (L_j^i) can be calculated as the sum of the $v_a - v_c^{(k)}$ and $v_c^{(k)} - v_e^{(k)}$ geodesic distances. The change in the length of each longitude can be monitored throughout the entire cardiac cycle, and GLS can be computed using the following formula:



$$GLS (\%) = 100 * \sum_{j=1}^n \left(\frac{L_j^{end-systole}}{L_j^{end-diastole}} - 1 \right)$$

For global circumferential strain (GCS) calculations, the inflow and outflow segments are omitted. Fifteen circumferential contours (i.e., latitudes) are created by slicing the mesh with horizontal planes at equal distances along the longitudinal axis. After generating the set of circumferential contours $\{C_j^{(i)}\}_{j=1...n}$, where $C_j^{(i)} = (v_1, v_2, \dots, v_l)$ is the list of vertices on a

single contour], the length of the j^{th} circumferential contour is computed as:

$$C_j^i = \sum_{i=1}^{l-1} \|v_{i+1} - v_i\|$$

GCS is calculated using the contour lengths at end-diastole and end-systole:

$$GCS (\%) = 100 * \sum_{j=1}^n \left(\frac{C_j^{end-systole}}{C_j^{end-diastole}} - 1 \right)$$

Global area strain (GAS) quantifies the change in the endocardial surface area between end-diastolic and end-systolic frames. The surface area of the \hat{m}_i triangle mesh can be assessed as:

$$A^i = \sum_{t \in T^i} \frac{\|(t_1 - t_3) \times (t_2 - t_3)\|}{2}$$

where $T^i = \{t_k \in R^3\}_{k=1...}$ is the set of triangles of the \hat{m}_i mesh. Similar to previous calculations, GAS is defined as:

$$GAS (\%) = 100 * \left(\frac{A^{end-systole}}{A^{end-diastole}} - 1 \right)$$

The volume of each mesh (or segment) is calculated using the shoelace formula (19). Let T be the set of triangles \hat{m}_i mesh. For each $t = \{(x_1, y_1, z_1), (x_2, y_2, z_2), (x_3, y_3, z_3)\} \in T$, the volume of the tetrahedron bounded by the vertices of t and the origin:

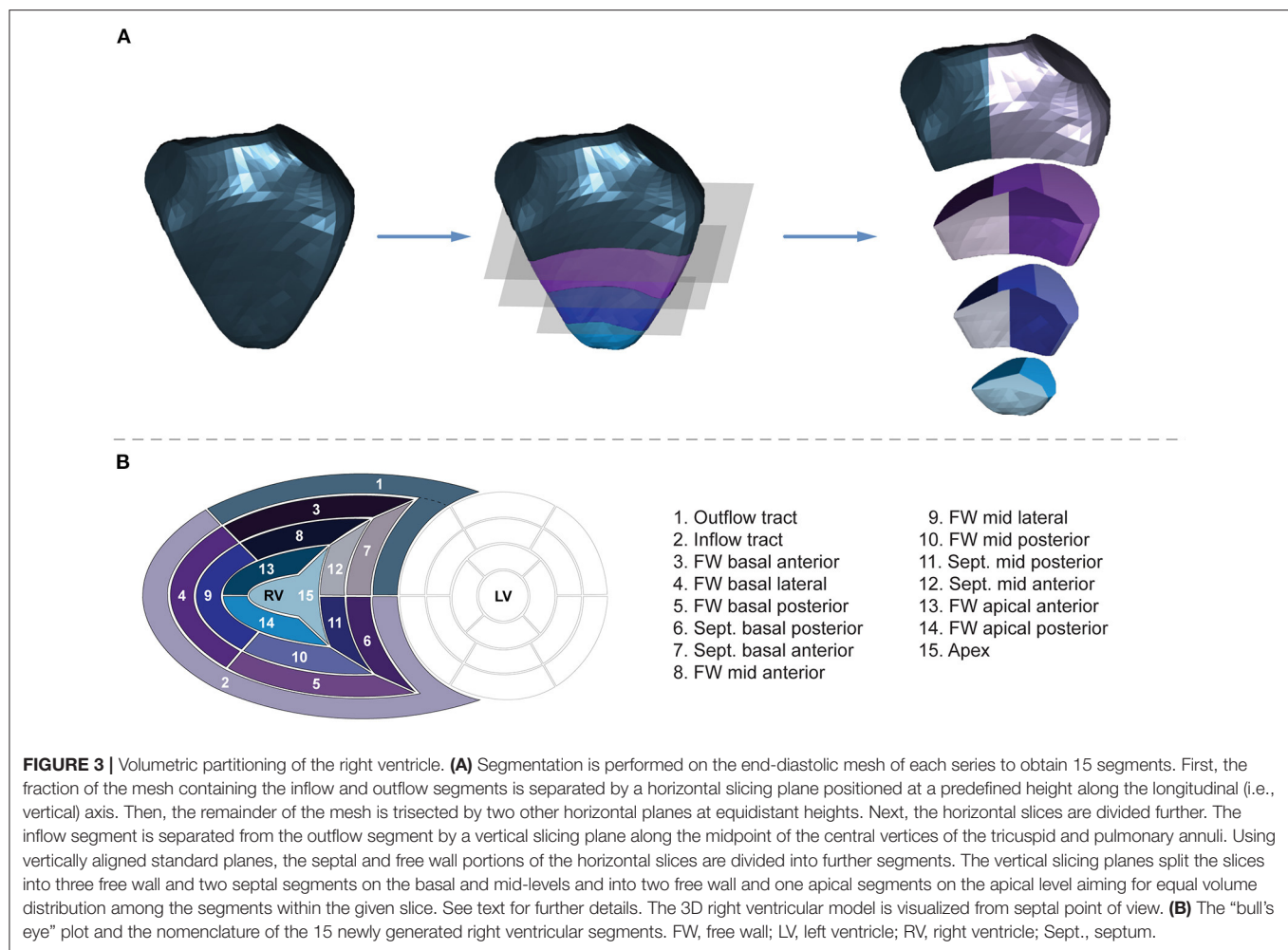
$$V_t := \frac{1}{6}(-x_3y_2z_1 + x_2y_3z_1 + x_3y_1z_2 - x_1y_3z_2 - x_2y_1z_3 + x_1y_2z_3)$$

Note that V_t is signed, meaning that its value may be negative if the normal vector of the triangle points toward the origin. According to the signed tetrahedron method, the volume of the \hat{m}_i mesh is the sum of the signed V_t volumes:

$$V = \sum_{t \in T} V_t$$

Motion decomposition is performed along the aforementioned directions in a vertex-based manner, as previously described (9). End-systolic volumes (ESV) and corresponding EFs generated by each motion component (longitudinal ESV and EF, radial ESV and EF, anteroposterior ESV and EF) can be quantified.

Beyond the global parameters, we can calculate regional metrics (i.e., septal and free wall longitudinal or area strains; basal-, mid-, and apical-level circumferential or area strains) and also segmental metrics for each of the 15 segments (segmental strains and volumes).



Reproducibility of Global and Segmental RV Metrics

Although the second, the third, and the fourth steps of the ReVISION pipeline (i.e., the orientation adjustment, the motion decomposition, the volumetric segmentation, and the calculation of metrics) are fully automated, and they do not introduce any additional observer-related variability, we sought to analyze how the differences in 3D contouring and 3D model reconstruction (using the dedicated TomTec software solution) affect the results of our analysis.

Study Population

To assess the reproducibility of global and segmental RV metrics, 10 healthy, sedentary control subjects (five males, 21 ± 2 years), 10 elite water polo athletes (five males, 21 ± 5 years, 22 ± 4 h of training per week), and 10 end-stage heart failure patients with reduced LV EF (seven males, 57 ± 14 years) were retrospectively identified in our database. Thus, subjects represented a wide range of cardiac volumes and function. The study protocol conforms with the principles outlined in the Declaration of Helsinki and the local regulatory and data protection standards (20). All subjects in our database

were enrolled as part of prospective studies (each approved by the Regional and Institutional Committee of Science and Research Ethics, approval no. 13687-0/2011-EKU and 034309-006/2014/OTIG) and provided written informed consent prior to enrollment to the archiving and analysis of their datasets and the publication of subsequent results.

3D Echocardiography

Echocardiographic examinations were performed with a commercially available ultrasound system (GE Vivid E95, 4Vc-D probe, Horten, Norway) in all cases. Beyond the conventional echocardiographic protocol, ECG-gated full-volume 3D datasets reconstructed from four cardiac cycles and optimized for the RV were obtained from apical view targeting a minimum volume rate of 25 volumes/second. Datasets were processed using a commercially available dedicated software solution (4D RV-Function 2, TomTec Imaging, Unterschleissheim, Germany), and RV end-diastolic volume (EDV), ESV, EF, 2D free wall, and septal longitudinal strain were measured. The 3D models of the RV were exported frame by frame throughout the cardiac cycle for further analysis with the ReVISION method.

Analyzing Intra- and Interobserver Reproducibility

To assess the intraobserver reproducibility of the parameters, the operator (BKL), who performed the first measurements, repeated the 3D reconstruction (using TomTec 4D RV-Function 2) and analysis of the RV models blinded to previous results. Then, a second experienced operator (AK) also performed the 3D reconstruction (with TomTec 4D RV-Function 2) and the ReVISION analysis of the same subjects in a blinded fashion in order to determine interobserver reproducibility.

Comparison of ReVISION- and TomTec-Derived RV Longitudinal Strains

Using the first series of measurements performed by the original operator (BKL), the correlations were assessed between RV longitudinal strain values computed with the ReVISION method (3D global, free wall, and septal longitudinal strain) and the TomTec 4D RV-Function 2 (2D free wall and septal longitudinal strain). In the calculation of RV longitudinal strains, an important technical difference should be noted between the two software solutions: the TomTec 4D RV-Function 2 assesses 2D free wall and septal longitudinal strains using 2D standard apical four-chamber views derived from the 3D datasets, whereas the ReVISION method calculates 3D global, free wall, and septal longitudinal strains using the reconstructed 3D meshes of the RV, as described above.

Statistical Analysis

The intra- and interobserver variability and reliability were evaluated using the intraclass correlation coefficient and the coefficient of variation, respectively. The correlations between the ReVISION- and TomTec-derived longitudinal strain measurements were quantified using Pearson correlation coefficients. A $p < 0.05$ was considered significant. All statistical analyses were performed in R (version 3.6.2, R Foundation for Statistical Computing, Vienna, Austria).

Comparison of 3DE- and CMRI-Derived Metrics

Study Population

Six healthy, sedentary control subjects (three males, 21 ± 2 years) without any known cardiovascular disease or risk factors, along with six healthy elite athletes of various sports disciplines (four males, 23 ± 8 years, 15 ± 6 h of training per week) and six heart failure patients with reduced LV EF in a stable clinical and hemodynamic condition (five males, 73 ± 7 years) were retrospectively identified in our database to match our predefined criterion of having a 3DE and a CMRI examination within 30 days. This population was used to investigate the agreement between the 3DE- and CMRI-based 3D RV models concerning the relative contribution of longitudinal, radial, and anteroposterior motion components. All analyses and measurements were performed blinded to the results assessed with the other imaging modality. The study protocol conforms with the principles outlined in the Declaration of Helsinki and the local regulatory and data protection standards (20). All subjects in our database were enrolled as part of prospective studies (each approved by the Regional and Institutional Committee of

Science and Research Ethics, approval no. 13687-0/2011-EKU and 034309-006/2014/OTIG) and provided written informed consent prior to enrollment to the archiving and analysis of their datasets and the publication of subsequent results.

3D Echocardiography

Echocardiographic examinations, 3D model reconstruction, and analyses were performed in the same way as explained in the previous section (*Reproducibility of Global and Segmental RV Metrics*) of this paper.

CMRI Protocol

CMRI examinations were conducted using a 1.5-Tesla MRI scanner (Achieva, Philips Medical Systems, Eindhoven, The Netherlands) with a five-channel cardiac coil. Retrospectively gated, balanced steady-state free precession cine images were acquired in conventional long- and short-axis views covering the LV and RV. Short-axis cine images were obtained with 8-mm slice thickness (no interslice gaps), in-plane resolution of 1.5×1.5 mm and temporal resolution of 25 phases per cardiac cycle.

Reconstruction of 3D RV Meshes From CMR Images

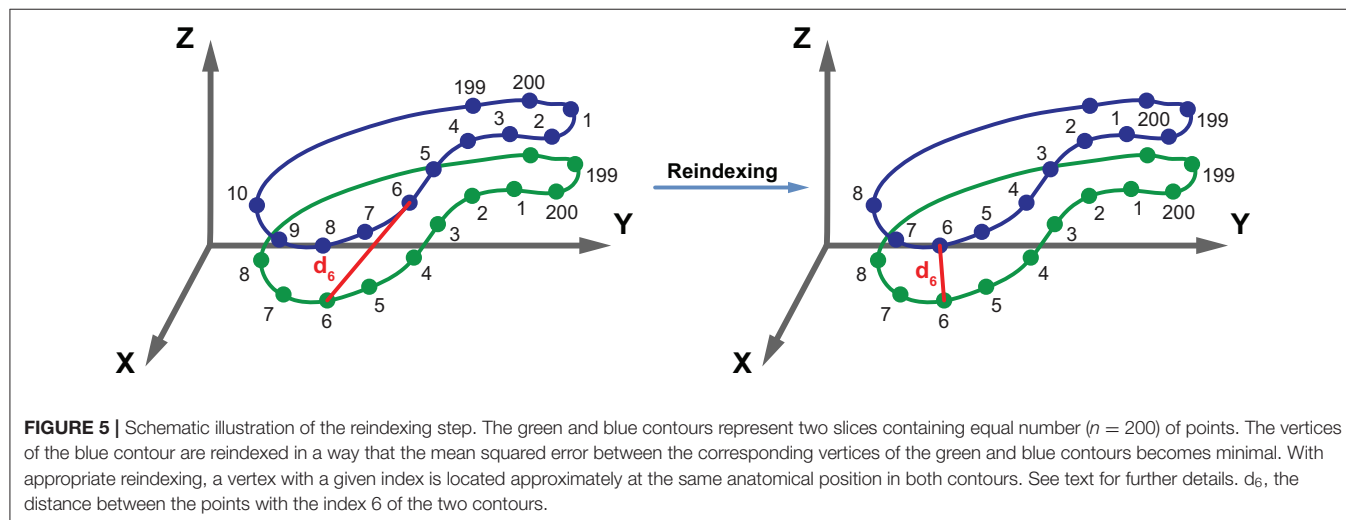
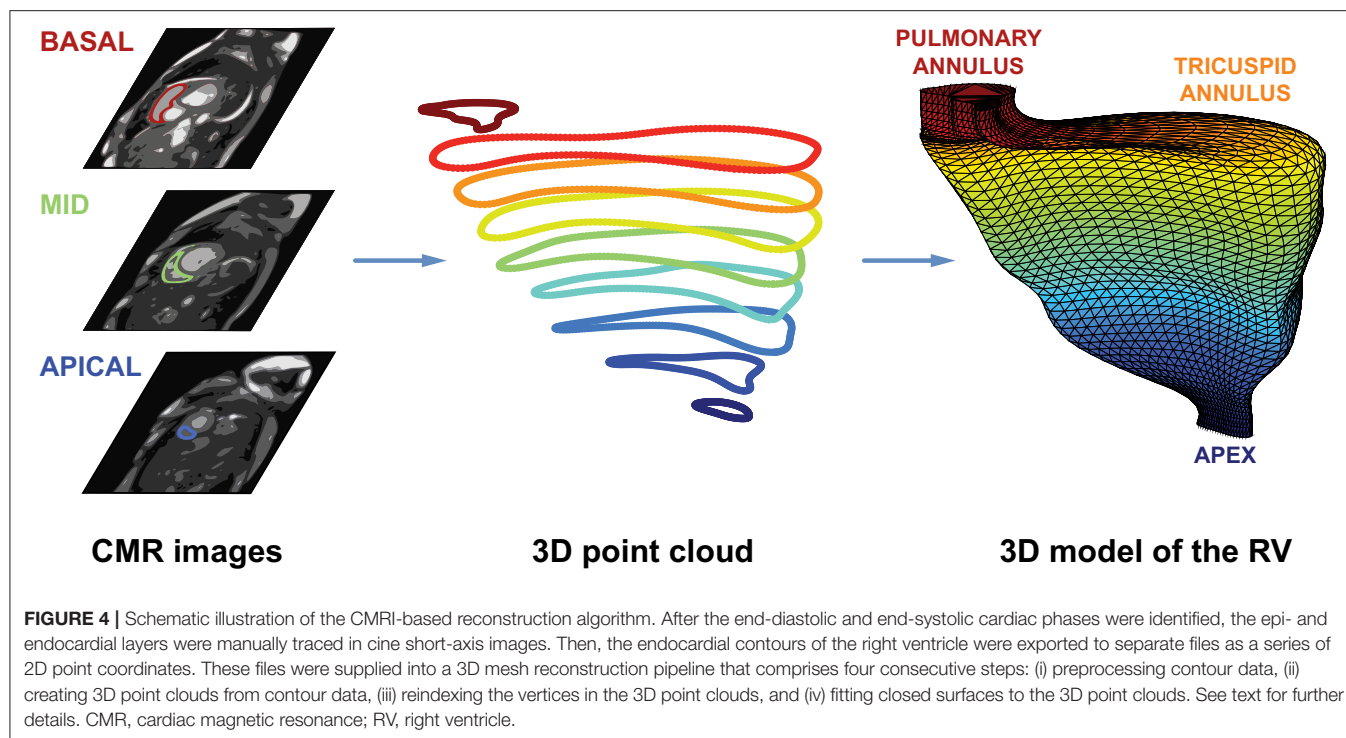
After the end-diastolic and end-systolic cardiac phases were identified, the epi- and endocardial layers were manually traced in cine short-axis images, and RV EDV, ESV, and EF were assessed with a dedicated post-processing software solution (Medis Qmass 7.6, Medis, Leiden, The Netherlands). The endocardial contours of the RV were exported to separate files as a series of 2D point coordinates. These files were supplied into a 3D mesh reconstruction pipeline that comprises four consecutive steps: (i) preprocessing contour data, (ii) creating 3D point clouds from contour data, (iii) reindexing the vertices in the 3D point clouds, and (iv) fitting closed surfaces to the 3D point clouds (**Figure 4**).

In the preprocessing step, a cubic B-spline (containing exactly 200 points) was fitted to the 2D contour points of each slice.

To create a 3D object from the 2D contours, point coordinates were converted to millimeters, and the z coordinates were also generated based on the position of the slice along the vertical axis of the RV. The slices were ordered; therefore, the first slice was always the closest to the apex ($z = 0$), and each slice is located 8 mm above the previous one. By convention, the center of each point cloud (i.e., set of contour points) was shifted to the origin.

As the next step, the 3D points (i.e., vertices) in the point clouds were reindexed. With appropriate reindexing, a vertex with a given index was located approximately at the same anatomical position in the end-diastolic and end-systolic phases, which was essential to perform the motion decomposition. First, the middle slice of the end-systolic point cloud was reindexed in a way that the mean squared error between the corresponding vertices of the end-diastolic and end-systolic slices became minimal:

$$I^* = \arg \min_I \sum_k \left\| \vec{R}_k - \vec{S}_{I(k)} \right\|_2^2$$



where R is the reference slice (i.e., the middle slice of the end-diastolic point cloud), S is the slice that is being reindexed (i.e., the middle slice of the end-systolic point cloud), and I is the function for reindexing that returns the corresponding index of the contour point in S for the k^{th} point of R (Figure 5). Then, the same method was applied to reassign the indices of the remaining slices within each point cloud using the previously reindexed middle slice as a reference.

Preceding the surface fitting, duplicates of the most basal and apical slices were placed 4 mm above and below the original ones. Then, a closed triangle mesh was fitted to the vertices

using the surface interpolation algorithm as implemented in the *geomdl* Python library (version 5.2.10) (21). As a result, the slices were covered by a triangle mesh; however, the top and bottom remained opened. To close the top and bottom of the mesh, constrained Delaunay triangulation was performed, ensuring that the triangulation is successful even if the shape of the given object is not convex (22). Finally, the volume of each mesh was calculated using the shoelace formula.

The entire 3D mesh reconstruction pipeline was implemented in Python (version 3.8.2, Python Software Foundation, Wilmington, Delaware, USA).

To validate the reconstruction process, the RV EDV, ESV, and EF derived from the reconstructed meshes were compared to those computed using the dedicated post-processing software. An excellent agreement was observed in all three metrics (Supplementary Figure 1).

Comparison of 3DE- and CMRI-Derived Metrics

To enable the comparison of 3DE- and CMRI-derived metrics within the same patient, we had to ensure that the meshes are aligned in the same orientation. To that end, 3DE- and CMRI-derived end-diastolic meshes were visualized, and their orientation was adjusted manually by an experienced operator (MT) to match the orientation of the 3DE-derived mesh. Then, the rotation matrix was extracted and was applied to the end-systolic CMRI mesh of the same patient as well. After adjusting the orientation of the CMRI-derived meshes, their motion was decomposed as described previously (9).

The correlations between 3DE-derived measurements and the corresponding CMRI-derived values were quantified using Pearson correlation coefficients, and Bland–Altman analyses were performed to assess the bias and limits of agreement. Paired Wilcoxon signed-rank test vs. null values was applied to test the significance of the bias. A $p < 0.05$ was considered significant. All statistical analyses were performed in R (version 3.6.2, R Foundation for Statistical Computing, Vienna, Austria).

RESULTS

Reproducibility of Global and Segmental RV Metrics

The results of the intra- and interobserver variability and reliability analyses are summarized in **Tables 1, 2**. Reproducibility of global EDV, ESV, and decomposed ESVs were high, which is consistent with our previous reports using the earlier versions of the ReVISION software (10, 11, 13). Regarding the 15 segments, a smooth base-to-apex gradient could be observed (**Table 2, Figures 6, 7**), with the inflow tract and basal segments having the lowest variability and the highest reliability and free wall apical segments exhibiting the highest variability and the lowest reliability. As the orientation adjustment, the motion decomposition, the volumetric segmentation, and the calculation of metrics are fully automated, it should be emphasized that the observed intra- and interobserver variability is related exclusively to the 3D RV model reconstruction that is performed using TomTec 4D RV-Function 2.

Three-dimensional GLS correlated robustly with both 2D free wall and septal longitudinal strains ($r = 0.907$ and $r = 0.891$, both $p < 0.001$, **Table 3**). When we analyzed free wall and septal longitudinal strains separately with our software solution, both 3D free wall and septal longitudinal strains showed strong correlations with the corresponding TomTec-derived values ($r = 0.920$ and $r = 0.919$, both $p < 0.001$, **Table 3**).

TABLE 1 | 3D echocardiographic parameters measured by the two operators in the reproducibility analysis.

	Operator 1		Operator 2
	1st measurements	2nd measurements	
3D RV EDV, mL	167.5 ± 63.1	174.2 ± 66.3	183.2 ± 64.3
3D RV ESV, mL	95.4 ± 55.7	98.4 ± 60.6	99.8 ± 56.2
LESV, mL	134.2 ± 58.6	140.8 ± 63.5	144.9 ± 60.5
RESV, mL	131.2 ± 55.2	135.3 ± 59.5	143.4 ± 58.4
AESV, mL	130.9 ± 62.8	135.9 ± 66.7	141.0 ± 62.9
3D RV GLS, %	−17.6 ± 7.1	−18.5 ± 7.9	−18.4 ± 7.5
3D RV GCS, %	−19.5 ± 9.0	−20.7 ± 9.4	−19.4 ± 7.5
3D RV GAS, %	−31.6 ± 12.2	−32.8 ± 13.2	−33.2 ± 12.1
Outflow tract EDV, mL	47.9 ± 19.0	51.5 ± 21.0	55.9 ± 20.4
Outflow tract ESV, mL	29.5 ± 15.9	31.6 ± 18.3	31.8 ± 17.1
Inflow tract EDV, mL	33.9 ± 12.5	35.2 ± 13.7	34.4 ± 12.8
Inflow tract ESV, mL	22.8 ± 11.2	24.5 ± 13.3	22.9 ± 12.8
FW basal anterior EDV, mL	14.3 ± 7.4	14.5 ± 6.5	16.0 ± 6.3
FW basal anterior ESV, mL	7.1 ± 5.6	6.8 ± 5.3	7.3 ± 4.7
FW basal lateral EDV, mL	11.7 ± 5.0	11.7 ± 4.5	12.3 ± 4.4
FW basal lateral ESV, mL	5.3 ± 4.0	5.2 ± 3.9	5.5 ± 3.6
FW basal posterior EDV, mL	8.5 ± 3.9	8.5 ± 4.0	8.4 ± 3.5
FW basal posterior ESV, mL	4.5 ± 3.2	4.5 ± 3.4	4.6 ± 3.2
Sept. basal posterior EDV, mL	8.3 ± 3.4	8.5 ± 3.2	9.2 ± 3.3
Sept. basal posterior ESV, mL	4.4 ± 3.0	4.2 ± 2.9	4.5 ± 2.7
Sept. basal anterior EDV, mL	6.5 ± 2.8	6.6 ± 2.7	6.7 ± 2.6
Sept. basal anterior ESV, mL	3.6 ± 2.4	3.6 ± 2.4	3.7 ± 2.3
FW mid anterior EDV, mL	8.5 ± 4.5	8.8 ± 4.2	9.8 ± 4.3
FW mid anterior ESV, mL	4.1 ± 3.4	3.8 ± 3.2	4.3 ± 2.9
FW mid lateral EDV, mL	7.3 ± 3.1	7.4 ± 3.0	7.9 ± 3.2
FW mid lateral ESV, mL	3.2 ± 2.3	3.1 ± 2.3	3.4 ± 2.2
FW mid posterior EDV, mL	3.8 ± 1.7	3.8 ± 1.7	3.8 ± 1.8
FW mid posterior ESV, mL	1.9 ± 1.3	1.9 ± 1.4	1.9 ± 1.4
Sept. mid posterior EDV, mL	5.2 ± 2.2	5.4 ± 2.3	5.8 ± 2.5
Sept. mid posterior ESV, mL	2.7 ± 1.9	2.7 ± 1.9	2.9 ± 1.8
Sept. mid anterior EDV, mL	3.5 ± 1.4	3.6 ± 1.4	3.7 ± 1.5
Sept. mid anterior ESV, mL	1.9 ± 1.3	1.9 ± 1.2	2.0 ± 1.2
FW apical anterior EDV, mL	2.1 ± 1.3	2.2 ± 1.3	2.5 ± 1.4
FW apical anterior ESV, mL	1.1 ± 1.0	1.1 ± 1.1	1.2 ± 1.0
FW apical posterior EDV, mL	1.1 ± 0.6	1.1 ± 0.5	1.2 ± 0.7
FW apical posterior ESV, mL	0.5 ± 0.4	0.5 ± 0.4	0.6 ± 0.4
Apex EDV, mL	5.1 ± 2.5	5.2 ± 2.3	5.5 ± 2.8
Apex ESV, mL	3.0 ± 2.1	2.9 ± 2.1	3.2 ± 2.2

Cell values are mean ± standard deviation.

AESV, anteroposterior end-systolic volume; EDV, end-diastolic volume; ESV, end-systolic volume; FW, free wall; GAS, global area strain; GCS, global circumferential strain; GLS, global longitudinal strain; LESV, longitudinal end-systolic volume; RESV, radial end-systolic volume; RV, right ventricular; Sept., septum.

Comparison of 3DE- and CMRI-Derived Metrics

The mean values of the measurements performed with the two imaging modalities are presented in **Table 4**. 3DE- and CMRI-derived volumes correlated robustly, and a systematic

TABLE 2 | Intra- and interobserver variability and reliability of global and segmental right ventricular metrics.

	Intraobserver reproducibility		Interobserver reproducibility	
	ICC (95% CI)	CV (%)	ICC (95% CI)	CV (%)
3D RV EDV	0.945 (0.898–0.970)	5.840	0.902 (0.758–0.953)	9.298
3D RV ESV	0.955 (0.918–0.975)	6.529	0.947 (0.904–0.971)	9.131
LESV	0.943 (0.895–0.969)	6.525	0.920 (0.836–0.959)	9.471
RESV	0.938 (0.889–0.966)	6.514	0.895 (0.785–0.946)	10.333
AESV	0.952 (0.912–0.974)	6.761	0.932 (0.862–0.965)	10.322
3D RV GLS	0.937 (0.881–0.966)	9.296	0.911 (0.841–0.951)	12.240
3D RV GCS	0.944 (0.892–0.971)	11.588	0.845 (0.731–0.913)	18.011
3D RV GAS	0.972 (0.946–0.985)	5.995	0.951 (0.902–0.975)	8.271
Outflow tract EDV	0.818 (0.686–0.898)	10.448	0.674 (0.422–0.819)	17.711
Outflow tract ESV	0.854 (0.745–0.918)	11.670	0.787 (0.639–0.879)	16.414
Inflow tract EDV	0.895 (0.815–0.942)	5.889	0.883 (0.793–0.935)	9.119
Inflow tract ESV	0.919 (0.855–0.956)	7.357	0.914 (0.843–0.953)	9.414
FW basal anterior EDV	0.878 (0.786–0.932)	9.999	0.803 (0.645–0.892)	16.974
FW basal anterior ESV	0.907 (0.834–0.949)	13.648	0.864 (0.763–0.924)	19.973
FW basal lateral EDV	0.919 (0.856–0.956)	8.499	0.856 (0.749–0.920)	12.475
FW basal lateral ESV	0.938 (0.888–0.966)	12.626	0.904 (0.829–0.947)	16.693
FW basal posterior EDV	0.937 (0.887–0.966)	8.528	0.892 (0.810–0.940)	13.269
FW basal posterior ESV	0.940 (0.892–0.967)	10.607	0.918 (0.853–0.955)	14.988
Sept. basal posterior EDV	0.888 (0.802–0.938)	9.302	0.806 (0.650–0.893)	13.187
Sept. basal posterior ESV	0.926 (0.868–0.960)	12.383	0.868 (0.769–0.927)	16.650
Sept. basal anterior EDV	0.938 (0.890–0.966)	8.321	0.876 (0.782–0.931)	13.294
Sept. basal anterior ESV	0.953 (0.914–0.974)	10.262	0.904 (0.829–0.947)	16.537
FW mid anterior EDV	0.881 (0.790–0.934)	13.051	0.833 (0.659–0.914)	16.636
FW mid anterior ESV	0.929 (0.872–0.961)	15.034	0.876 (0.782–0.931)	19.886
FW mid lateral EDV	0.887 (0.800–0.937)	11.484	0.877 (0.773–0.933)	11.708
FW mid lateral ESV	0.935 (0.884–0.965)	15.028	0.911 (0.842–0.951)	17.802
FW mid posterior EDV	0.840 (0.723–0.910)	13.812	0.790 (0.644–0.881)	16.231
FW mid posterior ESV	0.897 (0.817–0.943)	16.277	0.881 (0.790–0.933)	18.573
Sept. mid posterior EDV	0.893 (0.810–0.930)	11.051	0.886 (0.724–0.945)	11.087
Sept. mid posterior ESV	0.924 (0.864–0.958)	13.877	0.906 (0.832–0.948)	14.244
Sept. mid anterior EDV	0.859 (0.754–0.921)	12.028	0.820 (0.691–0.890)	14.455
Sept. mid anterior ESV	0.865 (0.764–0.925)	14.670	0.859 (0.754–0.921)	17.253
FW apical anterior EDV	0.764 (0.604–0.866)	19.717	0.764 (0.573–0.871)	20.048
FW apical anterior ESV	0.872 (0.769–0.930)	18.407	0.867 (0.768–0.927)	23.412
FW apical posterior EDV	0.664 (0.456–0.803)	22.065	0.608 (0.381–0.767)	25.802
FW apical posterior ESV	0.772 (0.615–0.870)	19.669	0.771 (0.601–0.872)	24.043
Apex EDV	0.883 (0.789–0.936)	11.067	0.868 (0.769–0.927)	12.545
Apex ESV	0.936 (0.885–0.965)	12.204	0.841 (0.725–0.911)	16.263

CI, confidence interval; CV, coefficient of variation; ICC, intraclass correlation coefficient.

Other abbreviations as in **Table 1**.

underestimation by 3DE could be seen (**Figure 8, Table 5**), which is in line with previous studies (23, 24). RV EF demonstrated a good correlation, and only a negligible bias could be observed between its values derived from the two imaging modalities (**Table 5**). The comparison of 3DE- and CMRI-derived ESVs after motion decomposition along the three aforementioned directions is illustrated in **Figure 9**. Strong correlations could be reported (Pearson correlation

coefficients > 0.9 of the three motion components), and similar to global RV volumes, a consistent underestimation of volumes by 3DE could also be detected in the values of the decomposed volumes (**Table 5**). Not surprisingly, the values of the decomposed EFs showed slightly weaker but highly significant correlations between the two modalities, and in addition, bias was found to be non-significant in all of them (**Figure 10, Table 5**).

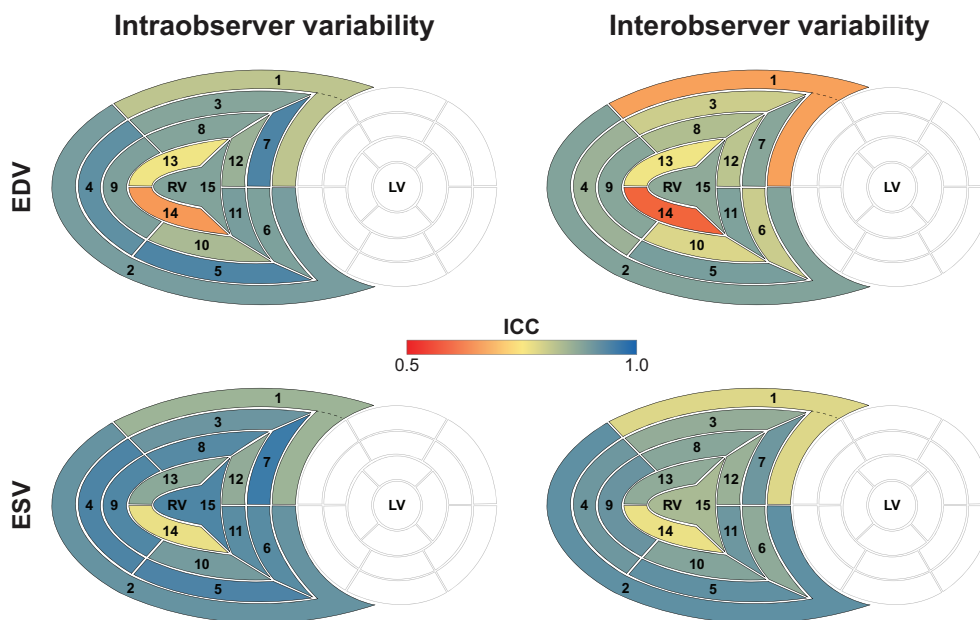


FIGURE 6 | Intra- and interobserver variability of right ventricular end-diastolic and end-systolic segmental volumes. The 15 segments are color-coded based on the value of the intraclass correlation coefficient: reddish colors indicate a lower, whereas blueish colors correspond to a higher value of intraclass correlation coefficient in the given segment. Segment numbers as defined in **Figure 3**. EDV, end-diastolic volume; ESV, end-systolic volume; ICC, intraclass correlation coefficient; LV, left ventricle; RV, right ventricle.

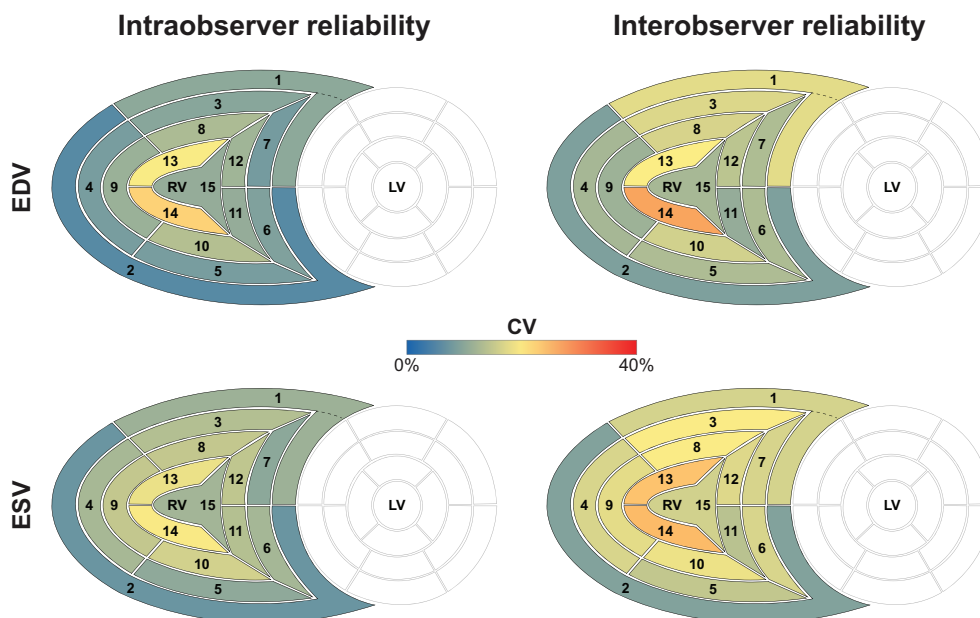


FIGURE 7 | Intra- and interobserver reliability of right ventricular end-diastolic and end-systolic segmental volumes. The 15 segments are color-coded based on the value of the coefficient of variation: reddish colors indicate a higher, whereas blueish colors correspond to a lower value of coefficient of variation. Segment numbers as defined in **Figure 3**. EDV, end-diastolic volume; ESV, end-systolic volume; CV, coefficient of variation; LV, left ventricle; RV, right ventricle.

DISCUSSION

The detailed assessment of RV function is the cornerstone of patient management in several cardiovascular diseases. The

option of measuring RV volumes and EF by 3DE opened up new horizons in terms of a relatively easy and quick but more thorough quantification of the “forgotten chamber.” 3DE-derived RV EF has a well-established added value over

TABLE 3 | Correlations between the ReVISION- and TomTec-derived right ventricular strains ($n = 30$).

		TomTec	
		2D free wall longitudinal strain	2D septal longitudinal strain
ReVISION	3D GLS	$r = 0.907$ $p < 0.001$	$r = 0.891$ $p < 0.001$
	3D free wall longitudinal strain	$r = 0.920$ $p < 0.001$	–
	3D septal longitudinal strain	–	$r = 0.919$ $p < 0.001$

Statistical test: Pearson correlation.

GLS, global longitudinal strain.

TABLE 4 | Summary of the 3D echocardiography- and cardiac magnetic resonance imaging-derived measurements.

	Healthy controls $n = 6$	Athletes $n = 6$	HFrEF patients $n = 6$
3D ECHOCARDIOGRAPHY			
RV EDV, mL	140.7 ± 19.9	185.4 ± 52.6	145.8 ± 37.6
RV ESV, mL	60.2 ± 13.8	87.5 ± 27.7	77.8 ± 27.4
RV EF, %	57.4 ± 5.9	52.8 ± 5.2	47.6 ± 5.8
LESV, mL	110.4 ± 13.7	140.8 ± 45.0	124.0 ± 35.7
RESV, mL	96.4 ± 16.4	135.2 ± 38.3	99.5 ± 34.7
AESV, mL	95.9 ± 15.5	148.0 ± 47.1	120.4 ± 29.3
LEF, %	21.3 ± 3.5	24.7 ± 6.6	15.0 ± 7.4
REF, %	31.4 ± 7.4	26.6 ± 8.2	33.0 ± 7.0
AEF, %	31.9 ± 3.3	20.6 ± 5.9	17.1 ± 3.4
CMRI			
3D RV EDV, mL	154.7 ± 23.9	200.1 ± 56.4	151.9 ± 37.6
3D RV ESV, mL	64.1 ± 10.6	92.3 ± 26.0	80.3 ± 26.6
3D RV EF, %	58.2 ± 5.7	53.6 ± 5.2	47.9 ± 5.2
LESV, mL	123.2 ± 14.9	157.4 ± 46.7	133.5 ± 38.0
RESV, mL	110.2 ± 20.3	140.3 ± 30.5	104.0 ± 33.8
AESV, mL	105.5 ± 20.0	156.0 ± 48.2	130.5 ± 33.0
LEF, %	19.9 ± 7.5	21.7 ± 4.2	12.6 ± 5.6
REF, %	28.8 ± 5.8	28.2 ± 9.8	32.5 ± 7.0
AEF, %	32.0 ± 4.2	22.6 ± 3.5	14.2 ± 2.6

Cell values are mean ± standard deviation.

AEF, anteroposterior ejection fraction; CMRI, cardiac magnetic resonance imaging; EF, ejection fraction; HFrEF, heart failure with reduced left ventricular ejection fraction; LEF, longitudinal ejection fraction; REF, radial ejection fraction.

Other abbreviations as in Table 1.

two-dimensional echocardiographic parameters (25). Beyond EF, however, more comprehensive metrics are needed, which can precisely characterize the complex mechanical pattern of the RV and is also able to detect subtle, often segmental dysfunction. By developing the new version of the ReVISION method, we aimed to provide a tool for the detailed evaluation of the different motion components and to enable segmental analysis using 3DE-derived RV models.

In our current technical paper, we have described a novel, rule-based method for standardizing the orientation of 3D RV models, which holds the potential to progress to an agnostic approach for the analysis of 3D models provided by other vendors or imaging modalities. This is a clear step forward from our previous approach, in which each input mesh series was superimposed to a reference mesh (pre-oriented manually by expert consensus). Moreover, we have developed and tested the volumetric partitioning of the 3D model into 15 segments to allow the assessment and visualization of regional differences and to detect potential changes in the segmental contraction pattern (Figures 11, 12). The reproducibility of global and segmental volumes was found acceptable and concordant with previous reports. Finally, using a custom CMRI-based 3D reconstruction algorithm, we have found a robust agreement between 3DE- and CMRI-derived decomposed volumes and EF, confirming the applicability and credibility of our method to express the relative contribution of longitudinal, radial, and anteroposterior motion components to global RV function.

Volumetric Segmentation of the RV

In contrast to its left counterpart, no generally accepted and standardized myocardial segmentation approach exists concerning the RV. This is attributable to its more complex 3D shape and the relatively inferior clinical relevance of segmental RV analysis in coronary artery disease compared to the LV. Nevertheless, regional alterations in RV myocardial mechanics may have a pivotal role in detecting subclinical alterations that cannot be captured by global metrics.

Various algorithms have been proposed for the volumetric segmentation of the RV. Mocerri et al. used the output of the TomTec solution (4D RV-Function 2, TomTec Imaging, Unterschleissheim, Germany) and divided the 3D endocardial surface into four septal (membranous, infundibular, trabecular, inlet) and four free wall regions (inferior, lateral, anterior, outflow tract) (1). In their method, the accurate identification of regions requires the anatomical position of each vertex to be consistent across time instants and patients. In healthy subjects, they found the area and circumferential strains to show the greatest values in the inferior free wall region, whereas longitudinal deformation predominated in the inferior free wall segment. They also reported that patients with pulmonary hypertension had significantly worse longitudinal, circumferential, and area strains compared to healthy controls in all of the regions. Moreover, GAS was found to be a powerful independent predictor of survival. Similar to these results, Satriano et al. reported that principle strain (assessed with contraction angle analysis) could reliably identify pulmonary arterial hypertension patients (26). In their analysis, six surface segments (septal body, septal apex, free wall body, free wall apex, inflow, and outflow) were separated. The greatest magnitude of difference (compared to healthy controls) was observed in the principal strain values of the free wall segments, suggesting that these segments suffer the most severe contractile impairment in patients with pulmonary arterial hypertension.

Addetia and coworkers also used the triangular mesh model generated with the TomTec software solution (4D RV-Function

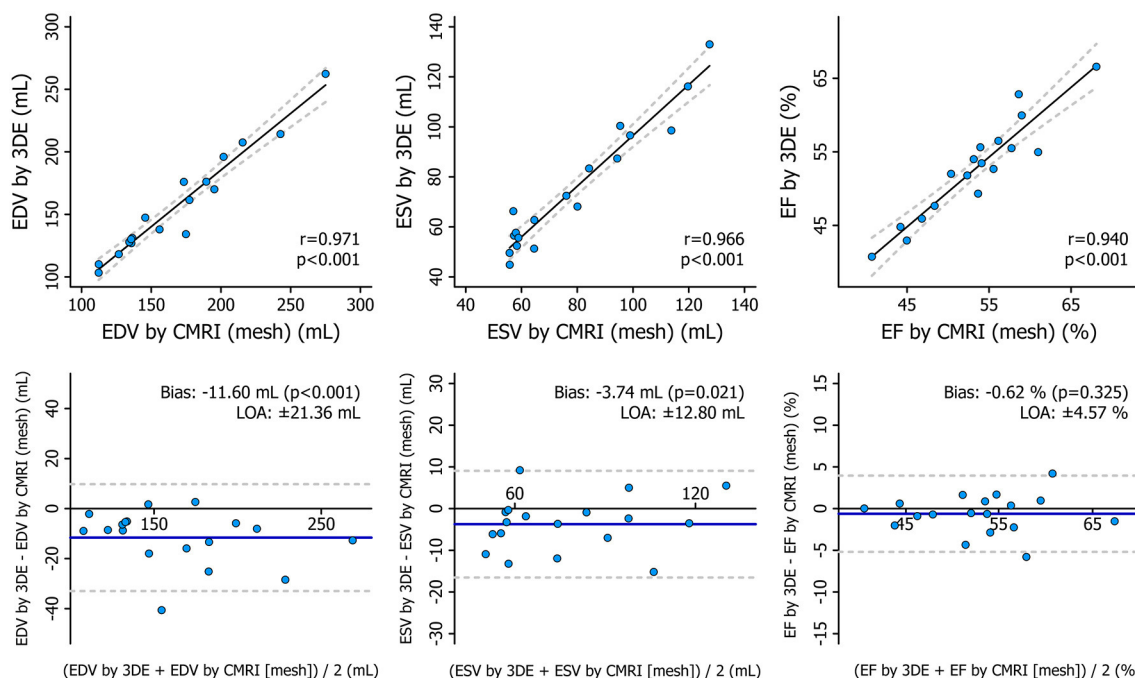


FIGURE 8 | Correlation and agreement between 3D echocardiography- and cardiac magnetic resonance imaging-derived measurements of right ventricular end-diastolic volume, end-systolic volume, and ejection fraction depicted by correlation and Bland–Altman plots. The correlations between 3D echocardiography-derived measurements and the corresponding cardiac magnetic resonance imaging-derived values were quantified using Pearson correlation coefficients, and Bland–Altman analyses were performed to assess the bias and limits of agreement. Paired Wilcoxon signed-rank test vs. null values was applied to test the significance of the bias. 3DE, 3D echocardiography; CMRI, cardiac magnetic resonance imaging; EDV, end-diastolic volume; EF, ejection fraction; ESV, end-systolic volume; LOA, limits of agreement.

TABLE 5 | Correlation and agreement between 3D echocardiography- and cardiac magnetic resonance imaging-derived measurements.

	Pearson correlation		Bland–Altman analysis	
	<i>r</i>	<i>p</i> -value	Bias	LOA
RV EDV	0.971	<0.001	−11.60 mL*	±21.36 mL
RV ESV	0.966	<0.001	−3.74 mL*	±12.80 mL
RV EF	0.940	<0.001	−0.62 %	±4.57 %
LESV	0.958	<0.001	−12.94 mL*	±20.67 mL
RESV	0.950	<0.001	−7.82 mL*	±21.25 mL
AESV	0.948	<0.001	−9.23 mL*	±24.83 mL
LEF	0.724	<0.001	2.27 %	±10.16 %
REF	0.810	<0.001	0.52 %	±9.16 %
AEF	0.771	<0.001	0.25 %	±10.53 %

**p* < 0.05, paired Wilcoxon signed-rank test vs. null values to test the significance of the bias.

LOA, limits of agreement.

Other abbreviations as in **Tables 1, 4**.

1.1, TomTec Imaging, Unterschleissheim, Germany) to divide the RV into four subvolumes: apex, body, inflow tract, and outflow tract (27). Then, they separated the septal and free wall surfaces of the body and the apex to analyze regional curvature indices on a total of six endocardial surfaces. In pulmonary

hypertension patients, they have elegantly demonstrated that the normal “bellows effect” vanishes as the RV free wall regions remain similarly convex from end-diastole to end-systole. This finding corresponds to the literature data and our own experience with the ReVISION method, as the radial motion of the RV free wall is affected early by pressure overload, and thus, it may be a better marker of even subclinical RV dysfunction compared to global measures and, importantly, to parameters referring to longitudinal shortening only (28). To establish the reference ranges for regional indices, they quantified volumes and EFs for the four above-mentioned subvolumes and curvature for the six above-mentioned endocardial surfaces in 245 healthy subjects, and they reported sex- and age-related differences in the values of these metrics (29).

More recently, Bernardino et al. proposed an automated, mesh-independent method for partitioning the RV cavity and computing regional volumes and EFs in three regions (apex, inlet, and outflow) (30). To avoid errors due to inconsistent anatomical vertex positioning between different 3D meshes, their method uses well-defined anatomic landmarks (the apex, the tricuspid, and the pulmonary annuli), and each vertex is assigned to the region whose representing landmark is located the closest based on geodesic distance. Although they used meshes exported from the TomTec solution (4D RV-Function 2, TomTec Imaging, Unterschleissheim, Germany) in the presented analysis,

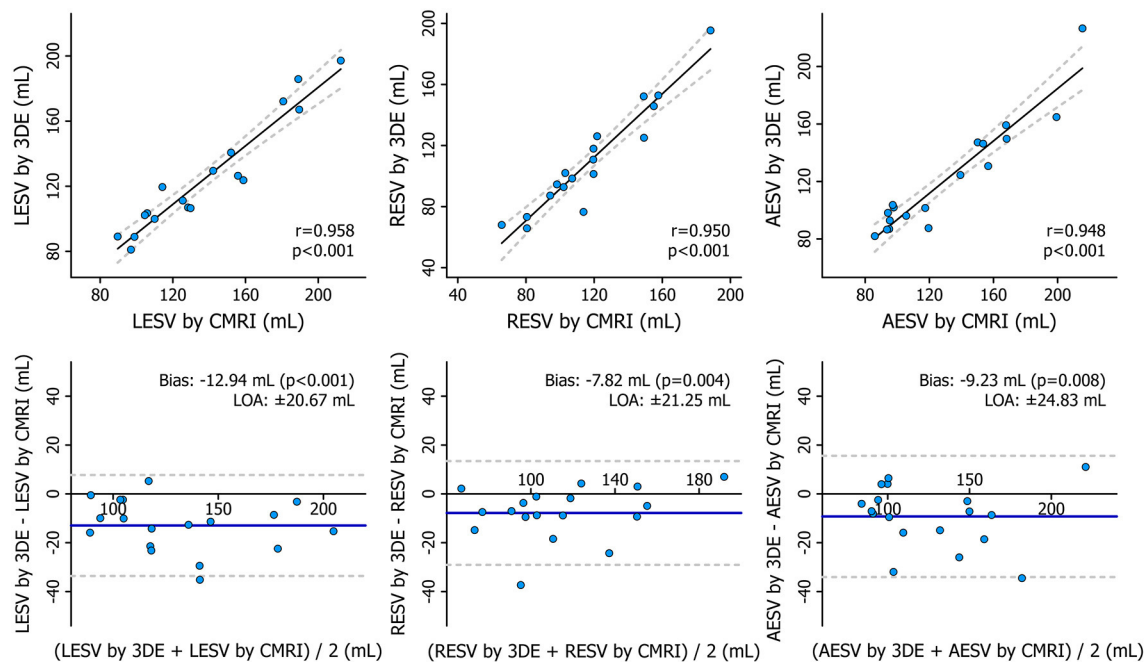


FIGURE 9 | Correlation and agreement between 3D echocardiography- and cardiac magnetic resonance imaging-derived measurements of right ventricular decomposed end-systolic volumes depicted by correlation and Bland–Altman plots. Statistical tests: same as in **Figure 8**. 3DE, 3D echocardiography; AESV, anteroposterior end-systolic volume; CMRI, cardiac magnetic resonance imaging; LESV, longitudinal end-systolic volume; LOA, limits of agreement; RESV, radial end-systolic volume.

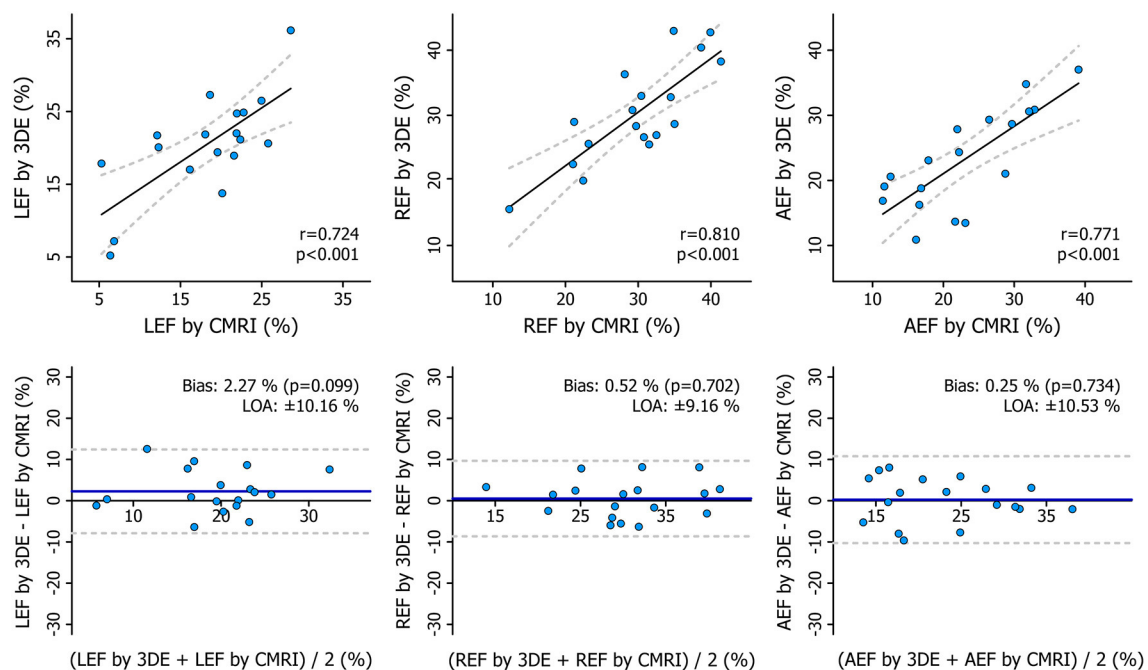


FIGURE 10 | Correlation and agreement between 3D echocardiography- and cardiac magnetic resonance imaging-derived measurements of right ventricular decomposed ejection fractions depicted by correlation and Bland–Altman plots. Statistical tests: same as in **Figure 8**. 3DE, 3D echocardiography; AEF, anteroposterior ejection fraction; CMRI, cardiac magnetic resonance imaging; LEF, longitudinal ejection fraction; LOA, limits of agreement; REF, radial ejection fraction.

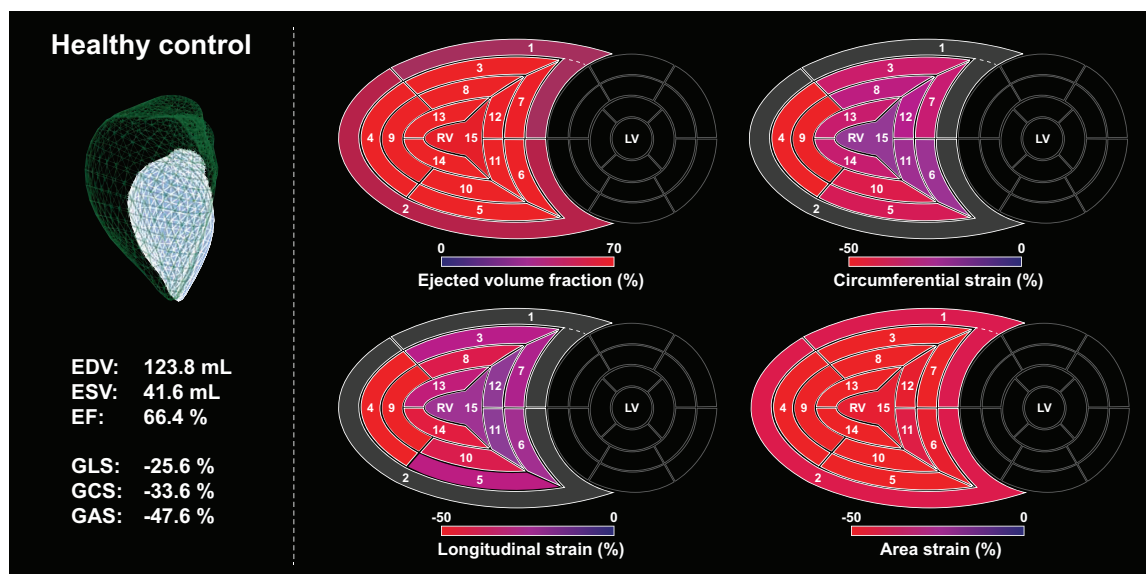


FIGURE 11 | A healthy, sedentary subject's (male, 23 years old) right ventricle analyzed using the ReVISION method. Right ventricular end-diastolic volume, end-systolic volume, and ejection fraction are normal, along with global longitudinal, circumferential, and area strains. Segmental values of the aforementioned metrics at end-systole are depicted on bull's eye heatmaps. Segment numbers as defined in **Figure 3**. In the upper left corner, the green mesh represents the end-diastolic volume, and the blue surface corresponds to the end-systolic volume. EDV, end-diastolic volume; EF, ejection fraction; ESV, end-systolic volume; GAS, global area strain; GCS, global circumferential strain; GLS, global longitudinal strain; LV, left ventricle; RV, right ventricle.

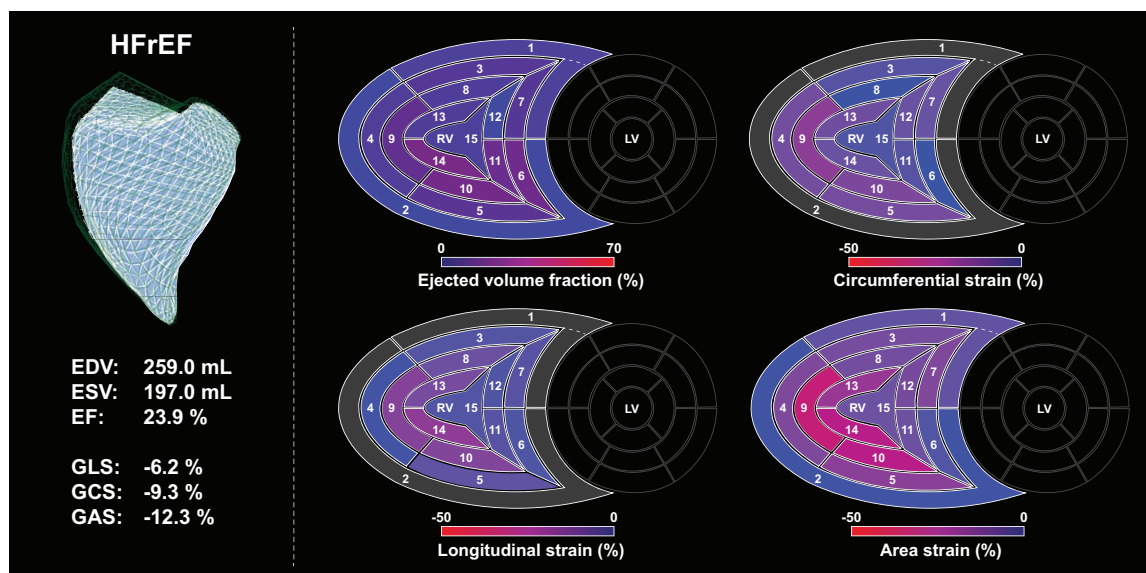


FIGURE 12 | Right ventricle of a patient (male, 29 years old) with end-stage heart failure with reduced left ventricular ejection fraction analyzed using the ReVISION method. Right ventricular end-diastolic and end-systolic volumes are increased, ejection fraction is severely reduced, along with global longitudinal, circumferential, and area strains. Segmental values of the aforementioned metrics at end-systole are depicted on bull's eye heatmaps, the loss of function can be easily appreciated when compared to the maps of the healthy control (**Figure 11**). Segment numbers as defined in **Figure 3**. In the upper left corner, the green mesh represents the end-diastolic volume, and the blue surface corresponds to the end-systolic volume. EDV, end-diastolic volume; EF, ejection fraction; ESV, end-systolic volume; GAS, global area strain; GCS, global circumferential strain; GLS, global longitudinal strain; HFrEF, heart failure with reduced (left ventricular) ejection fraction; LV, left ventricle; RV, right ventricle.

their method might be capable of analyzing 3D RV models reconstructed using other post-processing software solutions as well.

Besides the methods using the triangular meshes generated with the TomTec software, there is a commercially available RV-dedicated 3D speckle tracking tool from Canon Medical

Systems (Otagawa, Japan) for the calculation of global and regional longitudinal, circumferential, and area strains (31). During 3D reconstruction, this software solution uses manually appointed anatomical landmarks (attachment sites of the moderator band to the septum and anterior papillary muscle to the free wall) that separate the inlet, the outflow, and the apical segments. Finally, seven surface segments are identified, namely, inlet lateral, inlet inferior, inlet septum, outflow septum, outflow free wall, apical free wall, and apical septum (32). After evaluating the reliability and feasibility of this algorithm in a group of patients with various heart diseases, Ishizu et al. suggested that the assessment of RV dyssynchrony could be one of the major clinical implications of regional RV myocardial deformation by 3D speckle tracking echocardiography (32).

Overall, clinical data support the usefulness of the 3D-derived segmental RV analysis. Although the majority of studies focused on pulmonary hypertension, we may hypothesize a similar diagnostic and prognostic value in case of RV volume overload, ischemia, or even arrhythmogenic cardiomyopathy. Of note, our software offers a unique solution for RV segmentation, as it defines 15 segments and it is capable of computing segmental EFs and longitudinal, circumferential, and area strain values.

The Relative Contribution of Longitudinal, Radial, and Anteroposterior Motion Components to Global RV Function

In our current analysis, we found a robust agreement between 3DE- and CMRI-derived measurements of decomposed ESVs and EFs. These results also justify the concept of analyzing longitudinal, radial, and anteroposterior motions separately.

Previously, we aimed to characterize the RV mechanical pattern in healthy volunteers and various clinical settings via local and international collaborations. In a dual-center study involving 300 healthy subjects, we aimed to determine the physiological contribution of RV longitudinal, radial, and anteroposterior motion components to global RV EF (12). Despite the traditional view that the longitudinal shortening is the main driver of RV global function, we found that the anteroposterior shortening is a similarly prominent motion component. Moreover, there is an age-dependent increase (until the age of 60 years) in radial motion with a concomitant decrease in longitudinal shortening. However, individuals over 60 years of age represent a distinct group as radial motion decreases again, which may be attributable to the age-related increases in pulmonary pressures (12).

We also investigated the RV mechanical pattern of the athlete's heart. Evidently, regular vigorous physical exercise induces significant changes in cardiac morphology and function (33). The mechanical adaptation to intense, long-term exercise implies a functional shift in the RV: the relative contribution of longitudinal motion to global function was increased, whereas the radial shortening was significantly decreased (11). Moreover, this functional pattern correlated with aerobic exercise performance assessed with cardiopulmonary exercise testing,

representing a potential new resting marker of the athlete's heart (11).

RV function is commonly altered following cardiac surgeries, such as coronary artery bypass grafting, surgical valve repair, or heart transplantation (34–36). The most prominent change is the decline in longitudinal shortening, even if the global RV function is preserved (10). This deterioration of the long-axis RV function is quite persistent and independent of the side of the surgical procedure (37). Notably, RV systolic function (EF and stroke volume) is mostly preserved regardless of the surgery, as radial RV contraction might compensate for the decline in longitudinal shortening. We have confirmed this phenomenon in heart transplanted patients (10). Moreover, in one of our clinical outcome studies focusing on patients with severe mitral regurgitation (PREPARE-MVR: PRediction of Early Post-operAtive Right vEntricular failure in Mitral Valve Replacement/Repair patients), the characteristic contraction pattern (i.e., decreased radial and increased longitudinal contribution to global RV function) of this patient population underwent an instantaneous shift at open-heart surgery (mitral valve replacement or repair), and the radial motion became the dominant component in the early post-operative period (13). However, at 6-month follow-up, the normal RV contraction pattern (i.e., the equal contribution of longitudinal and radial components) was restored, suggesting functional RV reverse remodeling. Interestingly, the observed increase in preoperative longitudinal contractions was associated with decreased post-operative RV contractility as assessed by right heart catheterization; thus, it might predict perioperative RV failure (13).

All these results suggest that the ReVISION software enables the exploration of RV response to different physiological and pathophysiological processes and may also provide parameters that are predictive of outcomes. Further studies are underway to explore the diagnostic and prognostic value of the 3D assessment of RV mechanics in other clinical scenarios as well.

Limitations

The ReVISION method and the presented analyses have some limitations that should be acknowledged. First, the current version of our software relies on the 3D RV meshes generated using a specific commercially available software. However, we are continuously improving our software solution, and we are moving toward an agnostic approach that enables the processing of 3D models from other vendors or other imaging modalities as well. Second, a relatively limited number of subjects were included in our retrospective analysis. Thus, additional large-scale studies are required to evaluate the reliability, reproducibility, and repeatability of our parameters in a multicentric, prospective manner using datasets acquired with ultrasound systems of various manufacturers. Third, due to the retrospective nature of our study, same-day 3DE and CMRI examinations were not available for all subjects. In spite of this, we observed moderate-to-strong correlations between 3DE- and CMRI-derived measurements. Last, volumetric segmentation and strain analysis were not applicable to the CMRI-derived 3D meshes.

Therefore, we could not assess their agreement between the two modalities.

CONCLUSIONS

Since the first version of the ReVISION method was released, our algorithm has been continuously improved, and recently, various new features, such as the volumetric segmentation of the RV or the assessment of longitudinal, circumferential, and area strain have been implemented to enable more advanced and comprehensive analysis of the RV function using 3DE datasets. Beyond providing a detailed description of the updated ReVISION analysis pipeline, we also demonstrated the reproducibility of global and segmental RV volumes, and we compared the 3DE- and CMRI-derived metrics of the decomposed RV motion. Moreover, we updated the online interface of the software (a demo version is available at <https://www.revisionmethod.com>), which now allows the users to upload and analyze 3D RV meshes, to inspect the segments in 3D, to generate time-volume or time-strain curves, and to archive the findings of clinical cases. In conclusion, the ReVISION method may provide novel insights into global and also segmental RV function by defining parameters that are potentially more sensitive and predictive compared to conventional echocardiographic measurements in the context of different cardiac diseases.

DATA AVAILABILITY STATEMENT

The raw data supporting the conclusions of this article will be made available by the authors, without undue reservation.

ETHICS STATEMENT

The study protocol conforms with the principles outlined in the Declaration of Helsinki and the local regulatory and data protection standards. All subjects in the analyzed database were enrolled as part of prospective studies (each approved by the Regional and Institutional Committee of Science and Research Ethics, approval no. 13687-0/2011-EKU and 034309-006/2014/OTIG) and provided written informed consent prior to enrollment to the archiving and analysis of their datasets and the publication of subsequent results.

AUTHOR CONTRIBUTIONS

MT contributed significantly to the conceptualization of the ReVISION method, participated in the software development, analyzed the data, interpreted the results, and was a major contributor to writing the manuscript. LSt and MC were major developers of the ReVISION method and helped in writing the technical section of the paper. ÁB developed the cardiac magnetic resonance imaging-based mesh reconstruction algorithm and was a major contributor to writing the technical

section of the paper. BL performed the 3D echocardiographic examinations and analyzed the 3D echocardiographic datasets. FS and LSz participated in the acquisition and post-processing of the cardiac magnetic resonance imaging datasets. AF participated in the analysis of 3D echocardiographic datasets and helped in reviewing the literature. HV supervised the acquisition and post-processing of cardiac magnetic resonance imaging datasets. ZT made a major contribution to the conceptualization of the ReVISION method, supervised the software development, and participated in the interpretation of the results and manuscript preparation. BM provided the institutional background for the research. AK made a major contribution to the conception of the ReVISION method, performed the 3D echocardiographic examinations, analyzed 3D echocardiographic datasets, supervised the software development, participated in the interpretation of the results, and drafted the manuscript. All authors read and approved the final version of the manuscript.

FUNDING

This work was supported by the National Research, Development, and Innovation Office of Hungary (NKFI; NVKP_16-1-2016-0017—National Heart Program and the Hungarian Artificial Intelligence National Laboratory), the New National Excellence Program (ÚNKP-20-3-II-SE-54), and the Thematic Excellence Program (2020-4.1.1.-TKP2020) of the Ministry for Innovation and Technology in Hungary, within the framework of the Therapeutic Development and Bioimaging programs of the Semmelweis University. AK was supported by the János Bolyai Research Scholarship of the Hungarian Academy of Sciences.

ACKNOWLEDGMENTS

The authors would like to express their gratitude to András Soós and Zsófia Gion for their help in the preparation of illustrations.

SUPPLEMENTARY MATERIAL

The Supplementary Material for this article can be found online at: <https://www.frontiersin.org/articles/10.3389/fcvm.2021.622118/full#supplementary-material>

Supplementary Figure 1 | Correlation and agreement between right ventricular end-diastolic volume, end-systolic volume, and ejection fraction assessed using the reconstructed cardiac magnetic resonance imaging-derived meshes and those computed using the dedicated cardiac magnetic resonance imaging post-processing software. Statistical tests: the correlations between the reconstructed mesh-based measurements and the values computed using the dedicated cardiac magnetic resonance imaging post-processing software were quantified using Pearson correlation coefficients, and Bland-Altman analyses were performed to assess the bias and limits of agreement. Paired Wilcoxon signed-rank test vs. null values was applied to test the significance of the bias. 3DE, 3D echocardiography; CMRI, cardiac magnetic resonance imaging; EDV, end-diastolic volume; EF, ejection fraction; ESV, end-systolic volume; LOA, limits of agreement.

REFERENCES

- Moceri P, Duchateau N, Baudouy D, Schouver ED, Leroy S, Squara F, et al. Three-dimensional right-ventricular regional deformation and survival in pulmonary hypertension. *Eur Heart J Cardiovasc Imaging*. (2018) 19:450–8. doi: 10.1093/ehjci/jex163
- Gorter TM, van Veldhuisen DJ, Bauersachs J, Borlaug BA, Celutkienė J, Coats AJS, et al. Right heart dysfunction and failure in heart failure with preserved ejection fraction: mechanisms and management. Position statement on behalf of the Heart Failure Association of the European Society of Cardiology. *Eur J Heart Failure*. (2018) 20:16–37. doi: 10.1002/ehfj.1029
- Kovacs A, Lakatos B, Tokodi M, Merkely B. Right ventricular mechanical pattern in health and disease: beyond longitudinal shortening. *Heart Fail Rev*. (2019) 24:511–20. doi: 10.1007/s10741-019-09778-1
- Surkova E, Muraru D, Genovese D, Aruta P, Palermo C, Badano LP. Relative prognostic importance of left and right ventricular ejection fraction in patients with cardiac diseases. *J Am Soc Echocardiogr*. (2019) 32:1407–15.e3. doi: 10.1016/j.echo.2019.06.009
- Warnes CA. Adult congenital heart disease: importance of the right ventricle. *J Am Coll Cardiol*. (2009) 54:1903–10. doi: 10.1016/j.jacc.2009.06.048
- Lampert BC, Teuteberg JJ. Right ventricular failure after left ventricular assist devices. *J Heart Lung Transplant*. (2015) 34:1123–30. doi: 10.1016/j.healun.2015.06.015
- Kalogeropoulos AP, Al-Anbari R, Pekarek A, Wittersheim K, Pernetz MA, Hampton A, et al. The right ventricular function after left ventricular assist device (RVF-LVAD) study: rationale and preliminary results. *Eur Heart J Cardiovasc Imaging*. (2016) 17:429–37. doi: 10.1093/ehjci/jev162
- Haddad F, Hunt SA, Rosenthal DN, Murphy DJ. Right ventricular function in cardiovascular disease, part I. *Circulation*. (2008) 117:1436–48. doi: 10.1161/CIRCULATIONAHA.107.653576
- Lakatos B, Tóser Z, Tokodi M, Doronina A, Kosztin A, Muraru D, et al. Quantification of the relative contribution of the different right ventricular wall motion components to right ventricular ejection fraction: the ReVISION method. *Cardiovasc Ultrasound*. (2017) 15:8. doi: 10.1186/s12947-017-0100-0
- Lakatos BK, Tokodi M, Assabiny A, Tóser Z, Kosztin A, Doronina A, et al. Dominance of free wall radial motion in global right ventricular function of heart transplant recipients. *Clin Transplant*. (2018) 32:e13192. doi: 10.1111/ctr.13192
- Lakatos BK, Kiss O, Tokodi M, Tóser Z, Sydó N, Merkely G, et al. Exercise-induced shift in right ventricular contraction pattern: novel marker of athlete's heart? *Am J Physiol Heart Circ Physiol*. (2018) 315:H1640–8. doi: 10.1152/ajpheart.00304.2018
- Lakatos BK, Nabeshima Y, Tokodi M, Nagata Y, Tóser Z, Otani K, et al. Importance of nonlongitudinal motion components in right ventricular function: three-dimensional echocardiographic study in healthy volunteers. *J Am Soc Echocardiogr*. (2020) 33:995–1005.e1. doi: 10.1016/j.echo.2020.04.002
- Tokodi M, Németh E, Lakatos BK, Kispál E, Tóser Z, Staub L, et al. Right ventricular mechanical pattern in patients undergoing mitral valve surgery: a predictor of post-operative dysfunction? *ESC Heart Failure*. (2020) 7:1246–56. doi: 10.1002/ehf2.12682
- Cerqueira MD, Weissman NJ, Dilsizian V, Jacobs AK, Kaul S, Laskey WK, et al. Standardized myocardial segmentation and nomenclature for tomographic imaging of the heart. A statement for healthcare professionals from the Cardiac Imaging Committee of the Council on Clinical Cardiology of the American Heart Association. *Circulation*. (2002) 105:539–42. doi: 10.1081/JCMR-120003946
- Phelan D, Collier P, Thavendiranathan P, Popovic ZB, Hanna M, Plana JC, et al. Relative apical sparing of longitudinal strain using two-dimensional speckle-tracking echocardiography is both sensitive and specific for the diagnosis of cardiac amyloidosis. *Heart*. (2012) 98:1442–8. doi: 10.1136/heartjnl-2012-302353
- Czibalmos C, Csécs I, Dohy Z, Toth A, Suhai FI, Mussigbrodt A, et al. Cardiac magnetic resonance based deformation imaging: role of feature tracking in athletes with suspected arrhythmogenic right ventricular cardiomyopathy. *Int J Cardiovasc Imaging*. (2019) 35:529–38. doi: 10.1007/s10554-018-1478-y
- Corrado D, van Tintelen PJ, McKenna WJ, Hauer RNW, Anastakis A, Asimaki A, et al. Arrhythmogenic right ventricular cardiomyopathy: evaluation of the current diagnostic criteria and differential diagnosis. *Eur Heart J*. (2019) 41:1414–29. doi: 10.1093/eurheartj/ehz669
- Boggs PT, Roger JE. Orthogonal distance regression. *Contemp Math*. (1990) 112:183–94. doi: 10.1090/conm/112/1087109
- Cha Z, Tsuhan C. Efficient feature extraction for 2D/3D objects in mesh representation. In: *Proceedings 2001 International Conference on Image Processing (Cat No01CH37205)*, Thessaloniki (2001).
- World Medical Association. World Medical Association Declaration of Helsinki: ethical principles for medical research involving human subjects. *JAMA*. (2013) 310:2191–4. doi: 10.1001/jama.2013.281053
- Bingol OR, Krishnamurthy A. NURBS-Python: an open-source object-oriented NURBS modeling framework in Python. *SoftwareX*. (2019) 9:85–94. doi: 10.1016/j.softx.2018.12.005
- Paul Chew L. Constrained delaunay triangulations. *Algorithmica*. (1989) 4:97–108. doi: 10.1007/BF01553881
- Muraru D, Spadotto V, Cecchetto A, Romeo G, Aruta P, Ermacora D, et al. New speckle-tracking algorithm for right ventricular volume analysis from three-dimensional echocardiographic data sets: validation with cardiac magnetic resonance and comparison with the previous analysis tool. *Eur Heart J Cardiovasc Imaging*. (2016) 17:1279–89. doi: 10.1093/ehjci/jev309
- Nagata Y, Wu VC, Kado Y, Otani K, Lin FC, Otsuji Y, et al. Prognostic value of right ventricular ejection fraction assessed by transthoracic 3D echocardiography. *Circ Cardiovasc Imaging*. (2017) 10:e005384. doi: 10.1161/CIRCIMAGING.116.005384
- Nochioka K, Querejeta Roca G, Claggett B, Biering-Sorensen T, Matsushita K, Hung CL, et al. Right ventricular function, right ventricular-pulmonary artery coupling, and heart failure risk in 4 US communities: the atherosclerosis risk in communities (ARIC) study. *JAMA Cardiol*. (2018) 3:939–48. doi: 10.1001/jamacardio.2018.2454
- Satriano A, Pournazeri P, Hirani N, Helmersen D, Thakrar M, Weatherald J, et al. Characterization of right ventricular deformation in pulmonary arterial hypertension using three-dimensional principal strain analysis. *J Am Soc Echocardiogr*. (2019) 32:385–93. doi: 10.1016/j.echo.2018.10.001
- Addetia K, Maffessanti F, Yamat M, Weinert L, Narang A, Freed BH, et al. Three-dimensional echocardiography-based analysis of right ventricular shape in pulmonary arterial hypertension. *Eur Heart J Cardiovasc Imaging*. (2016) 17:564–75. doi: 10.1093/ehjci/jev171
- Kind T, Mauritz GJ, Marcus JT, van de Veerdonk M, Westerhof N, Vonk-Noordegraaf A. Right ventricular ejection fraction is better reflected by transverse rather than longitudinal wall motion in pulmonary hypertension. *J Cardiovasc Magn Reson*. (2010) 12:35. doi: 10.1186/1532-429X-12-35
- Addetia K, Maffessanti F, Muraru D, Singh A, Surkova E, Mor-Avi V, et al. Morphologic analysis of the normal right ventricle using three-dimensional echocardiography-derived curvature indices. *J Am Soc Echocardiogr*. (2018) 31:614–23. doi: 10.1016/j.echo.2017.12.009
- Bernardino G, Hodzic A, Langet H, Craene MD, Ballester MAG, Saloux E, et al. Volumetric parcellation of the right ventricle for regional geometric and functional assessment. *arXiv*. (2020). abs/2003.08423.
- Seo Y, Ishizu T, Ieda M, Ohte N. Right ventricular three-dimensional echocardiography: the current status and future perspectives. *J Echocardiogr*. (2020) 18:149–59. doi: 10.1007/s12574-020-00468-8
- Ishizu T, Seo Y, Atsumi A, Tanaka YO, Yamamoto M, Machino-Ohtsuka T, et al. Global and regional right ventricular function assessed by novel three-dimensional speckle-tracking echocardiography. *J Am Soc Echocardiogr*. (2017) 30:1203–13. doi: 10.1016/j.echo.2017.08.007
- Olah A, Kovacs A, Lux A, Tokodi M, Braun S, Lakatos BK, et al. Characterization of the dynamic changes in left ventricular morphology and function induced by exercise training and detraining. *Int J Cardiol*. (2019) 277:178–85. doi: 10.1016/j.ijcard.2018.10.092
- Maffessanti F, Gripari P, Tamborini G, Muratori M, Fusini L, Alamanni F, et al. Evaluation of right ventricular systolic function after mitral valve repair: a two-dimensional Doppler, speckle-tracking, and three-dimensional echocardiographic study. *J Am Soc Echocardiogr*. (2012) 25:701–8. doi: 10.1016/j.echo.2012.03.017
- Raina A, Vaidya A, Gertz ZM, Susan C, Forfia PR. Marked changes in right ventricular contractile pattern after cardiothoracic surgery: implications for post-surgical assessment of right ventricular function. *J Heart Lung Transplant*. (2013) 32:777–83. doi: 10.1016/j.healun.2013.05.004
- Keyl C, Schneider J, Beyersdorf F, Ruile P, Siepe M, Pioch K, et al. Right ventricular function after aortic valve replacement: a pilot study comparing

- surgical and transcatheter procedures using 3D echocardiography. *Eur J Cardiothorac Surg.* (2016) 49:966–71. doi: 10.1093/ejcts/ezv227
37. Kovacs A, Lakatos B, Nemeth E, Merkely B. Response to Ivey-Miranda and Farrero-Torres “is there dominance of free wall radial motion in global right ventricular function in heart transplant recipients or in all heart surgery patients?”. *Clin Transplant.* (2018) 32:e13286. doi: 10.1111/ctr.13286

Conflict of Interest: ZT is a cofounder and CEO of Argus Cognitive, Inc. (the company developing the ReVISION software), holds equity in the company, and receives financial compensation for his work. LSt and MC are employees of Argus Cognitive and receive compensation for their work.

The remaining authors declare that the research was conducted in the absence of any commercial or financial relationships that could be construed as a potential conflict of interest.

Copyright © 2021 Tokodi, Staub, Budai, Lakatos, Csákvári, Suhai, Szabó, Fábián, Vágó, Tóser, Merkely and Kovács. This is an open-access article distributed under the terms of the Creative Commons Attribution License (CC BY). The use, distribution or reproduction in other forums is permitted, provided the original author(s) and the copyright owner(s) are credited and that the original publication in this journal is cited, in accordance with accepted academic practice. No use, distribution or reproduction is permitted which does not comply with these terms.



OPEN ACCESS

Edited by:

Takashi Muramatsu,
Fujita Health University
Hospital, Japan

Reviewed by:

Rob Krams,
Queen Mary University of London,
United Kingdom
Christos Bourantas,
University College London,
United Kingdom

*Correspondence:

Georgios Sianos
gsianos@auth.gr

*ORCID:

Georgios Sofidis
orcid.org/0000-0001-5802-0379
Efstratios Karagiannidis
orcid.org/0000-0001-8328-5942
Andreas S Papazoglou
orcid.org/0000-0003-4981-8121
Dimitrios V. Moysidis
orcid.org/0000-0001-9083-0267
Anastasios Kartas
orcid.org/0000-0002-1170-9133
Nikolaos Stalikas
orcid.org/0000-0002-0190-5392
Eleftherios Panteris
orcid.org/0000-0002-5846-388X
Kleoniki Keklikoglou
orcid.org/0000-0002-6693-2033
Evangelia Chatzinikolaou
orcid.org/0000-0002-7171-5105
Georgios Sianos
orcid.org/0000-0002-3042-0757

Specialty section:

This article was submitted to
Cardiovascular Imaging,
a section of the journal
Frontiers in Cardiovascular Medicine

Received: 24 December 2020

Accepted: 22 February 2021

Published: 21 April 2021

Micro-CT-Based Quantification of Extracted Thrombus Burden Characteristics and Association With Angiographic Outcomes in Patients With ST-Elevation Myocardial Infarction: The QUEST-STEMI Study

Efstratios Karagiannidis^{1†}, Andreas S Papazoglou^{1†}, Georgios Sofidis^{1†}, Evangelia Chatzinikolaou^{2†}, Kleoniki Keklikoglou^{2,3†}, Eleftherios Panteris^{4†}, Anastasios Kartas^{1†}, Nikolaos Stalikas^{1†}, Thomas Zegkos¹, Fotios Girtovitis⁵, Dimitrios V. Moysidis^{1†}, Leandros Stefanopoulos⁶, Kleanthis Koupidis⁷, Stavros Hadjimiltiades¹, George Giannakoulas¹, Christos Arvanitidis^{2,8}, James S. Michaelson⁹, Haralambos Karvounis¹ and Georgios Sianos^{1*†}

¹ First Department of Cardiology, AHEPA University Hospital, Aristotle University of Thessaloniki, Thessaloniki, Greece,

² Hellenic Centre for Marine Research, Institute of Marine Biology, Biotechnology, and Aquaculture, Heraklion, Greece,

³ Biology Department, University of Crete, Heraklion, Greece, ⁴ Laboratory of Forensic Medicine and Toxicology, School of Medicine, Aristotle University of Thessaloniki, Thessaloniki, Greece, ⁵ Blood Centre, AHEPA University Hospital, Thessaloniki, Greece, ⁶ Lab of Computing, Medical Informatics, and Biomedical Imaging Technologies, Aristotle University of Thessaloniki, Thessaloniki, Greece, ⁷ School of Mathematics, Aristotle University of Thessaloniki, Thessaloniki, Greece, ⁸ LifeWatch ERIC, Sector II-II, Seville, Spain, ⁹ Massachusetts General Hospital and Harvard Medical School, Boston, MA, United States

Background: Angiographic detection of thrombus in STEMI is associated with adverse outcomes. However, routine thrombus aspiration failed to demonstrate the anticipated benefit. Hence, management of high coronary thrombus burden remains challenging. We sought to assess for the first time extracted thrombotic material characteristics utilizing micro-computed tomography (micro-CT).

Methods: One hundred thirteen STEMI patients undergoing thrombus aspiration were enrolled. Micro-CT was undertaken to quantify retrieved thrombus volume, surface, and density. Correlation of these indices with angiographic and electrocardiographic outcomes was performed.

Results: Mean aspirated thrombus volume, surface, and density (\pm standard deviation) were $15.71 \pm 20.10 \text{ mm}^3$, $302.89 \pm 692.54 \text{ mm}^2$, and 3139.04 ± 901.88 Hounsfield units, respectively. Aspirated volume and surface were significantly higher ($p < 0.001$) in patients with higher angiographic thrombus burden. After multivariable analysis, independent predictors for thrombus volume were reference vessel diameter (RVD) ($p = 0.011$), right coronary artery (RCA) ($p = 0.039$), and smoking ($p = 0.027$), whereas RVD ($p = 0.018$) and RCA ($p = 0.019$) were predictive for thrombus surface. Thrombus volume and surface were independently associated with distal embolization ($p = 0.007$ and $p = 0.028$, respectively), no-reflow phenomenon ($p = 0.002$ and $p = 0.006$, respectively),

and angiographically evident residual thrombus ($p = 0.007$ and $p = 0.002$, respectively). Higher thrombus density was correlated with worse pre-procedural TIMI flow ($p < 0.001$). Patients with higher aspirated volume and surface developed less ST resolution ($p = 0.042$ and $p = 0.023$, respectively).

Conclusions: Angiographic outcomes linked with worse prognosis were more frequent among patients with larger extracted thrombus. Despite retrieving larger thrombus load in these patients, current thrombectomy devices fail to deal with thrombotic material adequately. Further studies of novel thrombus aspiration technologies are warranted to improve patient outcomes.

Clinical Trial Registration: QUEST-STEMI trial ClinicalTrials.gov number: NCT03429608 Date of registration: February 12, 2018. The study was prospectively registered.

Keywords: micro-computed tomography, thrombus aspiration, thrombus, ST-elevation myocardial infarction, interventional cardiology

INTRODUCTION

Despite the tremendous progress in cardiovascular medicine over the last decades, ST-segment elevation myocardial infarction (STEMI) still remains one of the leading causes of mortality worldwide (1). Intracoronary thrombosis developed after plaque erosion or rupture, causing partial or total occlusion of coronary vessels which is the most common underlying pathophysiologic mechanism in STEMI. Thrombus burden (TB) is an important prognostic determinant (2), as it has been associated with an increase in the rate of major adverse cardiac and cerebrovascular events (MACCE) (3).

The optimal therapy for STEMI is timely performed primary percutaneous coronary intervention (pPCI) (4). However, myocardial recovery and restoration of epicardial coronary blood flow are often suboptimal due to thrombus embolization (5), leading to perturbed microvascular perfusion and obstruction of the microvasculature.

Manual aspiration thrombectomy (MATH) was first described in 1980 as a useful adjunctive therapy to conventional PCI with the potential to remove the thrombotic component of the culprit lesion (6, 7). However, large randomized controlled trials (RCTs) and meta-analyses failed to demonstrate the theoretically anticipated benefit for routine MATH, suggesting lack of synergy between MATH and pPCI with a subsequent increase in the risk of stroke (8–11). Therefore, current ESC guidelines do not recommend routine thrombus aspiration (class of recommendation IIIA) (12).

Several hypotheses might serve to explain why MATH did not succeed in the majority of recent trials, such as the presence of small amount of thrombus at the culprit

lesion before thrombectomy or of large amount of residual thrombus after thrombectomy (13). Indeed, it was shown that the elective application of MATH in certain cases with large thrombus burden (9, 14, 15) as a bail-out therapy showed some cardiovascular (CV) benefit (reduced CV death), which was counterbalanced by an increased risk of stroke. Previous studies utilizing optical coherence tomography (OCT) have shown that there is substantial amount of residual thrombus even after thrombectomy (13, 14, 16). Interestingly, STEMI patients with greater residual TB after MATH had microvascular dysfunction and more significant myocardial damage than those with smaller residual TB (14).

Thus, the prognostic significance of initial angiographic TB and post-aspiration residual TB has already been investigated. However, evidence on the association of extracted thrombotic material characteristics with post-pPCI angiographic outcomes is lacking.

Micro-computed tomography (micro-CT) is an emerging technology with high spatial resolution in the submicrometer range, which is increasingly employed in medicinal studies (17–20). Despite being initially used for skeletal imaging, the development of contrast agents, which amplify the low intrinsic contrast of soft-tissues in X-ray absorption, facilitates detailed micro-CT imaging of soft tissues (21). Since micro-CT allows non-destructive 3D imaging of both the internal and external structures of samples, exceeding the capabilities of histomorphometric analysis (21), it can be employed to accurately quantify extracted thrombotic material characteristics, which have been subjective to date. These novel imaging parameters could be used to improve patient risk stratification, enabling individualized treatment of patients with STEMI.

MATERIALS AND METHODS

The design of the QUEST-STEMI study has been previously described (22).

Abbreviations: ECG, Electrocardiogram; MACCE, Major Adverse Cardiac and Cerebrovascular events; MATH, Manual Aspiration Thrombectomy; MBG, Myocardial Blush Grade; Micro-CT, Micro-Computed Tomography; OCT, Optical Coherence Tomography; PCI, Percutaneous Coronary Intervention; RVD, Reference Vessel Diameter; STEMI, ST-Elevated Myocardial Infarction; TIMI, Thrombolysis In Myocardial Infarction; TB, Thrombus Burden.

Study Population and PCI Procedures

QUEST-STEMI (ClinicalTrials.gov Identifier: NCT03429608) is a prospective cohort trial including patients, who presented to AHEPA University Hospital with STEMI and underwent primary PCI and MATH at the discretion of the treating physician within 12 h of symptom onset. The eligibility criteria are depicted in **Table 1**. The Scientific Committee of AHEPA Hospital approved the study protocol, and all trial procedures comply with the principles set by the Declaration of Helsinki (23). Each participant provided written informed consent before being enrolled in the study.

Angiographic Analysis, ECG, and Thrombus Aspiration Procedure

Before primary PCI, each patient received guideline-directed pharmaceutical therapy (unfractionated heparin (100 IU/kg) and a loading dose of aspirin (325 mg) and either ticagrelor (180 mg) or clopidogrel (600 mg) (12). Intravenous GP IIb/IIIa inhibitors were administered at the interventionalist's discretion. Thrombus aspiration was undertaken according to standard practices, as described (12, 22). Briefly, after crossing the lesion with a wire, the thrombectomy catheter was advanced proximal to the occluded segment. Continuous manual suction was recommended *via* a proximal-to-distal approach, so that active aspiration was initiated before the catheter crossed the thrombotic occlusion (8, 10). The thrombectomy catheter was slowly passed through the lesion multiple times (at least two), so that a minimum of 40 cc of blood and material were extracted.

A 12-lead ECG was obtained at presentation and 90 min post-intervention. ST-segment deviation was assessed, as previously described (24). Based on the degree of resolution of ST-segment elevation, patients were classified into three groups: (1) complete ST resolution (>70%); (2) partial ST resolution (30–70%); and (3) absent ST resolution (<30%).

Coronary angiograms were analyzed by two experienced interventional cardiologists (GSi, GSo). Angiographic thrombus burden was assessed based on the modified TIMI (thrombolysis in myocardial infarction) thrombus classification scale by Sianos et al. (25). According to this classification, patients with TIMI Grade 5 thrombus are classified to another thrombus category (G0–G4) post-flow achievement with either guidewire crossing or a small balloon. Furthermore, baseline, post-MATH, and post-procedural antegrade coronary flow was evaluated based on TIMI classification (26). Reference vessel diameter (RVD), minimum luminal diameter, percentage of diameter stenosis, and lesion length were also calculated using quantitative coronary angiography. Presence of distal embolization (21) and angiographically evident residual thrombus were also recorded. For the present analysis, a patient was regarded to have angiographically evident residual thrombus, if modified TIMI thrombus grades 2–4 were present (27).

Micro-CT Analysis

The detailed protocol for the micro-CT scanning and analysis of aspirated thrombi has been previously described (22). Briefly, extracted thrombotic material was initially preserved in 10% formalin for 24 h and then successively dehydrated in ethanol

TABLE 1 | Eligibility criteria for the QUEST STEMI study.

Inclusion criteria	Exclusion criteria
<ul style="list-style-type: none"> • Patients with symptoms of myocardial infarction for >30 min • ST-segment elevation in ECG • Patients undergoing primary PCI and manual aspiration thrombectomy (at the discretion of the treating physician) within 12 h from symptom onset • Written informed consent 	<ul style="list-style-type: none"> • Patients who have received fibrinolytic therapy for index STEMI event • Known intolerance to heparin or anti-platelet medication

solutions up to 70% and stained using 0.3% phosphotungstic acid (PTA) in 70% ethanol according to Metscher's protocol (28). All scans were performed with a SkyScan 1172 microtomograph (Bruker, Kontich, Belgium, **Figure 1A**) at the Hellenic Center for Marine Research (HCMR) (48 kV, 204 μ A, no filter, 360° rotation). Projection images were reconstructed into cross sections using SkyScan's NRecon software (Bruker, Kontich, Belgium). The cross-section images were loaded into the software CT Analyser v.1.14.4.1 (CTAn, Bruker, Kontich, Belgium) to extract measurements for the volume and density of thrombi (**Figures 1B,C**) as mean grayscale values (\pm Standard Deviation), which were also converted to Hounsfield units (HU). The presence of different cell types within a thrombus was also quantified by comparing their density with *in-vitro* produced thrombi with known homogeneous composition, as described (22). The range of grayscale values used for the full thrombus specimen was 25–255. Red (erythrocyte-rich) thrombi showed densities 80–255 grayscale values, whereas clots with the highest platelet content (white thrombi) had densities in the range 25–80 (**Figure 2**). Analysis of the thrombi was undertaken by two independent blinded assessors.

STATISTICAL ANALYSIS

Statistical analysis was performed using SPSS v26 (SPSS software, Chicago, IL, USA) software. Continuous data are presented as mean and standard deviation, whereas categorical variables are expressed as counts and percentages. The inter- and intraobserver reproducibility of thrombus measurements were assessed based on data obtained from a subset of 34 subjects (30% of study population), performing Spearman's correlations, and the intraclass correlation coefficient (ICC) (29, 30).

The data were analyzed by non-parametric tests as indicated by the Shapiro–Wilk-test for normality. Group differences were tested using the Wilcoxon–Mann–Whitney-test for continuous measures. The Kruskal–Wallis *H*-test was used to compare between two or more groups of an independent variable on a continuous or ordinal dependent variable. Univariable analysis was initially carried out to clarify the association of demographic characteristics, history of smoking, medical history, statin, antiplatelet or anticoagulant use, pain-to-balloon time, pre-procedural TIMI flow, RVD, and culprit vessel with extracted

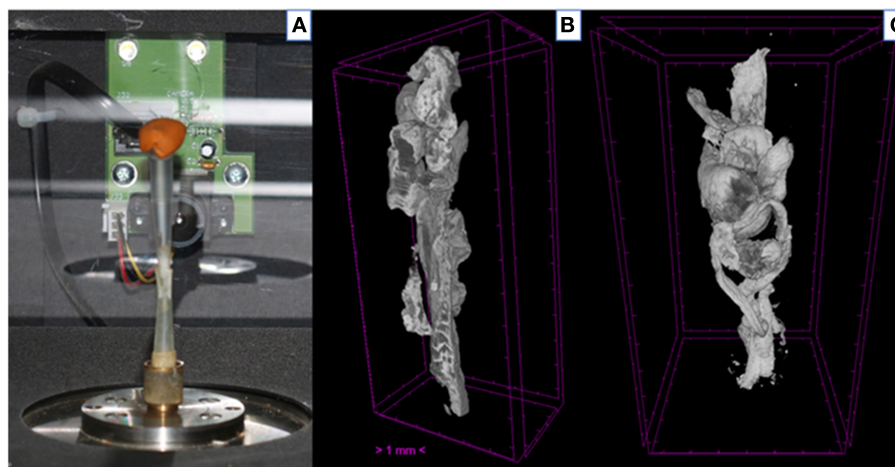


FIGURE 1 | Thrombus analysis via micro-computed tomography. **(A)** Thrombi are mounted on a specific head inside SkyScan 1172; **(B,C)** Representative computer generated renderings of thrombi. Clots were stained using 0.3% phosphotungstic acid and scanned via SkyScan 1172. NRecon (Bruker, Kontich, Belgium) software was used for the reconstruction of the projections.

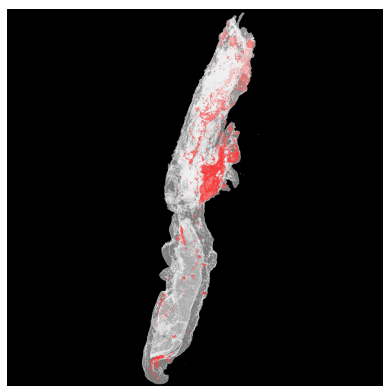


FIGURE 2 | 3D color visualization of a thrombus sample. A 3D model of a thrombus sample was created using CTAn software (Bruker, Kontich, Belgium), and color visualization was performed via CTVol software (Bruker, Kontich, Belgium). Erythrocyte-rich regions were rendered in red, whereas platelet-rich regions were rendered in white.

thrombus characteristics (volume, surface, and density) and with angiographic and electrocardiographic outcomes. The variables with statistical significance (p -value < 0.05) were included in the multivariable regression models.

Linear and logistic regression using stratified bootstrapping to account for the non-parametric nature of the data was used to identify independent predictors of thrombus characteristics and of angiographic outcomes. Correlation coefficients were investigated to address potential multicollinearity among the predicting variables in the created regression models (31). Multivariable logistic regression models, including both volume and surface as independent variables, demonstrated potential multicollinearity (correlation coefficients higher than 0.89). Therefore, thrombus volume and surface were not included

in the same model as independent predictors. R , R^2 , Durbin-Watson, and Nagelkerke R^2 metrics along with p -values are reported for the linear and logistic models, respectively.

RESULTS

Study Population

During the study period, 113 consecutive patients were enrolled based on the study eligibility criteria. The baseline clinical and angiographic characteristics are shown in **Tables 2, 3**. Mean age was 60.05 (± 12.12) years, and 89 patients (78.8%) were male. Smoking was reported by 69.9% of participants, and reperfusion was achieved on an average 330.2 (± 245.74) min from symptom onset. A no-reflow phenomenon was observed in 13.3% of patients and distal embolization in 23.9% of the participants. Residual thrombus was angiographically evident in 14 patients (12.4%), whereas MBG was equal to 0 or 1 in 36 (31.86%) of patients.

Micro-CT Findings on Extracted Thrombus Burden

Micro-tomography effectively quantified the volume, surface, and density of all aspirated thrombi. No sample disintegration was observed, and hence all thrombi were suitable for micro-CT scanning. The mean extracted thrombus volume, surface, and density were 15.71 (± 20.10) mm³, 302.89 (± 692.54) mm², and 3139.04 (± 901.88) HU, respectively.

Intraobserver and interobserver reliabilities were high for all thrombus volume (interobserver: 0.995; intraobserver: 1.000), thrombus surface (interobserver: 0.999; intraobserver: 0.999), and thrombus density (interobserver: 0.982; intraobserver: 0.982). Interclass correlation coefficients for thrombus volume, surface, and density were equal to 0.995 (95% C.I.: 0.981–0.998), 0.995 (95% C.I.: 0.991–0.996), and 0.987 (95% C.I.: 0.966–0.993), respectively.

TABLE 2 | Demographics and baseline characteristics.

Demographics and baseline characteristics	Mean (\pm SD) for continuous variables; count (<i>n</i>) with percentage (%) for categorical variables
Age	60 (\pm 12)
Male <i>n</i> (%)	89 (78.80%)
Medical history: <i>N</i> (%)	
A. Smoking	79 (69.90%)
B. Hypertension	37 (32.70%)
C. Dyslipidemia	23 (20.40%)
D. Diabetes mellitus	19 (16.80%)
E. Coronary artery disease	17 (15.00%)
Pain-to-balloon time (mean, range of minutes)	330 (30–720)
Prior medication <i>N</i> (%)	
I. Aspirin	14 (12.40%)
II. Clopidogrel	6 (5.30%)
III. Statins	19 (16.80%)
IV. Anti-coagulant	3 (2.70%)
V. Beta blockers	13 (11.50%)

Association of Extracted Thrombus Burden Characteristics With Intracoronary Thrombus Classification

Aspirated thrombus volume and surface were significantly higher (p -value < 0.001) in patients with higher intracoronary angiographic thrombus burden according to modified TIMI thrombus grade classification (**Figure 3A**). Similarly, aspirated thrombus density analysis revealed that higher values of density (indicating a higher proportion of erythrocytes within the clot) were significantly correlated with larger intracoronary angiographic thrombus burden according to modified TIMI thrombus grade classification (p -value = 0.037).

Determinants of Extracted Thrombus Burden Characteristics

Univariable analysis revealed that male gender, history of smoking, RVD, and right coronary artery (RCA) as the culprit vessel are significantly associated with higher extracted thrombus volume (p -values = 0.044, 0.001, 0.021, 0.017, respectively). Preprocedural TIMI flow was not associated with aspirated volume (p -value = 0.794). On bootstrapped multivariable linear regression analysis (**Table 4**), RVD (p -value = 0.011), RCA as the culprit vessel (p -value = 0.039), and history of smoking (p -value = 0.027) were independent predictors of higher extracted thrombus volume (**Figure 3B**).

Higher extracted thrombus surface was—both univariably and multivariably (**Table 4**)—significantly linked with larger RVD (p -value = 0.018) and RCA as the culprit vessel (p -value = 0.019; **Figure 3H**), whereas the association of surface with preprocedural TIMI flow was not significant (p -value = 0.860).

It is worth mentioning that the Durbin–Watson values of our regression models (for volume: 1.240 and for surface: 1.320)

TABLE 3 | Percutaneous coronary intervention procedure details and angiographic outcomes.

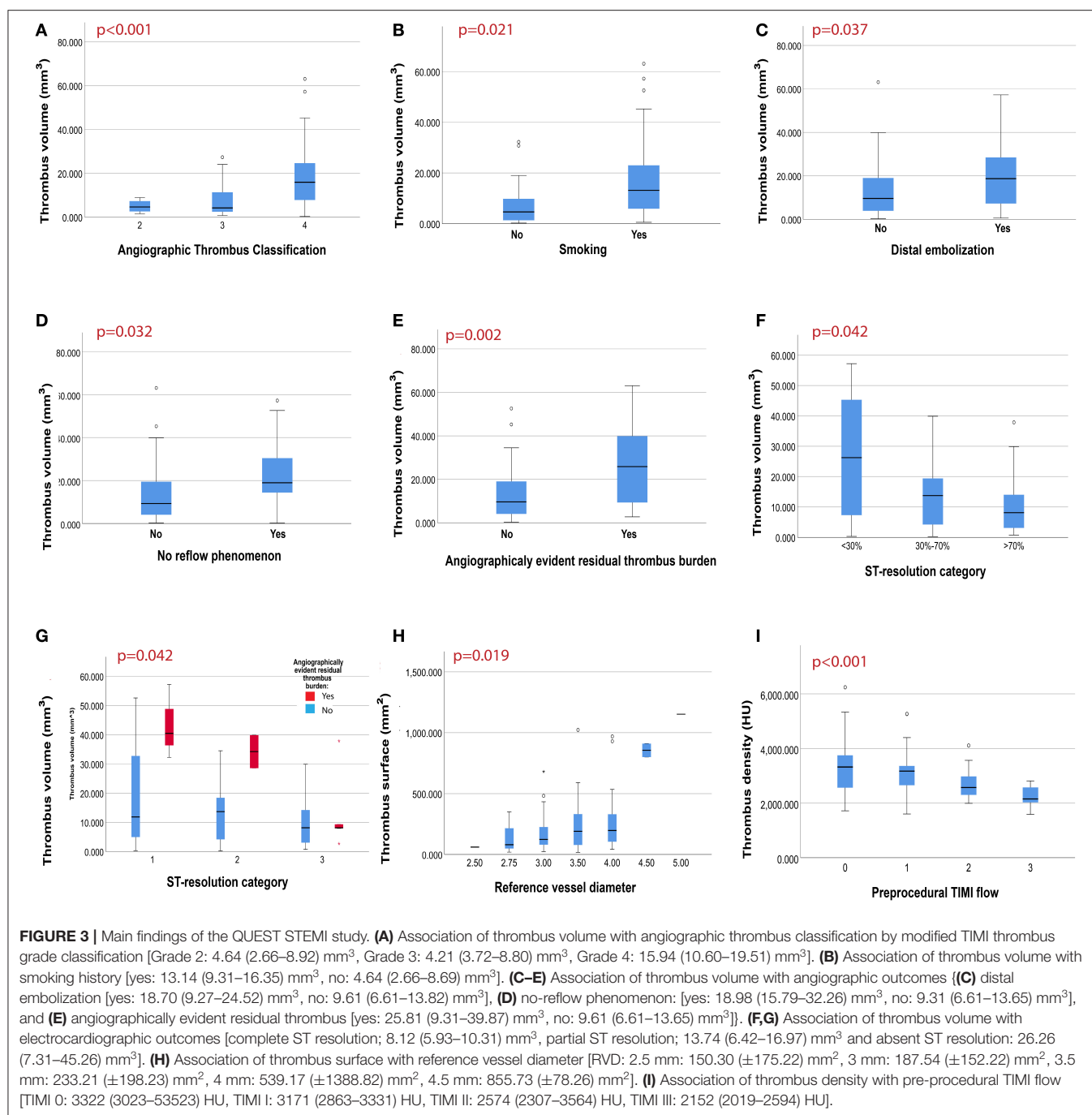
Infarct-related artery	
LM	2 (1.80%)
LAD	47 (42.34%)
LCx	17 (15.32%)
RCA	45 (40.54%)
Pre-procedural TIMI flow	
0	69 (62.16%)
1	20 (18.01%)
2	10 (9.00%)
3	12 (10.81%)
Modified TIMI thrombus grade classification*	
0	0
1	0
2	5 (4.50%)
3	31 (27.93%)
4	61 (54.95%)
Use of stenting—no. (%)	103 (91.20%)
GP2B3A antagonist use	41 (36.30%)
Post-procedural results	
Final TIMI flow	
0	2 (1.80%)
1	1 (0.90%)
2	18 (16.22%)
3	90 (81.08%)
Angiographic no reflow	15 (13.30%)
Distal embolization	27 (23.90%)
Angiographically evident residual thrombus burden	14 (12.40%)
Myocardial blush grade*	
0	31 (27.43%)
1	5 (4.4%)
2	15 (13.27%)
3	47 (41.59%)
ECG: ST-segment resolution	
Complete (>70%)	59 (52.21%)
Partial (30–70%)	41 (36.28%)
Absent (<30%)	13 (11.50%)
In-hospital death	10 (8.85%)

*In 14 patients (12.61%), thrombus grade could not be classified according to modified TIMI thrombus grade classification (25), and in 15 patients (13.27%) myocardial blush grade could not be calculated, because of inadequate angiographic documentation.

PCI, percutaneous coronary intervention; LM, left main artery; LAD, left anterior descending; LCx, left circumflex; RCA, right coronary artery; IRA, infarct-related artery; TIMI, thrombolysis in myocardial infarction; ECG, electrocardiography, GP2B3A, glycoprotein IIb/IIIa.

indicate that there is no significant autocorrelation. Despite, R^2 -values of these models propose a significant, but weak, predictive value (R^2 < 0.300).

As for thrombus density, univariable analysis demonstrated that higher density values (erythrocyte-rich clots) were significantly correlated with worse pre-procedural TIMI flow (p -value < 0.001; **Figure 3I**), but no other statistically



significant predictor of density was revealed and hence no multivariable regression model was performed.

Association of Extracted Thrombus Burden Characteristics With Angiographic Outcomes

Higher extracted thrombus volume was significantly linked with angiographic outcomes suggestive of poor patient prognosis, including distal embolization (p -value = 0.037), and no reflow

phenomenon (p -value = 0.032; **Figures 3C,D**). Additionally, angiographic evidence of residual thrombus was more frequent in patients with larger aspirated thrombus (p -value = 0.002; **Figure 3E**). Furthermore, a non-significant trend toward worse MBG in patients with larger extracted thrombus volume was observed (p = 0.073), hence multivariable regression analysis on MBG was not performed.

Bootstrapped multivariable logistic regression analyses (**Table 5**) showed that aspirated thrombus volume remained an independent predictor for (i) distal embolization (p -value =

TABLE 4 | Determinants of extracted thrombus burden characteristics.

Determinants of TB	Volume		Surface	
	Univariable <i>p</i> -value and stand. beta	Multivariable <i>p</i> -value and stand. beta	Univariable <i>p</i> -value and stand. beta	Multivariable <i>p</i> -value and stand. beta
Gender	<i>p</i> = 0.044 <i>B</i> = −0.171	<i>p</i> = 0.419 <i>B</i> = −0.034	<i>p</i> = 0.081 <i>B</i> = −0.112	<i>p</i> = 0.729 <i>B</i> = −0.026
History of smoking	<i>p</i> = 0.001 <i>B</i> = 0.285	<i>p</i> = 0.027 <i>B</i> = 0.193	<i>p</i> = 0.003 <i>B</i> = 0.226	<i>p</i> = 0.193 <i>B</i> = 0.102
RVD	<i>p</i> = 0.021 <i>B</i> = 0.294	<i>p</i> = 0.011 <i>B</i> = 0.272	<i>p</i> = 0.014 <i>B</i> = 0.236	<i>p</i> = 0.018 <i>B</i> = 0.348
RCA as the culprit vessel	<i>p</i> = 0.017 <i>B</i> = 0.039	<i>p</i> = 0.039 <i>B</i> = 0.203	<i>p</i> = 0.012 <i>B</i> = −0.040	<i>p</i> = 0.019 <i>B</i> = 0.219
Model metrics:		Durbin–Watson = 1.240, <i>R</i> = 0.444, adjusted <i>R</i> ² = 0.164, <i>p</i> < 0.001		Durbin–Watson = 1.320, <i>R</i> = 0.495, adjusted <i>R</i> ² = 0.205, <i>p</i> < 0.001

RCA refers to right coronary artery and RVD refers to reference vessel diameter.

Bold *p*- and beta- values represent statistically significant outcomes of multivariable analysis.

0.007), (ii) no-reflow phenomenon (*p*-value = 0.002) together with smoking (*p* = 0.015), and (iii) angiographically evident residual thrombus (*p*-value = 0.007).

Similarly, bootstrapped multivariable logistic regression analysis on thrombus surface (Table 6) showed that the higher surface of aspirated thrombus was independently associated with (i) distal embolization (*p*-value = 0.028) along with age (*p*-value = 0.024), (ii) no-reflow phenomenon (*p*-value = 0.006) along with smoking (*p*-value = 0.021), and (iii) angiographically evident residual thrombus (*p*-value = 0.002) along with RCA (*p*-value = 0.016). On the other hand, multivariable regression analysis on MBG was not performed, since univariable analysis did not yield statistically significant results (*p*-value = 0.226).

Of note, multivariable model metrics indicate that the predictive models for angiographically evident residual thrombus explain the most of the variation compared with the other models (volume, smoking, age, RCA: Nagelkerke *R*² = 0.587 and surface, age, smoking, RCA: Nagelkerke *R*² = 0.544). However, the other multivariable models created for the prediction of distal embolization and no-reflow phenomenon have weak, but statistically significant, predictive value (Nagelkerke *R*² < 0.300).

Additionally, thrombus density was not associated with distal embolization (*p*-value = 0.246), no-reflow phenomenon (*p*-value = 0.859), angiographically evident residual thrombus (*p*-value = 0.549), or MBG (*p*-value = 0.155) in univariable analysis and therefore no multivariable regression model was executed.

Association of Extracted Thrombus Burden Characteristics With Electrocardiographic Outcomes

ECG analysis revealed that patients with higher aspirated thrombus volume and surface developed significantly less ST resolution (*p*-value = 0.042 and 0.023, respectively). After classifying patients by the presence of angiographically evident residual thrombus, ST-segment resolution was less in patients with angiographically evident residual thrombus and

particularly in those with higher aspirated thrombus volume (Figures 3E,G). On the other hand, no significant correlation between thrombus density and ST-segment resolution (*p*-value = 0.451) was observed.

DISCUSSION

To our knowledge, this is the first study to comprehensively evaluate extracted thrombotic material in patients with STEMI using micro-CT. The main findings of our study (Figure 4) were as follows: (1) thrombus analysis by micro-CT is feasible, reliable, and reproducible; (2) larger thrombus (higher volume and surface) was extracted in patients with high intracoronary TB under angiographic imaging; (3) higher aspirated thrombus volume and surface were associated with adverse angiographic outcomes, including distal embolization and no-reflow phenomenon; (4) angiographically evident residual thrombus was more frequent among patients with larger retrieved thrombus; (5) a non-significant trend (*p* = 0.073) toward worse myocardial blush grade in patients with larger extracted thrombus volume was observed; (6) aspirated thrombus volume and surface were significantly higher in smokers; and (7) worse pre-procedural TIMI flow was observed in thrombi with higher density.

Thrombus is a typical histopathologic characteristic of patients suffering from STEMI, which has been linked with worse patient prognosis (32). Qualitative and quantitative assessment of coronary thrombi has been a challenge. Recently, OCT has been employed to effectively quantify and characterize intracoronary thrombus before (15) and after (14, 16) MATH.

In this study, using a novel technology (micro-CT) we aimed to develop a methodology for the visualization and the quantitative 3D analysis of extracted thrombotic material in patients with STEMI undergoing MATH during pPCI. Micro-CT is an established imaging modality, which facilitates high-resolution, non-destructive visualization of 3D structures along with quantitative volumetric measurements and tissue

TABLE 5 | Association of extracted thrombus volume with angiographic outcomes.

Multivariable analysis*	Angiographic outcomes	1. Distal embolization		2. No-reflow		3. Angiographically evident residual thrombus	
		Standardized beta	p-value	Standardized beta	p-value	Standardized beta	p-value
	Volume	0.060	0.007	0.085	0.002	0.078	0.007
	Age	0.047	0.039	−0.025	0.421	−0.086	0.104
	Smoking	−0.125	0.866	1.75	0.015	0.499	0.540
	RCA as the culprit vessel	0.706	0.337	−0.522	0.345	−2.790	0.025
Model metrics:		$\chi^2 = 13.526$, Nagelkerke $R^2 = 0.182$, $p = 0.035$		$\chi^2 = 17.862$, Nagelkerke $R^2 = 0.282$, $p = 0.013$		$\chi^2 = 38.488$, Nagelkerke $R^2 = 0.587$, $p < 0.001$	

*Each column represents a different multivariable regression model for each dependent predictor (1: distal embolization, 2: no reflow phenomenon, and 3: angiographically evident residual thrombus). Each row represents a different independent predictor. Statistically significant results are marked in bold. RCA refers to right coronary artery.

TABLE 6 | Association of extracted thrombus surface with angiographic outcomes.

Multivariable analysis*	Angiographic outcomes	1. Distal embolization		2. No-reflow		3. Angiographically evident residual thrombus	
		Standardized beta	p-value	Standardized beta	p-value	Standardized beta	p-value
	Surface	0.002	0.028	0.003	0.006	0.005	0.002
	Age	0.051	0.024	−0.015	0.566	−0.059	0.121
	Smoking	−0.312	0.611	1.595	0.021	0.286	0.776
	RCA as the culprit vessel	0.222	0.672	−0.526	0.421	−2.824	0.016
Model metrics:		$\chi^2 = 13.908$, Nagelkerke $R^2 = 0.196$, $p = 0.042$		$\chi^2 = 13.025$, Nagelkerke $R^2 = 0.211$, $p = 0.011$		$\chi^2 = 35.119$, Nagelkerke $R^2 = 0.544$, $p < 0.001$	

*Each column represents a different multivariable regression model for each dependent predictor (1: distal embolization, 2: no reflow phenomenon, and 3: angiographically evident residual thrombus). Each row represents a different independent predictor. Statistically significant results are marked in bold. RCA refers to right coronary artery.

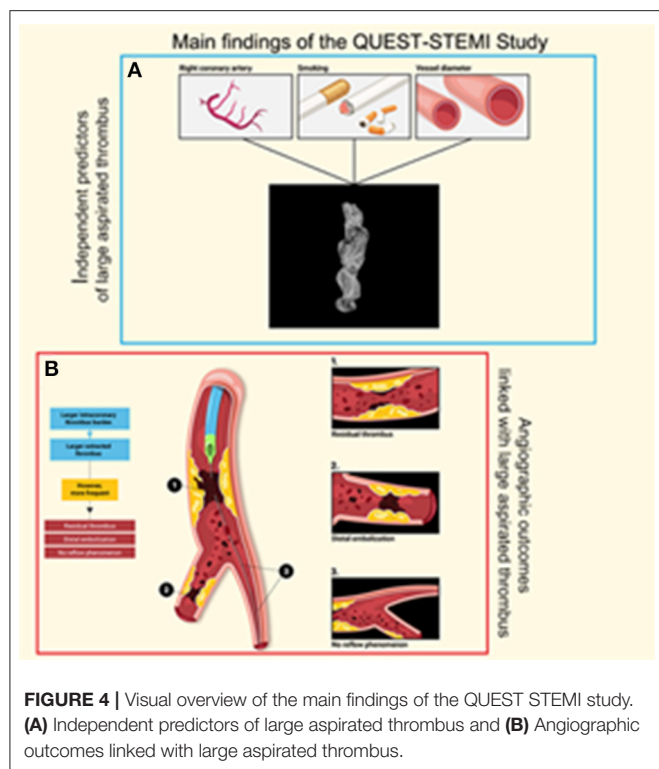
characterizations. Our results indicate that this method shows high reliability and repeatability for measuring the volume, surface, and density of extracted clots. Interestingly, micro-CT-quantified thrombus burden was strongly correlated with the intracoronary TB under angiographic imaging according to modified TIMI thrombus grade classification (25), suggesting that higher amount of thrombus is retrieved in patients with larger thrombotic load as seen in angiography.

In cases of large TB, fully optimizing stent expansion, while simultaneously preventing distal embolization and protecting the distal coronary vasculature, remains a clinical challenge, given the fact that routine MATH has not been proven effective (12). The inability of MATH to demonstrate a clinical benefit (8, 33, 34) might be the result of current MATH technology limitations, including inadequate retrieval of thrombus, thrombus embolization downstream prior to aspiration, and limited ability to deal with and not to dislodge large organized thrombotic material to other vascular territories during removal of the aspiration catheter (13). Interestingly, several trials using OCT demonstrated large residual thrombus after aspiration with current thrombus aspiration devices (16, 35). Hence, effective thrombus removal is crucial.

Our study is the first to show that angiographic outcomes, linked with worse prognosis, including distal embolization

(5), no-reflow phenomenon (36), and angiographically evident residual thrombus, are more frequent among patients with larger retrieved thrombus, as assessed quantitatively. Similarly, we observed a trend toward worse MBG in patients with larger aspirated thrombus volume. Moreover, in these patients a lower extent of ST-segment resolution was observed, which could be potentially attributed to a higher prevalence of residual thrombus. These findings suggest that, despite retrieving higher thrombus load, current MATH technology fails to adequately deal with thrombotic material in patients with large TB, who are at higher risk for adverse outcomes and who would theoretically benefit most from effective thrombus removal. Therefore, given the fact that residual thrombus due to ineffective thrombectomy has been associated with impaired microcirculatory perfusion and more significant myocardial injury (14), further studies are warranted to explore novel more effective thrombus aspiration technologies with the potential to improve patient outcomes (37).

Regarding variables correlated with larger extracted thrombus, we observed that aspirated thrombus volume was higher among smokers. This finding is in line with previous studies showing a greater thrombus burden in smokers (38). Smoking may induce a hypercoagulable state increasing blood viscosity (39) and promoting platelet aggregation and



thrombogenesis. These mechanisms could also explain our finding that smoking constitutes an independent risk factor for no-reflow phenomenon, although this relationship has not been yet confirmed (40). Apart from smoking, our data suggest that lumen diameter and RCA are predictive factors for larger retrieved thrombi. Larger coronary vessels can accommodate greater amounts of thrombotic material. Another potential explanation could be lower shear stress observed in vessels with greater diameter, as shear stress has been shown to influence the mechanisms supporting platelet aggregation and adhesion to the thrombogenic area through different pathways (41). Current literature also supports that thrombi in RCA tend to be larger possibly due to proximal propagation of thrombotic material related to fewer branch points (42, 43).

Moreover, micro-CT analysis of thrombus density demonstrated that patients with clots of high density (erythrocyte-rich thrombi) experienced worse pre-procedural TIMI flow. This finding is in line with previous histopathologic reports (44) showing that TIMI flow was worse in patients with red clots, compared to patients with white clots. A similar OCT-based study by Higuma et al. (35) showed that thrombi with greater erythrocyte-positive area were associated with worse angiographic outcomes.

LIMITATIONS

Our study has several limitations. Firstly, all patients were enrolled from a single center, which could limit the generalizability of our results. Secondly, the study lacks

intracoronary imaging data, thus the presence of residual thrombus was based on visual evaluation. Moreover, MATH was performed at the discretion of the interventionalist executing the pPCI and therefore the possibility of selection bias cannot be excluded. It is also possible that periprocedural IIB/IIIa inhibitor administration and operators' technique could have affected the outcomes of our study. However, all operators were strongly encouraged to follow the same thrombectomy procedure. Thus, derived outcomes should not have been substantially affected, by inconsistent aspiration techniques. Additionally, formalin used to preserve extracted clots may have caused thrombus shrinkage and subsequent underestimation of thrombus measurements. Similarly, sample staining with PTA has altered the measured density of the thrombotic material. However, both formalin fixation and PTA staining affected equally all specimens, since the same process was applied to all of them. Hence, we expect that these processes did not influence the comparability of our measurements. Last, this trial was not designed to investigate potential associations between micro-CT findings and hard clinical outcomes.

In conclusion, novel imaging techniques, such as micro-CT, can be employed for accurate and reproducible assessment of extracted thrombotic material, paving the way for more extensive research in this field. Our results indicate that the inadequacy of MATH to provide the anticipated benefit to patients with STEMI and large thrombotic load could be attributed to the limitations of current aspiration thrombectomy devices. A major question to be addressed by future studies is whether the development and optimization of more efficient MATH devices could facilitate effective thrombus removal and minimal residual thrombus burden and subsequently improve short- and long-term outcomes of coronary procedures in this challenging setting.

DATA AVAILABILITY STATEMENT

The datasets presented in this article are not readily available because data are available from corresponding author upon reasonable request and with permission of AHEPA University Hospital. Requests to access the datasets should be directed to Georgios Sianos, e-mail: gsianos@auth.gr.

ETHICS STATEMENT

The studies involving human participants were reviewed and approved by Scientific Committee, University General Hospital of Thessaloniki, AHEPA and Medical Ethics Committee, Medical School, Aristotle University of Thessaloniki. The patients/participants provided their written informed consent to participate in this study.

AUTHOR CONTRIBUTIONS

GSi, HK, JM, and GG developed the concept and the trial protocol. EK, AP, and GSi wrote the manuscript. AK, GSo, and SH were responsible for coronary angiography execution.

EP, KKO, and LS contributed to the research data management and statistical considerations, whereas DM, NS, and TZ were responsible for patient recruitment and follow-up execution. EC, KKe, and CA were responsible for micro-CT imaging execution, while FG contributed to the study with artificial clots creation. The principal investigator and supervisor of the whole study was GSi. All authors have read and approved the final manuscript.

REFERENCES

- Benjamin EJ, Paul M, Alvaro A, Bittencourt MS, Callaway CW, Carson AP, et al. Heart disease and stroke statistics-2019 update: a report from the American Heart Association. *Circulation*. (2019) 139:e56–528. doi: 10.1161/CIR.0000000000000659
- Tanboga IH, Topcu S, Aksakal E, Kalkan K, Sevimli S, Acikel M. Determinants of angiographic thrombus burden in patients with ST-segment elevation myocardial infarction. *Clin Appl Thromb*. (2014) 20:716–22. doi: 10.1177/1076029613483169
- Singh M, Berger PB, Ting HH, Rihal CS, Wilson SH, Lennon RJ, et al. Influence of coronary thrombus on outcome of percutaneous coronary angioplasty in the current era (the Mayo Clinic experience). *Am J Cardiol*. (2001) 88:1091–6. doi: 10.1016/S0002-9149(01)02040-9
- Ibanez B, James S, Agewall S, Antunes MJ, Bucciarelli-Ducci C, Bueno H, et al. 2017 ESC Guidelines for the management of acute myocardial infarction in patients presenting with ST-segment elevation: the task force for the management of acute myocardial infarction in patients presenting with ST-segment elevation of the European Society of Cardiology (ESC). *Eur Heart J*. (2018) 39:119–77. doi: 10.1093/eurheartj/ehx393
- Henriques JPS, Zijlstra F, Ottervanger JP, de Boer M-J, van 't Hof AWJ, Hoorntje JCA, et al. Incidence and clinical significance of distal embolization during primary angioplasty for acute myocardial infarction. *Eur Heart J*. (2002) 23:1112–7. doi: 10.1053/ehj.2001.3035
- DeWood MA, Spores J, Notske R, Mouser LT, Burroughs R, Golden MS, et al. Prevalence of total coronary occlusion during the early hours of transmural myocardial infarction. *N Engl J Med*. (1980) 303:897–902. doi: 10.1056/NEJM198010163031601
- Angerås O, Haraldsson I, Redfors B, Fröbert O, Petursson P, Albertsson P, et al. Impact of thrombus aspiration on mortality, stent thrombosis, and stroke in patients with ST-segment-elevation myocardial infarction: a report from the Swedish coronary angiography and angioplasty registry. *J Am Heart Assoc*. (2018) 7:e7680. doi: 10.1161/JAHA.117.007680
- Jolly SS, Cairns JA, Yusuf S, Meeks B, Pogue J, Rokoss MJ, et al. Randomized trial of primary PCI with or without routine manual thrombectomy. *N Engl J Med*. (2015) 372:1389–98. doi: 10.1056/NEJMoa1415098
- Jolly SS, James SK, Džavík V, Cairns JA, Mahmoud KD, Zijlstra F, et al. Thrombus aspiration in ST elevation myocardial infarction: an individual patient meta-analysis. *Circulation*. (2016) 135:143–52. doi: 10.1161/CIRCULATIONAHA.116.025371
- Lagerqvist B, Fröbert O, Olivecrona GK, Gudnason T, Maeng M, Alström P, et al. Outcomes 1 year after thrombus aspiration for myocardial infarction. *N Engl J Med*. (2014) 371:1111–20. doi: 10.1056/NEJMoa1405707
- Vlaar PJ, Svilaas T, van der Horst IC, Diercks GFH, Fokkema ML, de Smet BJGL, et al. Cardiac death and reinfarction after 1 year in the thrombus aspiration during percutaneous coronary intervention in acute myocardial infarction study (TAPAS): a 1-year follow-up study. *Lancet (London, England)*. (2008) 371:1915–20. doi: 10.1016/S0140-6736(08)60833-8
- Neumann FJ, Sousa-Uva M, Ahlsson A, Alfonso F, Banning AP, Benedetto U, et al. 2018 ESC/EACTS guidelines on myocardial revascularization. *Eur Heart J*. (2019) 40:87–165. doi: 10.1093/eurheartj/ehy394
- Powers ER. Aspiration thrombectomy: the possible importance of effective thrombus removal and minimal residual thrombus burden. *JACC Cardiovasc Interv*. (2016) 9:2012–3. doi: 10.1016/j.jcin.2016.07.037

FUNDING

This study was cofinanced by the European Regional Development Fund of the European Union and Greek national funds through the Operational Program Competitiveness, Entrepreneurship and Innovation, under the call RESEARCH–CREATE–INNOVATE (Project Code: T1EDK-04005).

- Higuma T, Soeda T, Yamada M, Yokota T, Yokoyama H, Izumiyama K, et al. Does residual thrombus after aspiration thrombectomy affect the outcome of primary PCI in patients with ST-segment elevation myocardial infarction? An optical coherence tomography study. *JACC Cardiovasc Interv*. (2016) 9:2002–11. doi: 10.1016/j.jcin.2016.06.050
- Amabile N, Hammam S, Fradi S, Souteyrand G, Veugeois A, Belle L, et al. Intra-coronary thrombus evolution during acute coronary syndrome: regression assessment by serial optical coherence tomography analyses. *Eur Heart J Cardiovasc Imaging*. (2015) 16:433–40. doi: 10.1093/ehjci/jeu228
- Bhindi R, Kajander OA, Jolly SS, Kassam S, Lavi S, Niemelä K, et al. Culprit lesion thrombus burden after manual thrombectomy or percutaneous coronary intervention-alone in ST-segment elevation myocardial infarction: the optical coherence tomography sub-study of the TOTAL (Thrombectomy versus PCI Alone) trial. *Eur Heart J*. (2015) 36:1892–900. doi: 10.1093/eurheartj/ehv176
- Jinnouchi H, Torii S, Kutyna M, Sakamoto A, Kolodgie FD, Finn AV, et al. Micro-computed tomography demonstration of multiple plaque ruptures in a single individual presenting with sudden cardiac death. *Circ Cardiovasc Imaging*. (2018) 11:e008331. doi: 10.1161/CIRCIMAGING.118.008331
- Kojonazarov B, Belenkov A, Shinomiya S, Wilhelm J, Kampschulte M, Mizuno S, et al. Evaluating systolic and diastolic cardiac function in rodents using microscopic computed tomography. *Circ Cardiovasc Imaging*. (2018) 11:e007653. doi: 10.1161/CIRCIMAGING.118.007653
- Zelt JGE, Mielniczuk LM. Micro computed tomography in experimental pulmonary arterial hypertension. *Circ Cardiovasc Imaging*. (2018) 11:e008631. doi: 10.1161/CIRCIMAGING.118.008631
- DiCorpo D, Tiwari A, Tang R, Griffin M, Aftreth O, Bautista P, et al. The role of micro-CT in imaging breast cancer specimens. *Breast Cancer Res Treat*. (2020) 180:343–57. doi: 10.1007/s10549-020-05547-z
- Sangaralingham SJ, Ritman EL, McKie PM, Ichiki T, Lerman A, Scott CG, et al. Cardiac micro-computed tomography imaging of the aging coronary vasculature. *Circ Cardiovasc Imaging*. (2012) 5:518–24. doi: 10.1161/CIRCIMAGING.112.973057
- Karagiannidis E, Konstantinidis NV, Sofidis G, Chatzinikolaou E, Sianos G. Rationale and design of a prospective, observational study for the quantitative estimation of thrombus burden in patients with ST-elevation myocardial infarction using micro-computed tomography: the QUEST-STEMI trial. *BMC Cardiovasc Disord*. (2020) 20:1–8. doi: 10.1186/s12872-020-01393-5
- World Medical Association. World Medical Association declaration of Helsinki: ethical principles for medical research involving human subjects. *JAMA*. (2013) 310:2191–4. doi: 10.1001/jama.2013.281053
- Harkness JR, Sabatine MS, Braunwald E, Morrow DA, Sloan S, Wiviott SD, et al. Extent of ST-segment resolution after fibrinolysis adds improved risk stratification to clinical risk score for ST-segment elevation myocardial infarction. *Am Heart J*. (2010) 159:55–62. doi: 10.1016/j.ahj.2009.10.033
- Sianos G, Papafakis MI, Serruys PW. Angiographic thrombus burden classification in patients with ST-segment elevation myocardial infarction treated with percutaneous coronary intervention. *J Invasive Cardiol*. (2010) 22(Suppl. B):6B–14B. Available online at: <https://pubmed.ncbi.nlm.nih.gov/20947930/>
- Chesebro JH, Knatterud G, Roberts R, Borer J, Cohen LS, Dalen J, et al. Thrombolysis in myocardial infarction (TIMI) trial, phase I: a comparison between intravenous tissue plasminogen activator and intravenous streptokinase. Clinical findings through hospital discharge. *Circulation*. (1987) 76:142–54. doi: 10.1161/01.CIR.76.1.142

27. Gibson CM, De Lemos JA, Murphy SA, Marble SJ, McCabe CH, Cannon CP, et al. Combination therapy with abciximab reduces angiographically evident thrombus in acute myocardial infarction a TIMI 14 substudy. *Circulation*. (2001) 103:2550–4. doi: 10.1161/01.CIR.103.21.2550
28. Metscher BD. Micro CT for comparative morphology: simple staining methods allow high-contrast 3D imaging of diverse non-mineralized animal tissues. *BMC Physiol*. (2009) 9:11. doi: 10.1186/1472-6793-9-11
29. Popovic ZB, Thomas JD. Assessing observer variability: a user's guide. *Cardiovasc Diagn Ther*. (2017) 7:317–24. doi: 10.21037/cdt.2017.03.12
30. McHugh ML. Interrater reliability: the kappa statistic. *Biochem Medica*. (2012) 22:276–82. doi: 10.11613/BM.2012.031
31. Midi H, Sarkar SK, Rana S. Collinearity diagnostics of binary logistic regression model. *J Interdiscip Math*. (2010) 13:253–67. doi: 10.1080/09720502.2010.10700699
32. Sianos G, Papafakis MI, Daemen J, Vaina S, van Mieghem CA, van Domburg RT, et al. Angiographic stent thrombosis after routine use of drug-eluting stents in ST-segment elevation myocardial infarction. The importance of thrombus burden. *J Am Coll Cardiol*. (2007) 50:573–83. doi: 10.1016/j.jacc.2007.04.059
33. Ge J, Schäfer A, Ertl G, Nordbeck P. Thrombus aspiration for ST-segment-elevation myocardial infarction in modern era: still an issue of debate? *Circ Cardiovasc Interv*. (2017) 10:1–12. doi: 10.1161/CIRCINTERVENTIONS.117.005739
34. Stone GW, Maehara A, Witzensichler B, Godlewski J, Parise H, Dambrink JHE, et al. Intracoronary abciximab and aspiration thrombectomy in patients with large anterior myocardial infarction: the INFUSE-AMI randomized trial. *JAMA*. (2012) 307:1817–26. doi: 10.1001/jama.2012.421
35. Higuma T, Soeda T, Abe N, Yamada M, Yokoyama H, Shibutani S, et al. A combined optical coherence tomography and intravascular ultrasound study on plaque rupture, plaque erosion, and calcified nodule in patients with ST-segment elevation myocardial infarction: incidence, morphologic characteristics, and outcomes after per. *JACC Cardiovasc Interv*. (2015) 8:1166–76. doi: 10.1016/j.jcin.2015.02.026
36. Iijima R, Shinji H, Ikeda N, Itaya H, Makino K, Funatsu A, et al. Comparison of coronary arterial finding by intravascular ultrasound in patients with “transient no-reflow” versus “reflow” during percutaneous coronary intervention in acute coronary syndrome. *Am J Cardiol*. (2006) 97:29–33. doi: 10.1016/j.amjcard.2005.07.104
37. Karagiannidis E, Sofidis G, Stalikas N, Koletsis T, Kartas A, Keklikoglou K, et al. Rationale and design of a prospective, single-arm trial for the evaluation of safety and feasibility of large thrombus burden aspiration in the context of ST elevation myocardial infarction. *Hell J Cardiol*. (2020) 61:450–2. doi: 10.1016/j.hjc.2020.04.002
38. Gupta T, Kolte D, Khera S, Harikrishnan P, Mujib M, Aronow WS, et al. Smoker's paradox in patients with ST-segment elevation myocardial infarction undergoing primary percutaneous coronary intervention. *J Am Heart Assoc*. (2016) 5:1–11. doi: 10.1161/JAHA.116.003370
39. Inoue T. Cigarette smoking as a risk factor of coronary artery disease and its effects on platelet function. *Tob Induc Dis*. (2004) 2:27. doi: 10.1186/1617-9625-2-1-27
40. Ndrepepa G, Tiroch K, Keta D, Fusaro M, Seyfarth M, Pache J, et al. Predictive factors and impact of no reflow after primary percutaneous coronary intervention in patients with acute myocardial infarction. *Circ Cardiovasc Interv*. (2010) 3:27–33. doi: 10.1161/CIRCINTERVENTIONS.109.896225
41. Ruggeri ZM, Loredana MG. Adhesion mechanisms in platelet function. *Circ Res*. (2007) 100:1673–85. doi: 10.1161/01.RES.0000267878.97021.ab
42. Srikanth S, Ambrose JA. Pathophysiology of coronary thrombus formation and adverse consequences of thrombus during PCI. *Curr Cardiol Rev*. (2012) 8:168–76. doi: 10.2174/157340312803217247
43. Ren H, Zheng Y, Hu X, Yang Y, Zhang Y, Sun Y, et al. High thrombus burden: a review of mechanisms and treatments. *Int J Clin Exp Med*. (2019) 12:13068–78. Available online at: <http://www.ijcem.com/files/ijcem0096007.pdf>
44. Yunoki K, Naruko T, Inoue T, Sugioka K, Inaba M, Iwasa Y, et al. Relationship of thrombus characteristics to the incidence of angiographically visible distal embolization in patients with ST-segment elevation myocardial infarction treated with thrombus aspiration. *JACC Cardiovasc Interv*. (2013) 6:377–85. doi: 10.1016/j.jcin.2012.11.011

Conflict of Interest: The authors declare that the research was conducted in the absence of any commercial or financial relationships that could be construed as a potential conflict of interest.

Citation: Karagiannidis E, Papazoglou AS, Sofidis G, Chatzinikolaou E, Keklikoglou K, Panteris E, Kartas A, Stalikas N, Zegkos T, Girtovitis F, Moysidis DV, Stefanopoulos L, Koupidis K, Hadjimiltiades S, Giannakoulas G, Arvanitidis C, Michaelson JS, Karvounis H and Sianos G (2021) Micro-CT-Based Quantification of Extracted Thrombus Burden Characteristics and Association With Angiographic Outcomes in Patients With ST-Elevation Myocardial Infarction: The QUEST-STEMI Study. *Front. Cardiovasc. Med*. 8:646064. doi: 10.3389/fcvm.2021.646064

Copyright © 2021 Karagiannidis, Papazoglou, Sofidis, Chatzinikolaou, Keklikoglou, Panteris, Kartas, Stalikas, Zegkos, Girtovitis, Moysidis, Stefanopoulos, Koupidis, Hadjimiltiades, Giannakoulas, Arvanitidis, Michaelson, Karvounis and Sianos. This is an open-access article distributed under the terms of the Creative Commons Attribution License (CC BY). The use, distribution or reproduction in other forums is permitted, provided the original author(s) and the copyright owner(s) are credited and that the original publication in this journal is cited, in accordance with accepted academic practice. No use, distribution or reproduction is permitted which does not comply with these terms.



Rational and Design of the SIMULATOR Study: A Multicentre Randomized Study to Assess the Impact of SIMULation-bAsed Training on Transoesophageal echocardiOgraphy leaRning for Cardiology Residents

OPEN ACCESS

Edited by:

Antonios Karanasos,
Hippokraton General Hospital, Greece

Reviewed by:

Giulia Elena Mandoli,
University of Siena, Italy
Erhan Tenekecioglu,
University of Health Sciences, Turkey

*Correspondence:

Théo Pezel
theo.pezelccf@gmail.com

Specialty section:

This article was submitted to
Cardiovascular Imaging,
a section of the journal
Frontiers in Cardiovascular Medicine

Received: 30 January 2021

Accepted: 26 April 2021

Published: 24 May 2021

Citation:

Pezel T, Bernard A, Lavie Badie Y, Dreyfus J, Audureau E, Bohbot Y, Fard D, Hubert A, Nguyen LS, Monteil C, Bière L, Le Ven F, Canu M, Ribeyrolles S, Mion B, Mouhat B, Bazire B, Fauvel C, Ternacle J, Cautela J, Cambet T, Le Tourneau T, Donal E, Lafitte S, Mansencal N and Coisne A (2021) Rational and Design of the SIMULATOR Study: A Multicentre Randomized Study to Assess the Impact of SIMULation-bAsed Training on Transoesophageal echocardiOgraphy leaRning for Cardiology Residents. *Front. Cardiovasc. Med.* 8:661355. doi: 10.3389/fcvm.2021.661355

Théo Pezel^{1,2,3,4*}, Anne Bernard^{5,6,7}, Yoan Lavie Badie⁸, Julien Dreyfus⁹, Etienne Audureau^{10,11}, Yohann Bohbot^{12,13,14}, Damien Fard¹⁵, Arnaud Hubert¹⁶, Lee S. Nguyen¹⁷, Cécile Monteil³, Loïc Bière¹⁸, Florent Le Ven¹⁹, Marjorie Canu²⁰, Sophie Ribeyrolles²¹, Baptiste Mion²¹, Basile Mouhat²², Baptiste Bazire²³, Charles Fauvel²⁴, Julien Ternacle²⁵, Jennifer Cautela²⁶, Théo Cambet²⁷, Thierry Le Tourneau²⁸, Erwan Donal¹⁶, Stéphane Lafitte²⁵, Nicolas Mansencal^{29,30} and Augustin Coisne^{31,32}

¹ University of Paris, Department of Cardiology, Lariboisière Hospital—APHP, Paris, France, ² INSERM UMRS 942, Paris, France, ³ Ilumens Healthcare Simulation Department, Paris University, Paris, France, ⁴ Division of Cardiology, Johns Hopkins University, Baltimore, MD, United States, ⁵ Service de Cardiologie, CHRU de Tours, Toulouse, France, ⁶ EA4245, Loire Valley Cardiovascular Collaboration, Université de Tours, Tours, France, ⁷ Centre Régional d'Enseignement par la Simulation en Santé, Faculté de Médecine de Tours, Tours, France, ⁸ Cardiac Imaging Center, Toulouse University Hospital, Toulouse, France, ⁹ Cardiology Department, Centre Cardiologique du Nord, Saint-Denis, France, ¹⁰ Clinical Epidemiology and Ageing (CEPIA), IMRB U955, UPEC, Creteil, France, ¹¹ CHU Henri Mondor, AP-HP, Creteil, France, ¹² Department of Cardiology, Amiens University Hospital, Amiens, France, ¹³ UR UPJV 7517, Jules Verne University of Picardie, Amiens, France, ¹⁴ Health Simulation Center SimUSanté®, Amiens University Hospital, Amiens, France, ¹⁵ Department of Cardiology, Cardiology Intensive Care Unit, Henri-Mondor University Hospital, AP-HP, INSERM U955, Université Paris-Est Créteil, Créteil, France, ¹⁶ Cardiologie, CHU de Rennes, LTSI, Rennes, France, ¹⁷ Research and Innovation, RICAP, CMC Ambroise Paré, Neuilly-sur-Seine, France, ¹⁸ Department of Cardiology, Angers University Hospital, Angers, France, ¹⁹ Department of Cardiology, Brest University Hospital, CHRU de la Cavale Blanche, Brest, France, ²⁰ Department of Cardiology, Grenoble University Hospital, Grenoble, France, ²¹ Department of Cardiology, Institut Mutualiste Montsouris, Paris, France, ²² Department of Cardiology, University Hospital, Besançon, France, ²³ University of Paris, Department of Cardiology, Bichat Hospital—APHP, Paris, France, ²⁴ Department of Cardiology, CHU Rouen, FHU REMOD-VHF, Rouen, France, ²⁵ Hôpital Cardiologique Haut-Lévêque, CHU de Bordeaux, Pessac, France, ²⁶ Aix-Marseille University, University Mediterranean Center of Cardio-Oncology, Unit of Heart Failure and Valvular Heart Diseases, Department of Cardiology, North Hospital, Assistance Publique—Hôpitaux de Marseille, Centre for CardioVascular and Nutrition Research (C2VN), Marseille, France, ²⁷ Explorations fonctionnelles cardiovasculaires, Louis Pradel Hospital, Hospices Civils de Lyon, Bron, France, ²⁸ Inserm UMR1087, Institut du thorax, Université de Nantes, CHU de Nantes, Nantes, France, ²⁹ Department of Cardiology, Ambroise Paré Hospital, Assistance Publique—Hôpitaux de Paris (AP-HP), Centre de référence des cardiomyopathies et des troubles du rythme cardiaque héréditaires ou rares, Université de Versailles-Saint Quentin (UVSQ), Boulogne-Billancourt, France, ³⁰ INSERM U-1018, CESP, Epidémiologie clinique, UVSQ, Université de Paris Saclay, Villejuif, France, ³¹ Department of Cardiovascular Explorations and Echocardiography—Heart Valve Clinic, CHU Lille, Lille, France, ³² University of Lille, Inserm, CHU Lille, Institut Pasteur de Lille, U1011-EGiD, Lille, France

Introduction: Simulation-based training in transesophageal echocardiography (TEE) seems promising. However, data are limited to non-randomized or single-center studies. To assess the impact of simulation-based vs. traditional teaching on TEE knowledge and performance for medical residents in cardiology.

Materials and Methods: Nationwide prospective randomized multicenter study involving 43 centers throughout France allowing for the inclusion of >70% of all French cardiology residents. All cardiology residents naive from TEE will be included. Randomization with stratification by center will allocate residents to either a control group receiving theoretical knowledge by e-learning only, or to an intervention group receiving two simulation-based training sessions on a TEE simulator in addition.

Results: All residents will undergo both a theoretical test (0–100 points) and a practical test on a TEE simulator (0–100 points) before and 3 months after the training. Satisfaction will be assessed by a 5-points Likert scale. The primary outcomes will be to compare the scores in the final theoretical and practical tests between the two groups, 3 months after the completion of the training.

Conclusion: Data regarding simulation-based learning in TEE are limited to non-randomized or single-center studies. The randomized multicenter SIMULATOR study will assess the impact of simulation-based vs. traditional teaching on TEE knowledge and performance for medical residents in cardiology, and whether such an educational program should be proposed in first line for TEE teaching.

Keywords: simulation-based, medical education, residents, transesophageal echoardiography, randomized study

INTRODUCTION

Excellent know-how in transthoracic (TTE) and transesophageal echocardiography (TEE) is an essential requirement for the training of cardiology residents (1–3). Although TTE is rapidly taught and practiced on patients during the cardiology residency with dedicated studies (4), TEE remains too often neglected. The reference hands-on TEE teaching may be hampered by the availability of the teacher and equipment according to trainees' working patterns, and by the procedure, which is semi-invasive by itself with the need of esophageal intubation. Simulation may be a key educational tool to improve accessibility of TEE training and to accelerate the learning curve (5).

Despite a growing interest in simulation-based training (6, 7), its accessibility remains limited in the cardiology field. In a recent international survey performed with 172 young cardiologists from 43 countries, only 48% of the participants had already participated in a simulation training, while 91% considered this teaching method as "necessary" in cardiology (8). To respond to this training demand, several teams already offer to their residents a simulation education on TEE mannequin for several years (9). In France, simulation-based teaching in cardiology has also experienced significant developments, both technologically and institutionally. Indeed, simulation-based teaching is soon to become a legal obligation in the evaluation of graduate medical students (Health Law 2022) (10). However, as of yet, no national French simulation educational program exists in cardiology. The lack of studies evaluating simulation educational programs and the cost of TEE simulator may explain the lack of national consensus.

While supervised real-life TEE experience is essential, recent studies suggested that simulation-based TEE teaching is

displaying significant benefit over conventional methods (11–17). To our knowledge, all these studies were non-randomized or randomized with limited single-centre sample size (11, 12, 14, 15, 18–23).

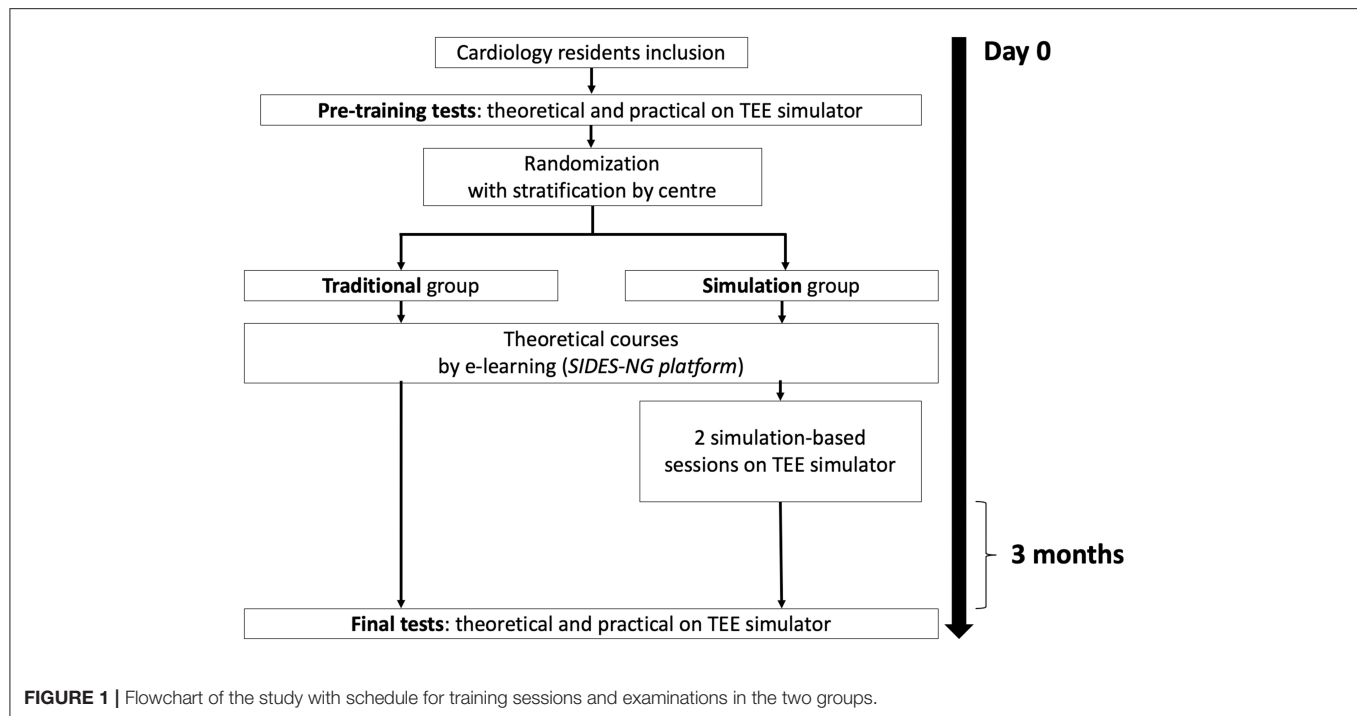
The SIMULATOR study is designed to assess the impact of SIMULATION-bAsed Training on transoesophageal echocardiOgraphy leaRning for cardiology residents comparing simulation-based vs. traditional teaching on TEE knowledge and performance in cardiology residents, in several French centres. Our hypothesis is that skills and knowledge in TEE may be enhanced by the simulation-based TEE teaching.

METHODS

Study Population and Centers

From November 2020 to November 2021, all consecutive residents in cardiology, of all training levels (year 1–4), who have never performed a TEE alone will be included in this randomized multicenter study conducted in 43 centers throughout France. The list of participating centers allowing for the inclusion of more than 70% of all French cardiology residents is provided in **Supplementary Table 1**. All residents who have already performed a TEE alone will be excluded. Residents will be invited via email from their local University coordinator to participate in the study.

The study will be approved by the Ethics committee of each center and authorized by the French data protection committee (*Commission Nationale Informatique et Liberté, CNIL*). Written informed consent will be obtained from all participants. Anonymized data supporting the findings of this study will be available from the corresponding author upon reasonable request. The study will be registered before starting



the recruitment of the participants, and study data and results will be added at the completion of the study. All authors and future study investigators of this study have read and approved the manuscript as written.

Randomization

Randomization with stratification by center will be performed at the individual (resident) level in 1:1 ratio, using a computer-based software (Research Randomizer 4.0; Social Psychology Network, Middletown, USA) to assign all the residents to the traditional group or to the simulation group. The random allocation sequence will be computer-generated by the statistician (E.A.) prior to the study using Stata v16.0 (StataCorp, College Station, TX, USA). Cluster-level randomization at the center level was not used for the present study, considering as minimal the risk of “contamination” of the effect of the training intervention in residents allocated in the control group.

Study Design

Each participant will complete two different tests during the study: (1) a pre-training test before starting the educational program; and (2) a final test performed 3 months after the end of the educational program. Each of these tests will include a theoretical test and a practical test on a TEE simulator (Figure 1). Notably, the pre-test will allow for an accurate assessment of each resident's theoretical and practical level in TEE at baseline.

Baseline Participants Characteristics

The following demographic data will be collected: age, sex, residency semester, having the national diploma in echocardiography (validation on the SIDES platform), number of TTE performed, number of TEE observed, desire for a

technical specialty in cardiology (cardiovascular imaging, interventional cardiology, electrophysiology, pediatric and congenital cardiology, or no technical specialty). All participants will answer a questionnaire on their prior experience of video games in childhood or currently, defined by more than 1 hour per week, as this seemed to be associated with performance on simulation-based models in previous studies (15, 24).

Theoretical Test

The theoretical test will include 20 video-based questions online that evaluate recognition of standard TEE views, normal anatomy and some cases of mitral regurgitation, as already described (13, 19, 22, 23). Beyond the mitral regurgitation, the presence and severity of pathology and advanced TEE skills such as quantification and haemodynamic calculations will not be assessed. The residents will be given 90 s to choose the best answer out of a multiple-choice of 5 for each question (23). These tests will be designed by the experts from the French Group of Cardiovascular imaging of the French Society of Cardiology. Each question will be scored on 5 points (5 points if all the propositions correct and 0 points if at least one error), for a total of 100 points per test.

Practical Tests

Immediately after each theoretical test (pre-training and final tests), all participants will be asked to demonstrate 10 basic views on a TEE simulator (Table 1), as previously described (14, 15). Of note, all residents of the two groups will have a few minutes before the practical test, to familiarize themselves with the handling of the simulator, without specific training and before the probe introduction. The standardized assessment that will be used by

TABLE 1 | List of basic TEE views, general anatomic structures (25, 26) and the mitral valve structures (27) that will be assessed in the study.

Basic TEE views	General anatomic structures	Mitral valve structures
ME 4-chamber	LA/LV/RA/RV/mitral valve	A2/P2
ME commissural view (2-chamber)	LV/Mitral valve/LA/LA appendage/circumflex artery/coronary sinus	P1/A2/P3 Antero-lateral commissure Antero-lateral muscle pillar
3-chamber	LA/LV/right coronary cusp/non-coronary cusp/mitral valve	A2/P2
ME bicaval	Interatrial septum/RA/LA/vena cava	
ME RV inflow-outflow	RV free wall/RV outflow tract/tricuspid valve	
ME aortic valve SAX	Right coronary, left coronary and non-coronary cusps/pulmonary valve/tricuspid valve/inter atrial septum	
Descending aorta SAX	Descending aorta/inferior wall/superior wall	
Descending aorta LAX	Descending aorta/round shape/wall (without interruption)	
ME ascending aorta SAX	Superior vena cava/ascending aorta/aortic valve/pulmonary artery	
ME ascending aorta LAX	Right pulmonary artery/ascending aorta/aortic valve	

LA, left atrium; LAX, long axis; LV, left ventricle; ME, midesophageal; RA, right atrium; RV, right ventricle; SAX, short axis; TEE, transesophageal echocardiography.

all teachers for the TEE grading scale of each views is presented in **Figure 2**. For each image, residents will have a maximum of 1 min to obtain their best view. The teacher will time the duration between TEE probe introduction and obtention of the specified view judged successful by the trainee. The modified Ferrero grading scale will be used to assess the quality of achievement of the views (14, 15, 23). In this grading system, each view will be marked out of 10 points according to the quality of the view. Of these 10 points, 5 will score for imaging angle and overall clarity of the view (poor quality = 0 points, average quality = 2 points, optimal quality = 5 points); and 5 will assess the presence of all the pertinent anatomic structures in the view (−1 point per missing structure not shown, and zero point if no structure identified) (**Table 1**). All teachers will ask for the 10 basic views in a pre-established order. Each view will be scored on 10 points, for a total of 100 points per practical test. These examinations will be evaluated by the local teacher, a certified national echocardiography teacher. Of note, residents will not be informed of their individual performance on theoretical or practical tests to avoid additional training beyond the study for performance purposes.

Traditional and Simulation-Based Training

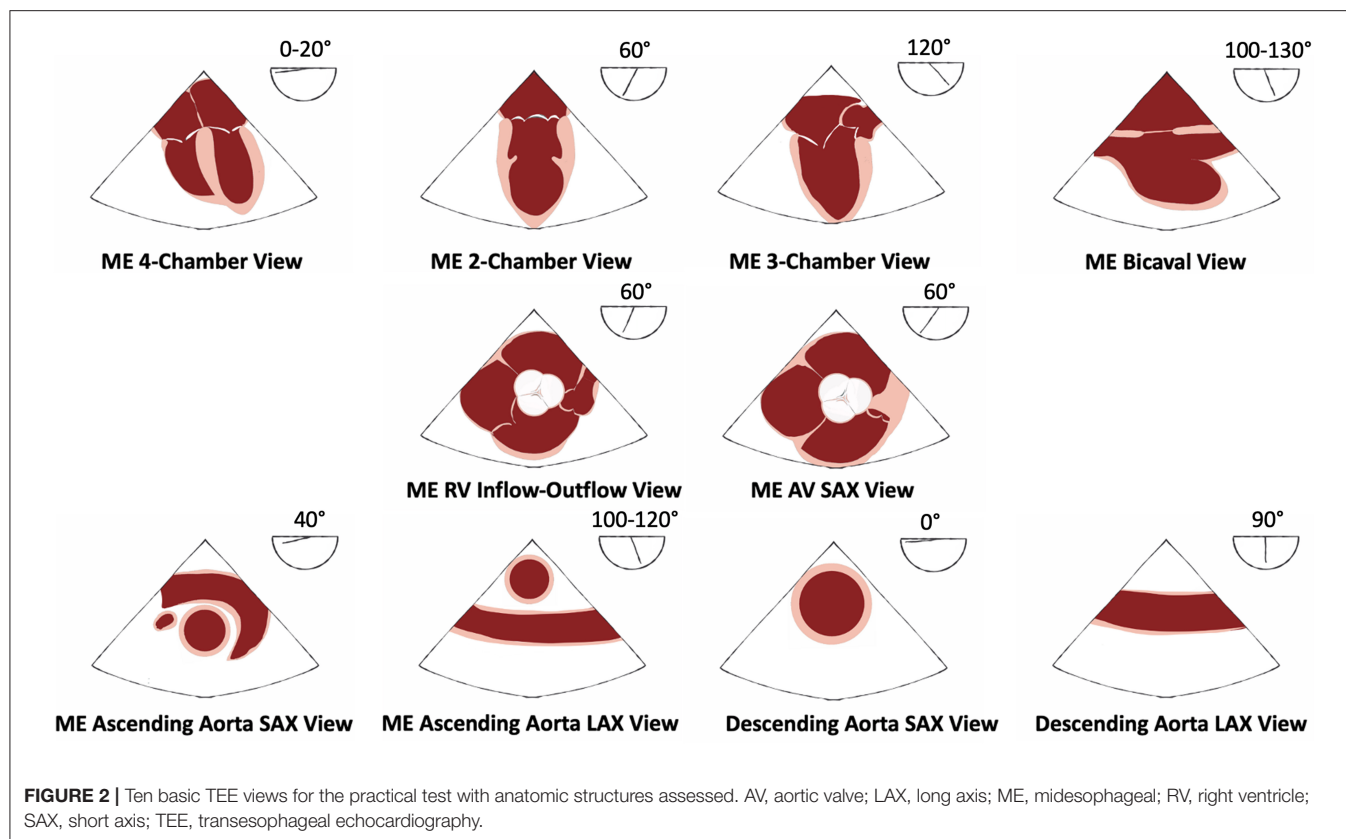
After the pre-training test, all participants will complete the following training sessions corresponding to the randomization. The first group (“traditional group”) will take part in a traditional didactic training using e-learning with the free-access online course on the *SIDES-NG platform* (website: <https://www.uness.fr/plateformes-sides/sides-ng>). This internet-based resource was developed by the French Group of Cardiovascular of the French Society of Cardiology and is freely accessible online. No session on TEE simulator will have to be performed during the study. The second group (“simulation group”) will access online courses too. Additionally, they will receive two one-on-one teaching sessions using a TEE simulator. The teaching program will be designed to facilitate sequential TEE examination according to ESC guidelines (3). The simulation session will involve standardized initial teaching of normal cardiac, including

anatomy of mitral valve with some mitral regurgitation cases, aortic valve, tricuspid valve, interatrial septum, and left atrial appendage, and demonstration of image acquisition by the teacher (time duration: 30 min) (25). The duration of each session will be 2 h with a 6:1 instructor to student ratio. Each subject will have a dedicated 20 min of hands-on to manipulate the probe and undertake a sequential TEE examination under the supervision of the teacher. Instruction and feedback will be primarily verbal, but physical assistance with probe movement will also be provided to obtain and optimize the 10 basic views. Other participants can watch their colleagues working on the TEE simulator. The time allocated on TEE simulator will be divided between the acquisition of basic views and normal cardiac anatomy, including anatomy of mitral valve, aortic valve, tricuspid valve, interatrial septum, and left atrial appendage (first session), and an in-depth learning of mitral valve anatomy in TEE using some cases of mitral regurgitation (second session). The two practical sessions will be taught by the same instructor in each center. The maximum time between the two sessions will be 2 months.

Three months after completion of the study, all participants will be invited to a final test to assess long-term retention. Participants will be asked not to access additional learning resources about TEE between the pre- and final tests. All participants in both groups will be allowed to perform TEE during their daily clinical practice throughout the study. They will have to quantify prospectively the number of TEE observed or performed after training using a personal logbook provided by the teacher.

TEE Simulator Protocol

For the “simulation group,” the same mannequin-based TEE simulators will be used for the study (“U/S Mentor Simulator,” 3D Systems-Simbionix, Littleton, USA). Functionalities of TEE simulators have been described previously (13). All trainers of the study are certified teachers in echocardiography and are accustomed to use simulation as a teaching method. To standardize the training and the practical test on TEE simulator, all trainers will follow a webinar of 30 min presenting the entire



content of each session and the final test. Eighteen simulators will be used for this study. Some University centers already have their own simulator and will perform the study without additional cost. For the other centers which do not have a simulator, we will be able to set up a system of delivery of the simulator on the other centers during a limited period allowing to carry out the study.

Satisfaction Assessment

After completion of the two training sessions, the participant satisfaction will be assessed by an anonymous questionnaire on the quality and effectiveness of the TEE training received during this study for the simulation group. As already published (15, 19), the questionnaire will include six statements on different aspects of the training such as (1) overall satisfaction and usefulness; (2) perceived benefit; (3) duration of the sessions; (4) relevance of the current level of training; (5) ideas of improvement; and (6) whether the participants would recommend this educational program for others. Satisfaction will be assessed using a 5-point Likert scale from 1 = strongly disagree to 5 = strongly agree. Responses will be deemed negative (Likert scale 1 and 2), neutral (Likert scale 3), or positive (Likert scale 4 and 5). The satisfaction of each participant will be scored on a total of 30 points.

Outcomes

The coprimary outcomes of the study to compare the two groups will be the scores in the final theoretical and practical tests after the training will be completed.

The secondary outcomes will be the change in theoretical and practical tests scores from pre- to final-training. In addition, we will assess the satisfaction of participants.

Statistical Analysis

Sample Size Calculation

Based on recent available literature (13, 15, 19, 21) and considering normalized 0–100 points score ranges for the two co-primary outcomes, a minimally important difference of 5 points (standard deviation 7 points) will be considered for the difference in change from pre- to post-training scores in theoretical and practical tests between the two randomized groups. Under these assumptions, a sample size of 50 subjects per group (for an overall population of 100 participants) will provide 90% power to detect a statistically significant difference between the two groups at a significance level of $\alpha = 2.5\%$, applying a Bonferroni correction to account for multiple testing of the two co-primary outcomes.

Statistical Methods

Demographic characteristics (age, sex, residency semester), having the national diploma in echocardiography, number of TTE performed, number of TEE observed, desire for a technical specialty in Cardiology collected at the time of randomization, will be summarized and compared between participants of the “traditional group” and the “simulation group.” Continuous data will be reported as means \pm standard deviation (SD) for

normally distributed data or as medians and interquartile range (IQR) for non-normally distributed data, as assessed through graphical methods and the use of the Shapiro-Wilk test for normality. Categorical data will be reported as counts and percentages. Between-groups comparisons will be performed using Student's *t*-test or Mann-Whitney test for continuous variables and using the Chi-2 or Fisher's exact test for categorical variables, as appropriate. Regarding the co-primary outcomes, on-parametric approaches (i.e., Mann-Whitney tests) will be favored over parametric tests due to the skewed distribution of test scores previously described in the literature (15). For within-groups comparisons (pre- vs. final tests), paired *t*-tests and Wilcoxon signed-rank tests will be performed for continuous variables. Longitudinal analysis of the evolution of the co-primary outcomes over the two time points (pre- and 3-month follow-up) will rely on mixed effects linear regression modeling, accounting for the correlation between repeated data over time. To address this risk of bias due to the difference of number of TEE observed between the residents, an adjustment for the number of TEE observed will be performed in the final analysis. Prespecified subgroup analyses will be performed after stratifying by prior experience of video games in childhood or currently. A two-tailed $p < 0.025$ will be considered statistically significant for the primary analyses, and a two-tailed $p < 0.05$ for all other comparisons. All data will be analyzed using the R software, version 3.6.3 (R Project for Statistical Computing, R Foundation, Vienna, Austria) and Stata v16.0 (StataCorp, College Station, TX, USA).

DISCUSSION

This study will be the largest multicentre randomized study to assess the impact of simulation-based TEE teaching on the level of skills and practices of residents in cardiology. Simulation-based teaching in cardiology is experiencing a period of significant technological and institutional development. Further, simulation-based teaching has recently become a legal obligation in the evaluation of graduate medical students in France (10).

Previous studies evaluated the difference between TEE simulation training and conventional didactic training and e-learning (11, 12, 14, 20, 21, 23) and only three studies compared simulation training with hands-on training (15, 19, 22) considered as the "gold-standard" for TEE teaching. The majority of these studies showed superiority of TEE simulation training compared to traditional methods (12, 14, 15, 19–23). However, all of these studies were non-randomized (20) or randomized but limited by their sample size and monocentric character. Our multicentric randomized study with stratification by center will reduce the bias of variability in the quality and effectiveness of instructors, which is an essential step in the validation of an educational program. Besides, the majority of studies only evaluated the participants' retention in short-term recall 1 week after TEE education (19), and only a few studies performed long-term recall at 3 months (15). Only two small single-center studies have suggested a benefit of simulation training for residents who played video games with better visual, spatial and motor

coordination than other students (15, 24). For that reason, we have chosen to also assess this element in the study.

Almost all of the studies evaluating the impact of simulation-based TEE teaching were performed with anesthesia residents (11, 13–15, 18–21, 23) or with cardiac surgery residents (22). To date, no study has been performed to assess the interest of simulation-based TEE teaching in cardiology residents. This may be explained by the earlier and faster development of simulation-based education in anesthesia-resuscitation and surgery compared with cardiology. However, TEE is most often challenging and stressful in cardiology as patients are usually awake under local anesthesia, and not under general anesthesia and as TEE exams usually need to provide a quick answer when guiding structural or surgical procedures with immediate consequences for the patient (26). Thus, TEE training in a safe environment with no risks for patients is particularly critical for cardiologists.

Study Limitations

This study will have some limitations. First, residents of the traditional group will not manipulate any TEE probe during the training program. It could be argued that the opportunity for probe manipulation in the simulation group might confer an advantage in understanding anatomical relationships. Second, as previously described in the majority of educational studies (27). There is a risk of contamination of control residents, meaning the simulation group could discuss outside of the training sessions with the traditional group. However, the potential consequences of this risk are very limited, because the simulation-teaching experience is essentially practical.

Third, the practical test assessor will not be blinded due to the cluster randomization. Nevertheless, this assessment will be standardized for all assessors by the dedicated webinar.

Fourth, this study is an introduction to the practice of TEE and the use of simulators are not allowing for learning of probe insertion or the skills to manage the potential complications during an examination on real patients. Even though the simulation-based teaching should be even more beneficial for TEE with pathological cases which requires greater expertise. Indeed, the aim of our study was to evaluate the impact of simulation-based learning on basic TEE skills and knowledge. Further studies should assess its impact on more advanced level of expertise. Moreover, this study will not evaluate the educational contribution of simulated-based TEE training on actual patients. Indeed, this method is time-consuming and hardly compatible with clinical routine, with difficulty in finding patients with acceptable image quality for beginners. Hands-on TEE training may also present a patient safety issue, as TEE can potentially be traumatic for the patient, especially without general anesthesia. Finally, the financial aspect is another limitation of simulation-based training. Indeed, a significant and constant investment is necessary for the purchase of a simulator, for the maintenance and the update of the software. For this reason, simulation centers are most often based on multiple funding (University, national, regional and international grants, sponsorships).

CONCLUSION

This multicentre randomized study will allow an assessment of the simulation-based TEE training impact compared to traditional teaching. Finally, the result of this study will highlight the interest of an educational program, including simulation-based TEE training.

DATA AVAILABILITY STATEMENT

The original contributions presented in the study are included in the article/Supplementary Material, further inquiries can be directed to the corresponding author/s.

ETHICS STATEMENT

The studies involving human participants were reviewed and approved by Commission Nationale Informatique et Liberte (CNIL); Ethics committee of Lariboisiere hospital. The patients/participants provided their written informed consent to participate in this study.

REFERENCES

- Ryan T, Berlacher K, Lindner JR, Mankad SV, Rose GA, Wang A. COCATS 4 task force 5: training in echocardiography: endorsed by the American Society of echocardiography. *J Am Soc Echocardiogr Off Publ Am Soc Echocardiogr.* (2015) 28:615–27. doi: 10.1016/j.echo.2015.04.014
- Steeds RP, Garbi M, Cardim N, Kasprzak JD, Sade E, Nihoyannopoulos P, et al. EACVI appropriateness criteria for the use of transthoracic echocardiography in adults: a report of literature and current practice review. *Eur Heart J Cardiovasc Imaging.* (2017) 18:1191–204. doi: 10.1093/ehjci/jew333
- Flachskampf FA, Wouters PF, Edvardsen T, Evangelista A, Habib G, Hoffman P, et al. Recommendations for transoesophageal echocardiography: EACVI update (2014). *Eur Heart J Cardiovasc Imaging.* (2014) 15:353–65. doi: 10.1093/ehjci/jeu015
- Bernard A, Chemaly P, Dion F, Laribi S, Remerand F, Angoulvant D, et al. Evaluation of the efficacy of a self-training programme in focus cardiac ultrasound with simulator. *Arch Cardiovasc Dis.* (2019) 112:576–84. doi: 10.1016/j.acvd.2019.06.001
- Okuda Y, Bryson EO, DeMaria S, Jacobson L, Quinones J, Shen B, et al. The utility of simulation in medical education: what is the evidence? *Mt Sinai J Med N Y.* (2009) 76:330–43. doi: 10.1002/msj.20127
- Pezel T, Coisne A, Picard F, Gueret P, French Commission of Simulation Teaching of the French Society of Cardiology. How simulation teaching is revolutionizing our relationship with cardiology. *Arch Cardiovasc Dis.* (2020) 113:297–302. doi: 10.1016/j.acvd.2020.03.010
- Bradley P. The history of simulation in medical education and possible future directions. *Med Educ.* (2006) 40:254–62. doi: 10.1111/j.1365-2929.2006.02394.x
- Pezel T, Coisne A, Mahmoud-Elsayed H, Mandoli GE, Moharem Elgamel S, Podlesnikar T, et al. EACVI Communication paper: first international young dedicated multimodal cardiovascular imaging simulation education event organized by the ESC. *Eur Heart J - Cardiovasc Imaging.* (2019) 21:124–6. doi: 10.1093/ehjci/jez299
- Dreyfus J, Donal E, Pezel T. Moving into a new era for echocardiography education with simulation and workshop-based training. *JACC Case Rep.* (2020) 2:505–7. doi: 10.1016/j.jaccas.2019.12.023
- Loi du 24 juillet 2019 relative à l'organisation et à la transformation du système de santé. Available online at: <https://www.legifrance.gouv.fr/affichTexte.do?cidTexte=JORFTEXT000038821260&categorieLien=id>

AUTHOR CONTRIBUTIONS

TP, AC, AB, and EA designed the trial. TP and AC wrote the manuscript. EA performed statistical analyses. YB performed the illustration of the Figure 2. All the undersigning authors have substantially contributed to the paper. All authors reviewed the paper.

ACKNOWLEDGMENTS

The authors thank Jérôme ESTEVES—Twin-Medical®, for the free provision of TEE simulators and all the team of the Ilumens Simulation Department (University of Paris).

SUPPLEMENTARY MATERIAL

The Supplementary Material for this article can be found online at: <https://www.frontiersin.org/articles/10.3389/fcvm.2021.661355/full#supplementary-material>

- Sohmer B, Hudson C, Hudson J, Posner GD, Naik V. Transesophageal echocardiography simulation is an effective tool in teaching psychomotor skills to novice echocardiographers. *Can J Anaesth J Can Anesth.* (2014) 61:235–41. doi: 10.1007/s12630-013-0081-x
- Damp J, Anthony R, Davidson MA, Mendes L. Effects of transesophageal echocardiography simulator training on learning and performance in cardiovascular medicine fellows. *J Am Soc Echocardiogr Off Publ Am Soc Echocardiogr.* (2013) 26:1450–6.e2. doi: 10.1016/j.echo.2013.08.008
- Sharma V, Chamos C, Valencia O, Meineri M, Fletcher SN. The impact of internet and simulation-based training on transoesophageal echocardiography learning in anaesthetic trainees: a prospective randomised study. *Anaesthesia.* (2013) 68:621–7. doi: 10.1111/anae.12261
- Ferrero NA, Bortsov AV, Arora H, Martinelli SM, Kolarczyk LM, Teeter EC, et al. Simulator training enhances resident performance in transesophageal echocardiography. *Anesthesiology.* (2014) 120:149–59. doi: 10.1097/ALN.0000000000000063
- Weber U, Zapletal B, Base E, Hambrusch M, Ristl R, Mora B. Resident performance in basic perioperative transesophageal echocardiography: comparing 3 teaching methods in a randomized controlled trial. *Medicine.* (2019) 98:e17072. doi: 10.1097/MD.00000000000017072
- Fox KF. Simulation-based learning in cardiovascular medicine: benefits for the trainee, the trained and the patient. *Heart Br Card Soc.* (2012) 98:527–8. doi: 10.1136/heartjnl-2011-301314
- Sidhu HS, Olubaniyi BO, Bhatnagar G, Shuen V, Dubbins P. Role of simulation-based education in ultrasound practice training. *J Ultrasound Med Off J Am Inst Ultrasound Med.* (2012) 31:785–91. doi: 10.7863/jum.2012.31.5.785
- Thampi S, Lee CCM, Agrawal RV, Ashokka B, Ti LK, Paranjothy S, et al. Ideal sequence of didactic lectures and simulation in teaching transesophageal echocardiography among anesthesiologists. *J Cardiothorac Vasc Anesth.* (2020) 34:1244–9. doi: 10.1053/j.jvca.2019.12.011
- Ogilvie E, Vlachou A, Edsell M, Fletcher SN, Valencia O, Meineri M, et al. Simulation-based teaching versus point-of-care teaching for identification of basic transoesophageal echocardiography views: a prospective randomised study. *Anaesthesia.* (2015) 70:330–5. doi: 10.1111/anae.12903
- Prat G, Charron C, Repesse X, Coriat P, Bailly P, L'her E, et al. The use of computerized echocardiographic simulation improves the learning curve for transesophageal hemodynamic assessment in critically ill patients. *Ann Intensive Care.* (2016) 6:27. doi: 10.1186/s13613-016-0132-x

21. Bose RR, Matyal R, Warraich HJ, Summers J, Subramaniam B, Mitchell J, et al. Utility of a transesophageal echocardiographic simulator as a teaching tool. *J Cardiothorac Vasc Anesth.* (2011) 25:212–5. doi: 10.1053/j.jvca.2010.08.014
22. Smelt J, Corredor C, Edsell M, Fletcher N, Jahangiri M, Sharma V. Simulation-based learning of transesophageal echocardiography in cardiothoracic surgical trainees: A prospective, randomized study. *J Thorac Cardiovasc Surg.* (2015) 150:22–5. doi: 10.1016/j.jtcvs.2015.04.032
23. Bloch A, von Arx R, Etter R, Berger D, Kaiser H, Lenz A, et al. Impact of simulator-based training in focused transesophageal echocardiography: a randomized controlled trial. *Anesth Analg.* (2017) 125:1140–8. doi: 10.1213/ANE.0000000000002351
24. Adams BJ, Margaron F, Kaplan BJ. Comparing video games and laparoscopic simulators in the development of laparoscopic skills in surgical residents. *J Surg Educ.* (2012) 69:714–7. doi: 10.1016/j.jsurg.2012.06.006
25. McGaghie WC, Issenberg SB, Petrusa ER, Scalese RJ. Effect of practice on standardised learning outcomes in simulation-based medical education. *Med Educ.* (2006) 40:792–7. doi: 10.1111/j.1365-2929.2006.02528.x
26. Lin Y, Cheng A, Hecker K, Grant V, Currie GR. Implementing economic evaluation in simulation-based medical education: challenges and opportunities. *Med Educ.* (2018) 52:150–60. doi: 10.1111/medu.13411
27. Keogh-Brown MR, Bachmann MO, Shepstone L, Hewitt C, Howe A, Ramsay CR, et al. Contamination in trials of educational interventions. *Health Technol Assess Winch Engl.* (2007) 11:107. doi: 10.3310/hta11430

Conflict of Interest: The authors declare that the research was conducted in the absence of any commercial or financial relationships that could be construed as a potential conflict of interest.

Copyright © 2021 Pezel, Bernard, Lavie Badie, Dreyfus, Audureau, Bohbot, Fard, Hubert, Nguyen, Monteil, Bière, Le Ven, Canu, Ribeyrolles, Mion, Mouhat, Bazire, Fauvel, Ternacle, Cautela, Cambet, Le Tourneau, Donal, Lafitte, Mansencal and Coisne. This is an open-access article distributed under the terms of the Creative Commons Attribution License (CC BY). The use, distribution or reproduction in other forums is permitted, provided the original author(s) and the copyright owner(s) are credited and that the original publication in this journal is cited, in accordance with accepted academic practice. No use, distribution or reproduction is permitted which does not comply with these terms.



Etiology-Discriminative Multimodal Imaging of Left Ventricular Hypertrophy and Synchrotron-Based Assessment of Microstructural Tissue Remodeling

Filip Loncaric^{1*}, Patricia Garcia-Canadilla^{1†}, Ana Garcia-Alvarez^{1,2}, Laura Sanchis², Susana Prat², Adelina Doltra², Eduard Quintana², Daniel Pereda², Hector Dejea^{3,4}, Anne Bonnin³, Marta Sitges^{1,2,5} and Bart Bijns^{1,6}

¹ Institut d'Investigacions Biomèdiques August Pi i Sunyer, Barcelona, Spain, ² Cardiovascular Institute, Hospital Clínic and Universitat de Barcelona, Barcelona, Spain, ³ Photon Science Department, Paul Scherrer Institut, Villigen, Switzerland, ⁴ Eidgenössische Technische Hochschule Zurich, Zurich, Switzerland, ⁵ Centro de Investigación en Red de Enfermedades Cardiovasculares (CERCA), Madrid, Spain, ⁶ Institució Catalana de Recerca i Estudis Avançats, Barcelona, Spain

OPEN ACCESS

Edited by:

Savvas Loizos,
Hygeia Hospital, Greece

Reviewed by:

Ali Yilmaz,
University Hospital Münster, Germany
Emmanuel Androulakis,
Royal Brompton & Harefield NHS
Foundation Trust, United Kingdom

*Correspondence:

Filip Loncaric
loncaric.filip@gmail.com

[†]These authors have contributed
equally to this work

Specialty section:

This article was submitted to
Cardiovascular Imaging,
a section of the journal
Frontiers in Cardiovascular Medicine

Received: 22 February 2021

Accepted: 07 April 2021

Published: 25 May 2021

Citation:

Loncaric F, Garcia-Canadilla P, Garcia-Alvarez A, Sanchis L, Prat S, Doltra A, Quintana E, Pereda D, Dejea H, Bonnin A, Sitges M and Bijns B (2021) Etiology-Discriminative Multimodal Imaging of Left Ventricular Hypertrophy and Synchrotron-Based Assessment of Microstructural Tissue Remodeling. *Front. Cardiovasc. Med.* 8:670734. doi: 10.3389/fcvm.2021.670734

Background: Distinguishing the etiology of left ventricular hypertrophy (LVH) is clinically relevant due to patient outcomes and management. Easily obtained, echocardiography-based myocardial deformation patterns may improve standard non-invasive phenotyping, however, the relationship between deformation phenotypes and etiology-related, microstructural cardiac remodeling has not been reported. Synchrotron radiation-based X-ray phase-contrast imaging (X-PCI) can provide high resolution, three-dimensional (3D) information on myocardial microstructure. The aim of this pilot study is to apply a multiscale, multimodality protocol in LVH patients undergoing septal myectomy to visualize *in vivo* and *ex vivo* myocardial tissue and relate non-invasive LVH imaging phenotypes to the underlying synchrotron-assessed microstructure.

Methods and findings: Three patients (P1-3) undergoing septal myectomy were comprehensively studied. Medical history was collected, and patients were imaged with echocardiography/cardiac magnetic resonance prior to the procedure. Myocardial tissue samples obtained during the myectomy were imaged with X-PCI generating high spatial resolution images (0.65 μ m) to assess myocyte organization, 3D connective tissue distribution and vasculature remodeling. Etiology-centered non-invasive imaging phenotypes, based on findings of hypertrophy and late gadolinium enhancement (LGE) distribution, and enriched by speckle-tracking and tissue Doppler echocardiography deformation patterns, identified a clear phenotype of hypertensive heart disease (HTN) in P1, and hypertrophic cardiomyopathy (HCM) in P2/P3. X-PCI showed extensive interstitial fibrosis with normal 3D myocyte and collagen organization in P1. In comparison, in P2/P3, X-PCI showed 3D myocyte and collagen disarray, as well as arterial wall hypertrophy with increased perivascular collagen, compatible with sarcomere-mutation HCM in both patients. The results of this pilot study suggest the association of non-invasive deformation phenotypes with etiology-related myocyte and connective tissue matrix disorganization. A larger patient cohort could

enable statistical analysis of group characteristics and the assessment of deformation pattern reproducibility.

Conclusion: High-resolution, 3D X-PCI provides novel ways to visualize myocardial remodeling in LVH, and illustrates the correspondence of macrostructural and functional non-invasive phenotypes with invasive microstructural phenotypes, suggesting the potential clinical utility of non-invasive myocardial deformation patterns in phenotyping LVH in everyday clinical practice.

Keywords: hypertrophic cardiomyopathy, hypertension, myocardial disarray, fibrosis, remodeling, synchrotron, speckle tracking, cardiac magnet resonance

INTRODUCTION

Distinguishing sarcomere protein gene mutation hypertrophic cardiomyopathy (HCM) from other etiologies of left ventricular hypertrophy (LVH) is clinically relevant, given the association with elevated risk for sudden death, familial inheritance, and different pharmacological management. The contemporary approach to diagnosing LVH is based on non-invasive multimodality imaging [echocardiography and magnetic resonance (CMR)] – where LV chamber size/shape remodeling, distribution of hypertrophy/fibrosis, and functional alterations form the basis for diagnosis (1, 2). Cardiac mechanics are influenced by the structural and pathophysiological processes underlying the LV remodeling. Therefore, easily obtained, echocardiography-based myocardial deformation patterns, reflecting cardiac mechanics and suggested as highly characteristic for specific etiologies (3), may improve phenotyping when added to the traditional data integration. Nevertheless, the relationship between deformation phenotypes and etiology-related microstructural cardiac remodeling has not been reported. While relatively novel in the field of cardiac imaging, synchrotron radiation-based X-ray phase-contrast imaging (X-PCI) can provide high resolution, three-dimensional (3D) histological information on myocardial microstructure *ex vivo* non-destructively (4–7) – providing a novel approach to visualize complex structural changes related to remodeling in different disease etiologies.

The aim of this pilot study is to apply a multiscale, multimodality protocol in LVH patients undergoing septal myectomy to visualize *in vivo* and *ex vivo* myocardial tissue with non-invasive and X-PCI imaging, respectively, and relate non-invasive LVH imaging phenotypes to the underlying synchrotron-assessed microstructure (Figure 1).

METHODS

Patients Under Study

The population under study were three patients (P1-3) with obstructive LVH referred for septal myectomy from the familial cardiomyopathy outpatient clinic. At the moment of inclusion, a clinical interview was performed. Medical history was reviewed and data on demographic characteristics, cardiovascular risk factors, comorbidities, pharmacological treatment was collected.

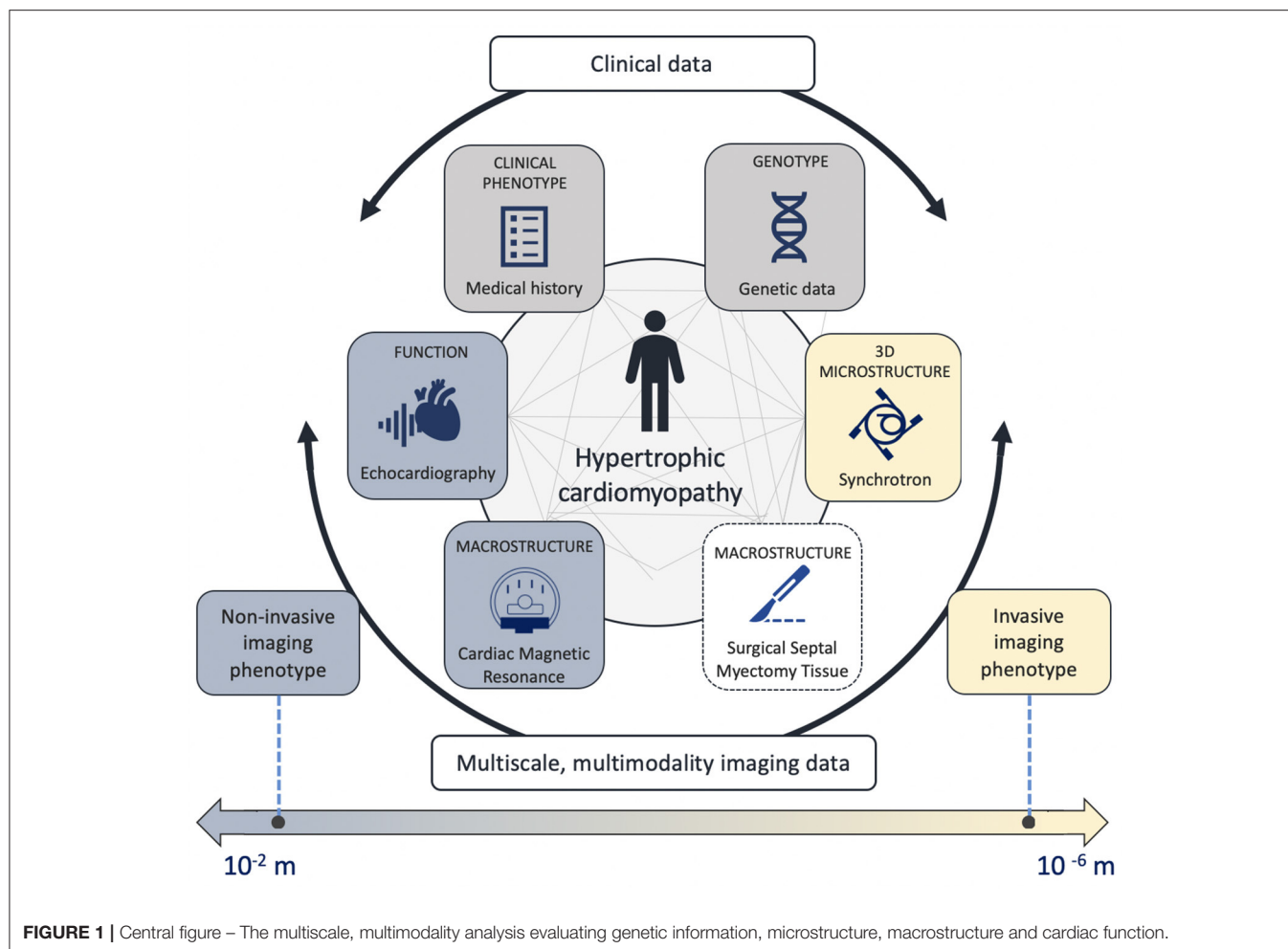
The 5-year HCM risk score was evaluated (8). Upper arm cuff blood pressure measurement in the sitting position was performed directly preceding the echo examination. Genomic DNA was obtained from peripheral blood and analyzed using NGS technology (*MiSeq*, *Illumina*). The most prevalent gene mutations involved in cardiomyopathies were scanned (i.e., hypertrophic cardiomyopathy (CM), laminopathies, Danon disease, dilatative CM, arrhythmogenic CM, non-compaction CM, Marfan syndrome, long QT syndrome, Holt-Oram, Ehlers-Danlos, and Brugada syndrome). A generational family pedigree was assessed to explore the genetic origin of disease.

Echocardiography

All participants underwent a comprehensive transthoracic echocardiographic examination, prior to the surgical myectomy, performed on a commercially available E95 system (*GE, Vingmed Ultrasound*, *Horten, Norway*) equipped with a 4Vc transthoracic transducer. In addition to full two-dimensional and Doppler echocardiography, additional parasternal short-axis, and 4-chamber, 2-chamber, and 3-chamber apical acquisitions with appropriate frame rates were obtained for speckle-tracking and Tissue Doppler analysis, respectively.

LV and LA volumes were assessed in the apical 4- and 2-chamber views. LV ejection fraction was calculated by using the biplane Simpson method. LA volumes were indexed to the BSA. Cardiac dimensions were measured in appropriate 2D views, as according to current guidelines (9). LV mass was calculated using the linear method and normalized by body surface area, whereas hypertrophy was defined as $>88 \text{ g/m}^2$ in females and $>102 \text{ g/m}^2$ in males (9). Relative wall thickness (RWT) was calculated by dividing the doubled value of the end-diastolic posterior wall thickness with the end-diastolic internal diameter of the LV. The type of LV remodeling was determined based on the RWT and indexed LV mass.

Resting LVOT peak velocity was measured by using continuous-wave Doppler echocardiography, and the LVOT pressure gradient peak estimated by using a simplified Bernoulli equation. The maximal LVOT gradient was defined as the highest recorded gradient, either in rest or during Valsalva maneuver. Pulsed-wave Doppler was performed in the apical 4-chamber view by placing the sample volume at the level of the leaflet tips to obtain mitral inflow velocities. Peak velocity of early (E) and late (A) diastolic filling, E velocity deceleration time and A wave duration were measured, and the E/A ratio calculated.



Isovolumic relaxation time (IVRT) was measured as the time difference between aortic valve closure and mitral valve opening as assessed in the five-chamber view using continuous-wave Doppler of the LV outflow tract. Tissue Doppler was used to measure early and late diastolic mitral annular velocity at the septal (e' and a' septal) and lateral (e' and a' lateral) annular sites. Myocardial deformation of the left ventricle (LV) was assessed with speckle tracking echocardiography (STE) on 2D grayscale images obtained from the three apical cardiac views and with tissue Doppler deformation imaging (TDI) in the 4-chamber view – both using GE Echopac software (*GE Medical Systems, version 202.41.0*). The endocardial border was manually marked at end-systole of the LV. A region of interest with six segments was automatically generated. If needed, manual adjustments were performed to achieve optimal tracking. Longitudinal strain curves were generated and end-systolic strain, defined by the aortic valve closure time, measured. The LV global longitudinal strain was calculated by averaging values of the 18 segments. The focus of analysis was the basal and mid septal region, as this is where myocardial tissue is removed during septal myectomy. Regional deformation was therefore explored by placing the region of interest (ROI) in different parts of the interventricular

septum. TDI-derived deformation was assessed using color-coded maps of myocardial deformation and by determining ROIs to generate regional TDI-derived longitudinal strain curves of myocardial areas within the adjacent ventricular segment.

Cardiac Magnetic Resonance Imaging

All cardiac magnetic resonance (CMR) exams were performed in a 3.0 Tesla scanner (Signa Architect, General Electric Healthcare), equipped with a 32-channel chest coil. All images were ECG-triggered and obtained in apnea. Standard short axis SSFP cines were obtained (slice thickness 6–8 mm, 2–4 mm gap) in order to calculate left and right ventricular volumes and function. Additionally, 4-, 3-, and 2-chamber SSFP cines were acquired. A standard phase contrast in-plane flow sequence in a 3-chamber view orientation (or a similar orientation with a good visualization of the LV outflow tract) was acquired in order to assess for the presence of flow obstruction. An additional through-plane phase contrast image was obtained at the point of maximal turbulence; VENC was appropriately adjusted in each case to avoid aliasing. A perfusion sequence in three standard short axis orientations (basal, midventricular and apical) was obtained after administration of a single bolus

of gadolinium-based contrast (0.15 mmol/kg). Seven min after contrast administration a standard Look-Locker sequence was acquired and the optimal inversion time selected for each patient. Immediately after, late gadolinium enhancement imaging (inversion recovery gradient echo and PSIR sequences) was acquired using the same imaging planes, slice thickness and spacing as the cine images; inversion time was adjusted during the acquisition, if necessary.

Surgical Myectomy and Tissue Handling

Septal tissue samples were obtained as a part of the planned surgical procedure performed at the center. Patients underwent myectomy as previously described (10). No additional invasive procedure was performed beyond the ones indicated for the management of the patient's clinical condition. The tissue that was removed by the expert judgement of the cardiac surgeon. The number and size of tissue specimens were dependent on the predisposing patient anatomy. The tissue was initially placed in a vile with a heparin solution, and afterwards fixed and stored in a formalin solution at room temperature in a standard formalin container regularly used in the clinical setting (*DiaPath SafeCapsule 31.7 ml*). Tissue samples were measured and photographed for reference.

Synchrotron Imaging and Data Analysis

Samples were imported to the TOMCAT beamline at Swiss Light Source (*Villigen, Switzerland*) according to the participating institution's ethical recommendations and the governing international legal requirements. Due to limited available beamtime, only the largest removed pieces of tissue were selected for scanning. The tissue was imaged using X-PCI. A multiscale protocol combining a low-resolution (LR) and a high-resolution (HR) setup (5.8 and 0.65 μm pixel size, respectively) was used (7). Briefly, the tissue sample was introduced in a tube with deionized degassed water in order to minimally affect the tissue structural conditions and avoid bubble formation. After positioning the sample on the rotation stage, image acquisition was performed using a 20 keV parallel synchrotron X-ray beam. The sample was first imaged at LR (5,001 projections, exposure time = 30 ms, field of view (FoV) = $11.83 \times 3.29 \text{ mm}^2$, 360° rotation) with a sample-detector distance of 333 cm. X-rays were converted to visible light through a LuAG:Ce 300 μm scintillator and detected by a sCMOS camera (PCO Edge 4.2). LR scans correspond well to traditional histology (11), enabling a non-destructive evaluation of the overall morphology of the septal tissue – allowing visualization of the endocardium, an overview of myocyte organization to locate regional disruptions, and the identification of patches of replacement fibrosis or areas with interstitial fibrosis. Furthermore, LR scans were also used to select several ROIs to be imaged at HR (2,501 projections, exposure time = 220 ms, FoV $1.64 \times 1.38 \text{ mm}^2$, 180° rotation), with a sample-detector distance of 20 cm, a LuAG:Ce 20 μm scintillator and a PCO.Edge 5.5 CMOS detector. Additionally, 50 pre-flat, 50 post-flat and 50 dark images were acquired for flat-field and dark-field corrections of each acquisition. The acquired projections were reconstructed using the Gridrec algorithm. In the case of HR, the single distance phase retrieval

method developed by Paganin was applied (12, 13) using specific ring correction (14). Several overlapping scans were acquired to cover the full sample in LR or the full ROI in HR. These scans were later stitched in order to obtain full sample/ROI datasets. HR images enabled assessment of individual myocyte organization, vessels morphology and collagen distribution.

X-PCI datasets were visualized and analyzed with *Fiji* (stitching/cropping) (15) and the open-source software *Ilastik* (collagen segmentation) (16) with the aim of reproducible segmentations of the different microstructural components. Specifically, the pixel classification workflow of *Ilastik* was used for collagen segmentation. Finally, 3D slicer was used to generate the 3D volume renders of segmented collagen (17).

RESULTS

Non-Invasive Imaging Phenotypes – Macrostructure and Function

Information on family history of HCM, demographic data and medical history is shown in **Table 1**, and additional echocardiographic measurements in **Supplementary Table 1**. All patients had severe symptomatic LV outflow tract obstruction with systolic anterior motion (SAM) of the mitral valve. The non-invasive imaging for P1-3 is illustrated in **Figures 2–4**.

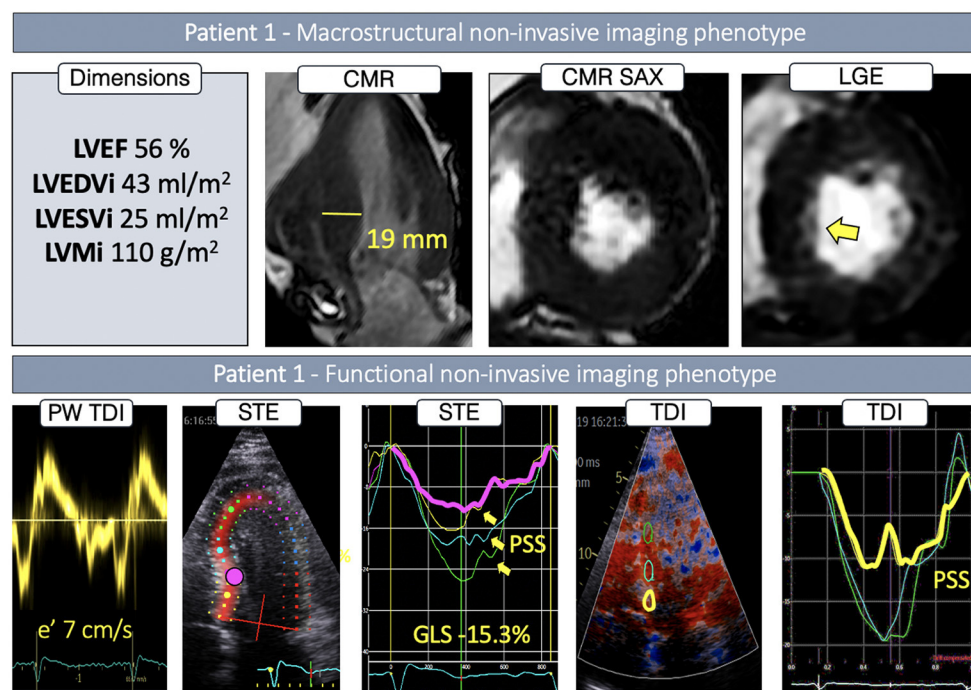
P1 had normal LV cavity dimensions, showing concentric LVH combined with pronounced basal anteroseptal hypertrophy (19 mm) (**Figure 2**), while LGE showed traces of septal intramyocardial and pronounced endocardial fibrosis (**Figure 2**, first row, yellow arrow). Global longitudinal strain was reduced, whereas regional STE deformation analysis revealed impaired deformation at both the basal, basal/mid and mid septum (**Figure 2**, yellow, pink and blue curves), associated with post-systolic shortening (PSS) (**Figure 2**, yellow arrows). Upon further exploration with TDI, areas with reduced deformation and PSS were identified in the basal septum.

P2 had normal LV dimensions and an asymmetric LVH localized in the inferoseptal region (17 mm) (**Figure 3**), with focal intramyocardial enhancement in the basal and mid inferior septum and both right ventricular insertion points (**Figure 3**, first row, yellow arrows). While global longitudinal strain was only slightly reduced, septal regional STE deformation analysis showed a heterogeneous deformation pattern: reduced, but normally profiled deformation in the basal segment (**Figure 3**, yellow curve), virtually completely absent deformation on the transition from basal to mid region (**Figure 3**, pink curve), and normalizing deformation toward the apex (**Figure 3**, blue and green curves). Exploration with color-coded TDI and TDI deformation curves confirmed these findings visualizing an isolated area with very abnormal deformation in the transition from basal to mid septum (**Figure 3**, blue septal region in the color-coded TDI, blue strain curve).

P3 had a slightly dilated LV, with an extreme, asymmetric LVH, localized throughout the whole septum (37 mm), and paired with severe enhancement in the septum and inferior interventricular junction (**Figure 4**). While ejection fraction was supranormal, global longitudinal strain and septal e' velocity

TABLE 1 | Clinical data and medical history.

	Patient 1	Patient 2	Patient 3
Age (years)	64	50	32
Gender	Male	Male	Female
Body mass index (kg/m ²)	32.0	26.5	22.8
Arterial hypertension	Yes	No	No
Diabetes mellitus	Yes	No	No
Hyperlipidemia	Yes	No	No
Sleep apnea	Yes	No	No
Atrial fibrillation	Paroxysmal	No	No
New York Heart Association Functional Classification	III	III	III
Known family history of HCM	–	Brother had obstructive HCM and underwent septal myectomy	–
Family history of SCD	No	No	No
Cardiac sarcomere protein gene mutations	Negative for tested variants	MYH7	Negative for tested variants
History of unexplained presyncope or syncope	No	No	Yes
History of arrhythmia	No	Non-sustained ventricular tachycardia (2017)	No
5-year HCM risk (%)	2.09	6.25	4.88

**FIGURE 2** | Non-invasive imaging phenotype of P1.

was severely reduced. Septal regional STE deformation analysis showed completely abnormal deformation throughout the basal and mid region (**Figure 4**, yellow, pink and blue curves), returning to normal values in the apex (**Figure 4**, green curve). Color-coded TDI and TDI deformation curves, based on smaller, more focused regions of interest, revealed an underlying heterogeneous deformation pattern. Deformation in the basal region was, in fact, normal (**Figure 4**, yellow curve), whereas the transition from

basal to mid septum showed completely abnormal deformation (**Figure 4**, blue curve), slowly recovering toward the apical region (**Figure 4**, green curve).

Invasive Imaging Phenotypes – Microstructure

After surgical removal in P1, the septal tissue showed a smooth endocardial fibrotic layer which could be visualized

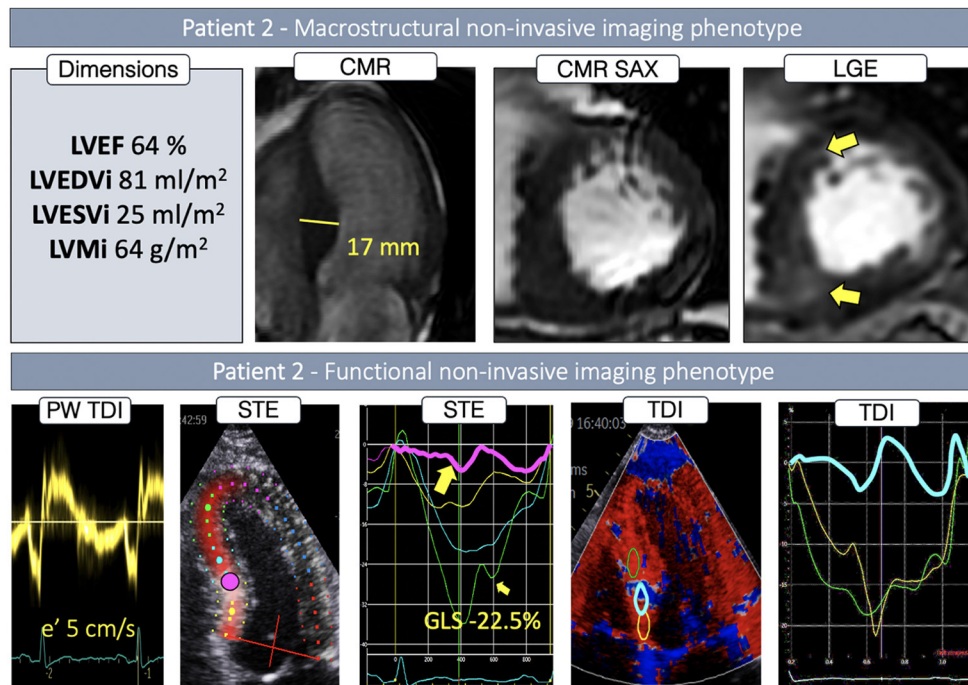


FIGURE 3 | Non-invasive imaging phenotype of P2.

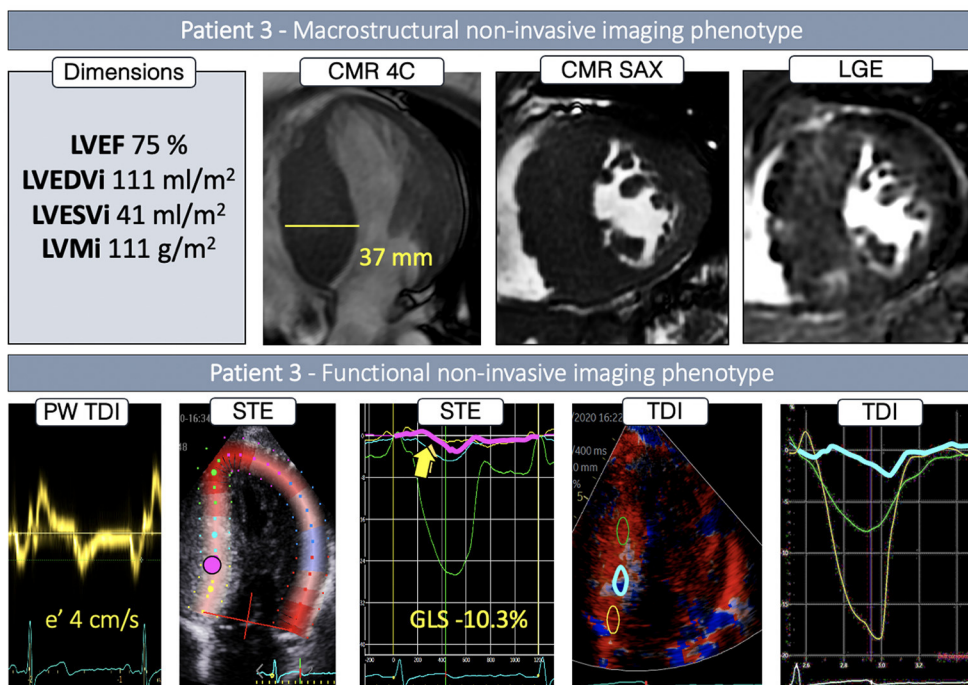


FIGURE 4 | Non-invasive imaging phenotype of P3.

with LR, and the underlying collagen organization with HR X-PCI (Figure 5A, orange frame, Supplementary Video 1, 2). HR revealed extensive interstitial fibrosis surrounding normally

arranged myocytes (Figure 5A, yellow frame). The segmented 3D collagen distribution was visualized (Figure 5A, second row, collagen shown in blue, Supplementary Video 3), demonstrating

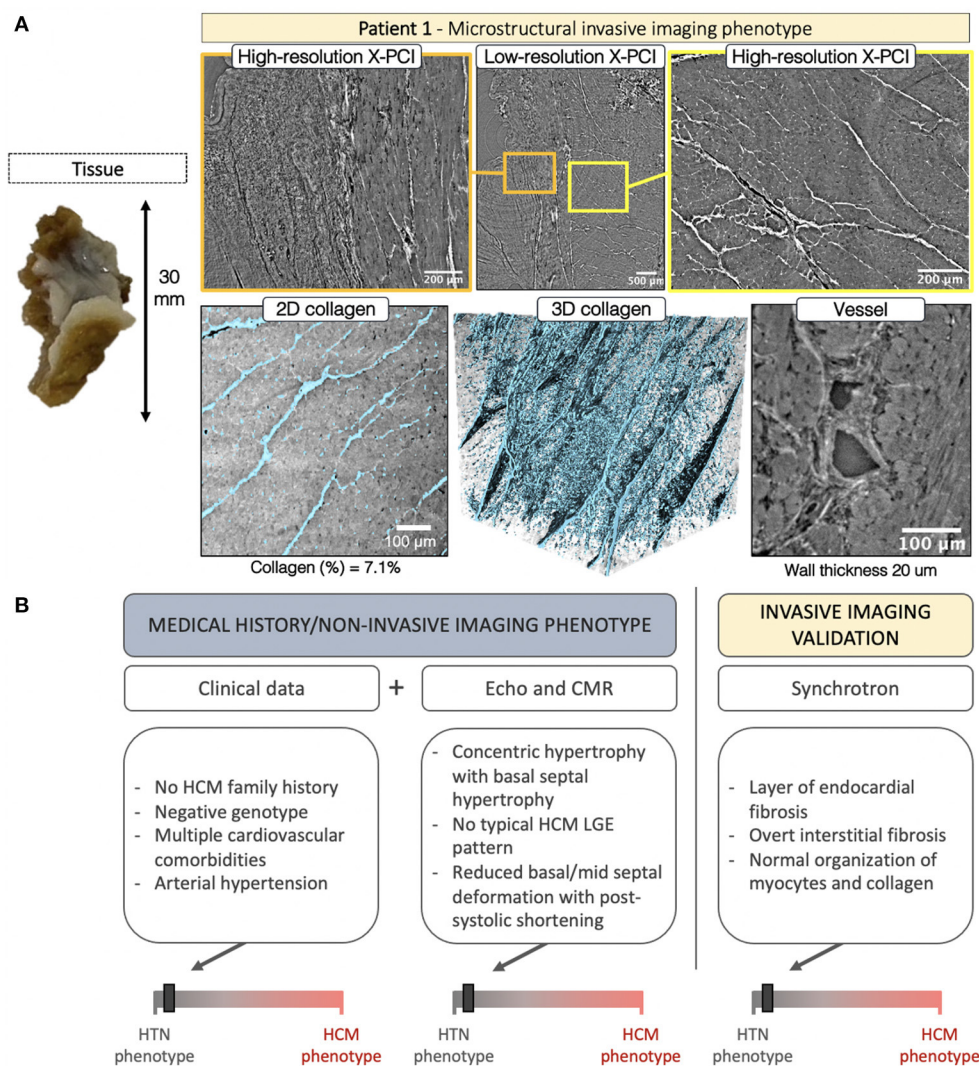


FIGURE 5 | (A) Invasive imaging phenotype of P1. **(B)** Clinical data described a patient with no family history of HCM, negative genotype, and a burden of cardiovascular comorbidities, including arterial hypertension. The non-invasive imaging concurred with the HTN clinical phenotype showing basal septal hypertrophy with no typical HCM LGE pattern and a characteristic hypertensive spatiotemporal deformation pattern in the basal and mid septum coupled with post-systolic deformation. The invasive imaging confirmed the non-invasive-imaging-based HTN phenotype with findings of normal myocyte, collagen and blood vessel organization.

extensive (quantified at 7.1% in the selected volume), but spatially normally organized, fibrosis. A blood vessel is shown with normal dimensions, normal perivascular collagen, and mild wall hypertrophy (20 μ m). The integration of clinical data for P1 is shown in **Figure 5B**.

In P2 the septal tissue revealed a localized (likely related to the SAM impact) fibrotic patch on the endocardial side (**Figure 6A**, yellow arrow). LR revealed regions of normal myocardial organization (**Figure 6A**, orange frame) alternated with patches of myocyte disarray (**Figure 6A**, yellow frame, **Supplementary Video 4**). Disarray was further explored with HR. Visualization of the 3D collagen distribution (**Figure 6A**, second row, collagen shown in blue) showed

increased fibrosis (13.4%), highly disorganized, except in the smaller regions of normal organization (**Figure 6A**, yellow arrow, **Supplementary Video 5**). The vasculature revealed abnormal vessels with intima/media hypertrophy (45 μ m) and increased perivascular collagen. The integration of data for P2 is shown in **Figure 6B**.

Septal myocardial samples from P3 showed no pronounced fibrotic patch visible on the endocardial side. LR, further enhanced with HR, revealed hypertrophied myocytes with overt myocyte disarray, interlaced with small patches of normal organization (**Figure 7A**, yellow frame, **Supplementary Video 6**). In the acquired tissue sample, collagen was not increased (1.9%), but showed spatial disarray (**Supplementary Video 7**).

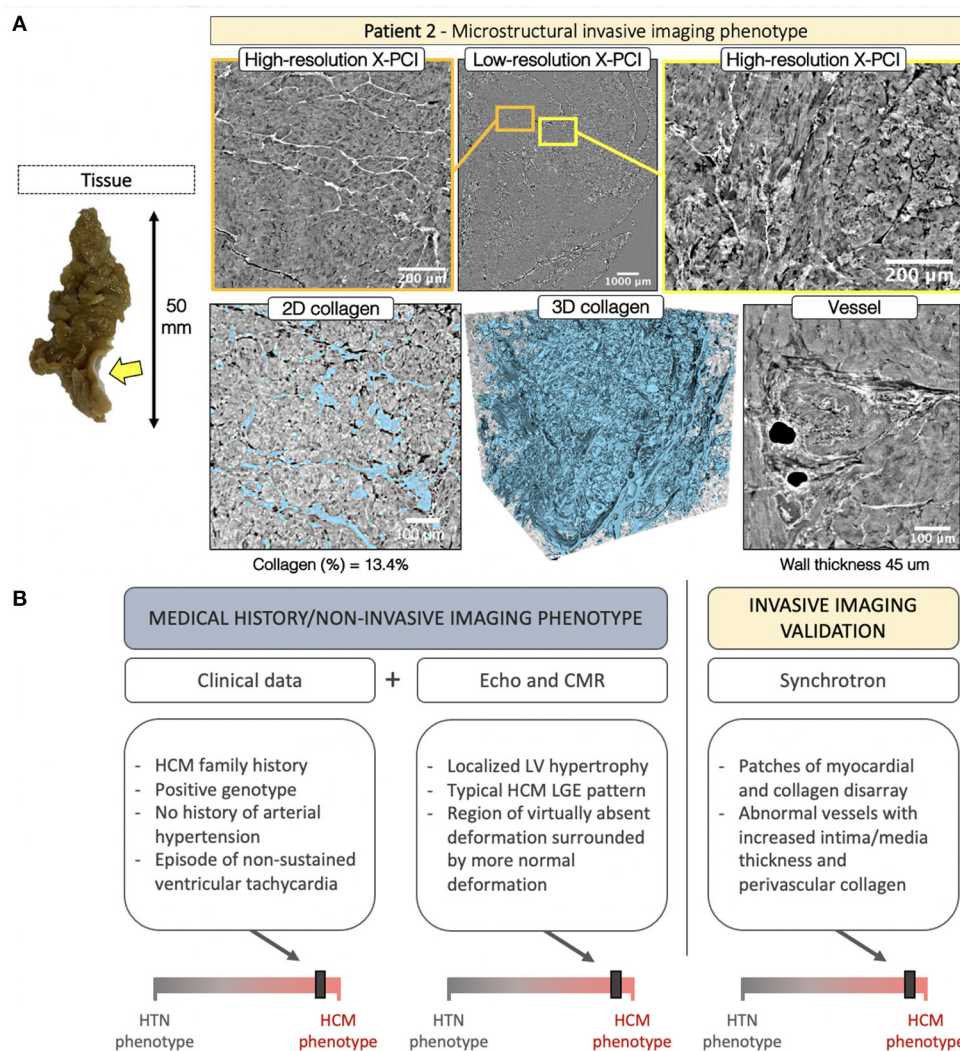


FIGURE 6 | (A) Invasive imaging phenotype of P2. **(B)** Clinical data described a patient with family history of obstructive HCM, history of arrhythmic episodes, and a positive genotype. Here, non-invasive imaging confirmed the clinical HCM phenotype. Although localized basal septal hypertrophy can also be seen in hypertension, the deformation pattern was characteristic of HCM, and the LGE findings concurred. Invasive imaging validated the non-invasive-imaging-based HCM remodeling phenotype with findings of myocardial disarray, abnormal collagen organization and hypertrophied blood vessels.

Pronounced hypervascularization was noted throughout the sample with an increased number of blood vessels, combined with wall hypertrophy (39 μ m) and increased perivascular collagen.

DISCUSSION

In this pilot study we demonstrate a unique multiscale, multimodality protocol to visualize *in vivo* and *ex vivo* myocardial tissue with non-invasive and X-PCI imaging. We report a novel approach to visualize 3D cardiac microstructure in LVH and relate the findings to the etiology-discriminative interpretation of non-invasive imaging data. The findings are hypothesis-generating, providing insights about the relationship

of myocyte and connective tissue matrix spatial disorganization and myocardial deformation – thus suggesting the potential clinical utility of deformation patterns in phenotyping left ventricular hypertrophy.

The Functional Consequences of Myoarchitectural Abnormalities

X-PCI has proven as a powerful tool for visualizing cardiac microstructure in cardiac biopsies of rat models, human fetal hearts, as well as in endomyocardial biopsies of heart transplantation patients. The modality enables imaging up to the scale of an individual myocyte, demonstrating feasibility of quantification of fiber orientation, vessels and collagen from multiscale 3D datasets; enabling multiresolution, 3D,

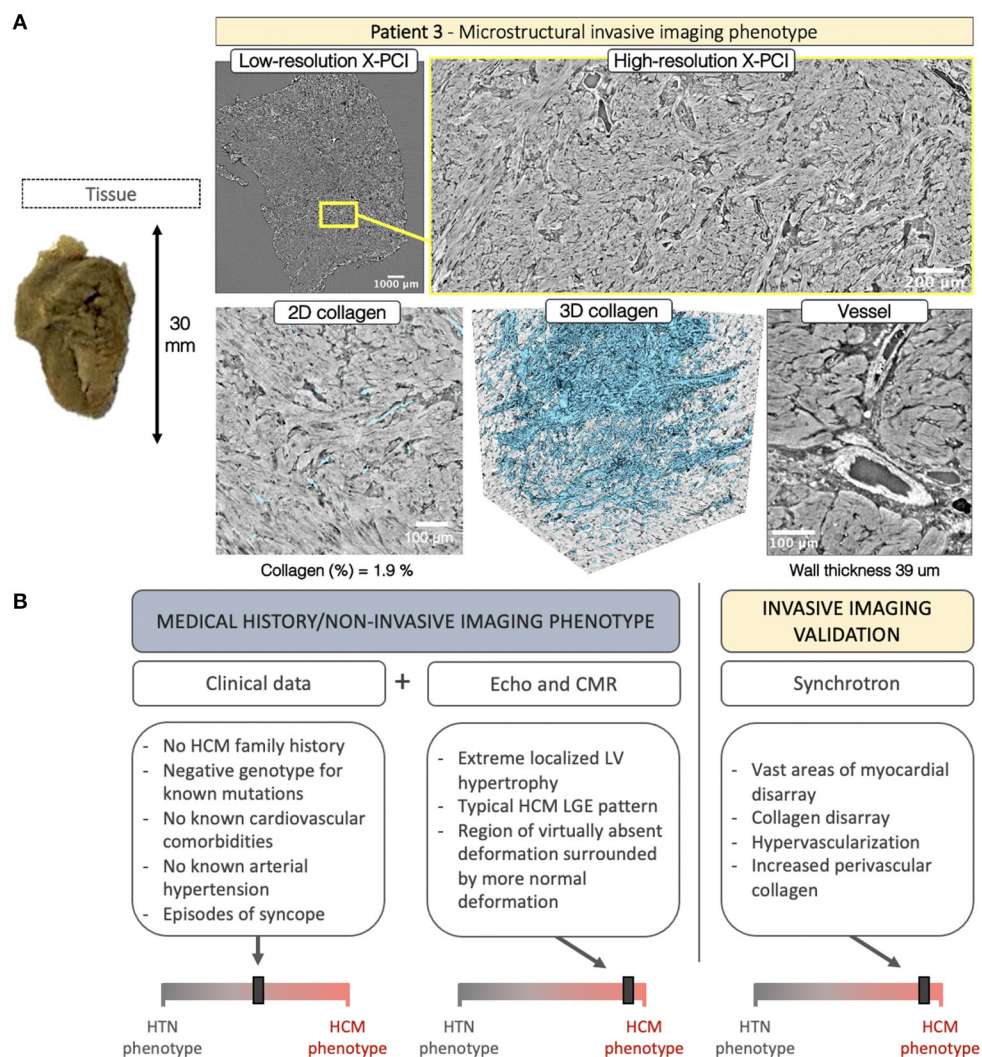


FIGURE 7 | (A) Invasive imaging phenotype of P3. **(B)** Clinical data was inconclusive, revealing negative family history of HCM, lack of cardiovascular comorbidities, a history presyncope, and a genotype negative for the most common mutations associated with HCM. Here, non-invasive imaging played a crucial role in revealing the etiology – showing extreme wall thickening in the septal region, with a characteristic HCM deformation pattern, and severe LGE in the septum. Invasive imaging confirmed the non-invasive-imaging HCM remodeling phenotype with findings of vast myocardial disarray, collagen disarray, hypervascular tissue and hypertrophied blood vessels.

quantitative *ex vivo* analysis of cardiac microstructure, without the need for artifact prone slice-processing that strains histological/microscopic reconstruction (4, 5, 7, 18). In our study, X-PCI and the subsequent analysis - applying machine-learning solutions to provide automated, 3D segmentations of myocardial structure - enabled a novel way to visualize and quantify the complex microstructural abnormalities that inherently influence cardiac mechanics in LVH.

The histological findings of myocyte (19, 20) and connective tissue matrix (21, 22) disorganization in HCM has evoked research relating abnormal myocardial architecture to LV function. A transgenic HCM mouse model demonstrated decreased sarcomere length and impaired systolic shortening in

regions of myocardial hypertrophy (23). In human hearts non-invasive imaging, histology, and *in vitro* experiments suggested an association between disarray, fibrosis, active contraction *in vitro*, and STE-derived deformation *in vivo* (24, 25). Similarly, diffusion tensor CMR and CMR-derived strain rate imaging inferred intramural disarray correlated with both active and passive myocardial function (26). The intrinsic contractile dysfunction can be recognized with deformation imaging even at the early disease stages, before onset of LVH (27). This described relationship between abnormal myoarchitecture and cardiac mechanics in HCM is captured by characteristic deformation patterns, easily obtained in everyday workflow, and potentially clinically useful in the process of distinguishing LVH

etiologies, especially when integrated with remaining clinical and imaging findings.

The Challenge of Distinguishing Disease Etiologies

Clinical practice relies on interpretation of available clinical information for diagnosis in LVH – medical history and physical examination, genetic analysis for the most frequent mutations, and insights gained from non-invasive cardiac imaging (28). The challenge for a genetic diagnosis is the considerable genetic heterogeneity of HCM, where the underlying genetic cause is only found in a percentage of patients fitting the phenotype (29). In our analysis, P3 had a “textbook” microstructural, macrostructural, and functional HCM phenotype, however, the genotyping approach was unsuccessful in identifying the causative genetic mutation strongly suggested to be present. Differentiating HCM from hypertensive heart disease is a process based on integrating findings from clinical history and multimodal non-invasive imaging – the distribution of LVH and LGE, frequency of LV outflow tract obstruction, severity of longitudinal dysfunction, functional asynchrony and deformation heterogeneity (2). Such integration is shown in **Figures 5B, 6B, 7B**. In this analysis, echo-based regional deformation patterns, reflective of the influence of structural and pathophysiological processes in LV remodeling on cardiac mechanics, are easily accessible and of potential clinical use (3).

The echocardiographic finding of basal septal hypertrophy has been shown to be a morphological marker of increased afterload in arterial hypertension (30, 31). Here intra-ventricular heterogeneity is the consequence of heterogeneous wall stress distribution in response to elevated blood pressure. In an average heart, the septum has a greater radius of curvature compared to the free wall (32, 33), leading to a disproportionately higher wall stress in the basal parts in the setting of high systemic pressure (33). This results with an imbalance between locally developed force and wall stress, and, consequently, decreased local deformation and PSS. Thus, in HTN, prolonged exposure to increased afterload can result in compensatory localized basal septal hypertrophy in an attempt to normalize wall stress and maintain deformation (3), and ultimately lead to LV outflow obstruction (34). Localized hypertrophy in HTN, as seen in P1 and opposed to P2, was associated with microstructurally described overt interstitial fibrosis (not clearly inferred by LGE), showing organized 3D structure of the collagen surrounding normally arranged myocytes. These microstructural findings support the hypertensive etiology of the hypertrophy, especially when combined with the HTN-related deformation pattern – reduction in peak systolic strain (30, 35) and PSS occurring in the basal and mid-septum (36).

Another type of intra-ventricular heterogeneity can be seen in HCM, where, as compared to the heterogeneity of loading in HTN, the heterogeneity is in the tissue structure itself. In our study, X-PCI of HCM myocardial tissue revealed both myocyte and connective tissue matrix 3D disorganization or disarray. The heterogeneous tissue and

compensatory hypertrophy leads to high variability in regional myocardial wall thickness and characteristic regional contractile heterogeneity (37–40). The structural finding of basal septal hypertrophy in HCM commonly overlaps with that seen in HTN (e.g., P1 vs. P2), however, with clearly different patterns of deformation. In P2 and P3, we noted a heterogeneous septal deformation pattern, with localized parts of the septum showing virtually absent deformation, unlike that seen in HTN, while surrounding regions show normal deformation pattern (with/without reduced amplitude).

Regional longitudinal strain is still burdened by reproducibility and inter-vendor variability (41–43). Nevertheless, regional spatiotemporal strain patterns contain important diagnostic information (3, 41), and remain consistent despite underlying variability in inter-observer segmentations and regional peak strain values (44). The results of this pilot study are hypothesis-generating, suggesting non-invasive deformation phenotypes are associated with etiology-related myocyte and connective tissue matrix 3D disorganization, thus inferring the potential clinical value of deformation patterns in everyday clinical analysis and phenotyping LV hypertrophy.

Scientific and Clinical Implications

The ability to explore microstructural organization is essential for understanding myocardial mechanics and resolving the etiology of non-invasive imaging phenotypes in LV hypertrophy. In contemporary translational research, electro-mechanical computational models of the heart integrate multiscale and multimodal imaging, and apply novel methods of data extraction from large datasets and across different resolutions, with the aim toward deciphering mechanistic descriptors of personalized structure and function (45). Detailed information on fiber orientation and fibrosis organization can be integrated to these models (46), a concept particularly relevant in HCM (47). Previously, fiber structure information has been extracted from diffusion tensor imaging (at low resolution) or localized microscopy (48), but this may be advanced with high resolution, 3D X-PCI data. Derived information about disease-specific patterns could help relate structural and dynamic features measured *in vivo* with high-resolution characterization of microstructure *ex vivo*, enabling personalized modeling of cardiac biomechanics, potentially bringing incremental insights to disease pathophysiology and tailoring risk assessment (49).

In a more clinical perspective, continuing evidence point out the inconsistencies of the single sarcomere gene hypothesis in HCM, suggesting the need to incorporate the influences of numerous disease modifiers, each exerting a small effect on phenotype expression (50–52). Here, the opportunity to explore the structure-function relationship, through the insights of combined *in vivo* and *ex vivo* imaging is highly relevant. Applying this methodology enables quantification of myocardial structure abnormalities potentially associated to sarcomere protein gene mutations and clinical risk, even in patients with no signs of macrostructural remodeling when assessed with traditional non-invasive imaging. In comparison to X-PCI, histology is a destructive imaging method, relying on tissue preparation – slicing and staining, and of limited (2D) analysis. Multiscale

analysis with CMR may provide better soft tissue contrast, however, at much lower resolutions and/or prolonged scan time. Furthermore, CMR-based techniques rely on indirect measures of myocardial structure, through the use of contrast agents or diffusion tensor imaging, whereas with X-PCI we can directly measure myocardial structure based on changes in X-ray intensity and phase. On an important note, X-PCI is currently a research methodology, and as such it is linked to synchrotron facilities with limited accessibility. Integration of X-PCI technology in traditional hospital CT machines is for now still not feasible (53), but the developments in compact synchrotrons (54) and grating based X-PCI technology (55) may lead to a translation of this methodology toward clinical, *ex vivo* use – particularly for imaging tissue biopsies. Application of these tools has already been suggested – for clinically relevant topics such as the assessment of *ex vivo* endomyocardial tissue in heart transplantation patients to assess graft rejection with more reproducibility (56), or assessment *in vivo* to clarify ambiguous findings in traditional mammography (57).

Limitations

Our pilot study consisted of a detailed, multi-modality *in vivo* and *ex vivo* analysis of a small sample, with the goal of applying existing X-PCI technology to the field of cardiac imaging to provide a novel visualization of microstructural organization in LVH, and to generate a hypothesis of structure/function relations by linking these invasive findings to non-invasive imaging phenotypes. Nonetheless, no causation can be claimed based on these initial results. The results motivate larger patient cohorts to enable statistical analysis/group comparison, as well as the assessment of reproducibility of deformation patterns (44).

All imaged tissue samples were derived from surgical myectomy; therefore, the sample size was limited and potentially not representative of the heart as a whole. However, septal tissue has consistently demonstrated structural abnormalities in prior studies (22, 24, 25, 52).

CONCLUSIONS

High-resolution, 3D X-PCI provides novel ways to visualize myocardial remodeling in excised myectomy tissue, and illustrates the correspondence of macrostructural and functional non-invasive phenotypes with invasive microstructural phenotypes, suggesting the potential clinical utility of non-invasive myocardial deformation patterns in phenotyping left ventricular hypertrophy. A larger patient cohort could enable statistical analysis of established differences and the assessment of the reproducibility of deformation patterns.

DATA AVAILABILITY STATEMENT

The data presented in the study are deposited in the PSI Public Data Repository, accession number <http://doi.psi.ch/detail/10.16907%2Fb97cdb87-83be-4176-87f4-2e89679ff333>.

ETHICS STATEMENT

The studies involving human participants were reviewed and approved by Ethics Committee of the Hospital Clinic of Barcelona. The patients/participants provided their written informed consent to participate in this study.

AUTHOR CONTRIBUTIONS

FL: conception, design, analysis and interpretation of data, and drafting of the manuscript. PG-C: analysis and interpretation of data, drafting of the manuscript, revising for important intellectual content, and final approval of the manuscript submitted. AG-A, HD, and AB: conception and design, revising for important intellectual content, and final approval of the manuscript submitted. LS, SP, AD, EQ, and DP: revising for important intellectual content and final approval of the manuscript submitted. MS and BB: conception and design, interpretation of data, revising for important intellectual content, and final approval of the manuscript submitted. All authors contributed to the article and approved the submitted version.

FUNDING

This work was supported by the Horizon 2020 European Commission Project H2020-MSCA-ITN (764738) and the Clinical Research in Cardiology of the Spanish Foundation of the Heart grant from the Spanish Cardiac Society (SEC/FEC-INV-CLI 20/028). MS holds a grant from Fundacio La Marató de TV3 (040310, Exp 2015.40.30). HC has received funding from the Strategic Focal Area Personalized Health and Related Technologies (PHRT) of the ETH Domain (2017-303). PG-C has received funding from the post-doctoral fellowships programme Beatriu de Pinós (2018-BP-00201) and the Horizon 2020 European Commission Project H2020-MSCA-ITN (801370).

ACKNOWLEDGMENTS

We acknowledge the Paul Scherrer Institut, Villigen, Switzerland for provision of synchrotron radiation beamtime at beamline TOMCAT of the SLS.

SUPPLEMENTARY MATERIAL

The Supplementary Material for this article can be found online at: <https://www.frontiersin.org/articles/10.3389/fcvm.2021.670734/full#supplementary-material>

Supplementary Video 1 | Patient 1 - Top to bottom scan of a subvolume of the HR X-PCI Paganin reconstructed dataset.

Supplementary Video 2 | Patient 1 - Top to bottom scan of a subvolume of the HR X-PCI Paganin reconstructed dataset.

Supplementary Video 3 | Patient 1 - A 3D visualization of the collagen organization.

Supplementary Video 4 | Patient 2 - Top to bottom scan of a subvolume of the HR X-PCI Paganin reconstructed dataset.

Supplementary Video 5 | Patient 2 - A 3D visualization of the collagen organization.

Supplementary Video 6 | Patient 3 - Top to bottom scan of a subvolume of the HR X-PCI Paganin reconstructed dataset.

Supplementary Video 7 | Patient 3 – A 3D visualization of the collagen organization.

Supplementary Figure 1 | Photographs of tissue collected after surgical myectomy.

Supplementary Table 1 | Echocardiographic measurements.

Supplementary Table 2 | Measurements of the septal myectomy tissue samples.

REFERENCES

1. Tower-Rader A, Kramer CM, Neubauer S, Nagueh SF, Desai MY. Multimodality imaging in hypertrophic cardiomyopathy for risk stratification. *Circulation*. (2020) 13:e009026. doi: 10.1161/CIRCIMAGING.119.009026
2. Cardim N, Galderisi M, Edvardsen T, Plein S, Popescu BA, D'Andrea A, et al. Role of multimodality cardiac imaging in the management of patients with hypertrophic cardiomyopathy: an expert consensus of the European Association of cardiovascular imaging endorsed by the Saudi heart association. *Eur Heart J Cardiovasc Imaging*. (2015) 16:280. doi: 10.1093/ehjci/jeu291
3. Cikes M, Sutherland GR, Anderson LJ, Bijnsens BH. The role of echocardiographic deformation imaging in hypertrophic myopathies. *Nat Rev Cardiol*. (2010) 7:384–96. doi: 10.1038/nrcardio.2010.56
4. Gonzalez-Tendero A, Zhang C, Balicevic V, Cárdenas R, Loncaric S, Butakoff C, et al. Whole heart detailed and quantitative anatomy, myofibre structure and vasculature from X-ray phase-contrast synchrotron radiation-based micro computed tomography. *Eur Heart J Cardiovasc Imaging*. (2017) 18:732–41. doi: 10.1093/ehjci/jev314
5. Garcia-Canadilla P, Dejea H, Bonnin A, Balicevic V, Loncaric S, Zhang C, et al. Complex congenital heart disease associated with disordered myocardial architecture in a midtrimester human fetus. *Circulation*. (2018) 11:e007753. doi: 10.1161/CIRCIMAGING.118.007753
6. Garcia-Canadilla P, Cook AC, Mohun TJ, Oji O, Schlossarek S, Carrier L, et al. Myoarchitectural disarray of hypertrophic cardiomyopathy begins pre-birth. *J Anatomy*. (2019) 235:962–76. doi: 10.1111/joa.13058
7. Dejea H, Garcia-Canadilla P, Cook AC, Guasch E, Zamora M, Crispi F, et al. Comprehensive analysis of animal models of cardiovascular disease using multiscale X-ray phase contrast tomography. *Sci Rep*. (2019) 9:6669. doi: 10.1038/s41598-019-54945-x
8. O'Mahony C, Jichi F, Pavlou M, Monserrat L, Anastasakis A, Rapezzi C, Biagini E et al. Hypertrophic cardiomyopathy outcomes investigators. A novel clinical risk prediction model for sudden cardiac death in hypertrophic cardiomyopathy (HCM risk-SCD). *Eur Heart J*. (2014) 35:2010–20.
9. Lang RM, Badano LP, Mor-Avi V, Afkalo J, Armstrong A, Ernande L, et al. Recommendations for cardiac chamber quantification by echocardiography in adults: an update from the American Society of Echocardiography and the European Association of Cardiovascular Imaging. *Eur Heart J Cardiovasc Imaging*. (2015) 16:233–71.
10. Hang D, Nguyen A, Schaff HV. Surgical treatment for hypertrophic cardiomyopathy: a historical perspective. *Ann Cardiothorac Surg*. (2017) 6:318–28. doi: 10.21037/acs.2017.04.03
11. Mirea I, Varray F, Zhu YM, Fanton L, Langer M, Jouk PS, et al. Very high-resolution imaging of post-mortem human cardiac tissue using X-ray phase contrast tomography. In: van Assen H, Bovendeerd P, Delhaas T, editors. *Functional Imaging and Modeling of the Heart. FIMH 2015*, Vol. 9126. Cham: Springer (2015).
12. Marone F, Stampanoni M. Re-gridding reconstruction algorithm for real-time tomographic imaging. *J Synchrotron Rad*. (2012) 19:1029–37. doi: 10.1107/S0909049512032864
13. Paganin D, Mayo SC, Gureyev TE, Miller PR, Wilkins SW. Simultaneous phase and amplitude extraction from a single defocused image of a homogeneous object. *J Micro*. (2002) 206:33–40. doi: 10.1046/j.1365-2818.2002.01010.x
14. Vo NT, Atwood RC, Drakopoulos M. Superior techniques for eliminating ring artifacts in X-ray micro-tomography. *Opt Express*. (2018) 26:28396–412. doi: 10.1364/OE.26.028396
15. Schindelin J, Arganda-Carreras I, Frise E, Kaynig V, Longair M, Pietzsch T, et al. Fiji: an open-source platform for biological-image analysis. *Nat Meth*. (2012) 9:676–82. doi: 10.1038/nmeth.2019
16. Berg S, Kutra D, Kroeger T, Straehle CN, Kausler BX, Haubold C, et al. ilastik: interactive machine learning for (bio)image analysis. *Nat Meth*. (2019) 16:1226–32. doi: 10.1038/s41592-019-0582-9
17. Fedorov A, Beichel R, Kalpathy-Cramer J, Finet J, Fillion-Robin J-C, Pujol S, et al. 3D slicer as an image computing platform for the quantitative imaging network. *Mag Res Imaging*. (2012) 30:1323–41. doi: 10.1016/j.mri.2012.05.001
18. Jouk P-S, Mourad A, Milisic V, Michalowicz G, Raoult A, Caillierie D, et al. Analysis of the fiber architecture of the heart by quantitative polarized light microscopy. Accuracy, limitations and contribution to the study of the fiber architecture of the ventricles during fetal and neonatal life. *Eur J Cardiothorac Surg*. (2007) 31:915–21. doi: 10.1016/j.ejcts.2006.12.040
19. Hughes SE. The pathology of hypertrophic cardiomyopathy. *Histopathology*. (2004) 44:412–27. doi: 10.1111/j.1365-2559.2004.01835.x
20. Maron BJ, Roberts WC. Quantitative analysis of cardiac muscle cell disorganization in the ventricular septum of patients with hypertrophic cardiomyopathy. *Circulation*. (1979) 59:689–706. doi: 10.1161/01.CIR.59.4.689
21. Shirani J, Pick R, Roberts WC, Maron BJ. Morphology and significance of the left ventricular collagen network in young patients with hypertrophic cardiomyopathy and sudden cardiac death. *J Am Coll Cardiol*. (2000) 35:36–44. doi: 10.1016/S0735-1097(99)00492-1
22. Factor SM, Butany J, Sole MJ, Wigle ED, Williams WC, Rojkind M. Pathologic fibrosis and matrix connective tissue in the subaortic myocardium of patients with hypertrophic cardiomyopathy. *J Am Coll Cardiol*. (1991) 17:1343–51. doi: 10.1016/S0735-1097(10)80145-7
23. Karlson WJ, McCulloch AD, Covell JW, Hunter JJ, Omens JH. Regional dysfunction correlates with myofiber disarray in transgenic mice with ventricular expression of ras. *Am J Physiol Heart Circulator Physiol*. (2000) 278:H898–906. doi: 10.1152/ajpheart.2000.278.3.H898
24. Kobayashi T, Popovic Z, Bhonsale A, Smedira NG, Tan C, Rodriguez ER, et al. Association between septal strain rate and histopathology in symptomatic hypertrophic cardiomyopathy patients undergoing septal myectomy. *Am Heart J*. (2013) 166:503–11. doi: 10.1016/j.ahj.2013.06.011
25. Dhillon A, Sweet W, Popovic ZB, Smedira NG, Thamilarasan M, Lytle BW, et al. Association of noninvasively measured left ventricular mechanics with in vitro muscle contractile performance: a prospective study in hypertrophic cardiomyopathy patients. *J Am Heart Assoc*. (2014) 3:e001269. doi: 10.1161/JAHA.114.001269
26. Tseng W-YI, Dou J, Reese TG, Wedeen VJ. Imaging myocardial fiber disarray and intramural strain hypokinesis in hypertrophic cardiomyopathy with MRI. *J Mag Res Imaging*. (2006) 23:1–8. doi: 10.1002/jmri.20473
27. Baudry G, Mansencal N, Reynaud A, Richard P, Dubourg O, Komajda M, et al. Global and regional echocardiographic strain to assess the early phase of hypertrophic cardiomyopathy due to sarcomeric mutations. *Eur Heart J Cardiovasc Imaging*. (2020) 21:291–8. doi: 10.1093/ehjci/jez084
28. Allen RD, Edwards WD, Tazelaar HD, Danielson GK. Surgical pathology of subaortic septal myectomy not associated with hypertrophic cardiomyopathy: a study of 98 cases (1996–2000). *Cardiovasc Pathol*. (2003) 12:207–15. doi: 10.1016/S1054-8807(03)00057-7
29. Charron P, Arad M, Arbustini E, Basso C, Bilinska Z, Elliott P et al. Genetic counselling and testing in cardiomyopathies: a position statement of the European society of cardiology working group on myocardial and pericardial. *Eur Heart J*. (2010) 31:2715–26. doi: 10.1093/eurheartj/ehq271
30. Gaudron PD, Liu D, Scholz F, Hu K, Florescu C, Herrmann S, et al. The septal bulge—an early echocardiographic sign in hypertensive heart disease. *J Am Soc Hyper*. (2016) 10:70–80. doi: 10.1016/j.jash.2015.11.006
31. Loncaric F, Nunno L, Mimbreno M, Marciniak M, Fernandes JF, Tirapu L, et al. Basal ventricular septal hypertrophy in systemic hypertension. *Am J Cardiol*. (2020) 125:1339–46. doi: 10.1016/j.amjcard.2020.01.045

32. Bogaert J, Rademakers FE. Regional nonuniformity of normal adult human left ventricle. *Am J Physiol Heart Circul Physiol*. (2001) 280:H610–20. doi: 10.1152/ajpheart.2001.280.2.H610
33. Heng MK, Janz RF, Jobin J. Estimation of regional stress in the left ventricular septum and free wall: an echocardiographic study suggesting a mechanism for asymmetric septal hypertrophy. *Am Heart J*. (1985) 110:84–90. doi: 10.1016/0002-8703(85)90519-8
34. Yalçın F, Yigit F, Erol T, Baltali M, Korkmaz ME, Müderrisoglu H. Effect of dobutamine stress on basal septal tissue dynamics in hypertensive patients with basal septal hypertrophy. *J Human Hypert*. (2006) 20:628–30. doi: 10.1038/sj.jhh.1002041
35. Baltabaeva A, Marciniak M, Bijnsens B, Moggridge J, He F, Antonios T, et al. Regional left ventricular deformation and geometry analysis provides insights in myocardial remodelling in mild to moderate hypertension. *Eur J Echocardi*. (2008) 9:501–8. doi: 10.1016/j.euje.2007.08.004
36. Bijnsens B, Claus P, Weidemann F, Strotmann J, Sutherland GR. Investigating cardiac function using motion and deformation analysis in the setting of coronary artery disease. *Circulation*. (2007) 116:2453–64. doi: 10.1161/CIRCULATIONAHA.106.684357
37. Piella G, De Craene M, Bijnsens BH, Tobon-Gómez C, Huguet M, Avegliano G, et al. Characterizing myocardial deformation in patients with left ventricular hypertrophy of different etiologies using the strain distribution obtained by magnetic resonance imaging. *Revista Española Cardiología*. (2010) 63:1281–91. doi: 10.1016/S1885-5857(10)70253-X
38. Kobayashi T, Dhillon A, Popovic Z, Bhonsale A, Smedira NG, Thamilarasan M, et al. Differences in global and regional left ventricular myocardial mechanics in various morphologic subtypes of patients with obstructive hypertrophic cardiomyopathy referred for ventricular septal myotomy/myectomy. *Am J Cardiol*. (2014) 113:1879–85. doi: 10.1016/j.amjcard.2014.03.020
39. Sun J, Xu T, Ni X, Yang X, Hu J, Wang S, et al. Echocardiographic strain in hypertrophic cardiomyopathy and hypertensive left ventricular hypertrophy. *Echocardiography*. (2019) 36:257–65. doi: 10.1111/echo.14222
40. Afonso L, Kondur A, Simegn M, Niraj A, Hari P, Kaur R, et al. Two-dimensional strain profiles in patients with physiological and pathological hypertrophy and preserved left ventricular systolic function: a comparative analyses. *BMJ Open*. (2012) 2:e001390. doi: 10.1136/bmjopen-2012-001390
41. Sperry BW, Sato K, Phelan D, Grimm R, Desai MY, Hanna M, et al. Regional variability in longitudinal strain across vendors in patients with cardiomyopathy due to increased left ventricular wall thickness. *Circulation*. (2019) 12:e008973. doi: 10.1161/CIRCIMAGING.119.008973
42. Mirea O, Pagourelas ED, Duchenne J, Bogaert J, Thomas JD, Badano LP, et al. Variability and reproducibility of segmental longitudinal strain measurement: a report from the EACVI-ASE strain standardization task force. *JACC Cardiovasc Imaging*. (2018) 11:15–24. doi: 10.1016/j.jcmg.2017.01.027
43. Mirea O, Pagourelas ED, Duchenne J, Bogaert J, Thomas JD, Badano LP, et al. Intervendor differences in the accuracy of detecting regional functional abnormalities: a report from the EACVI-ASE strain standardization task force. *JACC Cardiovasc Imaging*. (2018) 11:25–34. doi: 10.1016/j.jcmg.2017.02.014
44. Duchateau N, Loncaric F, Cikes M, Doltra A, Sitges M, Bijnsens B. Variability in the assessment of myocardial strain patterns: implications for adequate interpretation. *Ultraso Med Biol*. (2020) 46:244–54. doi: 10.1016/j.ultrasmedbio.2019.10.013
45. Lamata P, Casero R, Carapella V, Niederer SA, Bishop MJ, Schneider JE, et al. Images as drivers of progress in cardiac computational modelling. *Pro Biop Mol Biol*. (2014) 115:198–212. doi: 10.1016/j.pbiomolbio.2014.08.005
46. Land S, Niederer SA, Louch WE, Sejersted OM, Smith NP. Integrating multi-scale data to create a virtual physiological mouse heart. *Int Focus*. (2013) 3:20120076. doi: 10.1098/rsfs.2012.0076
47. Lyon A, Bueno-Orovio A, Zacur E, Ariga R, Grau V, Neubauer S, et al. Electrocardiogram phenotypes in hypertrophic cardiomyopathy caused by distinct mechanisms: apico-basal repolarization gradients vs. Purkinje-myocardial coupling abnormalities. *EP Europace*. (2018) 20:iii102–12. doi: 10.1093/europace/euy226
48. Romero D, Sebastian R, Bijnsens BH, Zimmerman V, Boyle PM, Vigmond EJ, et al. Effects of the purkinje system and cardiac geometry on biventricular pacing: a model study. *Ann Biomed Eng*. (2010) 38:1388–98. doi: 10.1007/s10439-010-9926-4
49. Krishnamurthy A, Villongco CT, Chuang J, Frank LR, Nigam V, Belezouli E, et al. Patient-specific models of cardiac biomechanics. *J Comput Physics*. (2013) 244:4–21. doi: 10.1016/j.jcp.2012.09.015
50. McLeod CJ, Bos JM, Theis JL, Edwards WD, Gersh BJ, Ommen SR, et al. Histologic characterization of hypertrophic cardiomyopathy with and without myofibrillar mutations. *Am Heart J*. (2009) 158:799–805. doi: 10.1016/j.ahj.2009.09.006
51. Maron BJ, Maron MS, Maron BA, Loscalzo J. Moving beyond the sarcomere to explain heterogeneity in hypertrophic cardiomyopathy. *J Am Coll Cardiol*. (2019) 73:1978–86. doi: 10.1016/j.jacc.2019.01.061
52. Marian AJ, Braunwald E. Hypertrophic cardiomyopathy: genetics, pathogenesis, clinical manifestations, diagnosis, and therapy. *Cir Res*. (2017) 121:749–70. doi: 10.1161/CIRCRESAHA.117.311059
53. Hetterich H, Willner M, Fill S, Herzen J, Bamberg F, Hipp A, et al. Phase-contrast CT: qualitative and quantitative evaluation of atherosclerotic carotid artery plaque. *Radiology*. (2014) 271:870–8. doi: 10.1148/radiol.14131554
54. Eggl E, Schleede S, Bech M, Achterhold K, Loewen R, Ruth RD, et al. X-ray phase-contrast tomography with a compact laser-driven synchrotron source. *PNAS*. (2015) 112:5567–72. doi: 10.1073/pnas.1500938112
55. Viermetz MP, Birnbacher LJB, Fehrer A, Willner M, Noel PB, Pfeiffer F, et al. High resolution laboratory grating-based x-ray phase-contrast CT. *Sci Rep*. (2018) 8:15884. doi: 10.1038/s41598-018-33997-5
56. Planinc I, Ilic I, Garcia-canadilla I, Dejea H, Skorik B, Jurin H, et al. X-ray Phase Contrast Imaging of Endo-Myocardial Biopsies Following Heart Transplantation - Agreement With Classical Histology. *Eur Heart J*. (2020) 22(Suppl S1):413.
57. Castelli E, Tonutti M, Arfelli F, Longo R, Quaia E, Rigon L, et al. Mammography with synchrotron radiation: first clinical experience with phase-detection technique. *Radiology*. (2011) 259:684–94. doi: 10.1148/radiol.11100745

Conflict of Interest: The authors declare that the research was conducted in the absence of any commercial or financial relationships that could be construed as a potential conflict of interest.

Copyright © 2021 Loncaric, Garcia-Canadilla, Garcia-Alvarez, Sanchis, Prat, Doltra, Quintana, Pereda, Dejea, Bonnin, Sitges and Bijnsens. This is an open-access article distributed under the terms of the Creative Commons Attribution License (CC BY). The use, distribution or reproduction in other forums is permitted, provided the original author(s) and the copyright owner(s) are credited and that the original publication in this journal is cited, in accordance with accepted academic practice. No use, distribution or reproduction is permitted which does not comply with these terms.



Age- and Sex-Specific Changes in CMR Feature Tracking-Based Right Atrial and Ventricular Functional Parameters in Healthy Asians

OPEN ACCESS

Edited by:

Antonios Karanasos,
Hippokration General Hospital, Greece

Reviewed by:

Alexios Antonopoulos,
National and Kapodistrian University
of Athens, Greece
Emmanuel Androulakis,
Royal Brompton & Harefield NHS
Foundation Trust, United Kingdom

*Correspondence:

Yucheng Chen
chenyucheng2003@126.com
Liang Zhong
zhong.liang@nhcs.com.sg

†These authors have contributed
equally to this work and share first
authorship

Specialty section:

This article was submitted to
Cardiovascular Imaging,
a section of the journal
Frontiers in Cardiovascular Medicine

Received: 09 February 2021

Accepted: 26 April 2021

Published: 04 June 2021

Citation:

Leng S, Guo J, Tan R-S, Chai P,
Teo L, Fortier MV, Gong C, Zhao X,
Ong CC, Allen JC, Ruan W, Koh AS,
Tan TH, Yip JW, Tan JL, Chen Y and
Zhong L (2021) Age- and Sex-Specific
Changes in CMR Feature
Tracking-Based Right Atrial and
Ventricular Functional Parameters in
Healthy Asians.
Front. Cardiovasc. Med. 8:664431.
doi: 10.3389/fcvm.2021.664431

Shuang Leng^{1†}, Jiajun Guo^{2†}, Ru-San Tan^{1,3}, Ping Chai^{4,5}, Lynette Teo^{5,6},
Marielle V. Fortier^{3,7,8}, Chao Gong², Xiaodan Zhao¹, Ching Ching Ong^{5,6}, John C. Allen³,
Wen Ruan^{1,3}, Angela S. Koh^{1,3}, Teng Hong Tan^{3,7}, James W. Yip^{4,5}, Ju Le Tan^{1,3},
Yucheng Chen^{2*} and Liang Zhong^{1,3*}

¹ National Heart Centre Singapore, Singapore, Singapore, ² Cardiology Division, Department of Medicine, West China
Hospital, Sichuan University, Chengdu, China, ³ Duke-NUS Medical School, Singapore, Singapore, ⁴ Department of
Cardiology, National University Heart Centre, Singapore, Singapore, ⁵ Yong Loo Lin School of Medicine, National University of
Singapore, Singapore, Singapore, ⁶ Department of Diagnostic Imaging, National University Hospital, Singapore, Singapore,
⁷ KK Women's and Children's Hospital, Singapore, Singapore, ⁸ Singapore Institute for Clinical Sciences, A*STAR, Singapore,
Singapore

Cardiovascular magnetic resonance (CMR) is the reference standard for non-invasive assessment of right-sided heart function. Recent advances in CMR post-processing facilitate quantification of tricuspid annular (TA) dynamics and longitudinal strains of the right ventricle (RV) and right atrium (RA). We aimed to determine age- and sex-specific changes in CMR-derived TA dynamics, and RV and RA functional parameters in healthy Asian adults. We studied 360 healthy subjects aged 21–79 years, with 30 men and 30 women in each of the six age groups. Functional parameters of RV and RA were measured on standard four-chamber cine CMR using fast feature tracking: (1) TA peak velocities (systolic velocity S', early diastolic velocity E', late diastolic velocity A') and TA plane systolic excursion (TAPSE); (2) RV global longitudinal strain (GLS) and strain rates; and (3) RA phasic longitudinal strains and strain rates. S' and TAPSE exhibited negative correlations with age. RV GLS was significantly higher in females than in males but not associated with age in both sexes. Females had similar E', lower A', and higher E'/A' ratios compared to males. Positive associations of E' and E'/A', and negative association of A' with age were observed in both sexes. Females had higher RA reservoir and conduit strains compared to males. There were significantly negative and positive associations between RA conduit and booster strains, respectively, with age. Age- and sex-specific reference ranges were established, and associations revealed, for fast CMR feature tracking parameters of right heart function in a large normal Asian population.

Keywords: cardiovascular magnetic resonance, feature tracking, right ventricular function, right atrial function, age, sex

INTRODUCTION

The right side of the heart has traditionally received less attention than the left, yet there is a growing body of evidence showing that right heart size and function are perhaps of equal importance in providing diagnostic and prognostic information in a wide range of cardiovascular diseases (1).

Cardiovascular magnetic resonance (CMR) imaging is the current gold standard for quantitation of right ventricular (RV) geometry and function (2). Guidelines recommend CMR for assessment of global RV functional parameters such as RV volumes, ejection fraction (EF), and cardiac output (3). Recent advances in CMR post-processing have facilitated reliable quantitation of tricuspid annular (TA) dynamics and longitudinal strains of the RV and right atrium (RA) using feature tracking (4–8). CMR-based TA systolic velocity (S'), early diastolic velocity (E'), late diastolic velocity (A'), and TA plane systolic excursion (TAPSE) have been reported to be significantly lower in patients diagnosed with heart failure (4), hypertrophic cardiomyopathy (4), repaired tetralogy of Fallot (rTOF) (4, 5), unrepaired atrial septal defect (5), and severe tricuspid insufficiency (6) than in normal controls. RV and RA longitudinal strains can be quantified either by feature tracking of the whole RV and RA endocardium, respectively (9, 10), or more rapidly by tracking discrete anatomical points on standard cine CMR (7, 8). A prior study demonstrated the prognostic utility of impaired fast CMR feature tracking-derived RA strain parameters for predicting clinical and hemodynamic deterioration in patients with pulmonary arterial hypertension (PAH) (7). The quantitative RV fast strain and strain rate parameters assessed from CMR identify abnormalities of RV function in rTOF and PAH and are predictive of exercise capacity, RV decompensation, and clinical risks in these patients (8).

The emerging importance of these parameters motivates efforts to define normal ranges and distributions in a healthy population. In addition, most CMR normal ranges for right heart size and volume have been established for Caucasians and may not be generalizable to other ethnicities (11). Accordingly, the aim of this study is to determine age- and sex-specific changes in CMR-derived RV and RA dimensions and functional (systolic and diastolic) parameters among healthy Asian subjects.

Abbreviations: A' , peak tricuspid annular late diastolic velocity; BSA, body surface area; CMR, cardiovascular magnetic resonance; ε_a , right atrial booster strain; ε_e , right atrial conduit strain; ε_s , right atrial reservoir strain; E' , peak tricuspid annular early diastolic velocity; EDV, end-diastolic volume; EF, ejection fraction; ESV, end-systolic volume; GLS, global longitudinal strain; GLSR_a, global longitudinal strain rate during late diastole, GLSR_e, global longitudinal strain rate during early diastole; GLSR_s, global longitudinal strain rate during systole; LV, left ventricle; PAH, pulmonary arterial hypertension; RA, right atrium; rTOF, repaired tetralogy of Fallot; RV, right ventricle; S' , peak tricuspid annular systolic velocity; SD, standard deviation; SR_a, right atrial booster strain rate; SR_e, right atrial conduit strain rate; SR_s, right atrial reservoir strain rate; SV, stroke volume; TA, tricuspid annular; TAPSE, tricuspid annular plane systolic excursion; TDI, tissue Doppler imaging.

MATERIALS AND METHODS

Study Population

In this multicenter study, 360 subjects (aged 21–79 years, 180 males and 180 females) without known cardiovascular disease were enrolled from three hospitals between 2014 and 2019. The subjects were recruited from the (1) Cardiac Aging study (12), (2) INITIATE study, and (3) Database of healthy controls in West China Hospital. All subjects (1) had no known cardiovascular disease and demonstrated no signs of cardiovascular disease in prior electrocardiographic or echocardiographic investigations, (2) displayed no uncontrolled cardiovascular risk factors at the time of enrollment (systolic blood pressure ≤ 140 mmHg and diastolic blood pressure ≤ 90 mmHg without anti-hypertensive treatment, total cholesterol < 6.2 mmol/L, fasting glucose < 7 mmol/L, body mass index < 30 kg/m², and current non-smoker status), and (3) had no significant kidney or lung disease. Other exclusion criteria were cerebrovascular disease or nervous system disease, cancer, autoimmune diseases, recent systemic infection (within a month), recent surgery or severe trauma (within a month), any recent medications, and a history of implantation of a pacemaker or other metals that are contraindicated for CMR. The institutional review board of each hospital approved the study protocol. Informed consent was obtained from each participant.

CMR Acquisition

CMR acquisitions were performed using a 3T magnetic resonance scanner (Ingenia, Philips Healthcare, The Netherlands) at National Heart Centre Singapore, a 1.5T MAGNETOM Aera magnetic resonance scanner (Siemens Healthineers, Erlangen, Germany) at National University Hospital Singapore, and a 3T MAGNETOM Tim Trio magnetic resonance scanner (Siemens Healthineers, Erlangen, Germany) at West China Hospital (Sichuan China). End-expiratory breath-hold-balanced steady-state free precession cine images were acquired in standard short- and long-axis views. Typical parameters for the Philips scanner were as follows: repetition time (TR)/echo time (TE), 3/1 ms; matrix, 240 × 240; flip angle, 45°; field of view, 300 × 300 mm; pixel spacing, 1.25 × 1.25 mm; slice thickness, 8 mm; number of frames, 30/40 per cardiac cycle. Parameters for the 1.5T Siemens scanner were: TR/TE, 33/1 ms; matrix, 192 × 180; flip angle, 58°; field of view, 320 × 300 mm; pixel spacing, 1.67 × 1.67 mm; slice thickness, 6 mm; number of frames, 30 per cardiac cycle. Parameters for the 3T Siemens scanner were: TR/TE, 3.4/1.3 ms; matrix, 192 × 162; flip angle, 50°; field of view, 320 × 270 mm; pixel spacing, 1.67 × 1.67 mm; slice thickness, 8 mm; and number of frames, 25 per cardiac cycle.

Echocardiography

A sub-study was conducted to validate CMR-derived TA dynamics against those measured using echocardiography. Echocardiography was performed on the same day as CMR using a commercial ultrasound system (Aloka $\alpha 10$, Japan). TA velocities and displacement were measured using tissue Doppler

imaging (TDI) and M-mode, respectively, in the apical four-chamber view.

CMR Data Analysis

The parameters measured were (1) RV volumes and RVEF (derived from standard CMR volumetric analysis), (2) Two-dimensional chamber dimensions (RV chamber diameters and RA area and diameters), (3) TA velocities (systolic velocity S' , early diastolic velocity E' , and late diastolic velocity A') and displacement (TAPSE), (4) RV longitudinal strain and strain rates, and (5) RA phasic (reservoir, conduit, and booster) longitudinal strains and strain rates.

Volumetric Analysis and Chamber Dimensions

Endocardial contours were manually traced from the stack of short-axis cine images to obtain RV end-diastolic volume (EDV) and end-systolic volume (ESV), from which stroke volume (SV) and EF were derived (Figures 1A,B). Papillary muscles and trabeculae were included in the blood volume (3). RV size was measured from the four-chamber view at end-diastole. RV basal diameter was measured at the level of the tricuspid valve, and mid-cavity diameter was measured in the middle third of the RV at the level of the left ventricular (LV) papillary muscle (13) (Figure 1C).

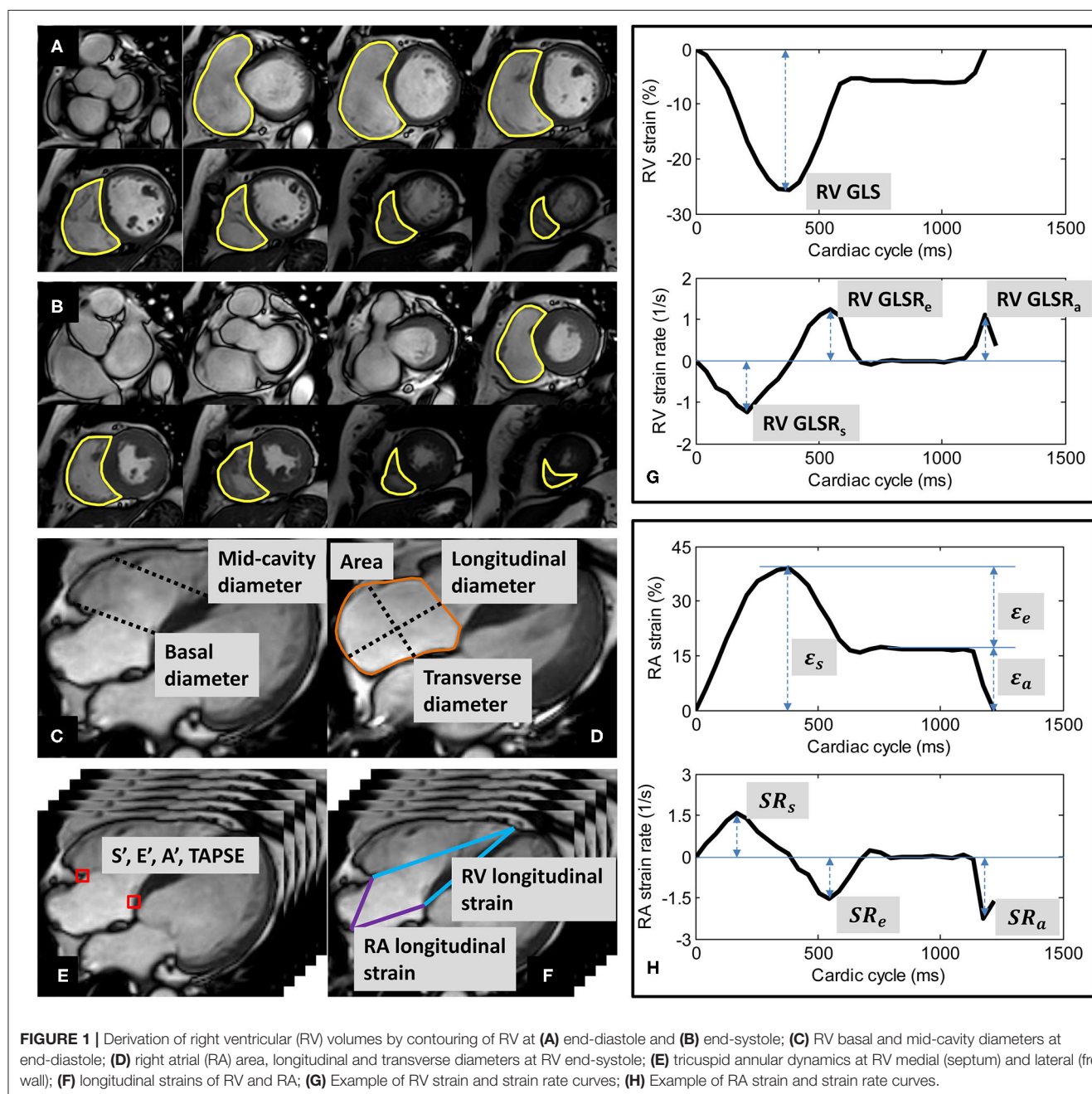


FIGURE 1 | Derivation of right ventricular (RV) volumes by contouring of RV at (A) end-diastole and (B) end-systole; (C) RV basal and mid-cavity diameters at end-diastole; (D) right atrial (RA) area, longitudinal and transverse diameters at RV end-systole; (E) tricuspid annular dynamics at RV medial (septum) and lateral (free wall); (F) longitudinal strains of RV and RA; (G) Example of RV strain and strain rate curves; (H) Example of RA strain and strain rate curves.

RA area and diameters were measured from the four-chamber view at RV end-systole. RA longitudinal diameter was measured as the distance between the midpoint of the line joining the medial and lateral (free wall) insertions of the tricuspid valve and the posterior wall (roof) of the RA. RA transverse diameter was measured as the orthogonal line bisecting the longitudinal diameter (14) (**Figure 1D**).

All chamber dimension measurements were reported as both absolute values and indexed values normalized to body surface area (BSA).

Tricuspid Annular Velocities and Displacement

Custom software developed in the MATLAB environment (MathWorks Inc., MA, USA) and validated in prior studies (4, 7, 8, 15–19) was used to perform the semi-automatic tracking of medial and lateral tricuspid valve insertions in the four-chamber view (**Figure 1E**). A video of the TA tracking and resultant TA velocity and displacement curves are shown in **Supplementary Materials**. Peak TA velocities were read off the velocity curve during systole (S'), early diastole (E'), late diastole (A'); TAPSE—TA displacement at end-systole—was read off the displacement curve (4, 7). We reported mean values for S' , E' , A' , and TAPSE averaged from medial and lateral TA measurements.

Longitudinal Strains of RV and RA

Using the same custom software, the RV epicardial apex and the RA roof point were tracked in the four-chamber view over the cardiac cycle (**Figure 1F**). We followed the convention of determining RV apex location by its proximity to the LV apex. The RV apex is close to but separated from the LV apex by the interventricular septal wall, which can be seen on the four-chamber view (13). The RA roof was localized to the intersection of the RA posterior wall and the RA longitudinal diameter.

The distance (L) from either the medial or the lateral tricuspid valve insertion to the RV epicardial apex on the four-chamber view was measured at any time point (t). RV strain value at time t with respect to RV end-diastole (time 0) was calculated using the formula for Lagrangian strain: $(L(t) - L(0)) \times 100/L(0)$ (8). RV global longitudinal strain (GLS)—strain value at end-systole—was read off the strain curve, and peak global longitudinal strain rates at RV systole (GLSR_s), early diastole (GLSR_e), and late diastole (GLSR_a) were calculated as first time-derivatives of the strain curve at the corresponding cardiac phases (8) (**Figure 1G**).

Similarly, RA longitudinal strain (ϵ) was derived from the time-varying distances between either the medial or the lateral tricuspid valve insertion and the RA roof point (7). RA reservoir strain (ϵ_s), conduit strain (ϵ_e) and booster strain (ϵ_a) were read off the generated strain curve at RV end-systole, diastasis, and pre-RA systole, respectively, and the corresponding peak strain rates (SR_s , SR_e , and SR_a) calculated as first time-derivatives of the strain curve at the corresponding cardiac phases (7) (**Figure 1H**).

A video showing the derivation of RV and RA strain is given in **Supplementary Materials**. Mean RV and RA strain and strain rate parameters averaged from medial and lateral TA measurements were used for all analyses. RV strain and strain rate parameters were presented as absolute values.

Conventional Feature Tracking Strain

A sub-study was conducted to validate the fast feature tracking-derived RA and RV strain measurements against those derived from conventional CMR RA and RV endocardial feature tracking using dedicated QStrain software (Version 2.0, Medis BV, Leiden, The Netherlands).

Statistical Analysis

The distribution normality of continuous variables was assessed using the Shapiro-Wilk test. Data were expressed as mean \pm standard deviation (SD), and reported across six pre-specified age groups stratified by sex. Age-specific reference limits were defined as mean \pm 1.96-SD. Values obtained in females and males were compared using Student's t -test. For either sex,

TABLE 1 | Demographics and right heart function parameters of the control population.

Parameters	Total (<i>n</i> = 360)	Men (<i>n</i> = 180)	Women (<i>n</i> = 180)	<i>P</i> -value
Demographics				
Age (years)	50 \pm 17	51 \pm 17	49 \pm 17	0.464
Height (cm)	163 \pm 9	169 \pm 7	158 \pm 6	<0.0001
Weight (kg)	61 \pm 11	66 \pm 10	56 \pm 9	<0.0001
BSA (m ²)	1.7 \pm 0.2	1.8 \pm 0.2	1.6 \pm 0.2	<0.0001
BMI (kg/m ²)	22.8 \pm 2.8	23.3 \pm 2.7	22.4 \pm 2.8	0.002
Systolic blood pressure (mmHg)	124 \pm 12	127 \pm 10	120 \pm 12	<0.0001
Diastolic blood pressure (mmHg)	76 \pm 9	78 \pm 7	74 \pm 10	<0.0001
Heart rate (beats per minute)	74 \pm 11	74 \pm 12	73 \pm 11	0.881
Right ventricular function (systolic and diastolic)				
RVEF (%)	58 \pm 7	57 \pm 7	60 \pm 7	0.001
S' (cm/s)	9.5 \pm 1.4	9.6 \pm 1.6	9.4 \pm 1.2	0.070
E' (cm/s)	10.5 \pm 2.9	10.3 \pm 3.0	10.8 \pm 2.9	0.138
A' (cm/s)	10.9 \pm 2.3	11.2 \pm 2.2	10.5 \pm 2.4	0.004
E'/A'	1.0 \pm 0.4	1.0 \pm 0.4	1.1 \pm 0.5	0.001
TAPSE (mm)	19.5 \pm 2.6	19.3 \pm 2.6	19.7 \pm 2.5	0.118
RV GLS (%)	24 \pm 4	23 \pm 3	26 \pm 3	<0.0001
RV GLSR _s (1/s)	1.3 \pm 0.3	1.3 \pm 0.3	1.3 \pm 0.2	0.052
RV GLSR _e (1/s)	1.5 \pm 0.4	1.3 \pm 0.4	1.6 \pm 0.5	<0.0001
RV GLSR _a (1/s)	1.2 \pm 0.4	1.2 \pm 0.4	1.2 \pm 0.4	0.703
Right atrial phasic function				
Reservoir strain ϵ_s (%)	46 \pm 9	43 \pm 8	48 \pm 9	<0.0001
Conduit strain ϵ_e (%)	24 \pm 8	22 \pm 7	26 \pm 9	<0.0001
Booster strain ϵ_a (%)	22 \pm 5	21 \pm 5	22 \pm 6	0.408
Reservoir strain rate SR_s (1/s)	2.4 \pm 0.5	2.3 \pm 0.5	2.4 \pm 0.5	0.019
Conduit strain rate SR_e (1/s)	−2.2 \pm 0.8	−2.0 \pm 0.7	−2.3 \pm 0.8	0.001
Booster strain rate SR_a (1/s)	−2.7 \pm 0.7	−2.7 \pm 0.6	−2.8 \pm 0.7	0.147

Data are presented as mean \pm SD. *P*-value is for *t*-test between sexes. BSA, body surface area; BMI, body mass index; RV, right ventricular; EF, ejection fraction; S' , peak systolic tricuspid annular velocity; E' , peak early diastolic tricuspid annular velocity; A' , peak late diastolic tricuspid annular velocity; TAPSE, tricuspid annular plane systolic excursion; GLS, global longitudinal strain; GLSR_s, peak systolic global longitudinal strain rate; GLSR_e, peak early diastolic global longitudinal strain rate; GLSR_a, peak late diastolic global longitudinal strain rate.

linear regression was used to characterize the relationship of right heart measurements with age. Intra- and inter-observer variability of study parameters was studied in a selected subgroup of 20 cases using Bland-Altman analysis and coefficient of variation. Statistical analyses were performed using SPSS software (Version 17.0, IBM, Chicago, IL, USA). $P \leq 0.05$ indicated statistical significance.

RESULTS

Baseline Characteristics and Summary Results

We recruited 360 healthy individuals (male:female 180:180, age range 21–79 years). Baseline demographics and right heart CMR measurements stratified by sex are given in **Table 1**. Age group-specific CMR measurements stratified by sex are

presented in **Tables 2, 3**. **Figures 2, 3** show RV volume and systolic and diastolic RV function parameters plotted against age with 5th, 50th, and 95th percentile values in males and females, respectively. **Figures 4, 5** show RA dimensions and phasic function parameters vs. age with 5th, 50th, and 95th percentile values in males and females, respectively. Measurements of right heart dimensions and volumes stratified by sex and age group are presented in **Supplementary Tables 1–3**.

Validation of Fast CMR Feature Tracking-Derived Measurements

Results from a sub-study of 60 subjects comprising 10 randomly selected from each of the six age groups showed that fast CMR feature tracking-derived TA dynamic measurements, RA and RV strain measurements were in good agreement with echocardiographic ($r = 0.76$ – 0.83 ,

TABLE 2 | Males: right heart function parameters by age group [mean \pm SD (reference range, lower/upper limits calculated as mean \pm 1.96-SD)].

Parameters	<30 (n = 30)	30–39 (n = 30)	40–49 (n = 30)	50–59 (n = 30)	60–69 (n = 30)	≥ 70 (n = 30)
Right ventricular function (systolic and diastolic)						
RV EF (%)	55 \pm 7 (42, 68)	55 \pm 7 (43, 68)	55 \pm 6 (44, 66)	58 \pm 7 (44, 71)	58 \pm 7 (45, 71)	62 \pm 7 (48, 76)
S' (cm/s)	10.6 \pm 1.7 (7.4, 13.9)	9.9 \pm 1.2 (7.5, 12.4)	9.7 \pm 1.4 (7.0, 12.4)	9.5 \pm 1.5 (6.7, 12.4)	9.2 \pm 1.6 (6.1, 12.3)	8.9 \pm 1.5 (5.9, 11.9)
E' (cm/s)	14.2 \pm 2.6 (9.1, 19.2)	12.3 \pm 1.9 (8.6, 16.0)	10.6 \pm 2.1 (6.6, 14.7)	9.2 \pm 1.6 (6.0, 12.3)	8.6 \pm 1.7 (5.2, 11.9)	7.7 \pm 1.7 (4.3, 11.0)
A' (cm/s)	9.8 \pm 1.7 (6.5, 13.0)	10.2 \pm 1.6 (7.0, 13.4)	10.7 \pm 1.8 (7.2, 14.3)	11.2 \pm 1.7 (8.0, 14.5)	12.1 \pm 2.3 (7.6, 16.6)	12.9 \pm 1.9 (9.1, 16.8)
E'/A'	1.4 \pm 0.3 (0.9, 1.9)	1.2 \pm 0.2 (0.8, 1.7)	1.0 \pm 0.3 (0.5, 1.5)	0.8 \pm 0.2 (0.5, 1.1)	0.7 \pm 0.2 (0.4, 1.0)	0.6 \pm 0.1 (0.3, 0.9)
TAPSE (mm)	20.4 \pm 2.8 (15.0, 25.8)	19.7 \pm 2.3 (15.1, 24.2)	19.5 \pm 2.5 (14.6, 24.4)	19.1 \pm 2.4 (14.5, 23.8)	18.9 \pm 2.4 (14.2, 23.6)	18.1 \pm 2.8 (12.5, 23.6)
RV GLS (%)	23 \pm 3 (18, 28)	23 \pm 3 (17, 28)	22 \pm 3 (16, 29)	23 \pm 3 (17, 30)	23 \pm 3 (17, 30)	24 \pm 3 (17, 31)
RV GLSR _s (1/s)	1.3 \pm 0.2 (0.9, 1.7)	1.2 \pm 0.2 (0.8, 1.6)	1.3 \pm 0.3 (0.7, 1.8)	1.3 \pm 0.3 (0.7, 1.8)	1.2 \pm 0.3 (0.7, 1.8)	1.3 \pm 0.3 (0.7, 1.9)
RV GLSR _e (1/s)	1.7 \pm 0.3 (1.1, 2.4)	1.6 \pm 0.3 (1.1, 2.1)	1.3 \pm 0.3 (0.8, 2.0)	1.2 \pm 0.3 (0.7, 1.8)	1.1 \pm 0.3 (0.4, 1.8)	1.1 \pm 0.2 (0.6, 1.6)
RV GLSR _a (1/s)	0.9 \pm 0.2 (0.5, 1.3)	1.1 \pm 0.3 (0.5, 1.6)	1.2 \pm 0.3 (0.5, 1.8)	1.2 \pm 0.2 (0.7, 1.7)	1.4 \pm 0.4 (0.7, 2.1)	1.6 \pm 0.3 (1.0, 2.1)
Right atrial phasic function						
Reservoir strain ϵ_s (%)	48 \pm 9 (30, 66)	45 \pm 8 (30, 61)	43 \pm 8 (27, 58)	41 \pm 8 (26, 57)	42 \pm 8 (27, 58)	41 \pm 8 (26, 57)
Conduit strain ϵ_e (%)	30 \pm 8 (14, 47)	27 \pm 5 (18, 36)	22 \pm 6 (10, 34)	20 \pm 5 (9, 30)	18 \pm 5 (8, 28)	18 \pm 4 (10, 26)
Booster strain ϵ_a (%)	18 \pm 3 (11, 24)	19 \pm 4 (10, 27)	20 \pm 4 (13, 28)	22 \pm 4 (14, 30)	24 \pm 6 (13, 36)	24 \pm 6 (12, 36)
Reservoir strain rate SR _s (1/s)	2.5 \pm 0.5 (1.5, 3.4)	2.4 \pm 0.5 (1.5, 3.3)	2.2 \pm 0.5 (1.3, 3.2)	2.2 \pm 0.5 (1.2, 3.1)	2.2 \pm 0.5 (1.1, 3.3)	2.3 \pm 0.6 (1.2, 3.4)
Conduit strain rate SR _e (1/s)	−2.9 \pm 0.7 (−4.2, −1.6)	−2.5 \pm 0.5 (−3.4, −1.6)	−2.0 \pm 0.5 (−3.1, −1.0)	−1.7 \pm 0.4 (−2.6, −0.9)	−1.6 \pm 0.4 (−2.4, −0.7)	−1.5 \pm 0.4 (−2.3, −0.7)
Booster strain rate SR _a (1/s)	−2.4 \pm 0.6 (−3.5, −1.3)	−2.3 \pm 0.5 (−3.3, −1.3)	−2.5 \pm 0.4 (−3.3, −1.7)	−2.6 \pm 0.6 (−3.7, −1.5)	−2.9 \pm 0.7 (−4.4, −1.5)	−3.1 \pm 0.7 (−4.4, −1.8)

RV, right ventricular; EF, ejection fraction; S', peak systolic tricuspid annular velocity; E', peak early diastolic tricuspid annular velocity; A', peak late diastolic tricuspid annular velocity; TAPSE, tricuspid annular plane systolic excursion; GLS, global longitudinal strain; GLSR_s, peak systolic global longitudinal strain rate; GLSR_e, peak early diastolic global longitudinal strain rate; GLSR_a, peak late diastolic global longitudinal strain rate.

TABLE 3 | Females: right heart function parameters by age group [mean \pm SD (reference range, lower/upper limits calculated as mean \pm 1.96-SD)].

Parameters	<30 (n = 30)	30–39 (n = 30)	40–49 (n = 30)	50–59 (n = 30)	60–69 (n = 30)	≥ 70 (n = 30)
Right ventricular function (systolic and diastolic)						
RVEF (%)	58 \pm 5 (48, 68)	58 \pm 8 (43, 73)	58 \pm 7 (43, 72)	58 \pm 6 (46, 70)	62 \pm 6 (50, 74)	63 \pm 7 (50, 77)
S' (cm/s)	10.0 \pm 1.2 (7.7, 12.4)	9.6 \pm 1.2 (7.2, 11.9)	9.5 \pm 1.3 (7.0, 12.0)	9.2 \pm 1.3 (6.7, 11.7)	9.0 \pm 1.1 (6.9, 11.2)	8.8 \pm 1.0 (6.9, 10.8)
E' (cm/s)	14.5 \pm 2.2 (10.2, 18.7)	12.1 \pm 1.7 (8.6, 15.5)	11.5 \pm 1.9 (7.7, 15.3)	10.5 \pm 2.1 (6.4, 14.7)	8.7 \pm 1.9 (4.9, 12.5)	7.5 \pm 1.5 (4.7, 10.4)
A' (cm/s)	8.5 \pm 1.7 (5.1, 11.9)	9.6 \pm 1.8 (6.0, 13.1)	10.2 \pm 1.9 (6.4, 14.0)	11.1 \pm 2.0 (7.2, 14.9)	11.5 \pm 2.4 (6.7, 16.2)	12.3 \pm 2.3 (7.8, 16.8)
E'/A'	1.7 \pm 0.4 (1.0, 2.5)	1.3 \pm 0.3 (0.7, 1.9)	1.2 \pm 0.3 (0.6, 1.7)	1.0 \pm 0.2 (0.5, 1.4)	0.8 \pm 0.2 (0.4, 1.2)	0.6 \pm 0.2 (0.3, 1.0)
TAPSE (mm)	20.8 \pm 2.4 (16.0, 25.6)	20.1 \pm 2.5 (15.2, 25.0)	20.2 \pm 2.4 (15.4, 25.0)	19.7 \pm 2.5 (14.8, 24.5)	19.3 \pm 2.3 (14.8, 23.7)	18.0 \pm 2.5 (13.2, 22.8)
RV GLS (%)	25 \pm 3 (19, 32)	26 \pm 3 (19, 33)	26 \pm 4 (18, 34)	25 \pm 3 (18, 32)	26 \pm 3 (19, 32)	27 \pm 4 (20, 34)
RV GLSR _s (1/s)	1.3 \pm 0.2 (0.9, 1.7)	1.3 \pm 0.2 (0.9, 1.7)	1.3 \pm 0.3 (0.8, 1.8)	1.3 \pm 0.2 (0.9, 1.8)	1.3 \pm 0.3 (0.8, 1.9)	1.4 \pm 0.3 (0.7, 2.0)
RV GLSR _e (1/s)	2.1 \pm 0.4 (1.3, 2.8)	1.7 \pm 0.3 (1.1, 2.3)	1.6 \pm 0.4 (0.9, 2.4)	1.5 \pm 0.5 (0.6, 2.4)	1.3 \pm 0.5 (0.4, 2.2)	1.2 \pm 0.3 (0.6, 1.8)
RV GLSR _a (1/s)	0.9 \pm 0.2 (0.5, 1.3)	1.1 \pm 0.3 (0.5, 1.7)	1.2 \pm 0.3 (0.6, 1.8)	1.3 \pm 0.3 (0.8, 1.8)	1.3 \pm 0.4 (0.6, 2.1)	1.7 \pm 0.4 (0.9, 2.4)
Right atrial phasic function						
Reservoir strain ϵ_s (%)	56 \pm 8 (40, 73)	49 \pm 7 (36, 63)	49 \pm 9 (33, 66)	44 \pm 9 (26, 62)	45 \pm 10 (25, 65)	44 \pm 7 (29, 58)
Conduit strain ϵ_e (%)	39 \pm 6 (26, 51)	30 \pm 6 (17, 43)	28 \pm 6 (17, 39)	23 \pm 6 (11, 35)	20 \pm 7 (6, 35)	18 \pm 5 (8, 29)
Booster strain ϵ_a (%)	18 \pm 4 (9, 26)	19 \pm 4 (10, 26)	22 \pm 5 (12, 31)	21 \pm 5 (11, 31)	25 \pm 5 (15, 36)	25 \pm 5 (16, 35)
Reservoir strain rate SR _s (1/s)	2.8 \pm 0.6 (1.5, 4.0)	2.4 \pm 0.5 (1.5, 3.3)	2.4 \pm 0.5 (1.5, 3.4)	2.2 \pm 0.4 (1.5, 3.0)	2.4 \pm 0.5 (1.3, 3.4)	2.4 \pm 0.4 (1.6, 3.2)
Conduit strain rate SR _e (1/s)	−3.4 \pm 0.7 (−4.7, −2.1)	−2.6 \pm 0.5 (−3.7, −1.6)	−2.5 \pm 0.5 (−3.5, −1.5)	−2.1 \pm 0.5 (−3.2, −1.0)	−1.7 \pm 0.5 (−2.7, −0.7)	−1.5 \pm 0.4 (−2.3, −0.8)
Booster strain rate SR _a (1/s)	−2.5 \pm 0.5 (−3.5, −1.4)	−2.5 \pm 0.7 (−3.8, −1.2)	−2.8 \pm 0.6 (−3.9, −1.6)	−2.8 \pm 0.7 (−4.2, −1.3)	−3.0 \pm 0.9 (−4.7, −1.2)	−3.1 \pm 0.7 (−4.5, −1.8)

RV, right ventricular; EF, ejection fraction; S', peak systolic tricuspid annular velocity; E', peak early diastolic tricuspid annular velocity; A', peak late diastolic tricuspid annular velocity; TAPSE, tricuspid annular plane systolic excursion; GLS, global longitudinal strain; GLSR_s, peak systolic global longitudinal strain rate; GLSR_e, peak early diastolic global longitudinal strain rate; GLSR_a, peak late diastolic global longitudinal strain rate.

$P < 0.0001$, **Supplementary Figure 1**) and conventional CMR endocardial tracking-derived results ($r = 0.75$ – 0.94 , $P < 0.0001$, **Supplementary Figures 2–4**).

Influence of Sex and Age on Right Ventricular Function

Among RV systolic functional parameters, RVEF and RV GLS were significantly higher in females than in males but there were no significant sex differences in S', TAPSE, and RV GLSR_s (**Table 1**). RVEF correlated positively with age in both males ($r = 0.31$, $P < 0.0001$) and females ($r = 0.30$, $P < 0.0001$). S' and TAPSE exhibited negative correlations with age in both males (S': $r = -0.36$, $P < 0.0001$; TAPSE: $r = -0.28$, $P < 0.0001$) and females (S': $r = -0.30$, $P < 0.0001$; TAPSE: $r = -0.31$, $P < 0.0001$). RV GLS and RV GLSR_s were not associated with age in both sexes (**Figures 2, 3**).

With respect to RV diastolic function, females had significantly lower A' and higher E'/A' ratios and RV GLSR_e compared to males, but no significant sex differences in E' and RV GLSR_a were observed (**Table 1**). Among male subjects, E' ($r = -0.75$, $P < 0.0001$), E'/A' ratio ($r = -0.80$, $P < 0.0001$) and RV GLSR_e ($r = -0.58$, $P < 0.0001$) decreased significantly with age, whereas A' ($r = 0.49$, $P < 0.0001$) and RV GLSR_a ($r = 0.57$, $P < 0.0001$) increased with age. Similar positive associations of E', E'/A', and RV GLSR_e, and negative associations of A' and RV GLSR_a with age were observed among females (all $P < 0.0001$) (**Figures 2, 3**).

Influence of Sex and Age on Right Atrial Phasic Function

Females had higher RA reservoir strain, conduit strain, reservoir strain rate, and conduit strain rate compared to males, while RA booster strain and strain rate were similar (**Table 1**). RA reservoir

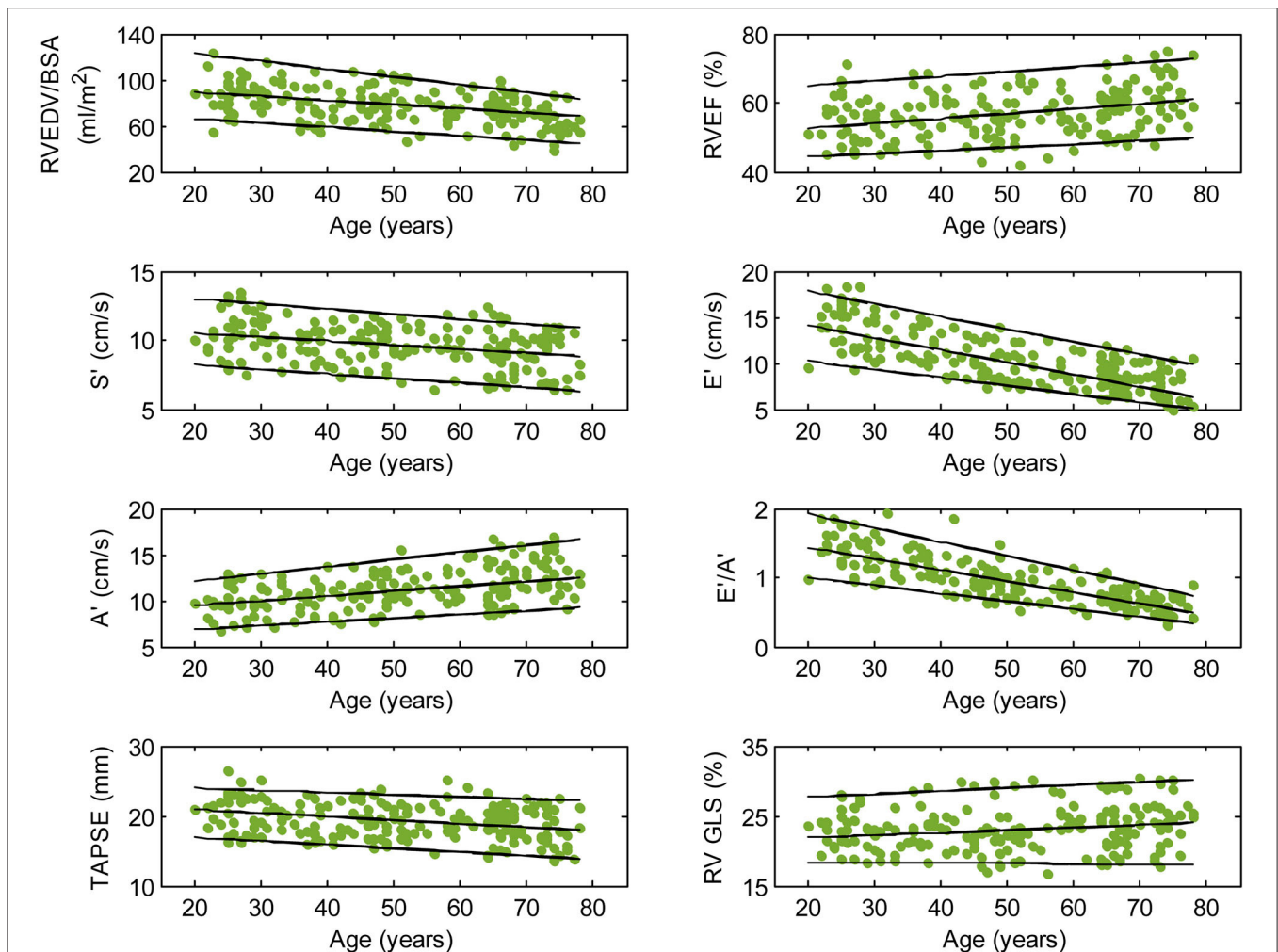


FIGURE 2 | Right ventricular parameters plotted against age in male subjects. (Central line) The 50th percentile; (Top line) The 95th percentile; (Bottom line) The 5th percentile.

strain, conduit strain, and strain rate correlated negatively with age among both males (reservoir strain: $r = -0.26$, $P < 0.0001$; conduit strain: $r = -0.61$, $P < 0.0001$; conduit strain rate: $r = -0.70$, $P < 0.0001$) and females (reservoir strain: $r = -0.38$, $P < 0.0001$; conduit strain: $r = -0.70$, $P < 0.0001$; conduit strain rate: $r = -0.75$, $P < 0.0001$). Booster strain and strain rate exhibited positive correlations with age among both males (booster strain: $r = 0.46$, $P < 0.0001$; booster strain rate: $r = 0.42$, $P < 0.0001$) and females (booster strain: $r = 0.51$, $P < 0.0001$; booster strain rate: $r = 0.34$, $P < 0.0001$) (Figures 4, 5).

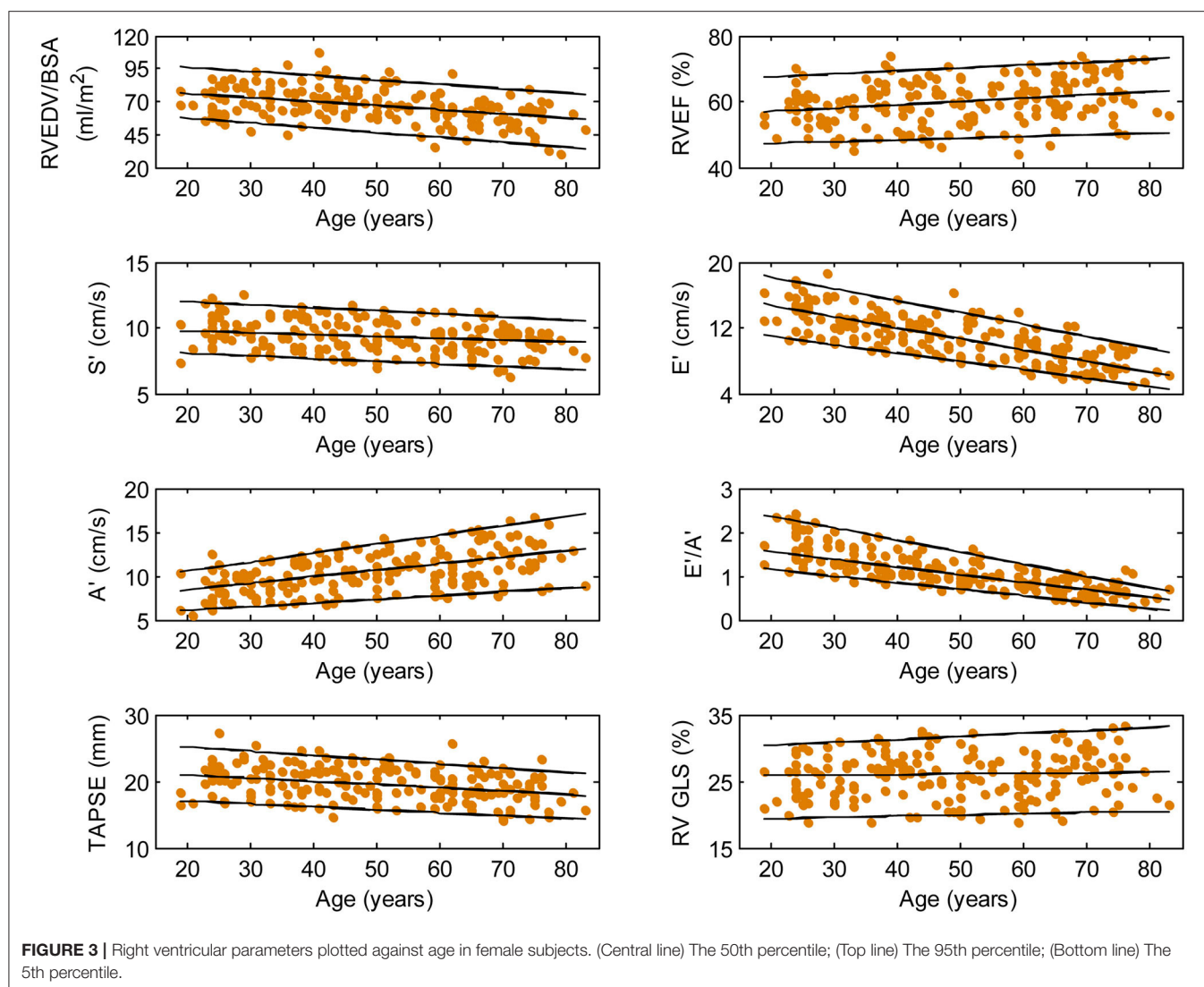
Influence of Sex and Age on Right Ventricular Dimensions

Absolute and indexed RV EDV, ESV, and SV were higher in males compared to females ($P < 0.0001$ for all). Males had larger absolute RV basal and mid-cavity diameters than females (both $P < 0.0001$) but not when normalized to BSA (Supplementary Table 1). RV volumes correlated negatively with

age among both males (EDV: $r = -0.50$, $P < 0.0001$; ESV: $r = -0.49$, $P < 0.0001$) and females (EDV: $r = -0.39$, $P < 0.0001$; ESV: $r = -0.41$, $P < 0.0001$), with similar correlations after normalization to BSA (males, EDV/BSA: $r = -0.43$, $P < 0.0001$; ESV/BSA: $r = -0.44$, $P < 0.0001$; females, EDV/BSA: $r = -0.45$, $P < 0.0001$; ESV/BSA: $r = -0.44$, $P < 0.0001$). Absolute and indexed RV basal and mid-cavity diameters were not significantly associated with age in both sexes.

Influence of Sex and Age on Right Atrial Dimensions

Males had larger absolute RA diameters and areas compared to females. After normalization to BSA, indexed RA longitudinal and transverse diameters were significantly smaller in males compared to females, while the indexed RA area was not significantly different (Supplementary Table 1). Among male subjects, age was positively correlated with indexed RA longitudinal diameter ($r = 0.32$, $P < 0.0001$). Among female



subjects, age was positively correlated with indexed RA longitudinal diameter ($r = 0.37$, $P < 0.0001$) and indexed RA area ($r = 0.30$, $P < 0.0001$).

Reproducibility

Good to excellent intra- and inter-observer reproducibility was observed for RV and RA dimensions and volumes, TA velocities and displacement, RV longitudinal strain and strain rates, and RA phasic strains and strain rates (Table 4).

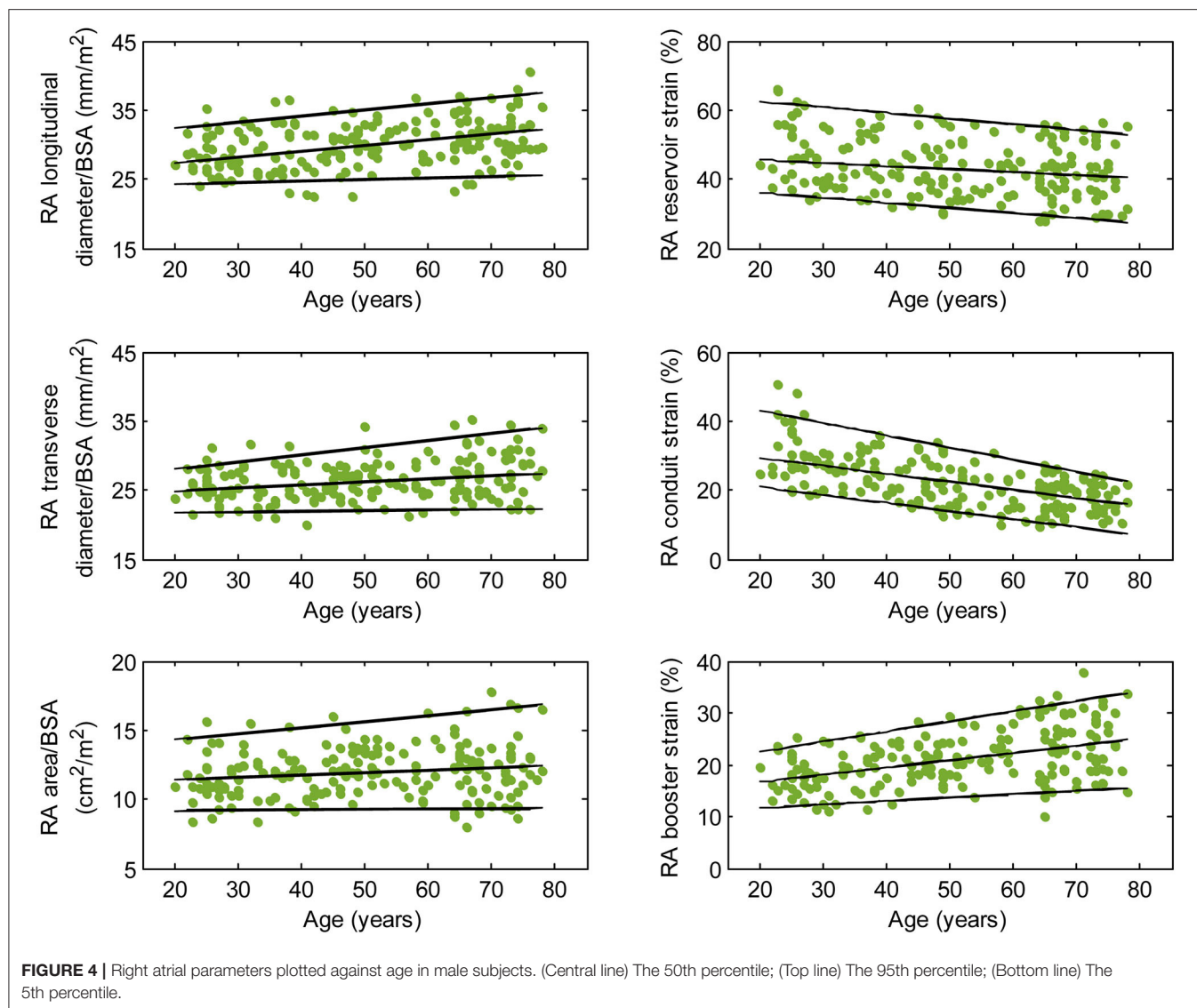
DISCUSSION

In this study, we investigated age- and sex-specific changes in CMR-based right heart dimensions and functional measurements in a large, healthy Asian population. Increased age was associated with impairment of S' and E' velocities, TAPSE, and RV GLSR_e and increases in A' velocity and RV GLSR_a, in both sexes. RV GLS and RV GLSR_s were not affected by age in both sexes. As age increased, RA reservoir and conduit strains

and strain rates decreased, while RA booster strain and strain rate increased.

CMR is recommended for many patients at the time of the transition from pediatric to adult congenital heart disease programmes, and this is the gold standard for RV volume, EF, flow quantification, and assessment of extracardiac anatomy. Additionally, CMR is recommended in the presence of clinical deterioration, non-diagnostic echo findings, and prior to surgical or transcatheter intervention (20). Data on age and sex-specific CMR reference ranges for right heart function in an Asian population are lacking at present. This information is crucial to CMR clinical practice in Asia. Moreover, our CMR-based method is simple, reproducible, and easily implemented for efficient RA and RV function assessment.

This work is novel for a number of reasons. First, it comprises the largest Asian CMR cohort reported to date, enrolling participants from multiple centers to provide broad generalizability of results and high precision in sample estimates of mean and SD. Second, CMR parameters were stratified not



only by sex but also by age categories across a broad age range of 21–79 years. The increased granularity of results is key to clinical implementation and interpretation in light of the sex- and age-related differences observed in many of the studied parameters. Third, this study is the first to report age- and sex-specific reference ranges for various recently published fast CMR feature tracking parameters used to assess RV systolic and diastolic function as well as phasic RA function.

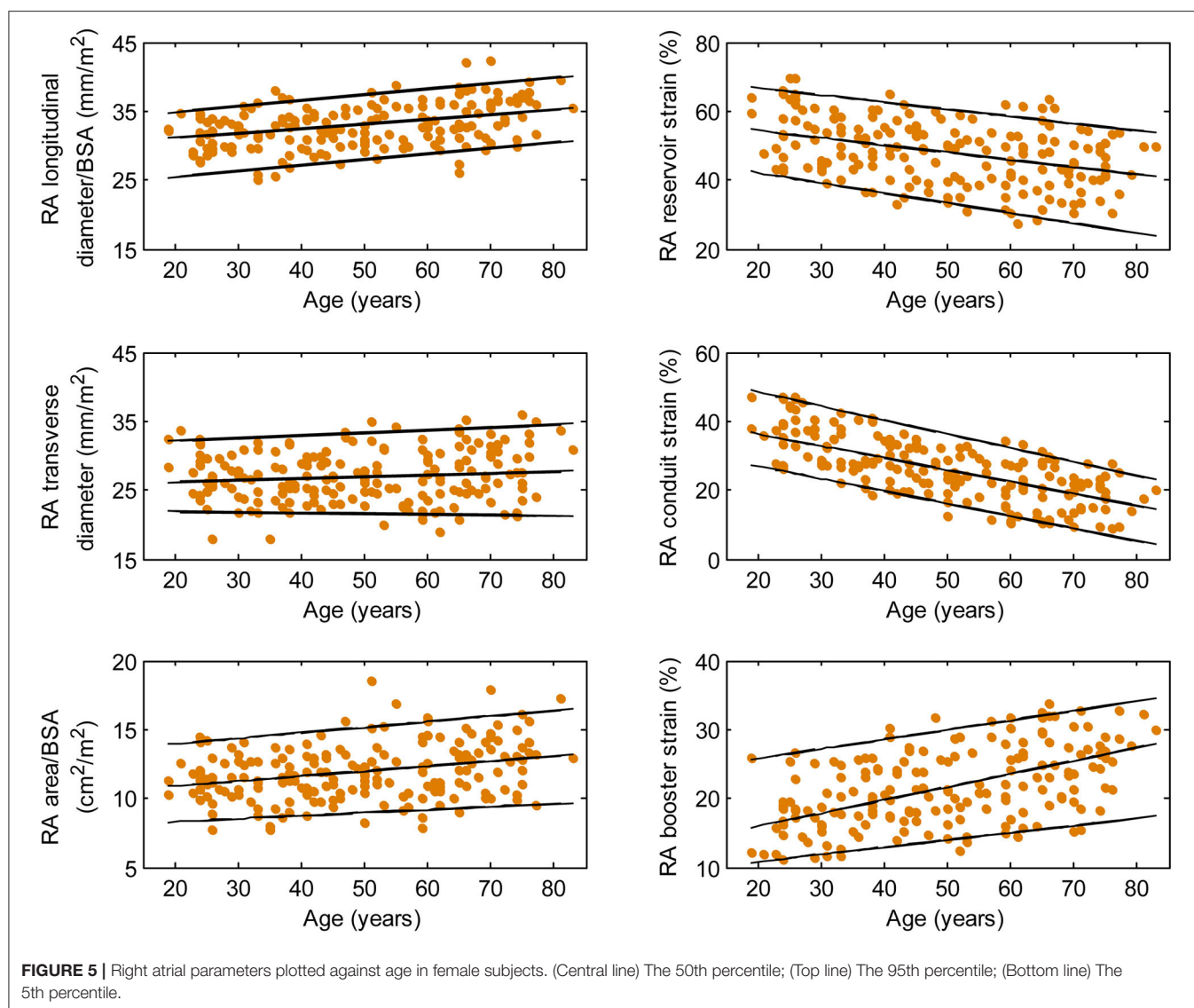
RV Functional Parameters

Asian subjects in our study have numerically smaller right heart size compared to Caucasians in another study (21) (RVEDV: 121 ± 34 vs. 154 ± 40 ml; indexed RVEDV: 72 ± 15 vs. 85 ± 17 ml/m²), which underscores the need for ethnic-specific reference values. Our study showed a negative correlation between RV volume and age and a positive correlation between RVEF and age, corroborating similar observations in Caucasian subjects (21). Beyond conventional RV volumes and EF, we quantitated

TA dynamics and RV longitudinal strain and strain rates—measurements for assessing RV function in both systole and diastole—and reported their age- and sex-specific reference ranges. Increasing age was associated with reductions in TAPSE, S', E', E'/A', and RV GLSR_e and increases in A' and RV GLSR_a in both sexes. These results agree with prior studies involving echocardiographic TDI (22) and conventional feature tracking CMR with endocardial contour tracing (23). Of note, we found that RV GLS and RV GLSR_s were not associated with age, which suggests that they are suited to be applied clinically as markers of disease progression unaffected by chronological aging. Our study replicated prior findings of higher systolic functional performance in females than in males as determined by RVEF (21) and RV GLS (24).

RA Functional Parameters

We previously demonstrated that RA function as assessed using our fast RA feature tracking method had important diagnostic



and prognostic implications in patients with PAH (7). RA volume and function (i.e., emptying fraction) assessment using volumetric analysis requires additional cine CMR acquisitions of atrial short-axis images and post-acquisitional analysis, which are not routinely performed. The area-length method, through geometric assumptions, shortens analysis time slightly (calculation still has to be repeated at all time phases) but is dogged by accuracy and reproducibility issues (25). In our study, we characterized the RA reservoir, conduit, and booster pump functions using strain and strain rate parameters that can be reproducibly and expeditiously measured. These parameters have been shown to be useful for detecting RA dysfunction, RV decompensation, and monitoring disease progression in patients with PAH (7). Among the healthy subjects in our study, females had higher reservoir and conduit strains but similar booster strain compared to males. This is concordant with a previous study of Caucasian subjects (25). In addition, we found age-related changes in RA function manifested as

a significant decrease in conduit strain and an increase in booster strain. We surmise the latter is necessary in order to maintain reservoir strain, which increased slightly with age. These results are in agreement with previous reports using speckle tracking echocardiography (26) and feature tracking CMR with endocardial contour tracing (27).

Advantages of Fast CMR Feature Tracking Parameters

This is the first study to establish age- and sex-specific reference ranges for CMR-derived TA dynamic parameters, which are a prerequisite for clinical applicability and adoption. The CMR-derived TA velocities correlated significantly with TDI-derived measurements, with no angle dependence and excellent reproducibility. This corroborates our previous work which demonstrated good correlation and agreement between CMR-derived mitral annular velocities and TDI measurements (18).

TABLE 4 | Intra- and inter-observer reproducibility for right heart dimension and function parameters.

Parameters	Intra-observer (n = 20)		Inter-observer (n = 20)	
	Bias (limits of agreement)	CV, %	Bias (limits of agreement)	CV, %
Right ventricular dimension				
RV basal diameter (mm)	0.1 (−1.7, 1.9)	1.6	−2.1 (−4.4, 0.2)	4.4
RV mid-cavity diameter (mm)	1.3 (−0.1, 2.6)	2.7	1.3 (−0.6, 3.2)	3.0
RVEDV (ml)	0.9 (−11.4, 13.2)	3.5	1.4 (−11.6, 14.5)	3.8
RVESV (ml)	−0.3 (−10.8, 10.2)	7.6	2.6 (−8.0, 13.2)	8.9
RVSV (ml)	1.3 (−7.4, 10.0)	4.2	−1.1 (−10.8, 8.6)	4.5
Right atrial dimension				
RA longitudinal diameter (mm)	−0.8 (−2.5, 0.9)	1.5	0.7 (−1.1, 2.6)	1.6
RA transverse diameter (mm)	−0.1 (−4.8, 4.7)	3.6	2.7 (−0.2, 5.5)	4.8
RA area (cm ²)	0.1 (−1.0, 1.1)	1.9	1.2 (−0.5, 2.9)	5.2
Right ventricular function (systolic and diastolic)				
RVEF (%)	0.6 (−6.7, 7.9)	4.2	−1.7 (−9.1, 5.7)	4.5
S' (cm/s)	−0.1 (−0.9, 0.7)	3.0	−0.2 (−1.3, 1.0)	4.4
E' (cm/s)	−0.5 (−1.4, 0.5)	4.7	−0.5 (−2.0, 1.0)	6.6
A' (cm/s)	−0.5 (−2.5, 1.5)	6.6	0.1 (−1.9, 2.0)	5.8
E'/A'	0.1 (−0.2, 0.3)	6.9	−0.1 (−0.3, 0.2)	10.3
TAPSE (mm)	0.1 (−1.2, 1.3)	2.3	0.1 (−1.0, 1.2)	2.1
RV GLS (%)	−0.1 (−1.5, 1.3)	1.9	−0.1 (−2.1, 1.9)	2.7
RV GLSR _s (1/s)	−0.02 (−0.16, 0.11)	3.9	−0.02 (−0.15, 0.10)	3.6
RV GLSR _e (1/s)	−0.01 (−0.24, 0.21)	4.5	−0.04 (−0.34, 0.25)	6.1
RV GLSR _a (1/s)	−0.03 (−0.20, 0.15)	5.5	−0.03 (−0.29, 0.24)	7.9
Right atrial phasic function				
ε _s (%)	0.3 (−2.9, 3.5)	2.9	0.9 (−4.2, 5.9)	4.7
ε _e (%)	0.4 (−2.5, 3.4)	5.5	0.3 (−3.5, 4.1)	6.8
ε _a (%)	−0.1 (−2.5, 2.4)	4.4	0.3 (−2.5, 3.2)	5.3
SR _s (1/s)	0.01 (−0.24, 0.26)	4.0	0.03 (−0.28, 0.33)	5.3
SR _e (1/s)	0.01 (−0.26, 0.27)	5.3	0.02 (−0.28, 0.32)	6.0
SR _a (1/s)	0.06 (−0.27, 0.39)	4.6	−0.03 (−0.38, 0.32)	4.8

CV, coefficient of variation; RV, right ventricular; EDV, end-diastolic volume; ESV, end-systolic volume; SV, stroke volume; EF, ejection fraction; RA, right atrial; S', peak systolic tricuspid annular velocity; E', peak early diastolic tricuspid annular velocity; A', peak late diastolic tricuspid annular velocity; TAPSE, tricuspid annular plane systolic excursion; GLS, global longitudinal strain; GLSR_s, peak systolic global longitudinal strain rate; GLSR_e, peak early diastolic global longitudinal strain rate; GLSR_a, peak late diastolic global longitudinal strain rate; ε_s, right atrial reservoir strain; ε_e, right atrial conduit strain; ε_a, right atrial booster strain; SR_s, right atrial reservoir strain rate; SR_e, right atrial conduit strain rate; SR_a, right atrial booster strain rate.

In addition to TA dynamics, we presented simplified strain indices relating time-varying distances between TA medial and lateral points and a fixed anatomical point at the RV apex or RA roof. Good correlation between the simplified longitudinal strains and those obtained from conventional endocardial contour-based feature tracking CMR was demonstrated, which is consistent with the results of our prior studies involving patients with rTOF, PAH, and age- and sex-matched controls (7, 8). In fact, the accuracy of conventional endocardial feature

tracking-derived longitudinal strain is degraded in subjects with vigorous TA motion, as contour tracking of the RV free wall segment adjacent to the tricuspid valve in the long-axis view becomes adversely affected (28). Compared to conventional contour-based strain measurements, the fast feature tracking strain measurements presented in this study are less dependent on RV and RA geometry, and more closely approximate the motion and reflect the function of longitudinal fibers in the RV, which are the greatest contributors to RV contraction (29). Our prior studies have shown that the simplified approach is not only faster but also more reproducible compared to the conventional CMR feature tracking approach (7, 8, 15, 16).

Limitations

There were some limitations in the present study. First, as CMR examinations were not performed repeatedly on the same subjects over time, the associations between age and CMR parameters are cross-sectional, not longitudinal. Nonetheless, the cross-sectional study design is commonly used in studies to establish reference ranges and make inferences regarding relationships in support of further research and clinical studies. We need a longitudinal study with repeated CMR scans on the same individual, which can help us investigate how age affects the heart structural and functional changes. Second, RV mass was not assessed in this study as RV mass is usually not quantified in a routine assessment because of the thin RV myocardium in healthy subjects.

CONCLUSIONS

We investigated age- and sex-related CMR measurements for right heart dimensions and function in a large Asian cohort that are of significant clinical and research utility in Asia. Using CMR, knowledge of age-, sex-, and ethnicity-specific distributions of right heart measurements should aid in the correct interpretation of disease states.

DATA AVAILABILITY STATEMENT

The original contributions presented in the study are included in the article/**Supplementary Materials**, further inquiries can be directed to the corresponding authors.

ETHICS STATEMENT

The studies involving human participants were reviewed and approved by SingHealth Centralized Institutional Review Board. The patients/participants provided their written informed consent to participate in this study.

AUTHOR CONTRIBUTIONS

R-ST, PC, LT, MF, CO, WR, AK, TT, JY, JT, YC, and LZ conceived the study design. SL, JG, CG, and XZ analyzed data. SL, R-ST, PC, LT, MF, CO, WR, AK, TT, JY, JT, YC, and LZ interpreted results. JA performed statistical analysis. SL drafted manuscript.

JG, R-ST, PC, LT, MF, CG, XZ, CO, JA, WR, AK, TT, JY, JT, YC, and LZ edited and revised manuscript. All authors read and approved the final manuscript.

FUNDING

This study was partially supported by the National Medical Research Council of Singapore (NMRC/OFIRG/0018/2016, MOH-000358, MOH-000351, NMRC/TA/0031/2015, and MOH-000153), SingHealth Duke-NUS Academic Medicine Research

Grant [AM/TP032/2020 (SRDUKAMR2032)]. The funder had no role in the design and conduct of the study, collection, management, analysis, interpretation of the data, preparation, and review or approval of the manuscript.

SUPPLEMENTARY MATERIAL

The Supplementary Material for this article can be found online at: <https://www.frontiersin.org/articles/10.3389/fcvm.2021.664431/full#supplementary-material>

REFERENCES

1. Sanz J, Sánchez-Quintana D, Bossone E, Bogaard HJ, Naeije R. Anatomy, function, and dysfunction of the right ventricle: JACC state-of-the-art review. *J Am Coll Cardiol*. (2019) 73:1463–82. doi: 10.1016/j.jacc.2018.12.076
2. Geva T. Is MRI the preferred method for evaluating right ventricular size and function in patients with congenital heart disease? MRI is the preferred method for evaluating right ventricular size and function in patients with congenital heart disease. *Circ Cardiovasc Imaging*. (2014) 7:190–7. doi: 10.1161/CIRCIMAGING.113.000553
3. Schulz-Menger J, Bluemke DA, Bremerich J, Flamm SD, Fogel MA, Friedrich MG, et al. Standardized image interpretation and post processing in cardiovascular magnetic resonance: Society for Cardiovascular Magnetic Resonance (SCMR) Board of Trustees Task Force on Standardized Post Processing. *J Cardiovasc Magn Reson*. (2013) 15:35. doi: 10.1186/1532-429X-15-35
4. Leng S, Jiang M, Zhao XD, Allen JC, Kassab GS, Ouyang RZ, et al. Three-dimensional tricuspid annular motion analysis from cardiac magnetic resonance feature-tracking. *Ann Biomed Eng*. (2016) 44:3522–38. doi: 10.1007/s10439-016-1695-2
5. Ito S, McElhinney DB, Adams R, Bhatla P, Chung S, Axel L. Preliminary assessment of tricuspid valve annular velocity parameters by cardiac magnetic resonance imaging in adults with a volume-overloaded right ventricle: comparison of unrepaired atrial septal defect and repaired tetralogy of Fallot. *Pediatr Cardiol*. (2015) 36:1294–300. doi: 10.1007/s00246-015-1160-2
6. Maffessanti F, Gripari P, Pontone G, Andreini D, Bertella E, Mushtaq S, et al. Three-dimensional dynamic assessment of tricuspid and mitral annuli using cardiovascular magnetic resonance. *Eur Heart J Cardiovasc Imaging*. (2013) 14:986–95. doi: 10.1093/ehjci/jet004
7. Leng S, Dong Y, Wu Y, Zhao XD, Ruan W, Zhang GC, et al. Impaired CMR-derived rapid semi-automated right atrial longitudinal strain is associated with decompensated hemodynamics in pulmonary arterial hypertension. *Circ Cardiovasc Imaging*. (2019) 12:e008582. doi: 10.1161/CIRCIMAGING.118.008582
8. Leng S, Tan RS, Guo JJ, Chai P, Zhang GC, Teo L, et al. Cardiovascular magnetic resonance-assessed fast global longitudinal strain parameters add diagnostic and prognostic insights in right ventricular volume and pressure loading disease conditions. *J Cardiovasc Magn Reson*. (2021) 23:38. doi: 10.1186/s12968-021-00724-5
9. De Siqueira MEM, Pozo E, Fernandes VR, Sengupta PP, Modesto K, Gupta SS, et al. Characterization and clinical significance of right ventricular mechanics in pulmonary hypertension evaluated with cardiovascular magnetic resonance feature tracking. *J Cardiovasc Magn Reson*. (2016) 18:39. doi: 10.1186/s12968-016-0258-x
10. Xie E, Yu R, Ambale-Venkatesh B, Bakhshi H, Heckbert SR, Soliman EZ, et al. Association of right atrial structure with incident atrial fibrillation: a longitudinal cohort cardiovascular magnetic resonance study from the Multi-Ethnic Study of Atherosclerosis (MESA). *J Cardiovasc Magn Reson*. (2020) 22:36. doi: 10.1186/s12968-020-00631-1
11. Kawut SM, Lima JA, Barr RG, Chahal H, Jain A, Tandri H, et al. Sex and race differences in right ventricular structure and function: the multi-ethnic study of atherosclerosis-right ventricle study. *Circulation*. (2011) 123:2542–51. doi: 10.1161/CIRCULATIONAHA.110.985515
12. Koh AS, Gao F, Leng S, Kovalik JP, Zhao XD, Tan RS, et al. Dissecting clinical and metabolomics associations of left atrial phasic function by cardiac magnetic resonance feature tracking. *Sci Rep*. (2018) 8:8138. doi: 10.1038/s41598-018-26456-8
13. Valsangiacomo Buechel ER, Mertens LL. Imaging the right heart: the use of integrated multimodality imaging. *Eur Heart J*. (2012) 33:949–60. doi: 10.1093/eurheartj/ehr490
14. Maceira AM, Cosin-Sales J, Roughton M, Prasad SK, Pennell DJ. Reference right atrial dimensions and volume estimation by steady state free precession cardiovascular magnetic resonance. *J Cardiovasc Magn Reson*. (2013) 15:29. doi: 10.1186/1532-429X-15-29
15. Leng S, Tan RS, Zhao XD, Allen JC, Koh AS, Zhong L. Fast long-axis strain: a simple, automatic approach for assessing left ventricular longitudinal function with cine cardiovascular magnetic resonance. *Eur Radiol*. (2020) 30:3672–83. doi: 10.1007/s00330-020-06744-6
16. Leng S, Tan RS, Zhao XD, Allen JC, Koh AS, Zhong L. Validation of a rapid semi-automated method to assess left atrial longitudinal phasic strains on cine cardiovascular magnetic resonance imaging. *J Cardiovasc Magn Reson*. (2018) 20:71. doi: 10.1186/s12968-018-0496-1
17. Leng S, Ge H, He J, Kong LC, Yang YN, Yan FH, et al. Long-term prognostic value of cardiac MRI left atrial strain in ST-segment elevation myocardial infarction. *Radiology*. (2020) 296:299–309. doi: 10.1148/radiol.20200176
18. Leng S, Zhao XD, Huang FQ, Wong JJ, Su BY, Allen JC, et al. Automated quantitative assessment of cardiovascular magnetic resonance-derived atrioventricular junction velocities. *Am J Physiol Heart Circ Physiol*. (2015) 309:H1923–35. doi: 10.1152/ajpheart.00284.2015
19. Ouyang RZ, Leng S, Sun AM, Wang Q, Hu LW, Zhao XD, et al. Detection of persistent systolic and diastolic abnormalities in asymptomatic pediatric repaired tetralogy of Fallot patients with preserved ejection fraction: a CMR feature tracking study. *Eur Radiol*. (2021). doi: 10.1007/s00330-020-07643-6
20. Di Salvo G, Miller O, Babu Narayan S, Li W, Budts W, Valsangiacomo Buechel ER, et al. Imaging the adult with congenital heart disease: a multimodality imaging approach-position paper from the EACVI. *Eur Heart J Cardiovasc Imaging*. (2018) 19:1077–98. doi: 10.1093/ehjci/jej102
21. Petersen SE, Aung N, Sanghvi MM, Zemrak F, Fung K, Paiva JM, et al. Reference ranges for cardiac structure and function using cardiovascular magnetic resonance (CMR) in Caucasians from the UK Biobank population cohort. *J Cardiovasc Magn Reson*. (2017) 19:18. doi: 10.1186/s12968-017-0327-9
22. Dalen H, Thorstensen A, Vatten LJ, Aase SA, Stoylen A. Reference values and distribution of conventional echocardiographic Doppler measures and longitudinal tissue Doppler velocities in a population free from cardiovascular disease. *Circ Cardiovasc Imaging*. (2010) 3:614–22. doi: 10.1161/CIRCIMAGING.109.926022
23. Peng JP, Zhao XD, Zhao L, Fan ZM, Wang Z, Chen H, et al. Normal values of myocardial deformation assessed by cardiovascular magnetic resonance feature tracking in a healthy Chinese population: a multicenter study. *Front Physiol*. (2018) 9:1181. doi: 10.3389/fphys.2018.01181
24. Qu YY, Li H, Rottbauer W, Ma GS, Buckert D, Rasche V. Right ventricular free wall longitudinal strain and strain rate quantification with cardiovascular magnetic resonance based tissue tracking. *Int J Cardiovasc Imaging*. (2020) 36:1985–96. doi: 10.1007/s10554-020-01895-5

25. Maceira AM, Cosin-Sales J, Prasad SK, Pennell DJ. Characterization of left and right atrial function in healthy volunteers by cardiovascular magnetic resonance. *J Cardiovasc Magn Reson.* (2016) 18:64. doi: 10.1186/s12968-016-0284-8
26. Peluso D, Badano LP, Muraru D, Dal Bianco L, Cucchini U, Kocabay G, et al. Right atrial size and function assessed with three-dimensional and speckle-tracking echocardiography in 200 healthy volunteers. *Eur Heart J Cardiovasc Imaging.* (2013) 14:1106–14. doi: 10.1093/ehjci/jet024
27. Truong VT, Palmer C, Young M, Wolking S, Ngo TNM, Sheets B, et al. Right atrial deformation using cardiovascular magnetic resonance myocardial feature tracking compared with two-dimensional speckle tracking echocardiography in healthy volunteers. *Sci Rep.* (2020) 10:5237. doi: 10.1038/s41598-020-62105-9
28. Bhawe NM, Visovatti SH, Kulick B, Kolias TJ, McLaughlin VV. Right atrial strain is predictive of clinical outcomes and invasive hemodynamic data in group 1 pulmonary arterial hypertension. *Int J Cardiovasc Imaging.* (2017) 33:847–55. doi: 10.1007/s10554-017-1081-7
29. Brown SB, Raina A, Katz D, Szerlip M, Wiegers SE, Forfia PR. Longitudinal shortening accounts for the majority of right ventricular contraction and improves after pulmonary vasodilator therapy in normal subjects and patients with pulmonary arterial hypertension. *Chest.* (2011) 140:27–33. doi: 10.1378/chest.10-1136

Conflict of Interest: The authors declare that the research was conducted in the absence of any commercial or financial relationships that could be construed as a potential conflict of interest.

Copyright © 2021 Leng, Guo, Tan, Chai, Teo, Fortier, Gong, Zhao, Ong, Allen, Ruan, Koh, Tan, Yip, Tan, Chen and Zhong. This is an open-access article distributed under the terms of the Creative Commons Attribution License (CC BY). The use, distribution or reproduction in other forums is permitted, provided the original author(s) and the copyright owner(s) are credited and that the original publication in this journal is cited, in accordance with accepted academic practice. No use, distribution or reproduction is permitted which does not comply with these terms.



Left Ventricular Remodeling and Myocardial Work: Results From the Population-Based STAAB Cohort Study

Floran Sahiti^{1,2}, Caroline Morbach^{1,2}, Vladimir Cejka¹, Judith Albert^{1,2}, Felizitas A. Eichner^{1,3}, Götz Gelbrich^{1,3,4}, Peter U. Heuschmann^{1,3,4†} and Stefan Störk^{1,2*†} on behalf of the STAAB Consortium

¹ Comprehensive Heart Failure Center, University and University Hospital Würzburg, Würzburg, Germany, ² Department of Medicine I, University Hospital Würzburg, Würzburg, Germany, ³ Institute of Clinical Epidemiology and Biometry, University of Würzburg, Würzburg, Germany, ⁴ Clinical Trial Center, University Hospital Würzburg, Würzburg, Germany

OPEN ACCESS

Edited by:

Matteo Cameli,
University of Siena, Italy

Reviewed by:

Leonid Goubergrits,
Charité – Universitätsmedizin
Berlin, Germany
Sabina Gallina,
University of Studies G. d'Annunzio
Chieti and Pescara, Italy

*Correspondence:

Stefan Störk
stoerk_s@ukw.de

[†]These authors have contributed
equally to this work

Specialty section:

This article was submitted to
Cardiovascular Imaging,
a section of the journal
Frontiers in Cardiovascular Medicine

Received: 18 February 2021

Accepted: 06 May 2021

Published: 11 June 2021

Citation:

Sahiti F, Morbach C, Cejka V, Albert J,
Eichner FA, Gelbrich G,
Heuschmann PU and Störk S (2021)
Left Ventricular Remodeling and
Myocardial Work: Results From the
Population-Based STAAB Cohort
Study.
Front. Cardiovasc. Med. 8:669335.
doi: 10.3389/fcvm.2021.669335

Introduction: Left ventricular (LV) dilatation and LV hypertrophy are acknowledged precursors of myocardial dysfunction and ultimately of heart failure, but the implications of abnormal LV geometry on myocardial function are not well-understood. Non-invasive LV myocardial work (MyW) assessment based on echocardiography-derived pressure-strain loops offers the opportunity to study detailed myocardial function in larger cohorts. We aimed to assess the relationship of LV geometry with MyW indices in general population free from heart failure.

Methods and Results: We report cross-sectional baseline data from the Characteristics and Course of Heart Failure Stages A-B and Determinants of Progression (STAAB) cohort study investigating a representative sample of the general population of Würzburg, Germany, aged 30–79 years. MyW analysis was performed in 1,926 individuals who were in sinus rhythm and free from valvular disease (49.3% female, 54 ± 12 years). In multivariable regression, higher LV volume was associated with higher global wasted work (GWW) (+0.5 mmHg% per mL/m², $p < 0.001$) and lower global work efficiency (GWE) (−0.02% per mL/m², $p < 0.01$), while higher LV mass was associated with higher GWW (+0.45 mmHg% per g/m², $p < 0.001$) and global constructive work (GCW) (+2.05 mmHg% per g/m², $p < 0.01$) and lower GWE (−0.015% per g/m², $p < 0.001$). This was dominated by the blood pressure level and also observed in participants with normal LV geometry and concomitant hypertension.

Conclusion: Abnormal LV geometric profiles were associated with a higher amount of wasted work, which translated into reduced work efficiency. The pattern of a disproportionate increase in GWW with higher LV mass might be an early sign of hypertensive heart disease.

Keywords: myocardial work, myocardial work efficiency, left ventricular geometry, left ventricular mass, LV dilatation, left ventricular geometric abnormality, left ventricular remodeling

INTRODUCTION

The constant exposure to cardiovascular risk factors and/or adverse hemodynamic conditions induces complex changes in left ventricular (LV) geometry, often starting as a physiological compensatory response (1, 2). Alterations in LV geometry such as LV dilatation and LV hypertrophy are acknowledged precursors of myocardial dysfunction and ultimately of heart failure (3–6), but the mechanisms are still not well-understood. Invasive recording of pressure-volume loops as the reference standard provides real-time assessment of LV loading conditions, contractility, and myocardial oxygen consumption (7). However, its (repeated) use in clinical routine is limited due to the investigation's invasive nature. Recent advances in imaging methods allow to approximate the intrinsic and functional cardiac performance with satisfactory precision, also accounting for loading conditions. A novel echocardiographic method has been introduced and validated against invasive measurements that non-invasively quantifies active myocardial function, i.e., systolic and early diastolic active myocardial work (MyW) (8). This approach allows differentiating constructive from wasted MyW, with the latter not contributing to LV output. The concept of MyW measurement is based on speckle-tracking derived longitudinal strain and systolic blood pressure and is widely applicable, including situations of screening. However, echocardiography-derived MyW has to be differentiated from the puristic definition of cardiac work derived from invasive pressure-volume loops, expressed in Joule or Centijoule (9). MyW approximates the work contributing to LV output, i.e., constructive work, and quantifies energy loss due to uncoordinated left ventricular contractions resulting in stretching of individual LV segments by the contraction of other LV segments, i.e., wasted work (10). Further, MyW might allow profound insights into LV performance and, given the strong correlation with cardiac glucose uptake as measured by positron emission tomography, might also serve as surrogate of regional and global myocardial metabolism (8, 10). LV geometry patterns have been shown to be of prognostic relevance in community studies (11, 12) and depend, i.e., on exposure to modifiable cardiovascular risk factors, such as hypertension and obesity (4, 13, 14). Thus, the detailed evaluation of MyW in relation to LV geometry might further advance the pathophysiological understanding of functional changes associated with abnormal LV geometry. Therefore, we aimed to assess the association of LV geometry with myocardial work in a well-characterized population-based sample of individuals free from heart failure.

Abbreviations: LV, left ventricle/ventricular; LVMi, left ventricular mass index; LVEDVi, left ventricular end diastolic volume index; CR, concentric remodeling; CH, concentric hypertrophy; EH, eccentric hypertrophy; GLS, global longitudinal strain; GWE, global work efficiency; GWI, global work index; GCW, global constructive work; GWW, global wasted work; STAAB, The Characteristics and Course of Heart Failure STages A/B and Determinants of Progression Cohort Study.

METHODS

Population

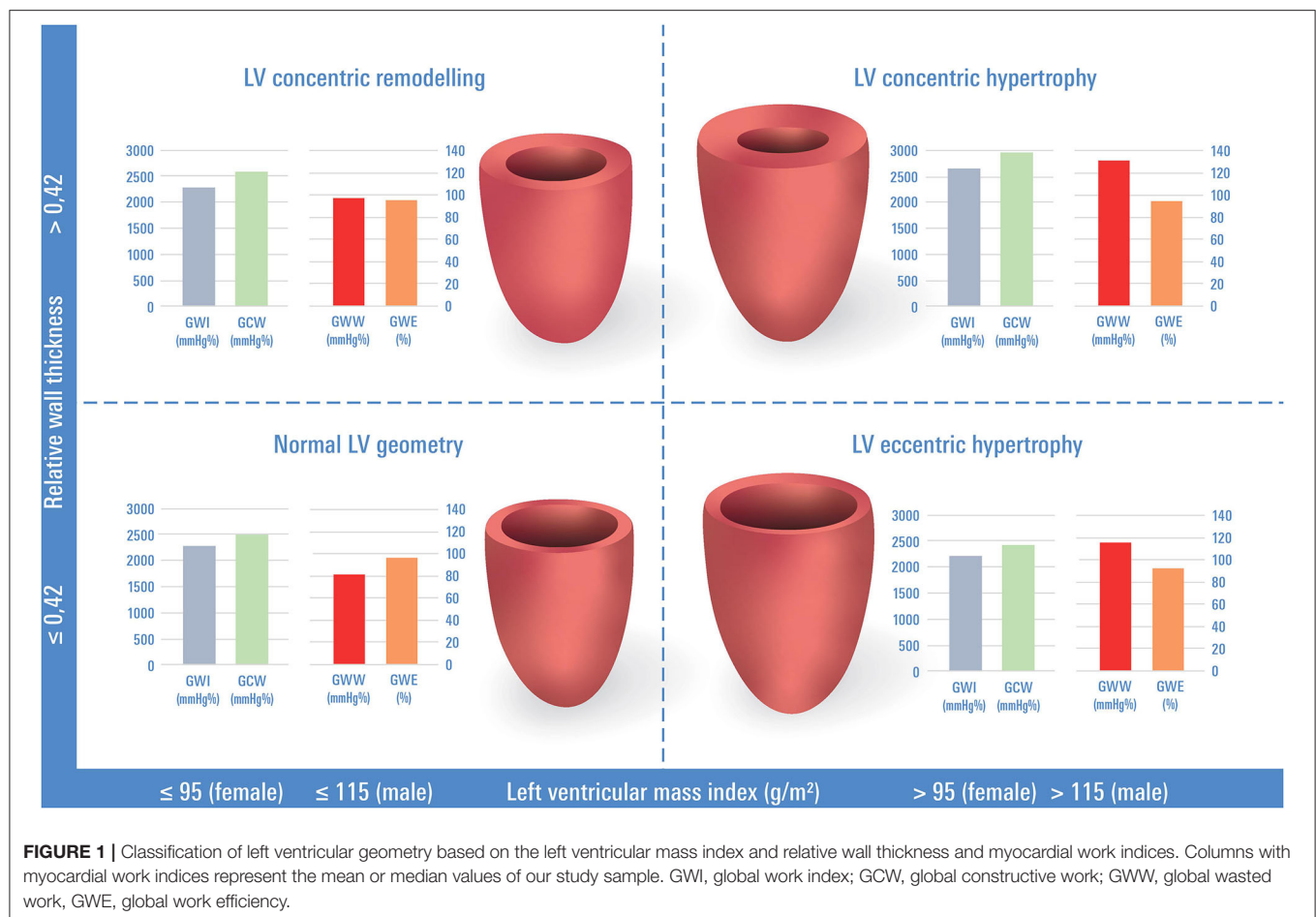
Within the Characteristics and Course of Heart Failure STages A/B and Determinants of Progression (STAAB) prospective cohort study, we recruited and comprehensively phenotyped a representative sample of the population of Würzburg, Germany, aged 30–79 years, $n = 5,000$, free of symptomatic heart failure. The study design and baseline characteristics have been published previously (15, 16). The STAAB study complies with the Declaration of Helsinki and was approved by the ethics committee, University of Würzburg (J-117.605-09/13). All participants provided written informed consent prior to any study-related examination. For the present analysis, we evaluated cross-sectional data of the baseline examination from the first half of the STAAB study population ($n = 2,473$). This group had been included between December 12, 2013, and September 2, 2016, was pre-specified for a planned interim analysis (15), and therefore met the sex and age stratification criteria of the total sample.

Baseline Examination

Participants were evaluated at the Joint Survey Unit of the Comprehensive Heart Failure Center and the Institute for Clinical Epidemiology and Biometry, University of Würzburg. Routine laboratory measurements were performed at the central laboratory of the University Hospital Würzburg, including fasting lipid profile, estimated glomerular filtration rate (eGFR), glycosylated hemoglobin (HbA1c), and NT-proBNP levels. Blood pressure (in a sitting position after 5 min of rest), body height and weight, hypertension history, and current anti-hypertensive pharmacotherapy were assessed according to standard operating procedures (14). According to ESC guidelines, the presence of hypertension was defined as blood pressure $\geq 140/90$ mmHg or on anti-hypertensive pharmacotherapy (17). We further sub-classified our sample according to blood pressure into four groups as recommended by current guidelines (17): (a) optimal blood pressure, i.e., systolic blood pressure (SBP) < 120 mmHg; (b) normal blood pressure, SBP 120–129 mmHg; (c) high-normal blood pressure, SBP 130–139 mmHg; and (d) grade 1 hypertension or higher, SBP ≥ 140 mmHg.

Echocardiographic Analysis and LV Geometry

Image acquisition was performed by trained and certified sonographers employing one echocardiography machine (Vivid S6® with M4S Sector Array Transducer operating at 1.5–4.3 MHz, GE Healthcare, Horten, Norway) with presets maintained according to a pre-specified protocol. The utility of performance measures of the echocardiography quality assurance program has been published previously (18). A minimum of three cardiac cycles was recorded. Two-dimensional images from the LV apical four-, two-, and three-chamber views were recorded with a frame rate of 50–80 s⁻¹ and stored digitally. We derived end-diastolic interventricular septum thickness (IVSd), LV posterior wall thickness (LVPWd), and LV end-diastolic diameter (LVEDD)



in the parasternal long-axis from an M-Mode recording, or—in case of suboptimal angulation—from a 2D measurement (19). We calculated LV mass using the corrected American Society of Echocardiography method (19): $LV\ mass\ (g) = 0.8\ (1.04\ [(LVEDD + IVSd + LVPWd)^3 - LVEDD^3]) + 0.6$ as well. LV relative wall thickness (RWT) was calculated as: $(2 \times \text{posterior wall thickness}) / LV\ end\text{-diastolic diameter}$ (1, 19). We further measured LV ejection fraction (LVEF) and LV end-diastolic volume using Simpson's biplane method (19). Early diastolic myocardial relaxation velocity (e') was assessed using tissue and PW-Doppler close to the septal and/or lateral mitral annulus. LA volume was measured biplane in apical four and two-chamber view and left atrial volume index (LAVi) was calculated as LA volume indexed to body surface area. Valve regurgitation was determined by the color Doppler multiplane vena contracta method, and valve stenosis was quantified by continuous-wave Doppler measurements (15). LV mass index (LVMI) and LV end-diastolic volume index (LVEDVi) were calculated, indexing LV mass and LV end-diastolic volume to body surface area, respectively. According to the latest guidelines (1, 19), we classified the participants into four different subgroups according to their respective LV geometry pattern (**Figure 1**): (a) normal LV geometry, $LVMi \leq 95\ g/m^2$ in women or $\leq 115\ g/m^2$ in men and $RWT \leq 0.42$; (b) concentric LV remodeling (CR),

$LVMi \leq 95\ g/m^2$ in women or $\leq 115\ g/m^2$ in men and $RWT > 0.42$; (c) concentric LV hypertrophy (CH), $LVMi > 95\ g/m^2$ in women or $> 115\ g/m^2$ in men and $RWT > 0.42$; (d) eccentric LV hypertrophy (EH), $LVMi > 95\ g/m^2$ in women or $> 115\ g/m^2$ in men and $RWT \leq 0.42$.

Myocardial Work Analysis

MyW analysis was performed off-line based on the stored echocardiography images and blood pressure measurements. Aortic and mitral valve closure and opening times were assessed by CW Doppler of the aortic valve and PW Doppler of the mitral valve. However, as potential changes in heart rate during the examination might affect the loop area, these time points were visually verified in the apical three-chamber view and manually adjusted where necessary. LV apical four-, two-, and three-chamber views were analyzed off-line using Automated Functional Imaging (EchoPAC®, Version 202, GE) to determine global longitudinal strain (GLS). Provision of peripheral blood pressure allowed the derivation of the MyW parameters as detailed by others (8, 10, 20).

A) Global constructive work [GCW (mmHg%)], i.e., the sum of positive work performed during shortening in

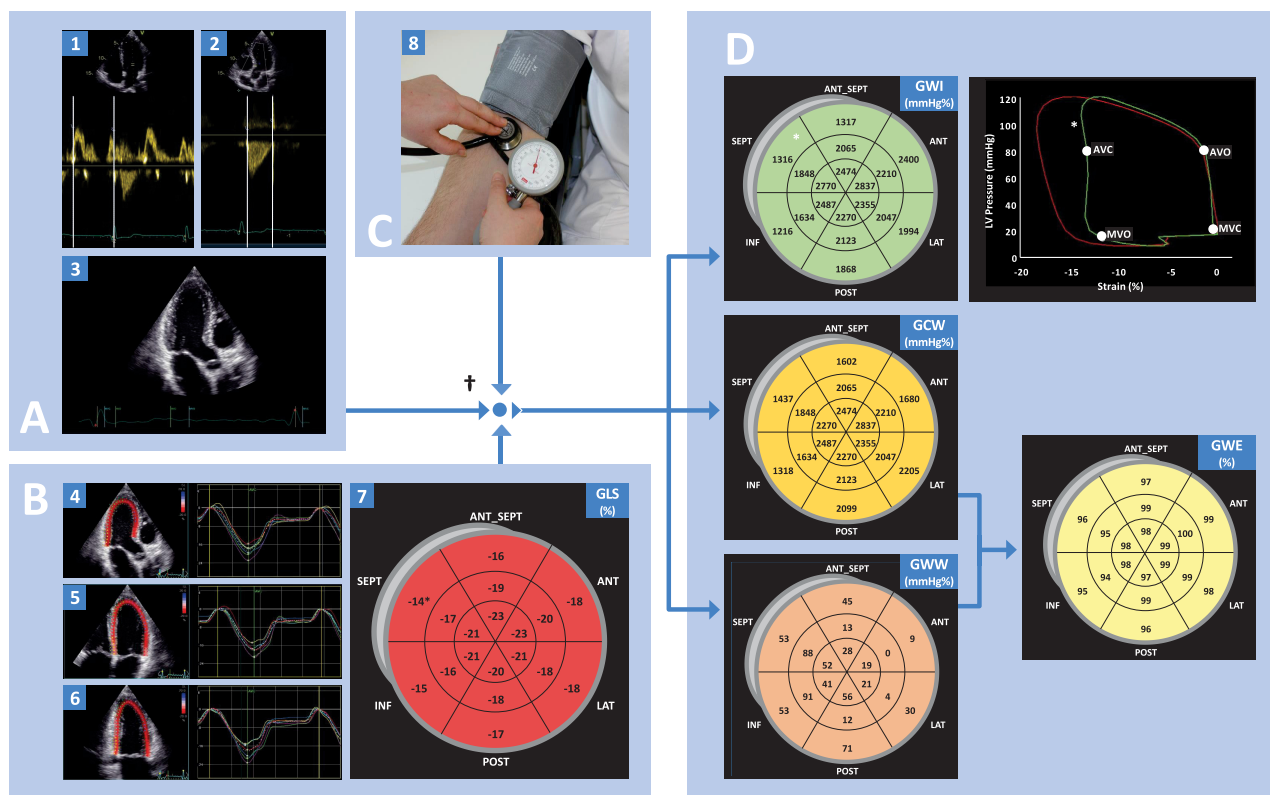


FIGURE 2 | Illustrative physiological background of LV myocardial work analysis. **(A)** Represents valvular times, with mitral valve opening and close measured using pulse-waved Doppler derived mitral inflow and aortic valve opening and closure measured by continuous-wave Doppler derived transaortic outflow. **(B)** Global longitudinal strain measured from 4, 3, and 2 chamber view. **(C)** Estimated LV Pressure measured from brachial cuff pressure. **(D)** Schematic presentation of segment-specific values of MyW indices, which later are expressed in global values. GCW and GWW are important physiological indices related to the shortening and lengthening of the LV segments. Work efficiency (GWE) is derived as the fraction of GCW and the sum of GCW and GWW. [†] Empiric reference curve of LV pressure as suggested in the validation study by Russell et al. (8). * indicates a segment-specific pressure-strain loop (in this case, we highlighted the septal basal segment).

systole and adding negative work during lengthening in isovolumic relaxation;

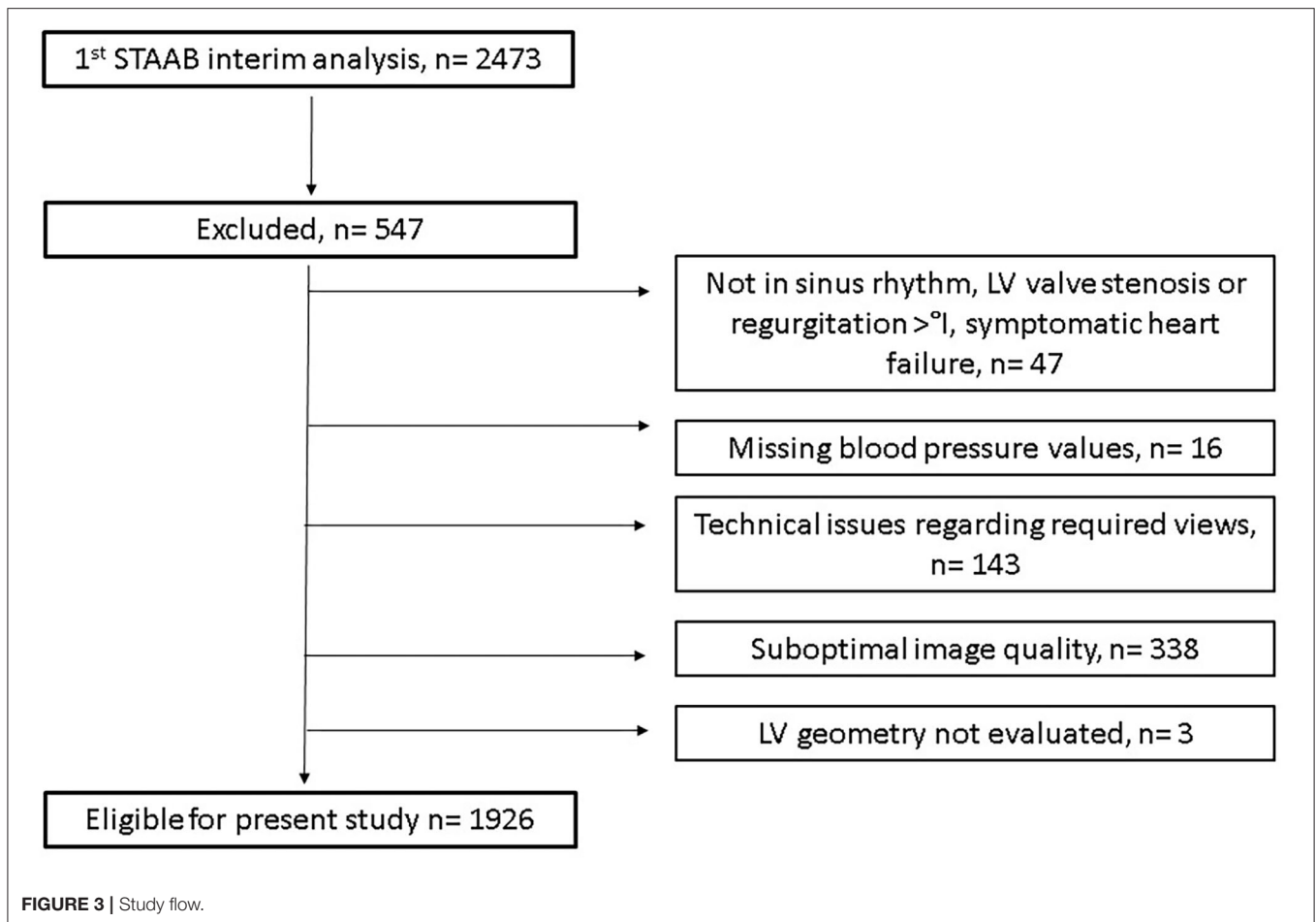
- B) Global wasted work [GWW (mmHg%)], i.e., the sum of negative work performed during lengthening in systole plus work performed during shortening against a closed aortic valve in isovolumic relaxation;
- C) Global work index [GWI (mmHg%)], i.e., the total work performed from mitral valve closure to mitral valve opening.
- D) Global work efficiency [GWE (%)], i.e., $GWE = GCW / (GCW + GWW)$.

All indices were calculated as the mean of respective segmental values (18-segment model). We excluded subjects from further analysis in whom >1 LV segment was unsuitable for analysis due to poor tracking or suboptimal image quality. Determination of MyW, as well as quality assurance measures, have been published previously (21). **Figure 2** illustrates step by step the approach to LV myocardial work analysis.

Data Analysis

Continuous variables are described as mean (standard deviation) and categorical variables as frequency (percent). Normal

distribution was checked using the Shapiro-Wilk test. Normal distributed variables were compared using the *t*-test, non-normal distributed variables using the Mann-Whitney *U*-test, and categorical variables using the chi-square test, respectively. Differences between groups were tested using the Kruskal-Wallis test, median test, and chi-square test. To test the relationship between LV geometry and MyW, we first ran a univariable linear regression analysis for each of MyW indices. Because we wanted to describe the relative contribution of systolic blood pressure, this variable was also tested, despite the fact that it is part of the derivation of myocardial work indices. In subsequent multivariable models, however, systolic blood pressure was omitted. Models were based on results of univariable regression and their physiological context. Thus, the multivariable model included age, sex, body mass index (BMI), LVEF, GLS, heart rate, low-density lipoprotein (LDL), glycosylated hemoglobin (HbA1c), hypertension, and measures of LV geometry such as LVMi and LVEDVi. The Jonckheere-Terpstra test was used for trend analysis. All tests were performed 2-sided. *P*-value < 0.05 were considered statistically significant. Statistical analysis was performed using SPSS (Version 26, SPSS Inc., Chicago, USA).



RESULTS

For the pre-planned interim analysis of the STAAB cohort study, 2,473 individuals were considered. Of those, a total of $n = 547$ participants were excluded from the current analysis for different reasons including technical issues regarding required views, poor tracking or suboptimal image quality, or missing blood pressure values (for details, see **Figure 3**). Therefore, a total sample of $n = 1,926$ individuals was included (49.3% women, with mean age 54 ± 12 years). Ninety-three percent of those had normal LV geometry, and 5% exhibited CR, 2% had EH, and <1% had CH, respectively. **Table 1** presents the clinical and echocardiographic characteristics for the total sample and stratified for groups defined by LV geometry.

Participants with normal LV geometry were younger and had lower BMI, SBP, NT-proBNP, LDL cholesterol, and HbA1c compared to abnormal geometric LV patterns (**Table 1**). Accordingly, participants with normal LV geometry exhibited less often obesity, hypertension, diabetes mellitus, or dyslipidemia. In contrast, coronary heart disease and anti-hypertensive treatment was more prevalent in individuals with abnormal LV geometry patterns. Even though still within the normal range, LVEF and GLS were more favorable in normal

LV geometry when compared to CR and EH (**Table 2**). LVEDV index was lower in CR and higher in EH participants. Diastolic function in abnormal LV geometry patterns was significantly less favorable when compared to normal LV geometry. MyW characteristics are shown in **Table 2**. When compared to normal LV geometry, we found higher values of GCW and GWI in CH, as well as of GWW in CR and EH. These effects resulted in compromised GWE with any type of abnormal LV geometry.

In multivariable linear regression analysis including age, sex, BMI, heart rate, LVEF, LDL, HbA1c, hypertension, LVMI, and LVEDVi, we found that higher LV muscle mass was associated with a higher GCW, but also with higher GWW, thus resulting in reduced GWE. In contrast, higher LV volume was associated with higher GWW only, which also resulted in lower GWE (**Table 3**). In a further step, we analyzed patients with normal LV geometry according to the presence of hypertension (**Table 4**). Individuals with hypertension were more often male, were older, and had higher BSA and BMI. They showed similar LV volumes but significantly higher LV mass and LA volume and less favorable measures of systolic and diastolic function. Individuals with hypertension revealed significantly higher GCW and GWI, but also GWW, resulting in lower GWE. A sensitivity analysis focusing on the current blood pressure category showed

TABLE 1 | Baseline characteristics in the total sample and according to left ventricular (LV) geometry.

	All subjects (N = 1,926)	LV normal geometry (N = 1,789)	LV concentric remodeling (N = 100)	LV concentric hypertrophy (N = 6)	LV eccentric hypertrophy (N = 31)
Age [years]	54 (12)	53 (12)	61 (10)*	69 (16)*	61 (9)*
Sex, women	950 (49.3)	879 (49.1)	48 (48.0)	4 (66.6)	19 (61.2)
BSA [m ²]	1.9 (0.2)	1.9 (0.2)	1.9 (0.2)	1.9 (0.3)	1.9 (0.2)
BMI [kg/m ²]	26.0 (4.3)	25.9 (4.1)	28.3 (4.7)*	30.1 (9.0)	28.1 (5.0)*
Heart rate [beats/min]	67 (10)	67 (10)	69 (10)*	60 (5)*	65 (12)
SBP [mmHg]	130 (18)	130 (17)	141 (18)*	148 (12)*	139 (23)*
DBP [mmHg]	78 (10)	78 (10)	81 (8)*	79 (13)	78 (14)
NT-proBNP [pg/ml]	52 (24, 97)	51 (24, 94)	52 (29, 108)	87 (63, 245)	154 (58, 305)*
LDL cholesterol [mg/dl]	122 (34)	122 (34)	126 (34)*	113 (27)	124 (44)*
HbA1c [%]	5.5 (0.6)	5.5 (0.5)	5.9 (1.0)*	5.8 (0.5)	6.1 (1.1)*
eGFR [ml/min]	87 (15)	87 (15)	83 (15)	85 (19)	86 (17)
Hypertension	848 (44.0)	735 (41.1)	79 (79.0)*	6 (100)*	28 (90.3)*
Diabetes	155 (8.0)	124 (6.9)	20 (20.0)*	3 (50.0)*	8 (25.8)*
Obesity	301 (15.6253)	253 (14.1)	33 (33.0)*	2 (33.3)	13 (41.9)*
Dyslipidemia	254 (13.2)	222 (12.4)	19 (19.0)	2 (33.3)	11 (35.5)*
Coronary heart disease	70 (3.6)	53 (2.9)	8 (8.0)*	1 (16.6)	8 (25.8)*
Peripheral artery disease	25 (1.3)	21 (1.2)	2 (2.0)	0 (0)	2 (6.5)*
Anti-hypertensive therapy	522 (27.1)	436 (24.4)	59 (59.0)*	5 (83.3)*	22 (70.9)*
ACEi/ARB	382 (19.8)	318 (17.7)	45 (45.0)*	5 (83.3)*	14 (45.2)*
Beta-blocker	242 (12.6)	200 (11.2)	26 (26.0)*	3 (50.0)*	13 (41.9)*
Diuretics	99 (5.1)	81 (4.5)	11 (11.0)*	2 (33.3)*	5 (16.1)*

*Explorative comparison with individuals with normal LV geometry (two-sided $p < 0.05$).

Data are n (%), mean (SD), or median (quartiles).

BSA, body surface area; BMI, body mass index; NT-proBNP, N-terminal-pro Brain Natriuretic Peptide; SBP, systolic blood pressure; DBP, diastolic blood pressure; LDL, low-density lipoprotein; HbA1c, glycosylated hemoglobin; eGFR, estimated glomerular filtration rate; ACEi, angiotensin converting enzyme inhibitor; ARB, angiotensin II receptor type 1 blocker. Medications history was obtained in $n = 1,914$ individuals.

a consistent pattern, i.e., higher GCW, GWI, and GWW with increasing blood pressure but lower GWE (Table 5). The strength of the association for the trends observed in Tables 4, 5 was maintained when adjusting for age.

DISCUSSION

The current study investigated the association of altered LV geometry with MyW indices in a large, population-based sample. Three major findings emerged. First, while the majority of individuals studied exhibited a normal LV geometry, a relevant proportion of participants revealed an abnormal LV geometry; these subjects were older and presented with a less favorable profile of cardiovascular risk factors. Second, both LV enlargement and LV hypertrophy were adversely associated with GWE, predominantly through increasing the amount of GWW. Third, when compared to participants without hypertension, individuals with normal LV geometry and concomitant hypertension exhibited larger LV mass and LA volume and less favorable measures of systolic and diastolic function. Their MyW pattern was characterized by higher GCW and GWW and thus lower GWE, comparable to the pattern found in LV hypertrophy.

Altered LV geometry, including its components LV mass and LV volume, constitute pivotal information of the standard echocardiography report (1), as they reliably indicate maladaptation due to adversely regulated hemodynamics (22). Such conditions trigger myocardial responses that aim at maintaining a normal cardiac output despite compromised energetics (23–25). When left untreated, these adaptive changes induce early, subclinical changes in LV geometry, advance toward subclinical impairment in LV function (1), and ultimately cause functional capacity loss (26). This complex configuration is mainly driven by changes at the histological and metabolic level, e.g., myocyte hypertrophy, apoptosis, and energy consumption (27). Not surprisingly, deteriorating LV geometry was shown to predict incident heart failure (28, 29).

An increased hemodynamic load, induced either by pressure, e.g., in hypertension, or by volume, e.g., in valvular disease, or by a combination of both stimuli, contributes to LV hypertrophy and/or dilation, resulting in different geometric adaptations (1, 2). Recently, changes in LV chamber geometry, i.e., an increase in LV mass and/or LV size, were reported to relate to impaired GLS (30). LV mass and LV volume further impact on electric conduction times resulting in prolonged QRS duration and potential consecutive LV dyssynchrony (31–34), which, in turn,

TABLE 2 | Baseline echocardiographic characteristics including myocardial work according to the LV geometry classification.

	All subjects (N = 1,926)	LV normal geometry (N = 1,789)	LV concentric remodeling (N = 100)	LV concentric hypertrophy (N = 6)	LV eccentric hypertrophy (N = 31)
IVSd [mm]	9 (1)	9 (1)	10 (1)*	11 (1)*	9 (1)*
LVPWd [mm]	8 (1)	8 (1)	10 (1)*	11 (1)*	11 (1)*
LVEDd [mm]	48 (5)	48 (5)	44 (4)*	51 (4)	55 (4)*
RWT	0.34 (0.05)	0.33 (0.05)	0.45 (0.04)*	0.44 (0.02)*	0.35 (0.04)*
LVM [g]	138 (39)	136 (37)	153 (36)*	219 (43)*	219 (42)*
LVMi [g/m ²]	72 (16)	71 (15)	78 (15)*	113 (13)*	112 (10)*
LVEDV [mL]	99 (25)	99 (25)	93 (22)*	100 (33)	123 (29)*
LVEDVi [mL/m ²]	52 (10)	52 (10)	47 (9)*	52 (16)	64 (14)*
LAV [mL]	46 (15)	46 (15)	47 (16)	54 (12)	55 (17)*
LAVi [mL/m ²]	24 (7)	24 (7)	25 (8)	28 (7)	29 (9)*
E prime lateral	11 (3)	11 (3)	9 (2)*	7 (2)*	8 (3)*
E prime septal	9 (2)	9 (2)	7 (2)*	5 (1)*	6 (2)*
LVEF [%]	61 (4)	61 (4)	60 (4)*	59 (3)	58 (7)*
Stroke volume [mL]	60 (15)	60 (15)	55 (14)*	58 (16)	70 (16)*
GLS [−%]	21 (3)	21 (3)	20 (2)*	21 (1)	19 (3)*
GCW [mmHg%]	2,506 (428)	2,501 (424)	2,575 (457)	2,965 (240)*	2,445 (526)
GWW [mmHg%]	83 (59, 119)	81 (58, 118)	98 (68, 133)*	130 (80, 191)	117 (90, 158)*
GWI [mmHg%]	2,278 (396)	2,276 (392)	2,311 (424)	2,670 (315)*	2,207 (502)
GWE [%]	96 (95, 97)	96 (95, 97)	95 (94, 97)*	94 (91, 96)	94 (93, 95)*

*Significantly different when compared to LV normal geometry (two-sided $p < 0.05$).

Data are n (%), mean (SD), or median (quartiles).

LVEF, left ventricular ejection fraction; GLS, global longitudinal strain; IVSd, interventricular septum diameter; LVPWd, left ventricular posterior wall diameter; LVEDd, left ventricular end-diastolic diameter; RWT, relative wall thickness; LVM, left ventricular mass; LVMi, left ventricular mass index; LVEDV, left ventricular end-diastolic volume; LVEDVi, left ventricular end-diastolic volume index; LAV, left atrial volume; LAVi, left atrial volume index; GCW, global constructive work; GWW, global wasted work; GWI, global work index; GWE, global work efficiency.

TABLE 3 | Univariable and multivariable regression analysis of myocardial work indices and different echocardiographic parameters.

	GCW [mmHg%]		GWW [mmHg%]		GWI [mmHg%]		GWE [%]	
	Mean 2,506, SD 428		Median 83, quartiles 59, 119		Mean 2,278, SD 396		Mean 96, SD 2	
	Univariable analysis	Multivariable analysis [†]	Univariable analysis	Multivariable analysis [†]	Univariable analysis	Multivariable analysis [†]	Univariable analysis	Multivariable analysis [†]
Sex [Women]	+87.3***	ns	−0.5	+10.9***	+124***	+68.8***	+0.2*	−0.4***
Age [years]	+7.9***	+4.5***	+1.2***	+0.8***	+4.9***	+1.6*	−0.05***	−0.03***
BMI [kg/m ²]	−6.5**	−10.1***	+0.3	−1.3***	−4.9*	−5.7**	−0.02*	+0.05***
LVEF [%]	+19.4***	+11.0***	−2.1***	−1.4***	+21.9***	+13.1***	+0.1***	+0.08***
GLS [−%]	+50.4***	+51.4***	−2.5***	−1.2**	+50.9***	+48.4***	+0.2***	+0.1***
Heart rate [beats/min]	−4.9***	ns	+0.3**	+0.4***	−5.5***	−2.6**	−0.02***	−0.02***
Systolic BP [mmHg]	+16.6***	−	+1.1***	−	+14.3***	−	−0.02***	−
LDL-C [mg/dL]	+0.3	ns	+0.06	ns	+0.2	ns	−0.002	ns
HbA1c [%]	+10.5	−35.7*	+10.6***	ns	−1.7	ns	−0.5***	ns
LVEDVi [mL/m ²]	−2.0*	ns	+0.3**	+0.5***	−2.0*	ns	−0.02***	−0.02***
LVMi [g/m ²]	+2.4***	+2.0**	+0.7***	+0.4***	+1.1*	+1.5**	−0.03***	−0.01***
IVSd [mm]	+21.9**	−	+6.7***	−	+10.6	−	−0.3***	−
LVPWd [mm]	+16.6*	−	+6.1***	−	+4.3	−	−0.3***	−
LVEDd [mm]	−3.1	−	+0.6*	−	−4.8*	−	−0.03**	−
RWT	+539**	−	+109***	−	+351*	−	−4.5***	−
Hypertension	+304***	+343***	+29.2***	+19.4***	+253***	+316***	−0.9***	−0.3**

(−) indicates that the variable was not considered in the multivariable regression analysis.

GCW, global constructive work; GWW, global wasted work; GWI, global work index; GWE, global work efficiency; BMI, body mass index; LVEF, left ventricular ejection fraction; GLS, global longitudinal strain; LDL-C, low-density lipoprotein cholesterol; HbA1c, glycosylated hemoglobin; LVEDVi, left ventricular end-diastolic volume index; LVMi, left ventricular mass index; IVSd, interventricular septum diameter; LVPWd, left ventricular posterior wall diameter; RWT, relative wall thickness; * $p < 0.05$; ** $p < 0.01$; *** $p < 0.001$. [†]Multiple adjustment includes: sex, age, BMI, LVEF, GLS, heart rate, LDL, HbA1c, hypertension, LVEDVi, LVMi.

TABLE 4 | Echocardiographic patterns in participants with LV normal geometry according to the presence of hypertension.

	Total sample	Without hypertension	With hypertension	p
N (%)	1,789	1,054 (59)	735 (41)	
Women	879 (49)	572 (54)	307 (42)	<0.001
Age, years	53 (12)	49 (10)	59 (10)	<0.001
BSA [m ²]	1.9 (0.2)	1.87 (0.21)	1.94 (0.23)	<0.001
BMI [kg/m ²]	26 (4)	25 (4)	27 (4)	<0.001
SBP [mmHg]	130 (17)	121 (11)	142 (17)	<0.001
DBP [mmHg]	78 (10)	75 (7)	83 (10)	<0.001
LVEF [%]	61 (4)	61 (4)	60 (5)	<0.001
GLS [−%]	21 (3)	21 (4)	20 (2)	<0.001
E prime lateral (cm/s)	11 (3)	12 (3)	10 (3)	<0.001
E prime septal (cm/s)	9 (2)	9 (2)	8 (2)	<0.001
LAV [ml]	46 (15)	43 (14)	50 (17)	<0.001
LAVi [ml/m ²]	24 (7)	23 (6)	26 (8)	<0.001
LVEDVi [mL/m ²]	52 (10)	52 (11)	52 (10)	0.256
LVMI [g/m ²]	71 (15)	67 (13)	76 (15)	<0.001
GCW [mmHg%]	2,501 (424)	2,372 (310)	2,687 (491)	<0.001
GWW [mmHg%]	81 (58, 118)	74 (53, 100)	97 (67, 136)	<0.001
GWI [mmHg%]	2,276 (392)	2,167 (294)	2,431 (457)	<0.001
GWE [%]	96 (95, 97)	96 (95, 97)	96 (94, 97)	<0.001

Data are n (%), mean (SD), or median (quartiles).

BSA, body surface area; BMI, body mass index; SBP, systolic blood pressure; DBP, diastolic blood pressure; LVEF, left ventricular ejection fraction; GLS, global longitudinal strain; LAV, left atrial volume; LAVi, left atrial volume index; LVEDVi, left ventricular end-diastolic volume index; LVMI, left ventricular mass index; GCW, global constructive work; GWW, global wasted work; GWI, global work index; GWE, global work efficiency.

is also known to adversely affect GLS (30, 35). Echocardiography-based determination of MyW parameters now offers the possibility to non-invasively study the different components of active myocardial function and to apply this method to larger collectives. Covering both the impairment of longitudinal LV function and a potential LV dyssynchrony induced by conduction delays, MyW might advance our mechanistic understanding of the myocardial function and subsequent adaptive changes in individuals with abnormal LV geometry. We determined three pathological groups (see **Figure 1**), which serve as examples of a (well-acknowledged) disease paradigm characterizing the gradual alteration of LV morphology over time given certain risk constellations (1, 19).

Concentric LV Remodeling and Concentric Hypertrophy

CR dominated in our study sample, followed by EH and CH. CR is considered a late-stage response of the LV to adverse hemodynamic circumstances and is predominantly caused by pressure overload as induced by increased afterload (36) due to arterial hypertension or aortic stenosis (37), or volume overload (1). CR is associated with adverse LV function (38, 39) and an adverse prognosis when compared to normal LV geometry (4, 40,

41). In our sample, participants with CR were older and showed a less favorable risk factor and comorbidity profile and lower values of GLS when compared to participants with normal LV geometry. The more detailed analysis of LV myocardial function revealed a trend toward an increase in GCW and GWI (**Figure 1**), which might be a consequence of increased myocardial muscle power in LV hypertrophy, and was even more pronounced in CH. In addition to this increase in constructive myocardial work, participants with CR and CH exhibited significantly higher levels of GWW when compared to participants with normal LV geometry. The lower values of global work efficiency suggest that the proportionate increase in GWW exceeds the increase in GCW with progressing LV hypertrophy might be one explanation for impaired exercise capacity in individuals with LV hypertrophy and abnormal LV geometry (42). Further, these findings were even more pronounced in individuals with CH. As this subgroup was small in our study sample, we did not perform further statistical analyses. However, the CH pattern is of high clinical relevance, and further dedicated studies in hypertensive patients need to provide additional insights.

Arterial hypertension is one of the most prevalent cardiovascular risk factors and a major contributor to long-term changes in LV geometry (36, 37, 43, 44). A higher prevalence of hypertension was seen with a deviation from normal LV geometry. However, even in participants with measures of LV geometry within a normal range, we found notable differences in LV structure and function in individuals with and without hypertension. Among subjects with normal LV geometry, those with hypertension presented with equal LV size but with higher LV mass when compared to subjects without hypertension (**Table 4**). The LV myocardium of those with hypertension performed a higher amount of work, constructive (GWI, GCW) and wasted work, at a lower efficiency level. A detailed analysis of LV structure and function according to the current blood pressure during the study visit showed a similar pattern (**Table 5**). Higher SBP values were associated with higher LV mass though still within the normal range. Participants with normal and high-normal BP had higher LV mass when compared to participants with optimal BP. Further, normal and high-normal blood pressure were associated with significantly higher values of work performed by the myocardium, including wasted work, when compared to optimal blood pressure (**Table 5**). As part of the adaptation process, it appears that the LV hypertrophies to perform a higher amount of work. Due to a disproportionate increase in wasted work, work efficiency seems to be affected already in individuals with high-normal blood pressure, hence in a very early stage of disease (**Table 5**). Our results give a glimpse of mechanistic insights into the pathophysiology of hypertensive heart disease and highlight the importance of early and consistent treatment of arterial hypertension to reach optimal treatment goals.

Eccentric Hypertrophy

This phenotype is characterized by increased LV size (i.e., LV dilatation) in the presence of normal wall thickness. EH is typically found in states of chronic volume overload, such as significant mitral regurgitation (which was excluded from

TABLE 5 | MyW indices in individuals with normal LV geometry according to blood pressure category.

	Blood pressure categories					P for trend
	All individuals (N = 1,789)	Optimal SBP <120 (N = 570)	Normal SBP 120–129 (N = 398)	High-normal SBP 130–139 (N = 355)	Hypertensive SBP ≥140 (N = 466)	
Women	879 (49)	383 (67)	164 (41)	142 (40)	190 (41)	<0.001
Age [years]	53 (12)	49 (10)	50 (11)	56 (11)	59 (10)	<0.001
LVEF [%]	61 (4)	61 (4)	61 (4)	60 (4)	60 (5)	0.010
GLPS [–%]	21 (3)	22 (5)	21 (3)*	20 (2)	20 (3)	<0.001
SBP [mmHg]	130 (17)	112 (7)	125 (3)	134 (3)	152 (12)	<0.001
GCW [mmHg%]	2,501 (424)	2,224 (276)	2,406 (302)	2,545 (299)	2,888 (444)	<0.001
GWW [mmHg%]	81 (58, 118)	68 (49, 92)	77 (55, 110)	87 (62, 120)	105 (77, 149)	<0.001
GWI [mmHg%]	2,276 (392)	2,038 (267)	2,193 (286)	2,310 (289)	2,611 (425)	<0.001
GWE [%]	96 (95, 97)	96 (95, 97)	96 (95, 97)	96 (95, 97)	96 (94, 97)	<0.001
LVMi [g/m ²]	71 (15)	65 (14)	70 (14)	73 (14)	77 (15)	<0.001
LVEDVi [ml/m ²]	52 (10)	51 (10)	52 (10)	53 (11)	52 (10)	0.056
RWT	0.33 (0.05)	0.31 (0.05)	0.32 (0.05)	0.33 (0.04)	0.34 (0.05)	<0.001

Data are n (%), mean (SD), or median (quartiles).

P for trend (Jonckheere Terpstra trend test and Chi-square test, as appropriate).

BP, blood pressure; LVEF, left ventricular ejection fraction; GLS, global longitudinal strain; SBP, systolic blood pressure; GCW, global constructive work; GWW, global wasted work; GWI, global work index; GWE, global work efficiency; LVMi, left ventricular mass index; LVEDVi, left ventricular end-diastolic volume index; RWT, relative wall thickness.

our study sample), but also as an early manifestation of a cardiomyopathic process (1, 36). Further, previous work from our population-based cohort reported a higher proportion of increased LV volumes in individuals with structural heart disease with no clinical HF symptoms and absent CV risk factors known as the B-not-A group of HF (16). Participants with EH were older, more often female, had higher NT-proBNP levels, and a higher prevalence of hypertension, diabetes, and dyslipidemia when compared to normal LV geometry or CR. GCW and GWI were normal among individuals with EH, but GWW was markedly enhanced and GWE compromised. Of note, GWW and GWE were predominantly determined by larger LV volumes, potentially as a consequence of increased wall stress in larger LV volumes (45). Our results extend first analyses from NORRE (46), a multinational study to generate normal values for echocardiographic measures, where mild univariate associations between LV size and MyW indices were found that vanished in multivariable analysis, possibly due to issues of sample size and selection criteria. In contrast to a concentric increase in LV mass, an increase in LV size without an increase in LV wall thickness seems to be associated with an increase in GWW only, and lower GWE.

Cardiomyopathies are characterized by heterogeneous patterns of LV hypertrophy and progressive LV enlargement leading to myocardial dysfunction (47–49) and, on a histological level, by cardiomyocyte hypertrophy, myocardial disarray, and interstitial fibrosis (49). Recent work in patients with cardiomyopathy showed impaired MyW indices when compared to healthy controls (48, 50, 51). MyW analysis was hypothesized to reveal the effect of chronic remodeling on myocardial function in patients with cardiomyopathies, unmasking, i.e., a low capacity to adjust to an increased workload (52). Chan et al. (50) suggested that wasted work may be related to the increased myocardial wall

stress against a higher afterload. Likewise, wasted work results to be of great interest as a potential factor reducing LV work efficiency and ultimately might contribute to LV remodeling. LV remodeling and consecutive functional changes reflect myocardial glucose metabolism and energetics (53), which was shown to correlate with non-invasive echocardiography-derived MyW indices (8). Our results show additional insights into the relationship of LV mass and size with myocardial work and might contribute to the elucidation of pathophysiological processes in cardiomyopathies.

Limitations and Strengths

In this large population-based sample, cardiovascular risk factors were comprehensively and carefully assessed according to standard operating procedures. In particular, echocardiography was performed by well-trained and internally certified and quality-controlled sonographers (18). However, the current cross-sectional analysis cannot inform on longitudinal alterations and causal inferences. The size of the three subgroups emerging with an abnormal LV geometry was relatively small. Nevertheless, due to the representative mode of sampling, they mirror the frequencies of these abnormalities in the population free of heart failure. For the derivation of MyW parameters, ideally, blood pressure should be measured during the echocardiographic examination. In STAAB participants, blood pressure was measured in a sitting position after 5 min of rest in a separate room but immediately prior to the echocardiographic examination. Hence, the thus introduced imprecision is likely to be small. Technically and physiologically, information on MyW should not be regarded as the exact equivalent to investigations on pressure-volume loop recordings (10, 45, 54). As discussed elsewhere in detail, MyW does not account for radial, and circumferential LV function nor wall stress since LV radial

curvature and wall thickness are not part of its derivation from pressure-strain loops (45, 54). Comparison of MyW, particularly of GWW, between different hearts, however, is considered a valid measure since it is a relative measure that compensates for limited information about local geometry and consecutive potential differences in wall stress (10). Further, MyW integrates LV systolic longitudinal strain, blood pressure, and time intervals, thus comprehensively accounting for potential impairment (a) in LV longitudinal contraction and (b) and in cardiac conduction induced by abnormal LV geometry as apparent, e.g., in patients with heart failure.

CONCLUSION

MyW analysis is a non-invasive, echocardiography-based method facilitating new insights into the relationship of LV geometry and myocardial performance in this population-based cohort free from heart failure. Any deviation from a normal LV geometric profile was associated with an alteration of MyW. While LV dilation was associated with solely higher GWW, concentric remodeling and hypertrophy were associated with both higher GCW and GWW. A disproportionately higher GWW resulted in lower GWE. These altered MyW patterns were already present in hypertensive individuals with normal LV geometry and might thus serve as an early sign of incipient hypertensive heart disease. Longitudinal studies are needed to test this hypothesis and improve our understanding on the mechanisms of hypertensive heart disease and the time course of its evolvement.

DATA AVAILABILITY STATEMENT

The raw data supporting the conclusions of this article will be made available by the authors, without undue reservation.

ETHICS STATEMENT

The studies involving human participants were reviewed and approved by Ethics Committee of the Faculty of Medicine, University of Würzburg (vote #98/13) and data protection officer of the University of Würzburg (#J-117.605-09/13). The patients/participants provided their written informed consent to participate in this study.

REFERENCES

1. Marwick TH, Gillebert TC, Aurigemma G, Chirinos J, Derumeaux G, Galderisi M, et al. Recommendations on the use of echocardiography in adult hypertension: a report from the European Association of Cardiovascular Imaging (EACVI) and the American Society of Echocardiography (ASE) [dagger]. *Eur Heart J Cardiovasc Imaging*. (2015) 16:577–605. doi: 10.1093/ehjci/jev076
2. Lavie CJ, Patel DA, Milani RV, Ventura HO, Shah S, Gilliland Y. Impact of echocardiographic left ventricular geometry on clinical prognosis. *Prog Cardiovasc Dis*. (2014) 57:3–9. doi: 10.1016/j.pcad.2014.05.003

AUTHOR CONTRIBUTIONS

FS, CM, GG, PH, and SS conceived and designed the study. FS, CM, VC, JA, FE, GG, PH, and SS analysis and interpretation of data. FS drafted the manuscript. CM, VC, JA, FE, GG, PH, and SS revised the manuscript critically for intellectual content. All authors contributed to the article and approved the submitted version.

FUNDING

This study was supported by the German Ministry of Research and Education within the Comprehensive Heart Failure Center, Würzburg (BMBF 01EO1004 and 01EO1504). FS was supported by an MD/PhD fellowship of the Interdisciplinary Center for Clinical Research (IZKF) of the Medical Faculty, University of Würzburg.

ACKNOWLEDGMENTS

STAAB Consortium consists of: Frantz (Department of Medicine I, Division of Cardiology, University Hospital Würzburg); C. Maack (Comprehensive Heart Failure Center, University Hospital and University of Würzburg); G. Ertl (University Hospital Würzburg); M. Fassnacht (Department of Medicine I, Division of Endocrinology, University Hospital Würzburg); C. Wanner (Department of Medicine I, Division of Nephrology, University Hospital Würzburg); R. Leyh (Department of Cardiac & Thoracic Surgery, University Hospital Würzburg); J. Volkmann (Department of Neurology, University Hospital Würzburg); J. Deckert (Department of Psychiatry, Psychosomatics and Psychotherapy, Center of Mental Health, University Hospital Würzburg); H. Faller (Department of Medical Psychology, University of Würzburg); R. Jahns (Interdisciplinary Bank of Biomaterials and Data Würzburg, University Hospital Würzburg). We greatly appreciate the time of all STAAB participants and their willingness to provide data to the study. We also thank the Mayor of the City of Würzburg and the local registration office for their sustained support of our study. We thank the entire study team, study nurses, technicians, data managers, and students for their efforts on the STAAB study. We also thank M. Ertl, G. Fette, and F. Puppe from the CHFC DataWarehouse, Institute of Informatics VI, University of Würzburg, as well as T. Ludwig, ICE-B, for diligent data management.

3. Inoko M, Kihara Y, Morii I, Fujiwara H, Sasayama S. Transition from compensatory hypertrophy to dilated, failing left ventricles in Dahl salt-sensitive rats. *Am J Physiol*. (1994) 267(6 Pt 2):H2471–82. doi: 10.1152/ajpheart.1994.267.6.H2471
4. Bluemke DA, Kronmal RA, Lima JA, Liu K, Olson J, Burke GL, et al. The relationship of left ventricular mass and geometry to incident cardiovascular events: the MESA (Multi-Ethnic Study of Atherosclerosis) study. *J Am Coll Cardiol*. (2008) 52:2148–55. doi: 10.1016/j.jacc.2008.09.014
5. Velagaleti RS, Gona P, Pencina MJ, Aragam J, Wang TJ, Levy D, et al. Left ventricular hypertrophy patterns and incidence of heart failure with

- preserved versus reduced ejection fraction. *Am J Cardiol.* (2014) 113:117–22. doi: 10.1016/j.amjcard.2013.09.028
6. de Simone G, Gottdiener JS, Chinali M, Maurer MS. Left ventricular mass predicts heart failure not related to previous myocardial infarction: the Cardiovascular Health Study. *Eur Heart J.* (2008) 29:741–7. doi: 10.1093/eurheartj/ehm605
 7. Bastos MB, Burkhoff D, Maly J, Daemen J, den Uil CA, Ameloot K, et al. Invasive left ventricle pressure-volume analysis: overview and practical clinical implications. *Eur Heart J.* (2020) 41:1286–97. doi: 10.1093/eurheartj/ehz552
 8. Russell K, Eriksen M, Aaberge L, Wilhelmsen N, Skulstad H, Remme EW, et al. A novel clinical method for quantification of regional left ventricular pressure-strain loop area: a non-invasive index of myocardial work. *Eur Heart J.* (2012) 33:724–33. doi: 10.1093/eurheartj/ehs016
 9. Schramm W. The units of measurement of the ventricular stroke work: a review study. *J Clin Monit Comput.* (2010) 24:213–7. doi: 10.1007/s10877-010-9234-4
 10. Russell K, Eriksen M, Aaberge L, Wilhelmsen N, Skulstad H, Gjesdal O, et al. Assessment of wasted myocardial work: a novel method to quantify energy loss due to uncoordinated left ventricular contractions. *Am J Physiol Heart Circ Physiol.* (2013) 305:H996–1003. doi: 10.1152/ajpheart.00191.2013
 11. Lieb W, Gona P, Larson MG, Aragam J, Zile MR, Cheng S, et al. The natural history of left ventricular geometry in the community: clinical correlates and prognostic significance of change in LV geometric pattern. *JACC Cardiovasc Imaging.* (2014) 7:870–8. doi: 10.1016/j.jcmg.2014.05.008
 12. Lind L, Sundstrom J. Change in left ventricular geometry over 10 years in the elderly and risk of incident cardiovascular disease. *J Hypertens.* (2019) 37:325–30. doi: 10.1097/HJH.0000000000001897
 13. Milani RV, Lavie CJ, Mehra MR, Ventura HO, Kurtz JD, Messerli FH. Left ventricular geometry and survival in patients with normal left ventricular ejection fraction. *Am J Cardiol.* (2006) 97:959–63. doi: 10.1016/j.amjcard.2005.10.030
 14. Cuspidi C, Facchetti R, Bombelli M, Sala C, Tadic M, Grassi G, et al. Prevalence and correlates of new-onset left ventricular geometric abnormalities in a general population: the PAMELA study. *J Hypertens.* (2016) 34:1423–31. doi: 10.1097/HJH.0000000000000956
 15. Wagner M, Tiffe T, Morbach C, Gelbrich G, Stork S, Heuschmann PU, et al. Characteristics and Course of Heart Failure Stages A-B and Determinants of Progression - design and rationale of the STAAB cohort study. *Eur J Prev Cardiol.* (2017) 24:468–79. doi: 10.1177/2047487316680693
 16. Morbach C, Gelbrich G, Tiffe T, Eichner FA, Christa M, Mattern R, et al. Prevalence and determinants of the precursor stages of heart failure: results from the population-based STAAB cohort study. *Eur J Prev Cardiol.* (2020). doi: 10.1177/2047487320922636. [Epub ahead of print].
 17. Mancia G, Fagard R, Narkiewicz K, Redon J, Zanchetti A, Bohm M, et al. 2013 ESH/ESC guidelines for the management of arterial hypertension: the Task Force for the Management of Arterial Hypertension of the European Society of Hypertension (ESH) and of the European Society of Cardiology (ESC). *Eur Heart J.* (2013) 34:2159–219. doi: 10.1093/eurheartj/ehs151
 18. Morbach C, Gelbrich G, Breunig M, Tiffe T, Wagner M, Heuschmann PU, et al. Impact of acquisition and interpretation on total inter-observer variability in echocardiography: results from the quality assurance program of the STAAB cohort study. *Int J Cardiovasc Imaging.* (2018) 34:1057–65. doi: 10.1007/s10554-018-1315-3
 19. Lang RM, Badano LP, Mor-Avi V, Afkalo J, Armstrong A, Ernande L, et al. Recommendations for cardiac chamber quantification by echocardiography in adults: an update from the American Society of Echocardiography and the European Association of Cardiovascular Imaging. *Eur Heart J Cardiovasc Imaging.* (2015) 16:233–70. doi: 10.1093/ehjci/jev014
 20. Owashi KP, Hubert A, Galli E, Donal E, Hernandez AI, Le Rolle V. Model-based estimation of left ventricular pressure and myocardial work in aortic stenosis. *PLoS ONE.* (2020) 15:e0229609. doi: 10.1371/journal.pone.0229609
 21. Morbach C, Sahiti F, Tiffe T, Cejka V, Eichner FA, Gelbrich G, et al. Myocardial work - correlation patterns and reference values from the population-based STAAB cohort study. *PLoS ONE.* (2020) 15:e0239684. doi: 10.1371/journal.pone.0239684
 22. Velagaleti RS, Gona P, Levy D, Aragam J, Larson MG, Tofler GH, et al. Relations of biomarkers representing distinct biological pathways to left ventricular geometry. *Circulation.* (2008) 118:2252–8. doi: 10.1161/CIRCULATIONAHA.108.817411
 23. Gaasch WH, Zile MR. Left ventricular structural remodeling in health and disease: with special emphasis on volume, mass, and geometry. *J Am Coll Cardiol.* (2011) 58:1733–40. doi: 10.1016/j.jacc.2011.07.022
 24. Ganau A, Devereux RB, Roman MJ, de Simone G, Pickering TG, Saba PS, et al. Patterns of left ventricular hypertrophy and geometric remodeling in essential hypertension. *J Am Coll Cardiol.* (1992) 19:1550–8. doi: 10.1016/0735-1097(92)90617-V
 25. Cheng S, Xanthakis V, Sullivan LM, Lieb W, Massaro J, Aragam J, et al. Correlates of echocardiographic indices of cardiac remodeling over the adult life course: longitudinal observations from the Framingham Heart Study. *Circulation.* (2010) 122:570–8. doi: 10.1161/CIRCULATIONAHA.110.937821
 26. Fox ER, Taylor J, Taylor H, Han H, Samdarshi T, Arnett D, et al. Left ventricular geometric patterns in the Jackson cohort of the Atherosclerotic Risk in Communities (ARIC) study: clinical correlates and influences on systolic and diastolic dysfunction. *Am Heart J.* (2007) 153:238–44. doi: 10.1016/j.ahj.2006.09.013
 27. Konstam MA, Kramer DG, Patel AR, Maron MS, Udelson JE. Left ventricular remodeling in heart failure: current concepts in clinical significance and assessment. *JACC Cardiovasc Imaging.* (2011) 4:98–108. doi: 10.1016/j.jcmg.2010.10.008
 28. Triposkiadis F, Butler J, Abboud FM, Armstrong PW, Adamopoulos S, Atherton JJ, et al. The continuous heart failure spectrum: moving beyond an ejection fraction classification. *Eur Heart J.* (2019) 40:2155–63. doi: 10.1093/eurheartj/ehz158
 29. Nadruz W. Myocardial remodeling in hypertension. *J Hum Hypertens.* (2015) 29:1–6. doi: 10.1038/jhh.2014.36
 30. Voigt JU, Cijvic M. 2- and 3-dimensional myocardial strain in cardiac health and disease. *JACC Cardiovasc Imaging.* (2019) 12:1849–63. doi: 10.1016/j.jcmg.2019.01.044
 31. Dhinra R, Ho Nam B, Benjamin EJ, Wang TJ, Larson MG, D'Agostino RB, et al. Cross-sectional relations of electrocardiographic QRS duration to left ventricular dimensions: the Framingham Heart study. *J Am Coll Cardiol.* (2005) 45:685–9. doi: 10.1016/j.jacc.2004.11.046
 32. Palmieri V, Okin PM, de Simone G, Bella JN, Wachtell K, Gerds E, et al. Electrocardiographic characteristics and metabolic risk factors associated with inappropriately high left ventricular mass in patients with electrocardiographic left ventricular hypertrophy: the LIFE study. *J Hypertens.* (2007) 25:1079–85. doi: 10.1097/HJH.0b013e3280825638
 33. Stewart RA, Young AA, Anderson C, Teo KK, Jennings G, Cowan BR. Relationship between QRS duration and left ventricular mass and volume in patients at high cardiovascular risk. *Heart.* (2011) 97:1766–70. doi: 10.1136/heartjnl-2011-300297
 34. Ilkhanoff L, Liu K, Ning H, Nazarian S, Bluemke DA, Soliman EZ, et al. Association of QRS duration with left ventricular structure and function and risk of heart failure in middle-aged and older adults: the Multi-Ethnic Study of Atherosclerosis (MESA). *Eur J Heart Fail.* (2012) 14:1285–92. doi: 10.1093/eurjhf/hfs112
 35. Verdugo-Marchese M, Coiro S, Selton-Suty C, Kobayashi M, Bozec E, Lamiral Z, et al. Left ventricular myocardial deformation pattern, mechanical dispersion, and their relation with electrocardiogram markers in the large population-based STANISLAS cohort: insights into electromechanical coupling. *Eur Heart J Cardiovasc Imaging.* (2020) 21:1237–45. doi: 10.1093/ehjci/jeaa148
 36. Chahal NS, Lim TK, Jain P, Chambers JC, Kooner JS, Senior R. New insights into the relationship of left ventricular geometry and left ventricular mass with cardiac function: a population study of hypertensive subjects. *Eur Heart J.* (2010) 31:588–94. doi: 10.1093/eurheartj/ehp490
 37. Cameli M, Lisi M, Righini FM, Massoni A, Mondillo S. Left ventricular remodeling and torsion dynamics in hypertensive patients. *Int J Cardiovasc Imaging.* (2013) 29:79–86. doi: 10.1007/s10554-012-0054-0
 38. Zhang Z, Ma Q, Cao L, Zhao Z, Zhao J, Lu Q, et al. Correlation between left ventricular myocardial strain and left ventricular geometry in healthy adults: a cardiovascular magnetic resonance-feature tracking study. *Int J Cardiovasc Imaging.* (2019) 35:2057–65. doi: 10.1007/s10554-019-01644-3
 39. Mizuguchi Y, Oishi Y, Miyoshi H, Iuchi A, Nagase N, Oki T. Concentric left ventricular hypertrophy brings deterioration of systolic longitudinal,

- circumferential, and radial myocardial deformation in hypertensive patients with preserved left ventricular pump function. *J Cardiol.* (2010) 55:23–33. doi: 10.1016/j.jcc.2009.07.006
40. Teh RO, Kerse NM, Robinson EM, Whalley GA, Connolly MJ, Doughty RN. Left ventricular geometry and all-cause mortality in advanced age. *Heart Lung Circ.* (2015) 24:32–9. doi: 10.1016/j.hlc.2014.06.017
 41. Verdecchia P, Schillaci G, Borgioni C, Ciucci A, Battistelli M, Bartoccini C, et al. Adverse prognostic significance of concentric remodeling of the left ventricle in hypertensive patients with normal left ventricular mass. *J Am Coll Cardiol.* (1995) 25:871–8. doi: 10.1016/0735-1097(94)00424-O
 42. Lam CS, Grewal J, Borlaug BA, Ommen SR, Kane GC, McCully RB, et al. Size, shape, and stamina: the impact of left ventricular geometry on exercise capacity. *Hypertension.* (2010) 55:1143–9. doi: 10.1161/HYPERTENSIONAHA.109.146845
 43. Santos AB, Gupta DK, Bello NA, Gori M, Claggett B, Fuchs FD, et al. Prehypertension is associated with abnormalities of cardiac structure and function in the atherosclerosis risk in communities study. *Am J Hypertens.* (2016) 29:568–74. doi: 10.1093/ajh/hpv156
 44. Hendriks T, Said MA, Janssen LMA, van der Ende MY, van Veldhuisen DJ, Verweij N, et al. Effect of systolic blood pressure on left ventricular structure and function: a mendelian randomization study. *Hypertension.* (2019) 74:826–32. doi: 10.1161/HYPERTENSIONAHA.119.12679
 45. Flachskampf FA. Letter to the editor regarding the recent publication of Hiemstra et al., myocardial work in nonobstructive hypertrophic cardiomyopathy: implications for outcome. *J Am Soc Echocardiogr.* (2021) 34:201. doi: 10.1016/j.echo.2020.10.007
 46. Manganaro R, Marchetta S, Dulgheru R, Sugimoto T, Tsugu T, Ilardi F, et al. Correlation between non-invasive myocardial work indices and main parameters of systolic and diastolic function: results from the EACVI NORRE study. *Eur Heart J Cardiovasc Imaging.* (2020) 21:533–41. doi: 10.1093/ehjci/jez203
 47. Schultheiss HP, Fairweather D, Caforio ALP, Escher F, Hershberger RE, Lipshultz SE, et al. Dilated cardiomyopathy. *Nat Rev Dis Primers.* (2019) 5:32. doi: 10.1038/s41572-019-0084-1
 48. Galli E, Vitel E, Schnell F, Le Rolle V, Hubert A, Lederlin M, et al. Myocardial constructive work is impaired in hypertrophic cardiomyopathy and predicts left ventricular fibrosis. *Echocardiography.* (2019) 36:74–82. doi: 10.1111/echo.14210
 49. Marian AJ, Braunwald E. Hypertrophic cardiomyopathy: genetics, pathogenesis, clinical manifestations, diagnosis, and therapy. *Circ Res.* (2017) 121:749–70. doi: 10.1161/CIRCRESAHA.117.311059
 50. Chan J, Edwards NFA, Khandheria BK, Shiino K, Sabapathy S, Anderson B, et al. A new approach to assess myocardial work by non-invasive left ventricular pressure-strain relations in hypertension and dilated cardiomyopathy. *Eur Heart J Cardiovasc Imaging.* (2019) 20:31–9. doi: 10.1093/ehjci/jez131
 51. Hiemstra YL, van der Bijl P, El Mahdiui M, Bax JJ, Delgado V, Marsan NA. Myocardial work in nonobstructive hypertrophic cardiomyopathy: implications for outcome. *J Am Soc Echocardiogr.* (2020) 33:1201–8. doi: 10.1016/j.echo.2020.05.010
 52. Loncaric F, Marciniak M, Nunno L, Mimbreno M, Fernandes JF, Fabijanovic D, et al. Distribution of myocardial work in arterial hypertension: insights from non-invasive left ventricular pressure-strain relations. *Int J Cardiovasc Imaging.* (2021) 37:145–54. doi: 10.1007/s10554-020-01969-4
 53. Tran DH, Wang ZV. Glucose metabolism in cardiac hypertrophy and heart failure. *J Am Heart Assoc.* (2019) 8:e012673. doi: 10.1161/JAHA.119.012673
 54. Smiseth OA, Donal E, Penicka M, Sletten OJ. How to measure left ventricular myocardial work by pressure-strain loops. *Eur Heart J Cardiovasc Imaging.* (2021) 22:259–61. doi: 10.1093/ehjci/jeaa301

Conflict of Interest: The authors declare that the research was conducted in the absence of any commercial or financial relationships that could be construed as a potential conflict of interest.

Copyright © 2021 Sahiti, Morbach, Cejka, Albert, Eichner, Gelbrich, Heuschmann and Störk. This is an open-access article distributed under the terms of the Creative Commons Attribution License (CC BY). The use, distribution or reproduction in other forums is permitted, provided the original author(s) and the copyright owner(s) are credited and that the original publication in this journal is cited, in accordance with accepted academic practice. No use, distribution or reproduction is permitted which does not comply with these terms.



The Predictive Value of Right Ventricular Longitudinal Strain in Pulmonary Hypertension, Heart Failure, and Valvular Diseases

Marijana Tadic^{1*}, Nicoleta Nita¹, Leonhard Schneider¹, Johannes Kersten¹, Dominik Buckert¹, Birgid Gonska¹, Dominik Scharnbeck¹, Christine Reichart¹, Evgeny Belyavskiy², Cesare Cuspidi³ and Wolfgang Rottbauer¹

¹ Klinik für Innere Medizin II, Universitätsklinikum Ulm, Ulm, Germany, ² Department of Cardiology, Charité-University-Medicine (Campus Virchow – Klinikum), Berlin, Germany, ³ Department of Medicine and Surgery, University of Milan-Bicocca, Milan, Italy

OPEN ACCESS

Edited by:

Carla Sousa,
São João University Hospital
Center, Portugal

Reviewed by:

Mariana Paiva,
Centro Hospitalar Universitário de São
João (CHUSJ), Portugal
Helena Nascimento,
Centro Hospitalar de Entre o Douro e
Vouga E.P.E., Portugal

*Correspondence:

Marijana Tadic
marijana_tadic@hotmail.com

Specialty section:

This article was submitted to
Cardiovascular Imaging,
a section of the journal
Frontiers in Cardiovascular Medicine

Received: 20 April 2021

Accepted: 24 May 2021

Published: 17 June 2021

Citation:

Tadic M, Nita N, Schneider L, Kersten J, Buckert D, Gonska B, Scharnbeck D, Reichart C, Belyavskiy E, Cuspidi C and Rottbauer W (2021) The Predictive Value of Right Ventricular Longitudinal Strain in Pulmonary Hypertension, Heart Failure, and Valvular Diseases. *Front. Cardiovasc. Med.* 8:698158. doi: 10.3389/fcvm.2021.698158

Right ventricular (RV) systolic function has an important role in the prediction of adverse outcomes, including mortality, in a wide range of cardiovascular (CV) conditions. Because of complex RV geometry and load dependency of the RV functional parameters, conventional echocardiographic parameters such as RV fractional area change (FAC) and tricuspid annular plane systolic excursion (TAPSE), have limited prognostic power in a large number of patients. RV longitudinal strain overcame the majority of these limitations, as it is angle-independent, less load-dependent, highly reproducible, and measure regional myocardial deformation. It has a high predictive value in patients with pulmonary hypertension, heart failure, congenital heart disease, ischemic heart disease, pulmonary embolism, cardiomyopathies, and valvular disease. It enables detection of subclinical RV damage even when conventional parameters of RV systolic function are in the normal range. Even though cardiac magnetic resonance-derived RV longitudinal strain showed excellent predictive value, echocardiography-derived RV strain remains the method of choice for evaluation of RV mechanics primarily due to high availability. Despite a constantly growing body of evidence that support RV longitudinal strain evaluation in the majority of CV patients, its assessment has not become the part of the routine echocardiographic examination in the majority of echocardiographic laboratories. The aim of this clinical review was to summarize the current data about the predictive value of RV longitudinal strain in patients with pulmonary hypertension, heart failure and valvular heart diseases.

Keywords: right ventricle, longitudinal strain, outcome, pulmonary hypertension, heart failure, aortic stenosis, mitral regurgitation, tricuspid regurgitation

INTRODUCTION

The right ventricle (RV) has a complex anatomy and position in the thorax and therefore its assessment has long been limited and included a few conventional parameters that are easy to measure. Studies reported a significant prognostic effect of these RV parameters in a wide range of cardiovascular (CV) conditions such as pulmonary hypertension, congenital heart disease,

pulmonary embolism, heart failure, cardiomyopathies, and valvular disease (1–6). Interestingly, RV parameters were reported as significant independent predictors of outcome in the general population and patients with arterial hypertension (7, 8). The development of imaging techniques provided detailed insight into RV structure, function and mechanics. Cardiac magnetic resonance and 3D echocardiography significantly improved our knowledge about RV structure and function, but speckle-tracking imaging enabled efficient and prompt echocardiographic assessment of RV mechanics (9).

RV longitudinal strain represents the cornerstone of RV mechanics evaluation with excellent reproducibility and high predictive value in patients with different aforementioned CV diseases (10–13). It has higher sensitivity and specificity in the detection of subclinical RV damage in patients with cardiomyopathies, cardiac amyloidosis and cancer (14–16). Although cardiac magnetic resonance provides more possibilities, that include the accurate evaluation of RV volumes and function, its relatively low availability and high level of competence that this kind of imaging demands, represent the main obstacles for its adoption in everyday clinical practice. Echocardiography-derived RV strain remains the method of choice for the evaluation of RV mechanics. Despite a constantly growing body of evidence that support RV longitudinal strain evaluation in the majority of CV patients, its assessment has not become part of the routine echocardiographic examination in majority of echocardiographic laboratories.

The aim of this clinical review was to summarize the current data about the predictive value of RV longitudinal strain in patients with pulmonary hypertension, heart failure, and valvular diseases in order to emphasize the importance of its evaluation in routine echocardiographic examination in these conditions.

RIGHT VENTRICULAR STRAIN—BASIC CHARACTERISTICS

The retrosternal position of the RV and its unique crescent-shaped geometry with inflow and outflow tracts in almost the same plane is challenging for echocardiographic assessment (17). Several echocardiographic views should be used for appropriate evaluation of RV structure and function and not all of them are part of the basic echocardiographic examination that underwent the majority of CV patients. Therefore, practically all parameters that are recommended by the guidelines (RV diameters, TAPSE, FAC, s' , E/e' , sPAP) are assessed in a 4-chamber view (18), which is easy to access.

The evaluation of RV longitudinal strain is also performed in 4-chamber view, which certainly represents an advantage because it does not demand additional time for acquisition (**Figure 1**). RV wall is significantly thinner than in the left ventricle (LV) and consists of only two layers that are predominantly longitudinally and obliquely directed in the free wall (17). The deep subendocardial fibers have longitudinal direction from base to apex, while the superficial subepicardial fibers normally have circumferential direction, parallel to the AV groove (19), but they turn obliquely as they approach to the apex of the heart

and continue onto the LV. The continuity of RV and LV fibers significantly contributes to ventricular interdependence (19), which is important for both RV and LV function.

The technical aspects of image acquisition for speckle-tracking assessment are specific because they need to provide optimal images for post processing and high level of reproducibility for strain assessment. The suggested frame rate is between 40 and 90 frames per second for analysis of cardiac deformation. With increase of heart rate requires a higher frame rate to allow optimal speckle-tracking echocardiography. The acquisition of high-quality images is necessary for strain analysis, which considers the optimal gain settings and breath-hold techniques to clearly define the endocardial and epicardial borders and to avoid artifact associated to rib or lung motions and translational heart movement. RV focused apical 4-chamber view is necessary for RVLS evaluation. The optimal RV focused view should provide the visualization of the whole RV, the RV-free wall, and avoid foreshortening of the RV apex.

There is still no consensus about the region of interest that should be included in evaluation of RVLS. Some authors suggest a full RV chamber six-segmental model including the interventricular septum into the calculation of RVLS, whereas more authors accepted a three-segmental model, which involves only the RV free wall (20). The six-segment model is more feasible than three-segment model due to easier tracking of the whole RV. Absolute LS values derived from the free wall of the RV are significantly higher than from the whole RV. The authors that promote three-segmental model claim that the septum is traditionally seen as part of the LV and therefore should not be included into RVLS assessment.

The normal values of RVLS are still a matter of debate. Study that included significant number of patients reported lower RVLS values in men than in women, independently of the three- or six-segment model (21). Reference limits of normality for RVLS were -20% for men and -20.3% for women, whereas for RV free-wall LS limits were -22.5% for men and -23.3% for women (21).

There are several commercially available software platforms that enable post-process evaluation of raw data. EchoPac (GE) and TomTec are the most frequently used in clinical and research circumstances. EchoPac provided six-segment model and curve for each RV segment (including interventricular septum) and three-segmental model can be derived from these curves involving only segments of RV free wall. However, it is vendor dependent tool and can be used only for evaluation of echocardiographic images obtained by GE machines. TomTec is a vendor-independent software that can measure all echocardiographic images and provides automatically three-segment model for RV free-wall LS evaluation (separate values for free-wall RV and interventricular septum).

RV strain has several advantages: angle-independency, less load-dependency, and accuracy in measurement of regional myocardial deformation. The major limitation of 2D RV strain is motion-dependent speckles loss outside the imaging plane, especially due to excessive motion of the RV lateral wall. Nevertheless, this has been largely overcome with the introduction of software that provides dedicated RV

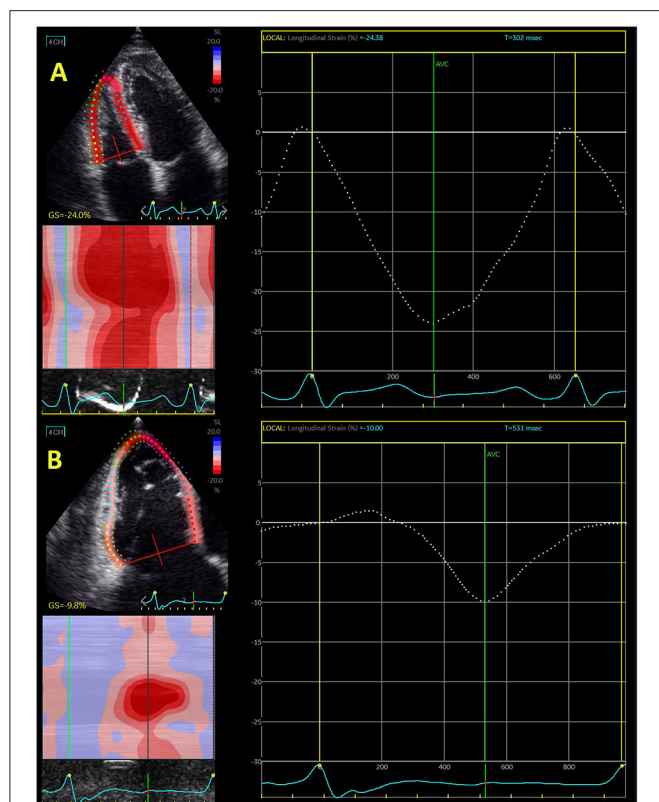


FIGURE 1 | Echocardiography-derived right ventricular global longitudinal strain in control subjects (A) and patient with severe functional tricuspid regurgitation (B).

longitudinal strain analysis and separate evaluation of RV free-wall longitudinal strain and RV global longitudinal strain. The important limitations are also lack of agreement about method that should be used for RVLS evaluation (three- vs. six-model) and unknown normal values for RVLS. Advantages and limitations are presented in **Table 1**. Even though all parameters of RV systolic function—TAPSE, FAC, and RV free-wall longitudinal function were reported as independent predictors of overall and CV mortality in patients with different CVD, RV free-wall longitudinal strain was proven to be the only independent predictor in analysis adjusted for multiple demographic, clinical and echocardiographic characteristics (22, 23). Study that used echocardiographic and CMR evaluation of RV function showed good correlation between TAPSE, s' , FAC, and global RV longitudinal strain and CMR-derived RV ejection fraction (24). Free-wall RV longitudinal strain showed the highest diagnostic accuracy and very high sensitivity and specificity to predict reduced EV ejection fraction (RVEF) $<45\%$ (24).

RV STRAIN IN PULMONARY ARTERIAL HYPERTENSION

The majority of studies investigated the predictive role of RV longitudinal strain in patients with idiopathic pulmonary arterial

hypertension (PAH), but the number of researches that examined patients with pulmonary hypertension in pulmonary diseases (COPD, interstitial fibrosis) and connective tissue diseases (erythematosus lupus, systemic sclerosis) is constantly increasing.

In patients with PAH, conventional parameters of RV systolic function, including TAPSE, FAC, s' , and RVEF, may be normal despite abnormal RV strain, which is an additional reason for the usage of RV strain in these patients. RV longitudinal strain can identify subclinical RV dysfunction at the early phase of disease and may serve as an important marker of subtle RV systolic dysfunction when conventional parameters, primarily TAPSE, are in the normal range (25, 26).

Small study that included 42 patients with PAH investigated the influence of different echocardiographic parameters on 4-year outcome and reported that RV free-wall longitudinal strain showed the best specificity and sensitivity in prediction of CV events in this population, significantly better than TAPSE, FAC, s' , and RV index of myocardial performance (27). PAH patients with RV free-wall longitudinal strain $<-19.4\%$ experienced fewer cardiovascular events than those with RV free-wall strain $\geq -19.4\%$ (27). Another study that investigated 51 PAH patients demonstrated that RV global longitudinal strain $\geq -15.5\%$ was independent predictor of adverse clinical events and mortality (28). The large study that included 575 patients with confirmed or suspected PAH reported significant decline in RV free-wall longitudinal strain proportional to worse functional class, shorter 6-min walk distance, higher N-terminal pro-B-type natriuretic peptide level, and the presence of right heart failure (29). RV free-wall longitudinal strain predicted survival after adjustment for pulmonary pressure, pulmonary vascular resistance, and right atrial pressure (29). Haec et al. (30) involved 150 PH patients and demonstrated that RV free-wall strain $\geq -19\%$, unlike TAPSE and FAC, was an independent predictor of all-cause mortality in these patients. All findings are summarized in **Table 2**.

Badagliacca et al. (31) recently identified 3 different RV free-wall strain patterns in PAH patients based on the time period from peak-systolic strain to return to the baseline point-set for the basal and mid-RV free wall segments. The authors reported that the shape of the RV strain curve and the longer time necessary to return RV strain to the baseline point were associated with worse outcome. Therefore, pattern 3, which corresponded to slow and steady gradual movement of a strain-derived curve, had the worst event-free survival during follow-up of 24 months (31) (**Table 2**).

Not only RV strain at baseline, but also its change during therapy and follow-up is important for prognosis of PAH patients. Hardegree et al. (32) reported that $\geq 5\%$ improvement in RV free-wall longitudinal strain had >7 -fold lower mortality during the follow-up of 4 years.

Meta-analysis that involved 1,169 PH patients revealed that RV free-wall strain $>-19\%$ had a significantly higher risk for the combined endpoint (mortality and PH-related events), while patients with $>-22\%$ had a significantly higher risk for all-cause mortality (33). It showed that a relative reduction of RV longitudinal strain $<10\%$ was insignificant for survival after multivariate analysis, while a relative reduction $>10\%$ of RV

longitudinal strain represented significant and independent risk factor of adverse outcome in PH patients (33) (Table 4).

The role of CMR-derived RV longitudinal strain in prediction of adverse outcome in PAH patients is insufficiently known because of scarce data. Recent study that included 80 PAH patients provided CMR analysis of all RV and right atrial (RA) structural, functional and strain parameters and showed that RV

longitudinal strain, TAPSE, FAC, and RA longitudinal strain were predictors of adverse outcome in these patients (34). Sato et al. (35) showed the improvement of CMR-derived RV strain during ambrisentan and tadalafil combination therapy in PAH patients with systemic sclerosis (Table 3).

RV STRAIN IN HEART FAILURE

RV dysfunction is known indicator of poor survival in patients with heart failure (HF) (55). Conventional echocardiographic parameters for assessment of RV systolic function such as TAPSE and FAC have already been proven as independent predictors of adverse outcome in HF (56). Dini et al. (57) showed not only that a reduced RV function at baseline was independent predictor of poor outcome, but also that the reversibility of abnormal RV function, assessed by TAPSE, was related with a better prognosis, independently of LVEF improvement, LV reverse remodeling, and cardiac resynchronization therapy. Study that included patients after acute myocardial infarction reported that FAC, used for evaluation of RV systolic function, was associated with an increased risk of all-cause mortality, CV death, sudden death, HF, and stroke (58). Another investigation that used tissue Doppler parameter for evaluation of RV systolic function (s') in patients with HF with preserved LVEF showed that $s' < 5$ cm/s was predictor of CV mortality, recurrent HF, and ischemic stroke (59).

Investigations proved that RV longitudinal strain is deteriorated at early stage of HF (3). Data from the literature indicate that RV longitudinal strain provides a more accurate and

TABLE 1 | Advantages and limitations for evaluation of RV longitudinal strain.

Advantages	Disadvantages
Additional parameter of RV systolic function	No agreement about normal values
High predictive value	No agreement about three- and six-segment models
High reproducibility	High temporal resolution necessary
Evaluation of mechanical function of the full RV wall thickness	Problem with imaging window and visualization of the RV free wall
Relatively load independent	Visualization of RV endocardial border sometimes can be challenging
Angle independent	Stable cardiac rhythm
High availability	
Low costs	
Short scan duration	
No need for advanced training	

RV, right ventricle.

TABLE 2 | Predictive value of RV longitudinal strain in pulmonary hypertension.

References	Sample size	RV free-wall/global GLS cut-off	Follow-up period (months)	Main findings
Motoji et al. (27)	42	−19.4%	48	RV free-wall longitudinal strain showed the best specificity and sensitivity in prediction of CV events in this population, significantly better than TAPSE, FAC, s' and RV index of myocardial performance.
Park et al. (28)	51	−15.5%	45 ± 15	RV global longitudinal strain $\geq -15.5\%$ was independent predictor of adverse clinical events and mortality.
Fine et al. (29)	575	−15%	18	RV free-wall longitudinal strain predicted survival after adjustment for pulmonary pressure, pulmonary vascular resistance, and right atrial pressure.
Haeck et al. (30)	150	−19%	31	RV free-wall longitudinal strain, unlike TAPSE and FAC, was independent an predictor of all-cause mortality in these patients.
Badagliacca et al. (31)	108	–	24	The authors reported that the shape of the RV strain curve and the longer time necessary to return RV strain to the baseline point were associated with worse outcome.
Hardegree et al. (32)	50	−12.5%	48	$\geq 5\%$ improvement in RV free-wall longitudinal strain had > 7 -fold lower mortality during the follow-up of 4 years.
Hulshof et al. (33)	1,169	−19%	–	RV free-wall strain $> -19\%$ had a significantly higher risk for the combined endpoint (mortality and PAH-related events).
Leng et al. (34)	80	−25.2%	24	CMR-derived RV longitudinal strain, TAPSE, FAC, and RA longitudinal strain were predictors of adverse outcome in these patients.
Sato et al. (35)	21	–	9	Improvement of CMR-derived RV strain during ambrisentan and tadalafil combination therapy in PAH patients with systemic sclerosis.

CMR, cardiac magnetic resonance; CV, cardiovascular; FAC, fractional area change; GLS, global longitudinal strain; PAH, pulmonary arterial hypertension; RA, right atrium; RV, right ventricle; s' , systolic velocity of the lateral segment of tricuspid annulus; TAPSE, tricuspid annular plane systolic excursion.

TABLE 3 | Predictive value of RV longitudinal strain in heart failure.

References	Sample size	RV free-wall/global GLS cut-off	Follow-up period (months)	Main findings
Cameli et al. (45)	590	−15%	18 ± 11	Free-wall RV longitudinal strain was the strongest predictor of combined outcome, even stronger than LV global longitudinal strain, which support importance of RV strain in prognostic stratification in HF patients.
Hamada-Harimura et al. (46)	618	−13.1%	14	In patients with acute HF decompensation RV free-wall longitudinal strain was an independent predictor of cardiac events (CV death or unplanned hospitalization due to HF worsening).
Vizzardi et al. (47)	60	−18%	32 ± 13	RV free-wall longitudinal strain, but not TAPSE, FAC, and s', was independent predictor of CV events (hospitalization and CV mortality) in HFrEF patients.
Carluccio et al. (48)	200	−15.3%	28	RV free-wall longitudinal strain was a better predictor than TAPSE in HFrEF patients with the best discriminatory value of RV free-wall longitudinal strain.
Kusunose et al. (49)	58	−16%	5	RV longitudinal strain in HFrEF patients was a good predictor of functional capacity improvement (VO2 peak) in HFrEF patients who were referred for cardiac rehabilitation.
Motoki et al. (11)	171	−14.8%	60	RV free-wall strain was a predictor of adverse CV events (death, cardiac transplantation, and hospitalization due to HF) independently of age, LVEF, tricuspid s', E/e' septal, and right atrial volume index in a population of patients with chronic HFrEF.
Houard et al. (50)	266	−19%	56	Echocardiography-derived RV free-wall longitudinal strain was a better predictor of overall and CV mortality than TAPSE, FAC, and CMR-derived RVEF, RV longitudinal strain.
Carluccio et al. (51)	288	−15.3%	30 ± 23	Global RV longitudinal strain did not remain independent predictor of composite outcome (all-cause death/HF-related hospitalization) in the models that included LV parameters and other RV parameters, whereas RV free-wall strain remained an independent predictor in all models.
Lisi et al. (52)	27	–	–	RV free-wall strain had the highest diagnostic accuracy for detecting severe myocardial fibrosis, much better than TAPSE, right atrial longitudinal strain and VO2 peak.
Park et al. (53)	799	−12%	32	In patients with acute HF was found that global RV longitudinal strain was a predictor of all-cause mortality regardless of LV global longitudinal strain and clinical characteristics.
Bosch et al. (54)	657	−15.3%	24	The authors reported that RV free-wall longitudinal strain, sPAP and their ratio were independent predictors of composite endpoint (mortality and HF hospitalization) in the whole population of HF patients.

CMR, cardiac magnetic resonance; CV, cardiovascular; FAC, fractional area change; GLS, global longitudinal strain; HF, heart failure; HFpEF, heart failure with preserved ejection fraction; HFrEF, heart failure with reduced ejection fraction; LV, left ventricle; RV, right ventricle; s', systolic velocity of the lateral segment of tricuspid annulus; sPAP, systolic pulmonary pressure; TAPSE, tricuspid annular plane systolic excursion.

less preload dependent estimation of the overall performance of the RV in HF patients (3). The majority of data are focused on patients with HF with reduced LVEF (HFrEF) (45, 46, 60). However, data regarding HF with preserved LVEF (HFpEF) also emphasize the important role of RV longitudinal strain in these patients (3). **Table 3** summarizes all findings in this field.

Study that involved patients with HFpEF referred for heart transplantation reported that free-wall and global RV longitudinal strains, NT-pro-BNP, FAC, and LV end-diastolic volume were independent predictors of combined outcome (hospitalization for acute heart failure, cardiovascular death, heart transplantation, intra-aortic balloon pump implantation, and ventricular assist device implantation) (45). Free-wall RV longitudinal strain was the strongest predictor of combined outcome, even stronger than LV global longitudinal strain, which support importance of RV strain in prognostic stratification

in HF patients (45). Another investigation showed that only RV free-wall longitudinal strain, but not TAPSE, FAC, and s', was independent predictor of CV events (hospitalization and CV mortality) in HFrEF patients during 3-year follow-up (47). Carluccio et al. (48) revealed that RV free-wall longitudinal strain was a better predictor than TAPSE in HFrEF patients with the best discriminatory value of RV free-wall longitudinal strain for the prediction of adverse outcomes was −15.3%. Small study revealed that RV longitudinal strain <−16% in HFrEF patients was a good predictor of functional capacity improvement (VO2 peak) in HFrEF patients who were referred for cardiac rehabilitation (49). Another investigation found that RV free-wall strain was a predictor of adverse CV events (death, cardiac transplantation, and hospitalization due to HF) independently of age, LVEF, tricuspid s', E/e' septal, and right atrial volume index in a population of patients with chronic HFrEF who were followed for 5 years (11). The cut-off

value used for RV free-wall strain was -14.8% . Study that combined CMR and echocardiographic evaluation of the RV in HFrEF patients showed that echocardiography-derived RV free-wall longitudinal strain was a better predictor of overall and CV mortality than TAPSE, FAC, and CMR-derived RVEF, RV longitudinal strain during 4.7-year follow-up period (50). **Figure 2** illustrates RV free-wall longitudinal strain in control subjects and HFrEF patient.

Iacoviello et al. (60) demonstrated that both global and free-wall RV longitudinal strain were independent predictors of all-cause and CV mortality in chronic HFrEF patients during 3-year follow-up. Even though TAPSE, FAC, and s' were predictors of mortality in univariate analysis, they were not included in multivariate analysis. On the other hand, Carluccio et al. (11) found superior predictive value of RV free-wall strain over RV global strain in HFrEF patients over 30-month follow-up. Global RV longitudinal strain did not remain independent predictor of composite outcome (all-cause death/HF-related hospitalization) in the models that included LV parameters (LVEF, LV longitudinal strain, left atrial volume index) and other RV parameters (tricuspid regurgitation severity, RV dimensions, systolic pulmonary pressure), whereas RV free-wall strain remained an independent predictor in all models (51) (**Table 3**).

The investigation that combined echocardiographic analysis with myocardial histologic analysis reported that RV free-wall longitudinal strain was the main determinant of myocardial fibrosis, which may explain high prognostic value of this parameter in HF patients (52). RV free-wall strain had the highest diagnostic accuracy for detecting severe myocardial fibrosis, much better than TAPSE, right atrial longitudinal strain and VO2 peak (52).

In patients with acute HF decompensation RV free-wall longitudinal strain was an independent predictor of cardiac events (CV death or unplanned hospitalization due to HF worsening) (46). Other echocardiographic parameters such as LVEF, TAPSE, FAC, RV and LV global longitudinal strains were not proven to be the independent predictors of outcome in these patients (46). The cut-off value for RV free-wall longitudinal strain that showed the highest sensitivity and specificity was -13.1% (46). In the similar group of patients with acute HF authors found that global RV longitudinal strain was a predictor of all-cause mortality regardless of LV global longitudinal strain and clinical characteristics (53). Patients with reduced biventricular longitudinal strain ($>-9\%$ for LV and $>-12\%$ for RV) had the worst prognosis (53). The predictive power of RV global longitudinal strain was more significant in the absence of PH (**Table 3**).

Bosch et al. (54) reported gradual and significant deterioration of RV longitudinal strain from controls across HFpEF to HFrEF patients. The authors reported that RV free-wall longitudinal strain, sPAP and their ratio were independent predictors of composite endpoint (mortality and HF hospitalization) in the whole population of HF patients (61). Unfortunately, the separate analyses of HFrEF and HFpEF patients were not performed and therefore predictive value of RV longitudinal strain in HFpEF remains to be determined.

RV STRAIN IN VALVULAR HEART DISEASES

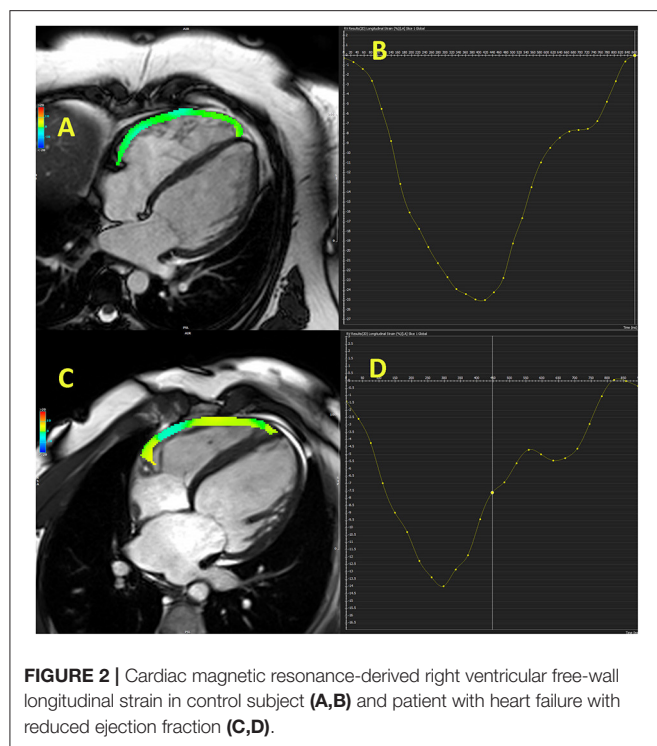
The effect of RV function in patients with valvular disease has been investigated in the last several years and it has become evident that effect of RV dysfunction on outcome in these patients is not irrelevant. The majority of studies reported deterioration of RV longitudinal strain in patients with valvular diseases (61, 62), but some recent investigations revealed a significant predictive value of RV strain in patients with aortic stenosis, mitral and tricuspid regurgitation (12, 13, 40, 63). Data are still scarce but warrant a special attention due to constantly increasing number of transcatheter interventions in valvular diseases and importance to develop new scores for better risk stratification in patients who undergo these interventions. **Table 4** summarized all findings.

Aortic Stenosis

Study that investigated RV free-wall longitudinal strain before and 1 year after transcatheter or surgical aortic valve replacement (TAVR or SAVR) showed that RV longitudinal strain did not significantly improve after TAVR, but it significantly deteriorated in SAVR group, even though TAVR group had worse baseline clinical characteristics (more patients in NYHA class III and IV and significantly higher EuroSCORE) (36). However, it must be noted that RV strain improved in TAVR group for 2.4% in absolute values, which was still not enough to reach statistical significance in a relative small sample ($n = 101$). Interestingly, TAPSE and FAC also significantly reduced after SAVR and remained the same in TAVR group (36). This difference potentially could be due to pericardiotomy during SAVR. Another investigation that included patients after SAVR revealed that RV free-wall longitudinal strain $>-15\%$ had high sensitivity and specificity for development of low output cardiac syndrome in the first 30 days after surgery, which may qualify RV strain for risk stratification undergoing SAVR (37). The same group of authors recently provided results from long follow-up and showed that RV free-wall longitudinal strain was independent predictor of low output cardiac syndrome, but not of in-hospital mortality, hospital stay, or vasoplegic syndrome (38).

Dahou et al. (63) investigated patients with low-flow low-gradient aortic stenosis and found that 2-year survival in patients with RV free-wall longitudinal strain $>-13\%$ was significantly lower than in those with RV free-wall longitudinal strain $<-13\%$. RV free-wall longitudinal strain $>-13\%$ was an independent predictor of mortality in these patients, regardless age, aortic stenosis severity, myocardial infarction and LV longitudinal strain (63). Stress RV longitudinal strain, measured during low dose dobutamine stress, has incremental prognostic value over LV longitudinal strain, LVEF and RV strain at rest (63) (**Table 4**).

Research that included HF patients due to severe aortic stenosis undergoing TAVR reported that RV global longitudinal strain and RV-arterial coupling (TAPSE/sPAP and RV longitudinal strain/sPAP) provided better risk stratification than other RV echocardiographic parameters during long-term follow up of 10 years (39). TAPSE, FAC, s' , sPAP, tricuspid



regurgitation and tricuspid annulus diameter were not proven to be the independent predictors of 10-year mortality after TAVR (39).

Recent large study that involved 334 patients who underwent TAVR reported no significant change in RV free-wall longitudinal strain at 1-year follow-up, in both groups with baseline impaired and normal RV systolic function (12). However, RV longitudinal strain was associated with 1-year all-cause mortality. The authors found a 6% higher risk for 1-year mortality for each unit increase in RV longitudinal strain. Other parameters of RV systolic function (TAPSE, FAC, s'), as well as LVEF, existence of tricuspid regurgitation and sPAP were not independent predictors of 1-year mortality in these patients (12). These findings support the routine assessment of RV longitudinal strain in patients undergoing SAVR or TAVR in order to improve the risk stratification (Table 4).

Mitral Regurgitation

RV systolic function is a very important in patients undergoing mitral valve surgery and some studies showed its strong predictive value for long-term mortality in a large population of patients who underwent cardiac surgery (valve, valve + CABG, CABG) (64). RV systolic function, assessed by TAPSE, FAC, and s' , remained depressed shortly after mitral valve surgery (65).

Study that involved patients who underwent mitral valve surgery reported significant deterioration of RV free-wall longitudinal strain in these patients (40). The authors found smaller reductions in patients who underwent robotic-assisted mitral valve repair than in patients who underwent standard

mitral valve repair. The patients who underwent robotic-assisted mitral valve repair also showed greater recovery in RV longitudinal strain at 1-year follow-up comparing with pre-surgery values (40). Similar investigation that involved patients who underwent surgical mitral valve repair showed that only resolution of RV longitudinal strain at 1 month predicted the subsequent myocardial recovery (41). TAPSE, FAC, and s' did not have any role in this prediction. Patients with preserved RV systolic function had a lower risk of hospitalization due to HF compared to those with reduced RV function (41) (Table 4).

Large research that involved 568 patients with severe ischemic mitral regurgitation who underwent surgical valve repair and 131 patients with concomitant tricuspid valve repair demonstrated that the RV continued to dilate while the LV reduced during follow-up after surgery (42). RVEF decreased, while LVEF increased during 6.3-year follow-up. RV longitudinal strain showed continuous deterioration during follow-up period. The largest decline in RV longitudinal strain occurred in the first month after surgery, while it remained constant after first year of follow-up (42). RV longitudinal strain, FAC and TAPSE were significantly lower in patients who underwent tricuspid valve repair than in those who did not undergo tricuspid valve repair. RV strain and FAC did not significantly recover during follow-up, while TAPSE significantly improved in both groups—with and without tricuspid valve repair. These findings showed that surgical treatment of functional mitral and tricuspid regurgitation along with revascularization failed to induce improve RV function and reverse remodeling (Table 4).

Functional mitral regurgitation has been currently treated with interventional “edge-to-edge” technique and study that investigated patients with moderate and severe mitral regurgitation, who underwent MitraClip procedure, demonstrated no acute improvement (within 7 days) in CMR-derived RVEF, RV end-diastolic volume and tricuspid regurgitation (66).

Findings from aforementioned studies warrant further examinations to identify optimal timing and approach of intervention for functional mitral and tricuspid regurgitation.

Tricuspid Regurgitation

Isolated or concomitant functional tricuspid regurgitation has been extensively investigated in last decade. It has been shown that tricuspid regurgitation significantly deteriorated the outcome in patients with mitral regurgitation. However, surgical intervention seems not to improve RV function in these patients (42). Interventional “edge-to-edge” repair significantly increased interest for predictors that may improve outcome after this intervention. Hirasawa et al. (67) reported that reduction of RV free-wall longitudinal strain was proportional to the level of tricuspid regurgitation. Figure 1 shows difference in RV global longitudinal strain between control subjects and patients with severe functional tricuspid regurgitation.

Large study that included 1,089 patients with tricuspid regurgitation showed that reduced RV free-wall longitudinal strain ($>-18\%$), TAPSE (<18.5 mm) and FAC ($<35\%$) were independent predictors for 2-year all-cause mortality (66). The sensitivity and specificity to predict 2-year mortality gradually

TABLE 4 | Predictive value of RV longitudinal strain in patients with valvular heart disease.

References	Sample size	RV free-wall/global GLS cut-off	Follow-up period (months)	Main findings
Aortic stenosis				
Kempny et al. (36)	123	–	3	RV free-wall longitudinal strain before and 1 year after TAVR or SAVR showed that RV longitudinal strain did not significantly improve after TAVR, but it significantly deteriorated in SAVR group.
Balderas-Muñoz et al. (37)	75	–15%	1	Patients after SAVR revealed that RV free-wall longitudinal strain >–15% had high sensitivity and specificity for development of low output cardiac syndrome in the first 30 days after surgery.
Posada-Martinez et al. (38)	75	–17.3%	24	RV free-wall longitudinal strain was independent predictor of low output cardiac syndrome, but not of in-hospital mortality, hospital stay, or vasoplegic syndrome.
Vizzardi et al. (39)	56	–17%	120	RV global longitudinal strain and RV-arterial coupling provided better risk stratification than other RV echocardiographic parameters in TAVR patients during long-term follow-up.
Mitral regurgitation				
Orde et al. (40)	158	–	36	The patients who underwent robotic-assisted mitral valve repair also showed greater recovery in RV longitudinal strain at 1-year follow-up comparing with pre-surgery values.
Chang et al. (41)	108	–	31	Only resolution of RV longitudinal strain at 1 month predicted the subsequent myocardial recovery. TAPSE, FAC, and s' did not have any role in this prediction.
Elgharably et al. (42)	568	–	76	RVEF decreased, while LVEF increased during after concomitant surgery for ischemic mitral and tricuspid regurgitation. RV longitudinal strain showed continuous deterioration during follow-up period.
Tricuspid regurgitation				
Bannehr et al. (43)	1,089	–18%	24	Reduced RV free-wall longitudinal strain, TAPSE and FAC were independent predictors for all-cause mortality. The sensitivity and specificity to predict mortality gradually increased from FAC, across TAPSE, to RV longitudinal strain.
Prihadi et al. (22)	896	–23%	34	RV free-wall longitudinal strain was independently associated with all-cause mortality and incremental to FAC and TAPSE.
Ancona et al. (13)	250	–	24	The authors found that RV free-wall strain >–17% at baseline predicted RV heart failure, whereas patients with RV free-wall strain <–14% at follow-up had significantly better survival.
Romano et al. (44)	544	–16%	72	CMR-derived RV longitudinal strain was independent predictor of mortality after adjustment for clinical and imaging risk factors, including RV size and ejection fraction.

CMR, cardiac magnetic resonance; CV, cardiovascular; FAC, fractional area change; GLS, global longitudinal strain; RV, right ventricle; s', systolic velocity of the lateral segment of tricuspid annulus; SAVR, surgical aortic valve replacement; TAVR, transcatheter aortic valve replacement; TAPSE, tricuspid annular plane systolic excursion.

increased from FAC, across TAPSE, to RV longitudinal strain (43). Similar study that included 896 patients with significant tricuspid regurgitation defined reduced RV function as TAPSE <17 mm, FAC <35%, and RV free-wall longitudinal strain >–23% (22). Mortality was significantly higher in patients with decreased FAC, decreased TAPSE, and impaired RV free wall longitudinal strain. Multivariate analysis showed that RV free-wall longitudinal strain was independently associated with 2.8-year all-cause mortality and incremental to FAC and TAPSE (22). Reduced TAPSE and FAC also represented independent predictors for mortality after adjustment for age, LVEF, RV systolic pressure, significant left-sided valvular disease (22). However, after adjustment for concomitant diseases (diabetes mellitus, chronic kidney disease, coronary artery disease) as well as New York Heart Association class III/IV this independent predictive value vanished for FAC and TAPSE, but not for RV free-wall strain (22) (**Table 4**).

Investigation that enrolled 250 consecutive patients with severe tricuspid regurgitation investigated RV global and free-wall longitudinal strain and reclassified ~42–56% of patients with normal RV systolic function according to conventional

parameters in patients with impaired RV systolic function (13). The authors found that RV free-wall strain >–17% at baseline predicted RV heart failure, whereas patients with RV free-wall strain <–14% at follow-up had significantly better survival (13) (**Table 4**).

Recent study included 544 patients with severe functional tricuspid regurgitation with a median follow-up of 6 years (43). Patients with CMR-derived RV free-wall longitudinal strain >–16% had significantly lower survival compared with those with lower RV free-wall longitudinal strain (44). CMR-derived RV longitudinal strain was independent predictor of mortality after adjustment for clinical and imaging risk factors, including RV size and ejection fraction (**Table 4**).

Current studies support the evaluation of RV longitudinal strain due to its high predictive value in patients with tricuspid regurgitation. Data about the effect of interventional “edge-to-edge” tricuspid valve repair are expected and they will provide some new guidelines if RV longitudinal strain should be involved in routine echocardiographic examination and it seems that body of evidence that supports this evaluation is constantly enlarging.

CONCLUSION

RV longitudinal strain is a significant parameter of RV dysfunction that showed better sensitivity than conventional echocardiographic parameters. Latest investigation demonstrated its role in prediction of adverse outcome in wide range of CV conditions, but the most encouraging data came from studies that were focused on pulmonary hypertension, HFrEF and tricuspid regurgitation. Data about the predictive importance of RV longitudinal strain in HFpEF patients and those with aortic stenosis and mitral regurgitation are still scarce and warrant further investigation. Adding RV longitudinal strain to existing scores might significantly help

in the risk stratification, which could induce reclassification of some patients to higher risk group. Existing knowledge about the predictive value of RV longitudinal strain supports its routine echocardiographic evaluation in patients with CV diseases.

AUTHOR CONTRIBUTIONS

MT wrote the article. NN, LS, JK, and CR reviewed the literature. JK made figures. DB, BG, and DS helped in preparing the text of the manuscript. EB, CC, and WR reviewed the article with important scientific input. All authors contributed to the article and approved the submitted version.

REFERENCES

- Dong Y, Pan Z, Wang D, Lv J, Fang J, Xu R, et al. Prognostic value of cardiac magnetic resonance-derived right ventricular remodeling parameters in pulmonary hypertension: a systematic review and meta-analysis. *Circ Cardiovasc Imaging*. (2020) 13:e010568. doi: 10.1161/CIRCIMAGING.120.010568
- Graziani F, Lillo R, Panaioli E, Pieroni M, Camporeale A, Verrecchia E, et al. Prognostic significance of right ventricular hypertrophy and systolic function in Anderson-Fabry disease. *ESC Heart Fail*. (2020) 7:1605–14. doi: 10.1002/ehf2.12712
- Shah AM, Cikes M, Prasad N, Li G, Getchevski S, Claggett B, et al. Echocardiographic features of patients with heart failure and preserved left ventricular ejection fraction. *J Am Coll Cardiol*. (2019) 74:2858–73. doi: 10.1016/j.jacc.2019.09.063
- Lyhne MD, Kabrhel C, Giordano N, Andersen A, Nielsen-Kudsk JE, Zheng H, et al. The echocardiographic ratio tricuspid annular plane systolic excursion/pulmonary arterial systolic pressure predicts short-term adverse outcomes in acute pulmonary embolism. *Eur Heart J Cardiovasc Imaging*. (2021) 22:285–94. doi: 10.1093/ehjci/jeaa243
- Dini FL, Conti U, Fontanive P, Andreini D, Banti S, Braccini L, et al. Right ventricular dysfunction is a major predictor of outcome in patients with moderate to severe mitral regurgitation and left ventricular dysfunction. *Am Heart J*. (2007) 154:172–9. doi: 10.1016/j.ahj.2007.03.033
- Karam N, Stolz L, Orban M, Deseive S, Praz F, Kalbacher D, et al. Impact of right ventricular dysfunction on outcomes after transcatheter edge-to-edge repair for secondary mitral regurgitation. *JACC Cardiovasc Imaging*. (2021) 14:768–78. doi: 10.1016/j.jcmg.2020.12.015
- Kawut SM, Barr RG, Lima JA, Praestgaard A, Johnson WC, Chahal H, et al. Right ventricular structure is associated with the risk of heart failure and cardiovascular death: the Multi-Ethnic Study of Atherosclerosis (MESA)–right ventricle study. *Circulation*. (2012) 126:1681–8. doi: 10.1161/CIRCULATIONAHA.112.095216
- Tadic M, Cuspidi C, Celic V, Petrovic O, Pencic B, Mancina G, et al. The prognostic importance of right ventricular remodeling and the circadian blood pressure pattern on the long-term cardiovascular outcome. *J Hypertens*. (2020) 38:1525–30. doi: 10.1097/HJH.0000000000002432
- Erley J, Tanacli R, Genovese D, Tapaskar N, Rashedi N, Bucius P, et al. Myocardial strain analysis of the right ventricle: comparison of different cardiovascular magnetic resonance and echocardiographic techniques. *J Cardiovasc Magn Reson*. (2020) 22:51. doi: 10.1186/s12968-020-00647-7
- Stolfo D, Albani S, Biondi F, De Luca A, Barbati G, Howard L, et al. Global right heart assessment with speckle-tracking imaging improves the risk prediction of a validated scoring system in pulmonary arterial hypertension. *J Am Soc Echocardiogr*. (2020) 33:1334–44. doi: 10.1016/j.echo.2020.05.020
- Motoki H, Borowski AG, Shrestha K, Hu B, Kusunose K, Troughton RW, et al. Right ventricular global longitudinal strain provides prognostic value incremental to left ventricular ejection fraction in patients with heart failure. *J Am Soc Echocardiogr*. (2014) 27:726–32. doi: 10.1016/j.echo.2014.02.007
- Medvedofsky D, Koifman E, Jarrett H, Miyoshi T, Rogers T, Ben-Dor I, et al. Association of right ventricular longitudinal strain with mortality in patients undergoing transcatheter aortic valve replacement. *J Am Soc Echocardiogr*. (2020) 33:452–60. doi: 10.1016/j.echo.2019.11.014
- Ancona F, Melillo F, Calvo F, Attalla El Halabieh N, Stella S, Capogrosso C, et al. Right ventricular systolic function in severe tricuspid regurgitation: prognostic relevance of longitudinal strain. *Eur Heart J Cardiovasc Imaging*. (2021) jeab030. doi: 10.1093/ehjci/jeab030
- Steen H, Giusca S, Montenbruck M, Patel AR, Pieske B, Florian A, et al. Left and right ventricular strain using fast strain-encoded cardiovascular magnetic resonance for the diagnostic classification of patients with chronic non-ischemic heart failure due to dilated, hypertrophic cardiomyopathy or cardiac amyloidosis. *J Cardiovasc Magn Reson*. (2021) 23:45. doi: 10.1186/s12968-021-00711-w
- Fine NM, White JA, Jimenez-Zepeda V, Howlett JG. Determinants and prognostic significance of serial right heart function changes in patients with cardiac amyloidosis. *Can J Cardiol*. (2020) 36:432–40. doi: 10.1016/j.cjca.2020.01.020
- Tadic M, Baudisch A, Haßfeld S, Heinzel F, Cuspidi C, Burkhardt F, et al. Right ventricular function and mechanics in chemotherapy- and radiotherapy-naïve cancer patients. *Int J Cardiovasc Imaging*. (2018) 34:1581–7. doi: 10.1007/s10554-018-1379-0
- Tadic M. Multimodality evaluation of the right ventricle: an updated review. *Clin Cardiol*. (2015) 38:770–6. doi: 10.1002/clc.22443
- Rudski LG, Lai WW, Afalalo J, Hua L, Handschumacher MD, Chandrasekaran K, et al. Guidelines for the echocardiographic assessment of the right heart in adults: a report from the American Society of Echocardiography endorsed by the European Association of Echocardiography, a registered branch of the European Society of Cardiology, and the Canadian Society of Echocardiography. *J Am Soc Echocardiogr*. (2010) 23:685–713. doi: 10.1016/j.echo.2010.05.010
- Haddad F, Hunt SA, Rosenthal DN, Murphy DJ. Right ventricular function in cardiovascular disease, part I: anatomy, physiology, aging, and functional assessment of the right ventricle. *Circulation*. (2008) 117:1436–48. doi: 10.1161/CIRCULATIONAHA.107.653576
- Badano LP, Muraru D, Parati G, Haugaa K, Voigt JU. How to do right ventricular strain. *Eur Heart J Cardiovasc Imaging*. (2020) 21:825–7. doi: 10.1093/ehjci/jeaa126
- Muraru D, Onciul S, Peluso D, Soriani N, Cucchini U, Aruta P, et al. Sex- and method-specific reference values for right ventricular strain by 2-dimensional speckle-tracking echocardiography. *Circ Cardiovasc Imaging*. (2016) 9:e003866. doi: 10.1161/CIRCIMAGING.115.003866
- Prihadi EA, van der Bijl P, Dietz M, Abou R, Vollema EM, Marsan NA, et al. Prognostic implications of right ventricular free wall longitudinal strain in patients with significant functional tricuspid regurgitation. *Circ Cardiovasc Imaging*. (2019) 12:e008666. doi: 10.1161/CIRCIMAGING.118.008666
- Li Y, Wang Y, Ye X, Kong L, Zhu W, Lu X. Clinical study of right ventricular longitudinal strain for assessing right ventricular dysfunction

- and hemodynamics in pulmonary hypertension. *Medicine*. (2016) 95:e5668. doi: 10.1097/MD.0000000000000568
24. Focardi M, Cameli M, Carbone SF, Massoni A, De Vito R, Lisi M, et al. Traditional and innovative echocardiographic parameters for the analysis of right ventricular performance in comparison with cardiac magnetic resonance. *Eur Heart J Cardiovasc Imaging*. (2015) 16:47–52. doi: 10.1093/ehjci/jeu156
 25. Puwanant S, Park M, Popović ZB, Tang WHW, Farha S, George D, et al. Ventricular geometry, strain, and rotational mechanics in pulmonary hypertension. *Circulation*. (2010) 121:259–66. doi: 10.1161/CIRCULATIONAHA.108.844340
 26. van Kessel M, Seaton D, Chan J, Yamada A, Kermeen F, Hamilton-Craig C, et al. Prognostic value of right ventricular free wall strain in pulmonary hypertension patients with pseudo-normalized tricuspid annular plane systolic excursion values. *Int J Cardiovasc Imaging*. (2016) 32:905–12. doi: 10.1007/s10554-016-0862-8
 27. Motoji Y, Tanaka H, Fukuda Y, Ryo K, Emoto N, Kawai H, et al. Efficacy of right ventricular free-wall longitudinal speckle-tracking strain for predicting long-term outcome in patients with pulmonary hypertension. *Circ J*. (2013) 77:756–63. doi: 10.1253/circj.CJ-12-1083
 28. Park JH, Park MM, Farha S, Sharp J, Lundgrin E, Comhair S, et al. Impaired global right ventricular longitudinal strain predicts long-term adverse outcomes in patients with pulmonary arterial hypertension. *J Cardiovasc Ultrasound*. (2015) 23:91–9. doi: 10.4250/jcu.2015.23.2.91
 29. Fine NM, Chen L, Bastiansen PM, Frantz RP, Pelikka PA, Oh JK, et al. Outcome prediction by quantitative right ventricular function assessment in 575 subjects evaluated for pulmonary hypertension. *Circ Cardiovasc Imaging*. (2013) 6:711–21. doi: 10.1161/CIRCIMAGING.113.000640
 30. Haack ML, Scherptong RW, Marsan NA, Holman ER, Schali J, Bax JJ, et al. Prognostic value of right ventricular longitudinal peak systolic strain in patients with pulmonary hypertension. *Circ Cardiovasc Imaging*. (2012) 5:628–36. doi: 10.1161/CIRCIMAGING.111.971465
 31. Badagliacca R, Pezzuto B, Papa S, Poscia R, Manzi G, Pascarella A, et al. Right ventricular strain curve morphology and outcome in idiopathic pulmonary arterial hypertension. *JACC Cardiovasc Imaging*. (2021) 14:162–72. doi: 10.1016/j.jcmg.2020.08.017
 32. Hardegree EL, Sachdev A, Villarraga HR, Frantz RP, McGoon MD, Kushwaha SS, et al. Role of serial quantitative assessment of right ventricular function by strain in pulmonary arterial hypertension. *Am J Cardiol*. (2013) 111:143–8. doi: 10.1016/j.amjcard.2012.08.061
 33. Hulshof HG, Eijssvogels TMH, Kleinnibbelink G, van Dijk AP, George KP, Oxenburgh DL, et al. Prognostic value of right ventricular longitudinal strain in patients with pulmonary hypertension: a systematic review and meta-analysis. *Eur Heart J Cardiovasc Imaging*. (2019) 20:475–84. doi: 10.1093/ehjci/jeu120
 34. Leng S, Dong Y, Wu Y, Zhao X, Ruan W, Zhang G, et al. Impaired cardiovascular magnetic resonance-derived rapid semiautomated right atrial longitudinal strain is associated with decompensated hemodynamics in pulmonary arterial hypertension. *Circ Cardiovasc Imaging*. (2019) 12:e008582. doi: 10.1161/CIRCIMAGING.118.008582
 35. Sato T, Ambale-Venkatesh B, Lima JAC, Zimmerman SL, Tedford RJ, Fujii T, et al. The impact of ambrisentan and tadalafil upfront combination therapy on cardiac function in scleroderma associated pulmonary arterial hypertension patients: cardiac magnetic resonance feature tracking study. *Pulm Circ*. (2018) 8:2045893217748307. doi: 10.1177/2045893217748307
 36. Kempny A, Diller GP, Kaleschke G, Orwat S, Funke A, Schmidt R, et al. Impact of transcatheter aortic valve implantation or surgical aortic valve replacement on right ventricular function. *Heart*. (2012) 98:1299–304. doi: 10.1136/heartjnl-2011-301203
 37. Balderas-Muñoz K, Rodríguez-Zanella H, Fritche-Salazar JF, Ávila-Vanzini N, Juárez Orozco LE, Arias-Godínez JA, et al. Improving risk assessment for post-surgical low cardiac output syndrome in patients without severely reduced ejection fraction undergoing open aortic valve replacement. The role of global longitudinal strain and right ventricular free wall strain. *Int J Cardiovasc Imaging*. (2017) 33:1483–9. doi: 10.1007/s10554-017-1139-6
 38. Posada-Martínez EL, Fritche-Salazar JF, Arias-Godínez JA, Ortiz-Leon XA, Balderas-Muñoz K, Ruiz-Esparza ME, et al. Right ventricular longitudinal strain predicts low-cardiac output syndrome after surgical aortic valve replacement in patients with preserved and mid-range ejection fraction. *J Cardiothorac Vasc Anesth*. (2020). 35(6):1638–1645. doi: 10.1053/j.jvca.2020.12.008
 39. Vizzardi E, Gavazzoni M, Sciatti E, Dallapellegrina L, Bernardi N, Raddino R, et al. Right ventricular deformation and right ventricular-arterial coupling in patients with heart failure due to severe aortic stenosis undergoing TAVI: long-term results. *Am J Cardiovasc Dis*. (2020) 10:150–63.
 40. Orde SR, Chung SY, Pulido JN, Suri RM, Stulak JM, Oh JK, et al. Changes in right ventricle function after mitral valve repair surgery. *Heart Lung Circ*. (2020) 29:785–792. doi: 10.1016/j.hlc.2019.06.724
 41. Chang WT, Wu NC, Shih JY, Hsu CH, Chen ZC, Cheng BC. Right ventricular reserve post mitral valve repair is associated with heart failure hospitalization. *Pulm Circ*. (2020) 10:2045894020943858. doi: 10.1177/2045894020943858
 42. Elgharably H, Javadikasgari H, Koprivanac M, Lowry AM, Sato K, Blackstone EH, et al. Right versus left heart reverse remodelling after treating ischaemic mitral and tricuspid regurgitation. *Eur J Cardiothorac Surg*. (2020) ezaa326. doi: 10.1093/ejcts/ezaa326
 43. Bannehr M, Kahn U, Liebchen J, Okamoto M, Hähnel V, Georgi C, et al. Right ventricular longitudinal strain predicts survival in patients with functional tricuspid regurgitation. *Can J Cardiol*. (2021). doi: 10.1016/j.cjca.2021.01.006
 44. Romano S, Dell'atti D, Judd RM, Kim RJ, Weinsaft JW, Kim J, et al. Prognostic value of feature-tracking right ventricular longitudinal strain in severe functional tricuspid regurgitation: a multicenter study. *J Am Coll Cardiol Img*. (2021). doi: 10.1016/j.jcmg.2021.02.009
 45. Cameli M, Righini FM, Lisi M, Bennati E, Navarri R, Lunghetti S, et al. Comparison of right versus left ventricular strain analysis as a predictor of outcome in patients with systolic heart failure referred for heart transplantation. *Am J Cardiol*. (2013) 112:1778–84. doi: 10.1016/j.amjcard.2013.07.046
 46. Hamada-Harimura Y, Seo Y, Ishizu T, Nishi I, Machino-Ohtsuka T, Yamamoto M, et al. Incremental prognostic value of right ventricular strain in patients with acute decompensated heart failure. *Circ Cardiovasc Imaging*. (2018) 11:e007249. doi: 10.1161/CIRCIMAGING.117.007249
 47. Vizzardi E, D'Aloia A, Caretta G, Bordonali T, Bonadei I, Rovetta R, et al. Long-term prognostic value of longitudinal strain of right ventricle in patients with moderate heart failure. *Hellenic J Cardiol*. (2014) 55:150–5.
 48. Carluccio E, Biagioli P, Alunni P, Murrone A, Zuchi C, Coiro S, et al. Prognostic value of right ventricular dysfunction in heart failure with reduced ejection fraction: superiority of longitudinal strain over tricuspid annular plane systolic excursion. *Circ Cardiovasc Imaging*. (2018) 11:e006894. doi: 10.1161/CIRCIMAGING.117.006894
 49. Kusunose K, Seno H, Yamada H, Nishio S, Torii Y, Hirata Y, et al. Right ventricular function and beneficial effects of cardiac rehabilitation in patients with systolic chronic heart failure. *Can J Cardiol*. (2018) 34:1307–15. doi: 10.1016/j.cjca.2018.06.003
 50. Houard L, Benaets MB, de Meester de Ravenstein C, Rousseau MF, Ahn SA, Amzulescu MS, et al. Additional Prognostic Value of 2D right ventricular speckle-tracking strain for prediction of survival in heart failure and reduced ejection fraction: a comparative study with cardiac magnetic resonance. *JACC Cardiovasc Imaging*. (2019) 12:2373–85. doi: 10.1016/j.jcmg.2018.11.028
 51. Carluccio E, Biagioli P, Lauciello R, Zuchi C, Mengoni A, Bardelli G, et al. Superior prognostic value of right ventricular free wall compared to global longitudinal strain in patients with heart failure. *J Am Soc Echocardiogr*. (2019) 32:836–44. doi: 10.1016/j.echo.2019.02.011
 52. Lisi M, Cameli M, Righini FM, Malandrino A, Tacchini D, Focardi M, et al. RV Longitudinal deformation correlates with myocardial fibrosis in patients with end-stage heart failure. *JACC Cardiovasc Imaging*. (2015) 8:514–22. doi: 10.1016/j.jcmg.2014.12.026
 53. Park JH, Park JJ, Park JB, Cho GY. Prognostic value of biventricular strain in risk stratifying in patients with acute heart failure. *J Am Heart Assoc*. (2018) 7:e009331. doi: 10.1161/JAHA.118.009331
 54. Bosch L, Lam CSP, Gong L, Chan SP, Sim D, Yeo D, et al. Right ventricular dysfunction in left-sided heart failure with preserved versus reduced ejection fraction. *Eur J Heart Fail*. (2017) 19:1664–71. doi: 10.1002/ehf.873
 55. Meyer P, Filipatos GS, Ahmed MI, Iskandrian AE, Bittner V, Perry GJ, et al. Effects of right ventricular ejection fraction on outcomes

- in chronic systolic heart failure. *Circulation*. (2010) 121:252–8. doi: 10.1161/CIRCULATIONAHA.109.887570
56. Ghio S, Recusani F, Klersy C, Sebastiani R, Laudisa ML, Campana C, et al. Prognostic usefulness of the tricuspid annular plane systolic excursion in patients with congestive heart failure secondary to idiopathic or ischemic dilated cardiomyopathy. *Am J Cardiol*. (2000) 85:837–42. doi: 10.1016/S0002-9149(99)00877-2
 57. Dini FL, Carluccio E, Simioniuc A, Biagioli P, Reboldi G, Galeotti GG, et al. Right ventricular recovery during follow-up is associated with improved survival in patients with chronic heart failure with reduced ejection fraction. *Eur J Heart Fail*. (2016) 18:1462–71. doi: 10.1002/ehf.639
 58. Anavekar NS, Skali H, Bourgoun M, Ghali JK, Kober L, Maggioni AP, et al. Usefulness of right ventricular fractional area change to predict death, heart failure, and stroke following myocardial infarction (from the VALIANT ECHO Study). *Am J Cardiol*. (2008) 101:607–12. doi: 10.1016/j.amjcard.2007.09.115
 59. Shin HW, Kim H, Son J, Yoon HJ, Park HS, Cho YK, et al. Tissue Doppler imaging as a prognostic marker for cardiovascular events in heart failure with preserved ejection fraction and atrial fibrillation. *J Am Soc Echocardiogr*. (2010) 23:755–61. doi: 10.1016/j.echo.2010.05.003
 60. Iacoviello M, Citarelli G, Antoncetti V, Romito R, Monitillo F, Leone M, et al. Right ventricular longitudinal strain measures independently predict chronic heart failure mortality. *Echocardiography*. (2016) 33:992–1000. doi: 10.1111/echo.13199
 61. Di Franco A, Kim J, Rodriguez-Diego S, Khaliq O, Siden JY, Goldberg SR, et al. Multiplanar strain quantification for assessment of right ventricular dysfunction and non-ischemic fibrosis among patients with ischemic mitral regurgitation. *PLoS ONE*. (2017) 12:e0185657. doi: 10.1371/journal.pone.0185657
 62. Tadic M, Cuspidi C, Pencic B, Ivanovic B, Grassi G, Kocijancic V, et al. The impact of arterial hypertension on left ventricular strain in patients with aortic stenosis and preserved ejection fraction. *J Hypertens*. (2019) 37:747–53. doi: 10.1097/HJH.0000000000001963
 63. Dahou A, Clavel MA, Capoulade R, Bartko PE, Magne J, Mundigler G, et al. Right ventricular longitudinal strain for risk stratification in low-flow, low-gradient aortic stenosis with low ejection fraction. *Heart*. (2016) 102:548–54. doi: 10.1136/heartjnl-2015-308309
 64. Bootsma IT, de Lange F, Koopmans M, Haenen J, Boonstra PW, Symersky T, et al. Right ventricular function after cardiac surgery is a strong independent predictor for long-term mortality. *J Cardiothorac Vasc Anesth*. (2017) 31:1656–62. doi: 10.1053/j.jvca.2017.02.008
 65. Van Orman JR, Connelly K, Albinmoussa Z, Tousignant C. Early recovery of tricuspid annular isovolumic acceleration after mitral valve surgery - an observational study. *Can J Anaesth*. (2016) 63:920–7. doi: 10.1007/s12630-016-0651-9
 66. Lurz P, Serpytis R, Blazek S, Seeburger J, Mangner N, Noack T, et al. Assessment of acute changes in ventricular volumes, function, and strain after interventional edge-to-edge repair of mitral regurgitation using cardiac magnetic resonance imaging. *Eur Heart J Cardiovasc Imaging*. (2015) 16:1399–404. doi: 10.1093/ehjci/jev115
 67. Hirasawa K, van Rosendaal PJ, Dietz ME, Ajmone Marsan N, Delgado V, Bax JJ. Comparison of the usefulness of strain imaging by echocardiography versus computed tomography to detect right ventricular systolic dysfunction in patients with significant secondary tricuspid regurgitation. *Am J Cardiol*. (2020) 134:116–22. doi: 10.1016/j.amjcard.2020.07.063

Conflict of Interest: The authors declare that the research was conducted in the absence of any commercial or financial relationships that could be construed as a potential conflict of interest.

Copyright © 2021 Tadic, Nita, Schneider, Kersten, Buckert, Gonska, Scharnbeck, Reichart, Belyavskiy, Cuspidi and Rottbauer. This is an open-access article distributed under the terms of the Creative Commons Attribution License (CC BY). The use, distribution or reproduction in other forums is permitted, provided the original author(s) and the copyright owner(s) are credited and that the original publication in this journal is cited, in accordance with accepted academic practice. No use, distribution or reproduction is permitted which does not comply with these terms.



Automated Quality-Controlled Cardiovascular Magnetic Resonance Pericardial Fat Quantification Using a Convolutional Neural Network in the UK Biobank

Andrew Bard^{1,2†}, Zahra Raisi-Estabragh^{1,2†}, Maddalena Ardissino³, Aaron Mark Lee¹, Francesca Pugliese^{1,2}, Damini Dey⁴, Sandip Sarkar², Patricia B. Munroe¹, Stefan Neubauer⁵, Nicholas C. Harvey^{6,7} and Steffen E. Petersen^{1,2*}

OPEN ACCESS

Edited by:

Patrick Doebelin,
German Heart Center Berlin, Germany

Reviewed by:

Michael Schär,
Johns Hopkins University,
United States
Edyta Blaszczyk,
Charité University Medicine
Berlin, Germany

*Correspondence:

Steffen E. Petersen
s.e.petersen@qmul.ac.uk

[†]These authors have contributed
equally to this work and share first
authorship

Specialty section:

This article was submitted to
Cardiovascular Imaging,
a section of the journal
Frontiers in Cardiovascular Medicine

Received: 07 March 2021

Accepted: 17 May 2021

Published: 07 July 2021

Citation:

Bard A, Raisi-Estabragh Z, Ardissino M, Lee AM, Pugliese F, Dey D, Sarkar S, Munroe PB, Neubauer S, Harvey NC and Petersen SE (2021) Automated Quality-Controlled Cardiovascular Magnetic Resonance Pericardial Fat Quantification Using a Convolutional Neural Network in the UK Biobank. *Front. Cardiovasc. Med.* 8:677574. doi: 10.3389/fcvm.2021.677574

¹ William Harvey Research Institute, National Institute for Health Research (NIHR) Barts Biomedical Research Centre, Queen Mary University of London, Charterhouse Square, London, United Kingdom, ² St Bartholomew's Hospital, Barts Health National Health Service (NHS) Trust, London, United Kingdom, ³ Faculty of Medicine, Imperial College London, London, United Kingdom, ⁴ Biomedical Imaging Research Institute, Cedars-Sinai Medical Centre, Los Angeles, CA, United States, ⁵ Division of Cardiovascular Medicine, Radcliffe Department of Medicine, University of Oxford, National Institute for Health Research Oxford Biomedical Research Centre, Oxford University Hospitals NHS Foundation Trust, Oxford, United Kingdom, ⁶ Medical Research Council (MRC) Lifecourse Epidemiology Unit, University of Southampton, Southampton, United Kingdom, ⁷ National Institute for Health Research (NIHR) Southampton Biomedical Research Centre, University Hospital Southampton National Health Service (NHS) Foundation Trust, University of Southampton, Southampton, United Kingdom

Background: Pericardial adipose tissue (PAT) may represent a novel risk marker for cardiovascular disease. However, absence of rapid radiation-free PAT quantification methods has precluded its examination in large cohorts.

Objectives: We developed a fully automated quality-controlled tool for cardiovascular magnetic resonance (CMR) PAT quantification in the UK Biobank (UKB).

Methods: Image analysis comprised contouring an en-bloc PAT area on four-chamber cine images. We created a ground truth manual analysis dataset randomly split into training and test sets. We built a neural network for automated segmentation using a Multi-residual U-net architecture with incorporation of permanently active dropout layers to facilitate quality control of the model's output using Monte Carlo sampling. We developed an in-built quality control feature, which presents predicted Dice scores. We evaluated model performance against the test set ($n = 87$), the whole UKB Imaging cohort ($n = 45,519$), and an external dataset ($n = 103$). In an independent dataset, we compared automated CMR and cardiac computed tomography (CCT) PAT quantification. Finally, we tested association of CMR PAT with diabetes in the UKB ($n = 42,928$).

Results: Agreement between automated and manual segmentations in the test set was almost identical to inter-observer variability (mean Dice score = 0.8). The quality control method predicted individual Dice scores with Pearson $r = 0.75$. Model performance remained high in the whole UKB Imaging cohort and in the external dataset, with medium-good quality segmentation in 94.3% (mean Dice score = 0.77) and 94.4% (mean Dice score = 0.78), respectively. There was high correlation between CMR and CCT PAT measures (Pearson $r = 0.72$, p -value 5.3×10^{-18}). Larger CMR PAT area was

associated with significantly greater odds of diabetes independent of age, sex, and body mass index.

Conclusions: We present a novel fully automated method for CMR PAT quantification with good model performance on independent and external datasets, high correlation with reference standard CCT PAT measurement, and expected clinical associations with diabetes.

Keywords: cardiovascular magnetic resonance, pericardial fat, epicardial fat, obesity, automated image analysis, neural network, machine learning

INTRODUCTION

Pericardial adipose tissue (PAT), which surrounds the surface of the heart and adventitia of the coronary arteries, has been linked to a range of important cardiovascular and metabolic conditions, including atrial fibrillation (1), diabetes (2), and coronary artery disease (3). These relationships appear independent of subcutaneous fat, total body weight, and classical cardiovascular risk factors (4), suggesting distinct biological significance of PAT. Indeed, it has been proposed that adipocytokines and proinflammatory markers secreted by metabolically active PAT may act as mediators for these associations through promotion of a milieu for disease development at both local and systemic levels (5, 6). Thus, PAT may provide novel insights into disease processes and has a potential role as a marker of cardiovascular risk.

Technical difficulties in quantification of PAT in an efficient and radiation-free manner have precluded its systematic study in large cohorts. While cardiac computed tomography (CCT) PAT quantification is well-established (3, 7–9), exposure of large population cohorts to ionizing radiation is not ethically permissible (10). Cardiovascular magnetic resonance (CMR) is the reference imaging modality for assessment of cardiac structure and function and has been used in several large population studies, including the Multi-ethnic Study of Atherosclerosis (11), the Framingham Heart Study (12), and the UK Biobank (UKB) (13). Thus, CMR PAT quantification would have high utility for research, with potential for translation into clinical care; however, existing methods require dedicated acquisitions and, often, arduous manual image analysis (14, 15), limiting their applicability to large datasets with standard sequence acquisitions.

We present a novel fully automated method for PAT quantification using standard-of-care CMR images with in-built quality control (QC) developed and tested in the UKB. We test the correlation of this CMR PAT metric with reference standard CCT PAT quantification in an external dataset and investigate clinical validity through consideration of associations with diabetes in UKB. Reporting in this paper is in accordance with relevant aspects of the Proposed Requirements for Cardiovascular Imaging-Related Machine Learning Evaluation (PRIME) guidance (16).

MATERIALS AND METHODS

Setting and Study Population

The UKB incorporates data from over half a million participants recruited between 2006 and 2010 from across the UK. Individuals aged 40–69 years old were identified through National Health Service (NHS) registers and requested to participate *via* postal invites. There was detailed baseline characterization of participant demographics, lifestyle, and medical history (17). The UKB protocol is publicly available (18). The UKB Imaging Study, which includes detailed CMR imaging, aims to scan 100,000 of the original participants (approximately 50,000 completed, June 2021) (19).

CMR Image Acquisition

CMR imaging was with 1.5-T scanners (MAGNETOM Aera, Syngo Platform VD13A, Siemens Healthcare, Erlangen, Germany) using a standardized acquisition protocol, which is detailed elsewhere (13). Cardiac function was assessed using balanced steady state free precession cine sequences with standard long-axis cuts and a complete short-axis stack. No signal or image filtering was applied, with the exception of distortion correction.

Standard Operating Procedure for PAT Segmentation

The analysis protocol comprised segmentation of an en bloc PAT area from standard four-chamber cine images (single 2D slice), a universal component of standard CMR studies and one that demonstrates less variability in cut plane positioning compared to other acquisitions (e.g., short axis slices). For consistency, we measured PAT at phase 1 of the imaging cycle (approximately end-diastole). A single contour was drawn to select areas of high signal intensity adjacent to the epicardial surface of the left and right ventricular myocardium, resulting in output of an area measure in cm^2 (**Figure 1**). Areas of high signal intensity over the liver were not included, as this almost always represents adipose tissue below the diaphragm (**Figure 1B**).

Creation of a Ground Truth Manual Segmentation Dataset

We selected 500 random UKB participants with record of an imaging center visit using the random number generator package in R. We excluded participants with missing ($n = 45$) or inadequate quality ($n = 23$) CMR images. PAT contours

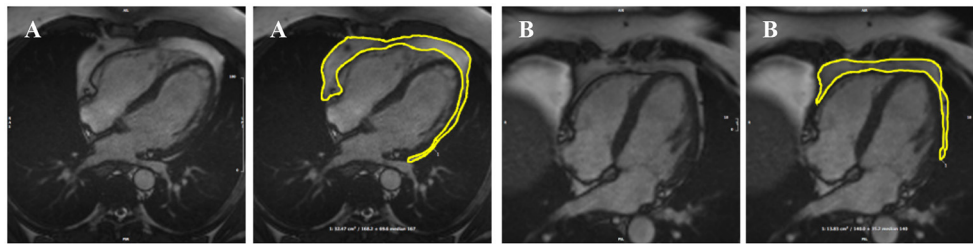


FIGURE 1 | Two examples of PAT contoured in end-diastole on four-chamber bSSFP cine-CMR, performed using CVI42[®] software according to the established SOP. A single contour was drawn to select areas of high signal intensity adjacent to the epicardial surface of the left and right ventricles, resulting in output of an area measure (A). Areas of high signal intensity over the liver were not included in the PAT measure as this almost always represents adipose tissue below the diaphragm (B). bSSFP, balanced steady state free precession; CMR, cardiovascular magnetic resonance; PAT, pericardial adipose tissue; SOP, standard operating procedure. Images reproduced with permission of UK Biobank[®].

were manually drawn for the remaining 432 participants. For the purposes of model training and evaluation, the sample was randomly split into training ($n = 345$) and test ($n = 87$) sets. Image analysis was performed blind to participant details using CVI42[®] post-processing software (Version 5.11, Circle Cardiovascular Imaging Inc., Calgary, Canada). Contours were drawn by AB and cross-checked by ZRE.

Neural Network Architecture

As the size of PAT does not alter during the cardiac cycle, it may be quantified on static images, without consideration to cardiac motion. Thus, PAT quantification can be framed as a simple foreground-segmentation problem using a single frame per experimental subject, from which the area it occupies can be extracted. The task is to predict whether individual pixels represent a point of interest (i.e., within PAT) or are a part of the background.

Great progress has been made with automated medical image segmentation using fully convolutional neural networks (20, 21), particularly using encoder-decoder architectures (22). We developed a neural network using a Multi-residual U-net (MultiResUNet) base architecture (23) with the incorporation of a permanently active dropout layer (24) at the end of each multi-residual block (Figure 2). The best trade-off between overall segmentation accuracy and prediction of that accuracy was obtained with a dropout rate $r = 0.3$, which we found to be optimal for model performance. This was selected as the largest r value at which the segmentation quality was not statistically reduced relative to a non-stochastic network (Supplementary Figure 1). To incorporate a measure of uncertainty that can be used for QC, we used permanently active dropout layers to add a stochastic component to their network outputs, meaning that multiple Monte Carlo (MC) samples can be drawn for any given input (24). This MC sampling from a stochastic neural network generates N samples of predicted probability maps $\{P_1 \dots P_N\}$, from which thresholding at 0.5 can generate Boolean segmentation maps $\{S_1 \dots S_N\}$. For our foreground detection problem, the final segmentation S for each

voxel (x) is defined by thresholding the voxelwise mean of S :

$$S(x) = \begin{cases} 1 & \frac{\sum_{i=1}^N S_i(x)}{N} \geq 0.5 \\ 0 & \text{otherwise} \end{cases}$$

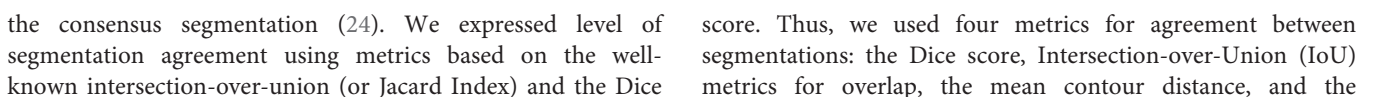
Network Implementation

The neural network was implemented and trained using the TensorFlow 2.0 Python API (25), software available from <https://www.tensorflow.org>. A combination of resampling images to enforce uniform resolution, robust data augmentation, and intensity normalization has previously been shown to increase the generalizability of segmentation networks (26). Inspired by this approach, all image data were first resampled to a uniform resolution (1.82×1.82 mm pixel spacing) and cropped/padded to a size of 208×208 pixels, including the test set. During training, data were augmented with rotation (up to 25°), altered resolution (resizing of up to 20%), random shearing up to 20%, and random panning of up to 25% of the image dimension. All data augmentation was performed on-the-fly, meaning that each complete training epoch utilized a different set of images. All images were normalized such that their pixel intensity range was between 0 and 1.

Training proceeded for a maximum of 300 complete epochs on a NVIDIA Tesla M40, using a batch size of eight images. The loss function used was the binary cross-entropy, and this was optimized using the Adam optimizer (27), with an initial learning rate of 0.01, $\beta_1 = 0.9$, $\beta_2 = 0.999$. The learning rate was decreased by a factor of 0.3 if, for 10 consecutive epochs, the loss was not decreasing. If 20 epochs elapsed with no decrease in the loss function, training was ceased and the weights yielding the lowest loss were restored.

Metrics for Assessment of Segmentation Agreement, Inter-observer Variability, and Model Performance

We evaluated agreement between manual segmentations of different expert observers (AB, ZRE, and SEP) and between manual and automated segmentation. When multiple MC samples are drawn from the stochastic neural network, their level of agreement is correlated with the quality of



symmetric Hausdorff distance (compares the closeness of foreground voxels borders). Both of the overlap metrics are bounded between 0 and 1, with 0 representing no overlap and 1 representing perfect overlap. For both of the distance metrics, lower distances represent closer agreement between segmentation results. In line with previous literature pertaining to QC (24, 28), we classified segmentation accuracy as poor, medium, or good based on Dice scores of <0.6 , $0.6\text{--}0.8$, and ≥ 0.8 respectively.

Correlation of Automated CMR PAT Quantification With CCT Measured PAT

We tested the correlation of our derived CMR PAT measurement with established CCT PAT measurements. We utilized the Barts Health NHS Trust local sub-study, from the Evaluation of Integrated Cardiac Imaging for the Detection and Characterization of Ischaemic Heart Disease (EVINCI) dataset (29), a clinical trial dataset including $n = 109$ participants with paired CMR and CCT imaging performed within a maximum interval of 37 days. We used the QFAT software (version 2.0, Cedars-Sinai Medical Center) for CCT PAT quantification (7, 8), which segments and quantifies epicardial and thoracic fat from non-contrast calcium scoring CCT. We utilized deep learning-based contouring with no manual adjustment. Voxels containing thoracic fat deposits were defined as those with a radiodensity of between -190 and -30 Hounsfield units. The total PAT volume was measured in cm^3 . For the CMR analysis, we used our automated pipeline: four-chamber cine images were resampled to a resolution of $1.82 \times 1.82 \text{ mm}$, padded/cropped to 208×208 pixels, normalized to have pixel intensities ranging between 0 and 1, and our stochastic network segmentation and QC applied with $N = 15$. Finally, the segmented area was extracted as the mean foreground area of the MC samples. Thus, we were able to test the performance of our automated image analysis pipeline on CMR studies within the EVINCI cohort and also to assess the correlation between these measures and CCT PAT quantification.

Association With Diabetes

Given the established association between diabetes and increased PAT, we tested the clinical validity of our PAT measures through consideration of associations with this condition. We applied our automated CMR PAT analysis tool to the entire UKB Imaging cohort for whom adequate imaging was available ($n = 42,928$). Diabetes was coded based on self-report of the diagnosis, self-reported use of “medication for diabetes,” or serum glycosylated hemoglobin $>48 \text{ mmol/mol}$. We tested the association of PAT area with diabetes status in multivariable logistic regression models with adjustment for age, sex, and body mass index (BMI). We present the results as odds ratio associated with a 10 cm^2 increase in PAT with corresponding 95% confidence intervals and p -values.

RESULTS

Model Training

We trained a MultiResUNet (23) with a Bayesian modification, such that multiple MC samples are drawn for each input, in order to perform QC and derive measures of uncertainty (24). Within this context, there is one hyperparameter that must be optimized after model training—that of the number (N) of MC samples drawn when segmenting an unseen image. When multiple MC samples are drawn during segmentation, they can be summarized in a number of ways. Firstly, they can be used to produce a single “best-guess” segmentation, *via* a simple voxel-wise voting procedure. It is expected that drawing more samples from a well-trained network will increase its accuracy, but with diminishing returns. Where the area of “foreground” pixels is particularly of interest (as in this use case, quantifying the area of PAT), we can report the mean and standard deviation of the areas across the N samples, which can be used for propagating uncertainty in downstream calculations. N was set to 15 for all further work, for the following reasons: Comparisons of segmentation accuracy with a deterministic neural network showed that consistent with prior work (24), there was no sacrifice in segmentation quality by using a stochastic network relative to a deterministic one when N was set to an appropriate level (Supplementary Figure 1A). Additionally, increasing N beyond 15 gave very little extra segmentation accuracy (Supplementary Figure 1A) or estimated standard deviation of area.

There are a number of different metrics that were proposed as correlates of final segmentation accuracy; however, it was concluded that, of these, both the most conceptually convenient and the most easily interpretable are those corresponding to often-used segmentation accuracy metrics—the Dice score and the IoU of the MC samples (24). We tested calculation of both IoU and Dice score globally or mean pairwise over the MC samples, finding that the best predictor of true segmentation accuracy was the mean pairwise Dice score between the MC samples, assessed on quantitative measures of agreement with the true Dice score of the test set (Supplementary Figure 2). Further details, as well as relevant equations, are detailed in the Supplementary Material.

Evaluation of Automated CMR PAT Segmentation Model Performance

The performance of the automated segmentation within the test set relative to manual segmentations was good and very similar to the agreement between human observers (mean Dice score = 0.8). This was the case both for raw segmentation metrics (Table 1) and under Bland–Altman analysis (Figures 3E–H). Arguably, this is the best performance that may be achieved by an automated segmentation algorithm and reflects the inherently challenging nature of the PAT segmentation task. A few cases ($n = 4$, 4.5%) had poor segmentation quality (Dice score < 0.6) (Figures 3A–D) and very large Hausdorff distances. This underlines the importance of the in-built QC feature, which would flag such cases. We also successfully applied the automated segmentation to the whole UKB imaging cohort ($n = 45,519$);

TABLE 1 | Standard segmentation performance metrics for pairwise comparisons of manually contoured PAT by 3 observers (O1–O3), and comparing automated segmentation with manual for the test set.

Metric	O1 vs. O2 (n = 50)	O1 vs. O3 (n = 50)	O2 vs. O3 (n = 50)	Automated vs. manual (O1) (n = 87)
Intersection-over-Union	0.689 (0.133)	0.636 (0.153)	0.678 (0.123)	0.677 (0.116)
Dice	0.808 (0.102)	0.766 (0.127)	0.801 (0.096)	0.800 (0.090)
Mean contour distance (mm)	2.78 (2.44)	3.83 (3.48)	3.79 (3.44)	2.79 (2.35)
Hausdorff distance (mm)	30.1 (23.8)	37.0 (28.6)	39.9 (28.8)	29.9 (22.9)

All values are mean (standard deviation).

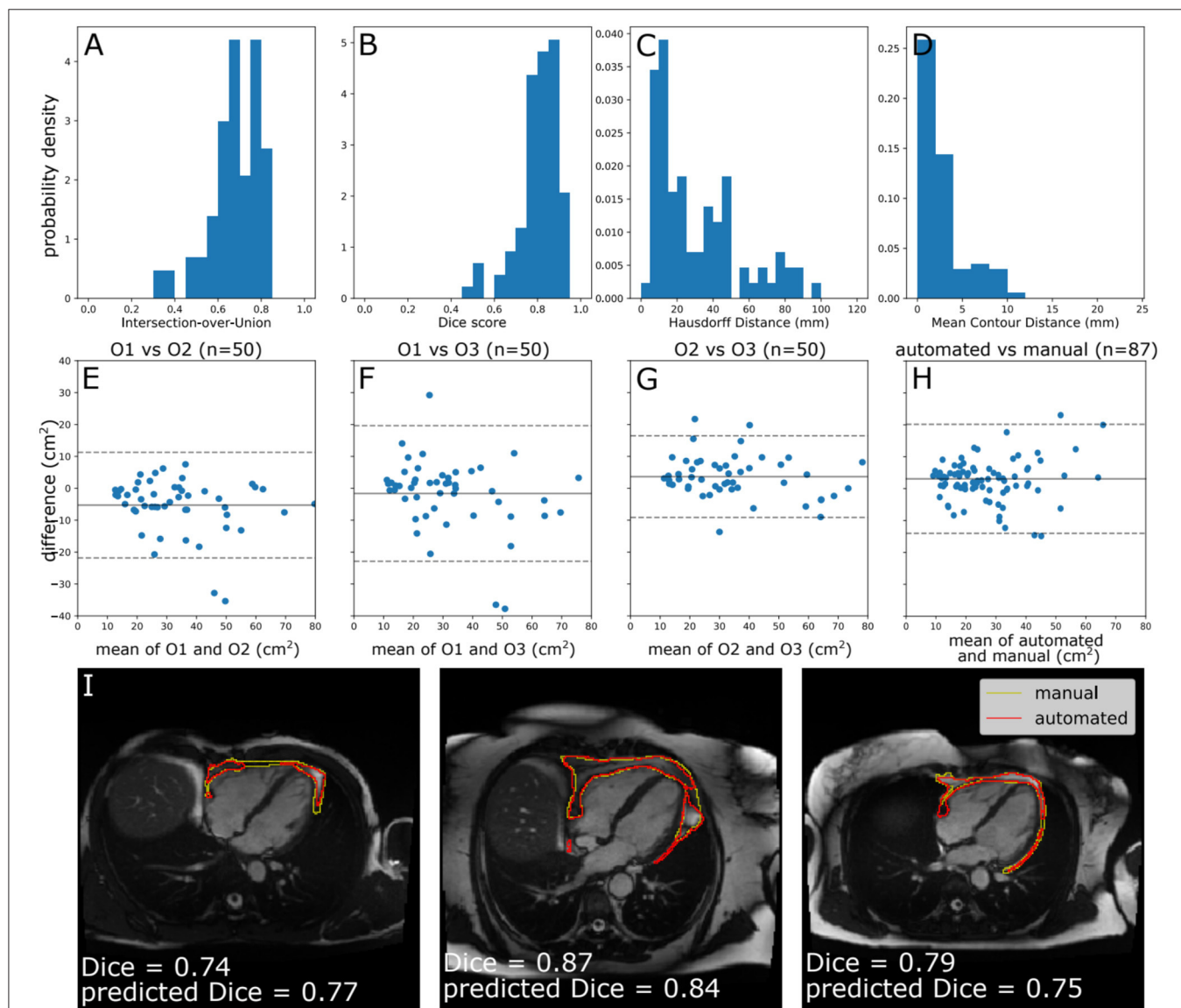


FIGURE 3 | Model performance. (A–D) Histograms of standard segmentation performance metrics on the test set (n = 87). (E–H) Bland–Altman plots of PAT area between manual measurement between measurements by different human observers, and a human observer (O1) and automated measurement. The x-axis denotes the average of two measurements and the y-axis denotes the difference between them. The dark line is the mean difference, and the dashed lines show ± 1.96 standard deviations from the mean. (E–G) show the inter-observer variability evaluated by three observers (O1–O3) on a randomly selected subset of the manually contoured training set (n = 50 subjects). (H) shows the agreement between automated and manual measurements in the manually contoured test set (n = 87 subjects). (I) Example segmentations from the test set, with annotations showing Dice score and the predicted Dice score. Images reproduced with permission of UK Biobank®.

94.3% of cases ($n = 42,928$) had predicted Dice score of medium or good quality (mean predicted Dice score = 0.77). Example segmentation results from the UKB test dataset can be seen in **Figure 3I**. The automated segmentation also performed well in the external EVINCII dataset, with the majority of studies having medium/good segmentation quality ($n = 103$, 94.4%), with an overall mean predicted Dice score of 0.78 (**Figure 4A**). Running on a laptop PC with an Intel® Core™ i7-1165G7 processor, using a MC sample size (N) of 15, the model and QC step took 2.1 s, including image pre-processing and final estimation of Dice score.

Correlation of Automated CMR PAT With CCT PAT Quantification

Within the EVINCII dataset, we tested the correlation of CMR PAT measures derived using our automated analysis with PAT derived using the QFAT tool from paired CCT scans. CMR studies with poor segmentation quality (predicted Dice score < 0.6) were excluded from the analysis ($n = 6$). For illustration, we present example segmentations with a range of Dice scores in **Figure 4C**. There was a strong, statistically significant correlation between CCT PAT volume and CMR PAT area (Pearson $r = 0.72$, p -value 5.3×10^{-18} , **Figure 4B**).

Application to the UK Biobank Imaging Cohort and Association With Diabetes

We applied our neural network to CMR scans from 45,519 UKB participants. We excluded cases with a segmentation Dice score of <0.6 ($n = 2,591$, 5.7%). The remaining 42,928 participants were included in the analysis; of these, 2,529 were diabetic. Consistent with existing evidence (2), larger PAT area was associated with greater risk of diabetes in univariate and multivariable models (**Table 2**). In fully adjusted models, every 10 cm² increase in PAT was associated with ~7% greater likelihood of diabetes independent of age, sex, and BMI.

DISCUSSION

Summary of Findings

We present a novel method for PAT quantification using standard-of-care CMR images, fully automated through a convolutional neural network with an in-built QC algorithm. The automated segmentation tool performed well within the test set, the whole UKB imaging cohort, and an external dataset, producing segmentation agreement close to that of human observers. Our segmentation method demonstrates validity against CCT PAT quantification, with a strong statistically significant correlation between paired CMR and CCT PAT measurements. Furthermore, we demonstrate, within the UKB, expected clinical association of CMR PAT with diabetes independent of age, sex, and BMI. Thus, the proposed CMR PAT method has great potential in facilitating investigation of the clinical significance of PAT in large population cohorts.

Comparison With Existing Work

Limited studies have attempted to quantify and study the clinical associations of CMR PAT. In a study from 1992,

Ross et al. (30) proposed a method for quantification of abdominal and subcutaneous fat on spin echo T1-weighted magnetic resonance imaging (MRI) sequences. They propose a signal intensity threshold for defining adipose tissue pixels; the area of adipose tissue regions was then calculated by summing adipose tissue pixels and multiplying by the pixel surface area; this area was then multiplied by slice thickness to derive the volume of adipose tissue. Unsupervised approaches for quantification of abdominal fat using this method have been developed using small datasets (31). More recently, these principles have been repurposed to derive CMR measures of thoracic fat using spin echo T1-weighted CMR acquisitions with zero slice gap and to investigate clinical associations in small cohorts (32–34). While this approach has had some utility, there are two fundamental limitations. Firstly, as the thresholding is based on pixel intensity levels, this is subject to variation based on technical (e.g., magnet strength, acquisition sequences, vendor) factors; as such, the threshold would need to be re-established depending on technical parameters. Secondly, because the methodology aims to derive a volumetric measure of adipose tissue, dedicated acquisitions with zero slice gap have been obtained. As standard protocols do not have zero slice gap (usually 5–8 mm slice gap), this approach, as it stands, is not suitable for application to standard-of-care CMR images.

Ding et al. (14) propose another approach for CMR PAT quantification; they present a limited study demonstrating feasibility of a fully automated pericardial fat quantification method from water/fat-resolved whole-heart non-contrast coronary magnetic resonance angiography. The very small sample size ($n = 10$) in this limited feasibility study precludes any meaningful assessment of model performance and the clinical validity of the proposed measurement is not known. Furthermore, as fat/water sequences are not routinely acquired as part of standard CMR studies, this methodology is unlikely to have wide application.

In a similar approach to our work, Rado et al. (15) quantify epicardial and pericardial fat areas from four-chamber cine images. They use a manual analysis protocol taking measurements in end-diastole and end-systole and making distinction between epicardial and pericardial fat area. They use their manual analysis measures ($n = 374$) to investigate associations with impaired glucose metabolism and left ventricular function. In developing our SOP, we also experimented with distinguishing between epicardial and pericardial fat areas. However, on inspection of a large number of studies, it became apparent that reliable distinction of these two areas was not possible for a substantial number of cases. Hence, we opted for a simpler approach of using a single en bloc contour. The strong correlation of our measure with CCT PAT quantification and observed associations with diabetes suggest that quantification according to our SOP does not detract from the potential utility of the measurement. Furthermore, the simplicity of our method enabled development of a fully automated analysis tool, which is essential for study of CMR PAT in large datasets.

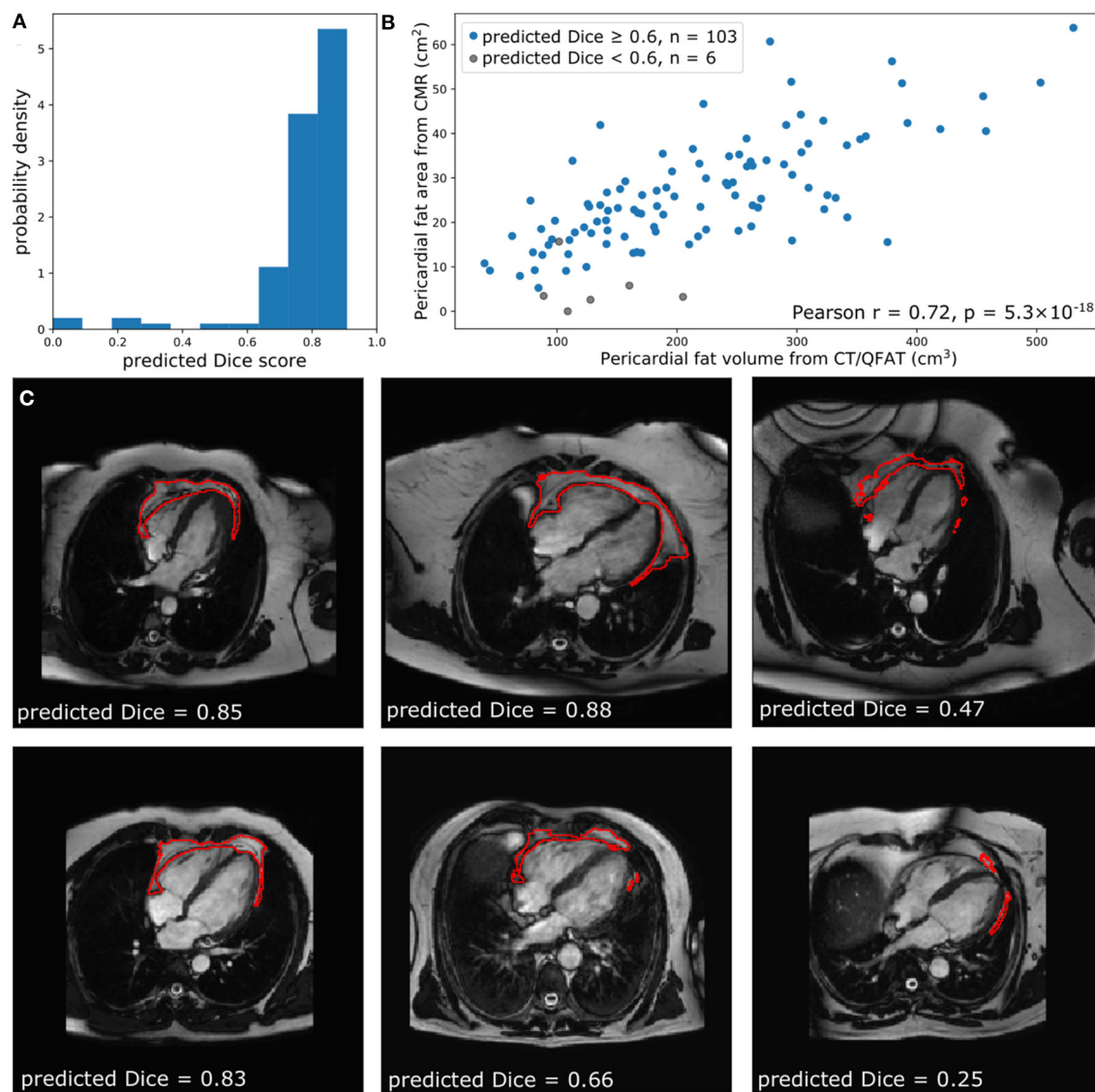


FIGURE 4 | Comparison of quantified PAT from CT and CMR. **(A)** The predicted Dice scores of the segmented data. **(B)** Correlation between PAT volume quantified via QFAT software and PAT area quantified using our method. Subjects with a predicted Dice < 0.6 were excluded from Pearson analysis. **(C)** Some example CMR images, their automatically segmented PAT, and the predicted segmentation quality are also shown for reference.

Technical Implications

In terms of the technical details of our neural network, the Multi-Residual U-net architecture (23) was vital, yielding far better results than “vanilla” U-nets (21) (data not shown). Meanwhile, a QC method has been demonstrated using an extension of a stochastic network, which approximates Bayesian MC sampling (24). Consistent with prior work, we find that measures of similarity between MC samples are correlated with segmentation quality; intuitively, this corresponds to how “sure” the network is of the output. However, in contrast, we found that the mean pairwise Dice score d^{MC} yielded best prediction, in contrast to the global intersection-over-union IoU^G used in previous work, and that an additional linear correction was required.

A potential consideration is whether better segmentation accuracy could be obtained *via* the removal of the stochastic component, thereby providing a single prediction. This would be undesirable for a number of reasons. Firstly, it is important to have some estimate of segmentation quality, which can only be provided if the actual segmentation is derived from our stochastic process. Secondly, a comparison with a non-deterministic MultiresUNet is provided in **Supplementary Figure 1**, and the accuracy is comparable with our stochastic model. However, note that dropout was not used within training of this network for the following reason: The MultiResUNet architecture makes extensive use of batch normalization. Because of a phenomenon known as variance shift, the combination of batch normalization

TABLE 2 | Logistic regression for prediction of diabetes in the UK Biobank dataset.

	Variable	Odds ratio	95% CI	p-value
Model 1	PAT Area (cm ²)	1.44	1.40, 1.47	8.43×10^{-164}
Model 2	PAT Area (cm ²)	1.36	1.32, 1.40	1.26×10^{-92}
	Male sex	1.32	1.20, 1.44	8.97×10^{-9}
	Age (years)	1.03	1.03, 1.04	4.66×10^{-30}
Model 3	PAT Area (cm ²)	1.07	1.03, 1.10	1.41×10^{-4}
	Male sex	1.80	1.63, 1.98	2.43×10^{-32}
	Age (years)	1.05	1.04, 1.05	7.91×10^{-54}
	BMI	1.18	1.17, 1.19	4.27×10^{-305}

The dataset includes 2,529 diabetics and 40,399 non-diabetics. Odds ratios for PAT area are indicated for an increase of 10 cm². BMI, body mass index; CI, confidence interval; PAT, pericardial adipose tissue.

and dropout often produces reduced accuracy once the dropout is “turned off” (35). However, this problem does not apply to our results, as the dropout is kept permanently active.

STRENGTHS AND LIMITATIONS

Using a modest manually annotated dataset, we have achieved good segmentation accuracy, with a mean Dice score of 0.80. However, the performance of machine learning tools may be reduced when applied to external datasets (decline in generalizability); to minimize this effect, we made use of robust data augmentation procedures during training (26). We are reassured by the good performance of our tool on the whole UKB imaging cohort and on the external EVINCII CMR dataset. We use a very simplified SOP taking PAT area measurement from a single 2D slice; clearly, this approach does not accurately quantify the volume of mediastinal fat. However, we demonstrate correlation of our measurement with established volumetric CCT PAT measure and replicate known clinical associations with diabetes. This suggests that our CMR PAT measure is valid as a marker to study associations with the PAT exposure. Indeed, we would argue that complicated acquisitions to quantify thoracic fat have hampered previous attempts to make wide practical use of this measure. A potential limitation of the method is that the model cannot distinguish between specific pathologies—e.g., fat or fluid. In UKB, and similar cohorts, we do not expect this to be a significant source of error, as there are very few participants with pericardial effusions. However, with broader application of the tool to clinical cohorts, such considerations may be more relevant. Further studies in large cohorts are now needed to establish the clinical utility of this CMR PAT measure in different settings and patient cohorts, and the proposed automated tool will facilitate such studies in large (and small) cohorts. As we use standard-of-care images, the CMR PAT measurement can be retrospectively applied to any existing dataset and, furthermore, if clinical value of this metric is established, it could be readily integrated into clinical practice.

CONCLUSION

We present a novel fully automated quality-controlled method for CMR PAT quantification using standard-of-care

four-chamber cine images. Throughout the study, we demonstrate that our QC method functions as intended, and we demonstrate that the segmentation performance of this method is equivalent to inter-observer variability and that the area extracted by our method is strongly correlated with measurements taken using reference standard CCT quantification. Finally, we demonstrate that our CMR PAT quantification method can recapitulate known clinical associations with diabetes. Overall, we present a novel tool that is now ready to be used for new research.

DATA AVAILABILITY STATEMENT

Publicly available datasets were analyzed in this study. This data can be found here: this project made use of data from UKB. Data access was granted through access application 2964. All derived data including pericardial fat area values and image segmentations will be returned to UKB, as per standard UKB data returns policy. Access to these data may be obtained by bone fide researchers through a formal application process. More information on data access procedures may be found through the UKB website: <https://www.ukbiobank.ac.uk>.

ETHICS STATEMENT

The studies involving human participants were reviewed and approved by UKB studies from the NHS National Research Ethics Service on 17th June 2011 (Ref 11/NW/0382) and extended on 10th May 2016 (Ref 16/NW/0274). Use of paired CT and CMR data from the EVINCI study was covered by a Data Protection Impact Assessment by the Data Protection Officer of Barts Health NHS Trust. For the original EVINCII study, local ethical approval was provided (REC Number: 10/H0721/79) and all subjects gave written informed consent. The patients/participants provided their written informed consent to participate in this study.

AUTHOR CONTRIBUTIONS

SEP, ZR-E, and MA conceived the idea, developed the contouring method, and contributed to manual analysis. AB led on the machine learning methodology, the main manual analysis of CMR data, and image analysis of cardiac CT data. ZR-E advised

on statistical analysis. AB and ZR-E wrote the manuscript. AML advised on technical methods. FP and DD advised on cardiac CT validation. DD advised on analysis of cardiac CT. NCH and SEP provided overall supervision. All authors contributed to drafting the final manuscript and provided critical feedback.

FUNDING

AB, SS, and SEP acknowledge support from the CAP-AI programme, London's first AI enabling programme focused on stimulating growth in the capital's AI Sector. CAP-AI was led by Capital Enterprise in partnership with Barts Health National Health Service (NHS) Trust and Digital Catapult and was funded by the European Regional Development Fund and Barts Charity. This work was supported by Health Data Research UK, an initiative funded by UK Research and Innovation, Department of Health and Social Care (England) and the devolved administrations, and leading medical research charities. ZR-E was supported by British Heart Foundation Clinical Research Training Fellowship No. FS/17/81/33318. SEP, PBM, and AML acknowledge support from the National Institute for Health Research (NIHR) Biomedical Research Centre at Barts. AML and SEP also received support from the SmartHeart Engineering and Physical Sciences Research Council (EPSRC) programme grant (www.nihr.ac.uk;EP/P001009/1). SEP and PBM acknowledge support from the NIHR Cardiovascular Biomedical Research Centre at Barts. SEP has received funding from the European Union's Horizon 2020

research and innovation programme under grant agreement No. 825903 (euCanSHare project). DD acknowledges support National Institutes of Health (NIH) grant no. 1R01HL133616 in development of the QFAT tool. SN was supported by the Oxford NIHR Biomedical Research Centre and the Oxford British Heart Foundation Centre of Research Excellence. DD was funded by NIH research grant NIH/NHLBI 1R01HL133616. NCH acknowledges support from the UK Medical Research Council (MRC #405050259, MRC LEU), NIHR Southampton Biomedical Research Centre, University of Southampton and University Hospital Southampton. This project was enabled through access to the MRC eMedLab Medical Bioinformatics infrastructure, supported by the Medical Research Council (www.mrc.ac.uk;MR/L016311/1).

ACKNOWLEDGMENTS

This study was conducted using the UKB resource under access application 2964. We would like to thank all the participants and staff involved with planning, collection, and analysis, including core lab analysis of the CMR imaging data.

SUPPLEMENTARY MATERIAL

The Supplementary Material for this article can be found online at: <https://www.frontiersin.org/articles/10.3389/fcvm.2021.677574/full#supplementary-material>

REFERENCES

- Wong CX, Ganesan AN, Selvanayagam JB. Epicardial fat and atrial fibrillation: current evidence, potential mechanisms, clinical implications, and future directions. *Eur Heart J*. (2017) 38:1294–302. doi: 10.1093/eurheartj/ehw045
- Li Y, Liu B, Li Y, Jing X, Deng S, Yan Y, et al. Epicardial fat tissue in patients with diabetes mellitus: a systematic review and meta-analysis. *Cardiovasc Diabetol*. (2019) 18:3. doi: 10.1186/s12933-019-0807-3
- Greif M, Becker A, Von Ziegler F, Lebherz C, Lehrke M, Broedl UC, et al. Pericardial adipose tissue determined by dual source CT is a risk factor for coronary atherosclerosis. *Arterioscler Thromb Vasc Biol*. (2009) 29:781–6. doi: 10.1161/ATVBAHA.108.180653
- Mahabadi AA, Berg MH, Lehmann N, Kalsch H, Bauer M, Kara K, et al. Association of epicardial fat with cardiovascular risk factors and incident myocardial infarction in the general population: the Heinz Nixdorf recall study. *J Am Coll Cardiol*. (2013) 61:1388–95. doi: 10.1016/j.jacc.2012.11.062
- Iacobellis G, Bianco AC. Epicardial adipose tissue: emerging physiological, pathophysiological and clinical features. *Trends Endocrinol Metab*. (2011) 22:450–7. doi: 10.1016/j.tem.2011.07.003
- Cheng KH, Chu CS, Lee KT, Lin TH, Hsieh CC, Chiu CC, et al. Adipocytokines and proinflammatory mediators from abdominal and epicardial adipose tissue in patients with coronary artery disease. *Int J Obes*. (2008) 32:268–74. doi: 10.1038/sj.ijo.0803726
- Commandeur F, Goeller M, Razipour A, Cadet S, Hell MM, Kwiecinski J, et al. Fully automated CT quantification of epicardial adipose tissue by deep learning: a multicenter study. *Radiol Artif Intell*. (2019) 1:e190045. doi: 10.1148/ryai.2019190045
- Eisenberg E, McElhinney PA, Commandeur F, Chen X, Cadet S, Goeller M, et al. Deep learning-based quantification of epicardial adipose tissue volume and attenuation predicts major adverse cardiovascular events in asymptomatic subjects. *Circ Cardiovasc Imaging*. (2020) 13:e009829. doi: 10.1161/CIRCIMAGING.119.009829
- Spearman JV, Meinel FG, Schoepf UJ, Apfaltrer P, Silverman JR, Krazinski AW, et al. Automated quantification of epicardial adipose tissue using CT angiography: evaluation of a prototype software. *Eur Radiol*. (2014) 24:519–26. doi: 10.1007/s00330-013-3052-2
- Petersen SE, Matthews PM, Bamberg F, Bluemke DA, Francis JM, Friedrich MG, et al. Imaging in population science: cardiovascular magnetic resonance in 100,000 participants of UK Biobank - rationale, challenges and approaches. *J Cardiovasc Magn Reson*. (2013) 15:46. doi: 10.1186/1532-429X-15-46
- Bild DE, Bluemke DA, Burke GL, Detrano R, Diez Roux AV, Folsom AR, et al. Multi-ethnic study of atherosclerosis: objectives and design. *Am J Epidemiol*. (2002) 156:871–81. doi: 10.1093/aje/kwfl113
- Salton CJ, Chuang ML, O'Donnell CJ, Kupka MJ, Larson MG, Kissinger KV, et al. Gender differences and normal left ventricular anatomy in an adult population free of hypertension: a cardiovascular magnetic resonance study of the Framingham Heart Study Offspring cohort. *J Am Coll Cardiol*. (2002) 39:1055–60. doi: 10.1016/S0735-1097(02)01712-6
- Petersen SE, Matthews PM, Francis JM, Robson MD, Zemrak F, Boubertakh R, et al. UK Biobank's cardiovascular magnetic resonance protocol. *J Cardiovasc Magn Reson*. (2015) 18:8. doi: 10.1186/s12968-016-0227-4
- Ding X, Pang J, Ren Z, Diaz-Zamudio M, Jiang C, Fan Z, et al. Automated pericardial fat quantification from coronary magnetic resonance angiography: feasibility study. *J Med Imaging*. (2016) 3:014002. doi: 10.1117/1.JMI.3.1.014002
- Rado SD, Lorbeer R, Gatidis S, Machann J, Storz C, Nikolaou K, et al. MRI-based assessment and characterization of epicardial and paracardial fat depots in the context of impaired glucose metabolism and subclinical left-ventricular alterations. *Br J Radiol*. (2019) 92:20180562. doi: 10.1259/bjr.20180562
- Sengupta PP, Shrestha S, Berthon B, Messas E, Donal E, Tison GH, et al. Proposed requirements for cardiovascular imaging-related machine learning

- evaluation (PRIME): a checklist: reviewed by the American College of Cardiology Healthcare Innovation Council. *JACC Cardiovasc Imaging*. (2020) 13:2017–35. doi: 10.1016/j.jcmg.2020.07.015
17. Raisi-Estabragh Z, Petersen SE. Cardiovascular research highlights from the UK Biobank: opportunities and challenges. *Cardiovasc Res*. (2020) 116:e12–5. doi: 10.1093/cvr/cvz294
 18. UK Biobank. *Protocol for a Large-Scale Prospective Epidemiological Resource*. (2007). Available at: <https://www.ukbiobank.ac.uk/wp-content/uploads/2011/11/UK-Biobank-Protocol.pdf> (accessed December 13, 2019).
 19. Raisi-Estabragh Z, Harvey NC, Neubauer S, Petersen SE. Cardiovascular magnetic resonance imaging in the UK Biobank: a major international health research resource. *Eur Hear J Cardiovasc Imaging*. (2020) 22:251–8. doi: 10.1093/ehjci/jeaa297
 20. Bai W, Sinclair M, Tarroni G, Oktay O, Rajchl M, Vaillant G, et al. Automated cardiovascular magnetic resonance image analysis with fully convolutional networks. *J Cardiovasc Magn Reson*. (2018) 20:65. doi: 10.1186/s12968-018-0471-x
 21. Ronneberger O, Fischer P, Brox T. U-net: convolutional networks for biomedical image segmentation. *Lect Notes Comput Sci*. (2015) 9351:234–41. doi: 10.1007/978-3-319-24574-4_28
 22. Drozdal M, Vorontsov E, Chartrand G, Kadoury S, Pal C. *Lecture Notes in Computer Science (Including Subseries Lecture Notes in Artificial Intelligence and Lecture Notes in Bioinformatics)*. (2016). Available at: <https://link.springer.com/bookseries/558> (accessed October 31, 2020).
 23. Ibtchaz N, Rahman MS. MultiResUNet: rethinking the U-Net architecture for multimodal biomedical image segmentation. *Neural Netw*. (2020) 121:74–87. doi: 10.1016/j.neunet.2019.08.025
 24. Roy AG, Conjeti S, Navab N, Wachinger C. Bayesian QuickNAT: model uncertainty in deep whole-brain segmentation for structure-wise quality control. *Neuroimage*. (2019) 195:11–22. doi: 10.1016/j.neuroimage.2019.03.042
 25. Abadi M, Agarwal A, Barham P, Brevdo E, Chen Z, Citro C, et al. *TensorFlow: Large-Scale Machine Learning on Heterogeneous Distributed Systems*. (2016). Available at: <http://arxiv.org/abs/1603.04467> (accessed June 15, 2021).
 26. Chen C, Bai W, Davies RH, Bhuvana AN, Manisty CH, Augusto JB, et al. Improving the generalizability of convolutional neural network-based segmentation on CMR images. *Front Cardiovasc Med*. (2020) 7:1–17. doi: 10.3389/fcvm.2020.00105
 27. Kingma DP, Ba JL. Adam: a method for stochastic optimization. In: *3rd Int Conf Learn Represent ICLR 2015 - Conf Track Proc*. San Diego, CA (2015). p. 1–15.
 28. Valindria VV, Lavdas I, Bai W, Kamnitsas K, Aboagye EO, Rockall AG, et al. Reverse classification accuracy: predicting segmentation performance in the absence of ground truth. *IEEE Transact Med Imaging*. (2017) 36:1597–606. doi: 10.1109/TMI.2017.2665165
 29. Neglia D, Rovai D, Caselli C, Pietila M, Teresinska A, Aguadé-Bruix S, et al. Detection of significant coronary artery disease by noninvasive anatomical and functional imaging. *Circ Cardiovasc Imaging*. (2015) 8:e002179. doi: 10.1161/CIRCIMAGING.114.002179
 30. Ross R, Leger L, Morris D, De Guise J, Guardo R. Quantification of adipose tissue by MRI: relationship with anthropometric variables. *J Appl Physiol*. (1992) 72:787–95. doi: 10.1152/jappl.1992.72.2.787
 31. Positano V, Gastaldelli A, Sironi AM, Santarelli MF, Lombardi M, Landini L. An accurate and robust method for unsupervised assessment of abdominal fat by MRI. *J Magn Reson Imaging*. (2004) 20:684–9. doi: 10.1002/jmri.20167
 32. Sicari R, Sironi AM, Petz R, Frassi F, Chubuchny V, De Marchi D, et al. Pericardial rather than epicardial fat is a cardiometabolic risk marker: an MRI vs echo study. *J Am Soc Echocardiogr*. (2011) 24:1156–62. doi: 10.1016/j.echo.2011.06.013
 33. Sironi AM, Gastaldelli A, Mari A, Ciociaro D, Positano V, Buzzigoli E, et al. Visceral fat in hypertension: influence on insulin resistance and β -cell function. *Hypertension*. (2004) 44:127–33. doi: 10.1161/01.HYP.0000137982.10191.0a
 34. Sironi AM, Petz R, De Marchi D, Buzzigoli E, Ciociaro D, Positano V, et al. Impact of increased visceral and cardiac fat on cardiometabolic risk and disease. *Diabet Med*. (2012) 29:622–7. doi: 10.1111/j.1464-5491.2011.03503.x
 35. Li X, Chen S, Hu X, Yang J. Understanding the disharmony between dropout and batch normalization by variance shift. In: *2019 IEEE/CVF Conference on Computer Vision and Pattern Recognition (CVPR)*. Long Beach, CA (2019). p. 2677–85.

Conflict of Interest: The intellectual property for the code presented in this paper belongs to Barts Health and not the authors.

Copyright © 2021 Bard, Raisi-Estabragh, Ardisino, Lee, Pugliese, Dey, Sarkar, Munroe, Neubauer, Harvey and Petersen. This is an open-access article distributed under the terms of the Creative Commons Attribution License (CC BY). The use, distribution or reproduction in other forums is permitted, provided the original author(s) and the copyright owner(s) are credited and that the original publication in this journal is cited, in accordance with accepted academic practice. No use, distribution or reproduction is permitted which does not comply with these terms.

Advantages of publishing in Frontiers



OPEN ACCESS

Articles are free to read
for greatest visibility
and readership



FAST PUBLICATION

Around 90 days
from submission
to decision



HIGH QUALITY PEER-REVIEW

Rigorous, collaborative,
and constructive
peer-review



TRANSPARENT PEER-REVIEW

Editors and reviewers
acknowledged by name
on published articles

Frontiers

Avenue du Tribunal-Fédéral 34
1005 Lausanne | Switzerland

Visit us: www.frontiersin.org

Contact us: frontiersin.org/about/contact



REPRODUCIBILITY OF RESEARCH

Support open data
and methods to enhance
research reproducibility



DIGITAL PUBLISHING

Articles designed
for optimal readership
across devices



FOLLOW US

@frontiersin



IMPACT METRICS

Advanced article metrics
track visibility across
digital media



EXTENSIVE PROMOTION

Marketing
and promotion
of impactful research



LOOP RESEARCH NETWORK

Our network
increases your
article's readership